UDK 66:54(05) CODEN HMIDA 8 ISSN 0367–598X

3

Hemijska industrija

Vol. 78

Časopis Saveza hemijskih inženjera Srbije

Chemical Industry

Specijalna sveska: Višefazni sistemi u hemijskom inženjerstvu

Special Issue: Multiphase Systems in Chemical Engineering

Posvećeno Profesoru Željku Grbavčiću

Dedicated to Professor Željko Grbavčić

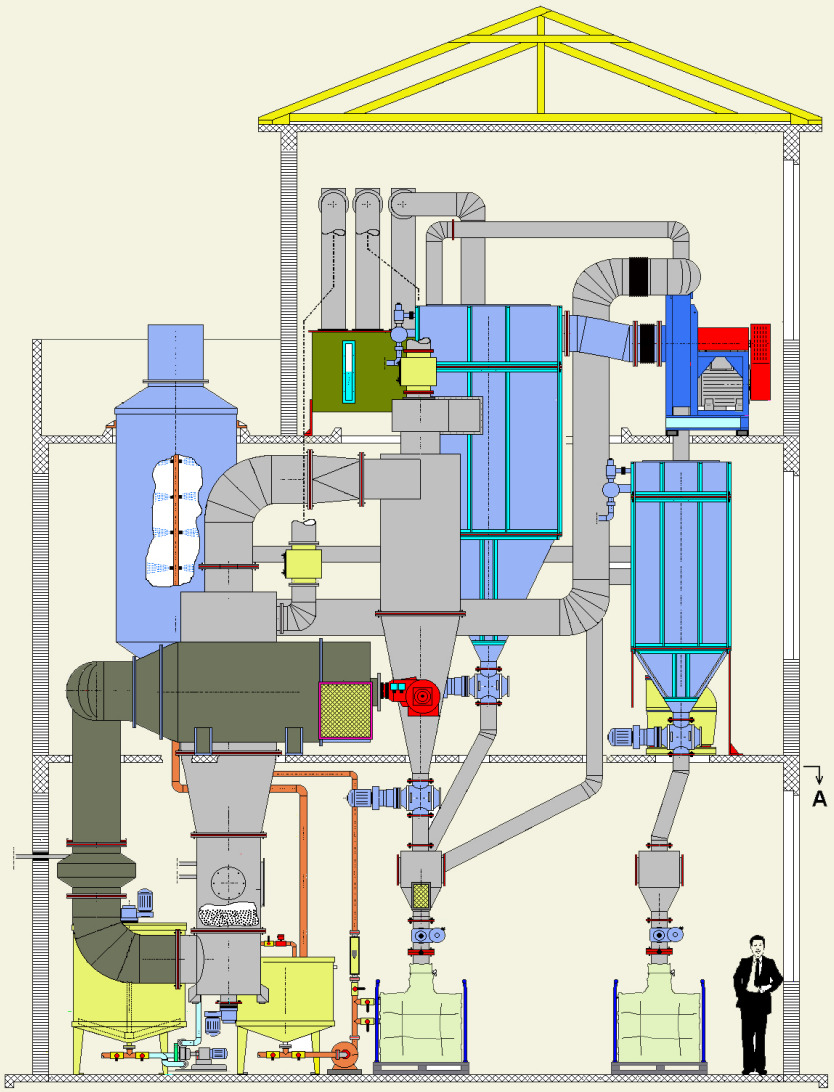

BEOGRAD, JULI-SEPTEMBAR 2024. HMIDA 8, 78(3) 131-314 (2024)

Aktivnosti Saveza hemijskih inženjera Srbije pomažu:

**MINISTARSTVO NAUKE,
TEHNOLOŠKOG RAZVOJA
I INOVACIJA
REPUBLIKE SRBIJE**

Tehnološko-metalurški fakultet
Univerziteta u Beogradu

Prirodno-matematički fakultet
Univerziteta u Novom Sadu

Institut za tehnologiju nuklearnih i
drugih mineralnih sirovina, Beograd

Tehnološki fakultet
Univerziteta u Novom Sadu

Institut za hemiju, tehnologiju i metalurgiju
Univerziteta u Beogradu

Fakultet tehničkih nauka
Univerziteta u Novom Sadu

Tehnološki fakultet
Univerziteta u Nišu, Leskovac

Fakultet tehničkih nauka
Univerziteta u Prištini
Kosovska Mitrovica

Institut IMS, Beograd

DCP HEMIGAL
Leskovac

Barič

Elixir Prahovo

Chemical Industry
Химическая промышленность

Hemijska industrija

Časopis Saveza hemijskih inženjera Srbije
Journal of the Association of Chemical Engineers of Serbia
Журнал Союза химических инженеров Сербии

VOL. 78 **Beograd, juli – septembar 2024.** **Broj 3**

Izdavač
Savez hemijskih inženjera Srbije
Beograd, Kneza Miloša 9/I

Glavni urednik
Bojana Obradović

Zamenica glavnog i odgovornog urednika
Emila Živković

Pomoćnik glavnog i odgovornog urednika
Ivana Drvenica

Urednici
Jelena Bajat, Dejan Bezbradica, Ivana Banković-Ilić, Dušan Mijin, Marija Nikolić, Đorđe Veljović, Tatjana Volkov-Husović

Članovi uredništva
Nikolaj Ostrovski, Milorad Cakić, Željko Čupić, Miodrag Lazić, Slobodan Petrović, Milovan Purenović, Aleksandar Spasić, Dragoslav Stoiljković, Radmila Šećerov-Sokolović, Slobodan Šerbanović, Nikola Nikačević, Svetomir Milojević

Članovi uredništva iz inostranstva
Dragomir Bukur (SAD), Jiri Hanika (Češka Republika), Valerij Meshalkin (Rusija), Ljubiša Radović (SAD), Constantinos Vayenas (Grčka)

Likovno-grafičko rešenje naslovne strane
Milan Jovanović

Redakcija
11000 Beograd, Kneza Miloša 9/I
Tel/fax: 011/3240-018
E-pošta: shi@ache.org.rs
www.ache.org.rs

Izlazi kvartalno, rukopisi se ne vraćaju

Za izdavača: Ivana T. Drvenica

Sekretar redakcije: Slavica Desnica

Izdavanje časopisa pomaže
Republika Srbija, Ministarstvo nauke, tehnološkog razvoja i inovacija

Uplata pretplate i oglasnog prostora vrši se na tekući račun Saveza hemijskih inženjera Srbije, Beograd, broj 205-2172-71, Komercijalna banka a.d., Beograd

Menadžer časopisa i kompjuterska priprema
Aleksandar Dekanski

Štampa
Razvojno-istraživački centar grafičkog inženjerstva, Tehnološko-metalurški fakultet, Univerzitet u Beogradu, Karnegijeva 4, 11000 Beograd

Indeksiranje
Radovi koji se publikuju u časopisu *Hemijska Industrija* ideksiraju se preko *Thompson Reuters Scietific®* servisa *Science Citation Index - Expanded™* i *Journal Citation Report (JCR)*

Specijalna sveska:
Višefazni sistemi u hemijskom inženjerstvu
Special Issue:
Multiphase Systems in Chemical Engineering

Gostujuće urednice / Guest Editors
Nevenka Bošković -Vragolović
University of Belgrade, Faculty of Technology and Metallurgy, Belgrade, Serbia
Zorana Arsenijević
University of Belgrade, Institute of Chemistry, Technology and Metallurgy, Belgrade, Serbia

SADRŽAJ/CONTENTS

SADRŽAJ nastavak
CONTENTS Continued

Multiphase systems in chemical engineering

Nevenka Bošković-Vragolović[1] and Zorana Arsenijević[2]

[1]*University of Belgrade, Faculty of Technology and Metallurgy, Karnegijeva 4, Belgrade, Serbia*
[2]*University of Belgrade, Institute of Chemistry, Technology and Metallurgy, Njegošvea 12, Belgrade, Serbia*

EDITORIAL

Available on-line at the Journal web address: http://www.ache.org.rs/HI/

Hem. Ind. **78(3)** 131-134 (2024)

We are pleased to present this special issue of the journal Hemijska industrija (Chemical Industry) dedicated to Professor Željko Grbavčić and his extraordinary scientific and professional contributions to the progress of chemical engineering, especially in the field of heterogeneous systems.

Dr. Željko Grbavčić (1948-2015) was a professor emeritus at the Faculty of Technology and Metallurgy at the University of Belgrade (FTM). He was born in Vrbas, where he began his primary education, and continued it in Belgrade, where he next graduated from high school. He obtained his B.Sc. in Chemical Engineering at the Faculty of Technology and Metallurgy in Belgrade in 1971 followed by the M.Sc. degree in 1975 and the PhD degree 1989 at the same Faculty. From 1972 to 1990, he worked at the Institute of Chemistry, Technology and Metallurgy (ICTM) in Belgrade, where he was at the position Director General from 1978 to 1980 and President of the ICTM Council from 1984 to 1988. In 1989 he was a visiting researcher at the Rensselaer Polytechnic Institute in Troy, USA. From 1990, he was employed as Assistant Professor at the FTM, followed by the appointment of Full Professor in 1995. In two mandates (1995 to 1998 and 2000 to 2004), he was appointed Vice Dean for Scientific research and collaboration with industry, FTM. He was also President of the FTM Council for two terms (2006 to 2012). In 2014, he was elected Professor Emeritus.

Since 2004, Prof. Željko Grbavčić was a member of the editorial board of the journal Hemijska industrija (Chemical Industry). From 2004 to 2010 he was President of the Management Board and from 2010 to 2015 President of the Association of Chemical Engineers, Serbia. He was also a corresponding member from 2004 and a full member since 2012 of the Academy of Engineering Sciences of Serbia (AINS). He was a member of the Serbian Chemical Society (SHD) and received the SHD Medal in 2008 for his outstanding contribution to the application of science in industry and for scientific and engineering achievements.

His journey into the world of chemical engineering began during his student years, when he met Professor Dragoljub Vuković, who recognized his undeniable talent for the chosen profession. He then entered the world of multiphase systems and left a permanent impression in this field.

The most important results of fundamental research in the field of multiphase systems, to which Professor Grbavčić devoted most of his attention, include (i) development of various techniques for experimental determination of transfer coefficients of momentum, heat and mass in fluidized beds, spout-fluidized beds and in pneumatic and hydraulic transport, (ii) development of mathematical models for determination of fluid-particle friction coefficients in particulate fluidized beds as well as basic fluid dynamic properties in spouted and spout-fluidized beds, and (iii) establishment of an analogy of momentum, heat and mass transfers in multiphase fluid-particle systems. In order to solve specific engineering problems, he has been intensively engaged in theoretical and experimental studies of drying processes of solutions, suspensions and pastes in moving particle beds, especially in fluidized beds, with the aim of developing drying processes with significantly lower energy consumption, as well as research into combined processes and multifunctional reactors for waste gas purification.

His overall scientific research has led to the publication of: 6 chapters in international and national monographs; 72 articles in prestigious international journals and 26 articles in leading national journals. He has presented 92 papers at international conferences and 76 papers at national conferences.

E-mail: nevenka@tmf.bg.ac.rs and zorana.arsenijevic@ihtm.bg.ac.rs

Professor Grbavčić led or participated in realization of: 22 national basic research as well as technological development projects funded by the Ministry of Science, 2 Yugoslav-American projects, 4 innovation projects, and over 40 technical and technological projects and investment studies that resulted in 7 innovative solutions. The immense engineering contribution of Professor Grbavčić is reflected in the construction of several industrial plants based on original process solutions.

After his transfer to the FTM, Professor Grbavčić began teaching, too, no less successfully. He taught subjects in several study programs, some of which are: Transfer Phenomena in Dispersed Systems, Mechanical Operations, Equipment Design in Chemical Industry, Process Scale-up, Multiphase Systems and others, for which he wrote 3 textbooks. Many colleagues and students recognized that there was much to learn from Professor Grbavčić. He was the supervisor at 9 doctoral theses, 11 master's theses, 49 bachelor's theses, 6 final BSc theses and 3 final MS theses, as well as he participated in numerous thesis defense committees at all study levels at the FTM, the Faculty of Technology in Novi Sad, Serbia, and the Technical Faculty in Bor, Serbia.

In the work that all researchers and professors are engaged in, an important and very demanding step is the application of the results and knowledge gained in practice, i.e. the connection between science and industry as well as the transfer of the experience gained to young colleagues. In all of this, Professor Grbavčić managed to embody the roles of scientist, engineer and professor. Despite his wide-ranging interests, he always found time to make contacts with colleagues and students and selflessly share his experience. Therefore, the merits of Professor Grbavčić are far greater than the numerous scientific papers, technical solutions and projects mentioned above. His approachable demeanor meant that his closest colleagues had in him first a great friend and then a teacher. All of us who worked and socialized with him will never forget his modesty, humor, energy, diligence, perseverance and vision.

The articles in this special issue dedicated to Professor Grbavčić come from different faculties and institutes and deal with different topics, but they have one common denominator: the authors of these articles pay tribute to their friend Professor Željko Grbavčić and his great contributions to the development of chemical engineering.

Višefazni sistemi u hemijskom inženjerstvu

Nevenka Bošković-Vragolović[1] i Zorana Arsenijević[2]

[1]Univerzitet u Beogradu, Tehnološko-metalurški fakultet, Karnegijeva 4, Beograd, Srbija
[2]Univerzitet u Beogradu, Institut za hemiju, tehnologiju i metalurgiju. Njegoševa 12, Beograd, Srbija

REČ UREDNIKA

Sa zadovoljstvom predstavljamo ovo specijalno izdanje časopisa Hemijska industrija posvećeno profesoru Željku Grbavčiću i njegovom izuzetnom naučnom i stručnom doprinosu u unapređenju hemijskog inženjerstva, a posebno u oblasti heterogenih sistema.

Dr Željko Grbavčić (1948-2015) bio je profesor emeritus na Tehnološko-metalurškom fakultetu Univerziteta u Beogradu. Rođen je u Vrbasu gde je počeo osnovno školovanje, a nastavio u Beogradu gde je završio i gimnaziju. Diplomirao je na Tehnološko-metalurškom fakultetu u Beogradu na Odseku za hemijsko inženjerstvo 1971. godine. Na istom fakultetu je magistrirao 1975. godine i doktorirao 1989. godine. Od 1972. do 1990. godine bio je zaposlen na Institutu za hemiju, tehnologiju i metalurgiju (IHTM) u Beogradu gde je stekao zvanje višeg naučnog saradnika. Od 1978-1980. godine obavljao je dužnost generalnog direktora IHTM, a od 1984-1988. godine bio je i predsednik Saveta IHTM. Tokom 1989. godine bio je na studijskom boravku na Politehničkom institutu Rensler (Rensselaer Polytechnic Institut), Troj, SAD. Od 1990. godine bio je zaposlen na Tehnološko-metalurškom fakultetu u zvanju docenta, gde je od 1995. radio u zvanju redovnog profesora. U periodu od 1995-1998. i 2000-2004. godine bio je prodekan za naučno istraživački rad i saradnju sa privredom. Od 2006-2012. godine u dva mandata je bio predesednik Saveta TMF. U zvanje profesora emeritusa izabran je 2014. godine.

Bio je član uredništva časopisa Hemijska industrija od 2004. godine. Od 2004.-2010. godine bio je predsednik Upravnog odbora, a od 2010.-2015. godine predsednik Skupštine Saveza hemijskih inženjera. Od 2004.-2012. godine bio je dopisni član, a od 2012. godine i redovni član Akademije inženjerskih nauka Srbije (AINS). Bio je član Srpskog hemijskog društva (SHD), a 2008. godine dobio je medalju SHD za izuzetan doprinos primeni nauke u industriji za naučne i inženjerske rezultate.

Njegov put u svet Hemijskog inženjerstva započeo je tokom studentskih dana u susretu sa profesorom Dragoljubom Vukovićem koji je u njemu prepoznao neosporan talenat za odabranu struku. Tada je zakoračio u svet višefaznih sistema i u toj oblasti ostavio neizbrisiv trag.

Najznačajniji rezultati fundamentalnih istraživanja u oblasti višefaznih sistema kojima se profesor Grbavčić najviše bavio su: razvoj različitih tehnika eksperimentalnog određivanja koeficijenata prenosa količine kretanja, toplote i mase u fluidizovanim slojevima, fontansko-fluidizovanim slojevima i pri pneumatskom i hidrauličkom transportu; razvoj matematičkih modela za određivanje koeficijenta trenja fluid-čestice u partikulativno fluidizovanim slojevima i za određivanje osnovnih fluido-dinamičkih karakteristika fontanskog i fontansko-fluidizovanog sloja; uspostavljanje analogije prenosa količine kretanja, toplote i mase u višefaznim sistemima fluid-čestice.

Celokupni naučno istraživački rad je rezultovao objavljivanjem: 6 poglavlja u međunarodnim i nacionalnim monografijama; 72 rada u prestižnim međunarodnim naučnim časopisima i 26 radova u vodećim nacionalnim časopisima. Saopštio je 92 rada na skupovima međunarodnog značaja i 76 na skupovima nacionalnog značaja.

U cilju rešavanja specifičnih inženjerskih problema intenzivno se bavio teorijskim i eksperimentalnim ispitivanjima procesa sušenja rastvora, suspenzija i pasta u pokretnim slojevima čestica, posebno u fluidizovanom sloju u cilju razvoja procesa sušenja uz znatno niži utrošak energije kao i istraživanjima kombinovanih postupaka i multifunkcionalnih reaktora za prečišćavanje otpadnih gasova.

Profesor Grbavčić je rukovodio odnosno učestvovao u realizaciji: 22 nacionalna projekta osnovnih istraživanja i tehnološkog razvoja resornog Ministarstva za nauku; 2 jugoslovensko-američka projekta; 4 inovaciona projekta; preko 40 tehničko tehnoloških projekata i investicionih elaborata odakle je proisteklo 7 tehničkih rešenja. Ogroman inženjerski

doprinos prof. Grbavčića ogleda se u izgradnji više industrijskih postrojenja koja su bazirana na originalnim procesnim rešenjima.

Prelaskom na fakultet profesor Grbavčić je počeo da se bavi, ništa manje uspešno, i nastavnim radom. Držao je predmete na više nastavnih programa, a neki od njih su: Fenomeni prenosa u disperznim sistemima, Mehaničke operacije, Projektovanje uređaja u hemijskoj industriji, Uvećanje razmera procesa, Višefazni sistemi i dr., za koje je napisao i 3 udžbenika. Da se od profesora Grbavčića može mnogo naučiti prepoznale su mnoge kolege i studenti tako da je bio mentor 9 doktorskih disertacija, 11 magistarskih radova, 49 diplomskih radova, 6 završnih radova i 3 master rada uz brojna učestvovanja u komisijama za odbrane radova na svim nivoima studija na Tehnološko-metalurškom fakultetu u Beogradu, Tehnološkom fakultetu u Novom Sadu i Tehničkom fakultetu u Boru.

U poslu kojim se bave svi istraživači i profesori važan i vrlo težak korak je da se dobijeni rezultati i znanja primene u praksi, odnosno da se spoji nauka i industrija i da se na kraju stečeno iskustvo podeli sa mladim kolegama. Upravo je u svemu tome uspeo profesor Grbavčić da u sebi objedini naučnika, inženjera i profesora. I pored svojih širokih interesovanja uvek je nalazio vremena za druženje i nesebično deljenje svojih iskustava i zbog toga su zasluge profesora Grbavčića mnogo veće od navedenih brojnih naučnih radova, tehničkih rešenja i projekata. Upravo neposredan pristup koji je imao značio je da su njegovi najbliži saradnici prvo u profesoru imali velikog prijatelja, a onda i učitelja. Svima nama koji su sa njim radili i družili se ostaje u sećanju zauvek njegova skromnost, duhovitost, energija, vrednoća, istrajnost i vizija.

Radovi u ovoj svesci posvećenoj profesoru Grbavčiću su stigli sa različitih fakulteta i instituta i razmatraju različite teme ali jedno im je zajedničko: autori ovih radova su odali poštovanje svom prijatelju profesoru Željku Grbavčiću i njegovim velikim zaslugama za razvoj hemijskog inženjerstva.

Material hold-up on inert particles in fluidized bed dryer

Mihal M. Đuriš[1], Zorana Lj. Arsenijević[1] and Tatjana S. Kaluđerović Radoičić[2]

[1]*University of Belgrade, Institute of Chemistry, Technology and Metallurgy, National Institute of the Republic of Serbia, Belgrade, Serbia*
[2]*University of Belgrade, Faculty of Technology and Metallurgy, Belgrade, Serbia*

Abstract

In this paper the influence of process parameters on the material hold-up in a fluidized bed dryer with inert particles was investigated. The experiments were performed in a pilot-scale dryer with a cylindrical column 0.215 m in diameter and 1.2 m height, with glass spheres of diameters d_p = 1.20 mm and 1.94 mm as inert particles. The material used for drying was $NaHCO_3$ slurry of two different concentrations, 10 and 20 wt.%. Dynamics of the material hold-up was determined for four different drying temperatures, in the range from 60 to 120 °C by taking the samples of coated particles during the drying process and measuring the mass with and without the coated material film. The obtained results showed strong positive dependence of the material hold-up on the initial slurry concentration as well as on the drying temperature. The rate of the material film coating formation is quicker at higher drying temperatures.

Keywords: Drying; slurry; powder material; process parameters; concentration; temperature.

Available on-line at the Journal web address: http://www.ache.org.rs/HI/

ORIGINAL SCIENTIFIC PAPER

UDC: 628.336.4:66.011

Hem. Ind. **78(3)** 135-145 (2024)

1. INTRODUCTION

Drying of solutions, slurries, and pastes to obtain the final product in powder form is a widespread process in chemical, pharmaceutical and food processing industries. There are many different techniques that can be applied for this purpose. The choice of the technique mainly depends on the initial moisture content and physical and rheological properties of the material to be dried. Techniques with better energy performance are favored, in combination with high drying rates and better control of the process. Both pre-drying and post-drying stages have an important influence on the selection of the appropriate dryer type for a particular application. Each type of dryer has specific characteristics that make it suitable or unsuitable for certain applications [1].

Drying of slurries in fluidized beds of inert materials was originally developed for drying pigments, chemicals, and some biomaterials to eliminate disadvantages of spray, drum, and paddle dryers [2-5]. This technology is based in principle on drying a thin layer of the slurry covering the surface of the inert particles (Figure 1) [6]. The main advantages of this drying process compared to other drying methods are: efficient heat and mass transfers due to the constant motion of particles; uniform drying as the particles are well mixed in the bed; high surface area-to-volume ratio of the fluidized bed which allows for efficient removal of moisture from the particles; better preservation of the dried product quality due to gentle fluidization and controlled drying conditions in the fluidized bed.

Mechanism of fluidized bed drying consists of three steps that occur simultaneously in different areas of the bed. In the first step, the slurry material forms a film that adheres to the surface of the inert particles. In the second step, the moisture is removed from the film material within very short time periods. The dry material remains in the form of a coating on the inert particle surfaces. In the final step, the coating is peeled off by friction and collisions and the dry material leaves the bed with the air stream. This final step is regarded as the critical step in the process, since the rate of material removal controls the magnitude of the surface available for the new material and establishment of a dynamic equilibrium in the system.

Corresponding authors: Mihal M. Đuriš, University of Belgrade, Institute of Chemistry, Technology and Metallurgy, National Institute of the Republic of Serbia, Njegoševa 12, 11000 Belgrade, Serbia
Paper received: 30 June 2023; Paper accepted: 25 July 2024; Paper published: 19 September 2024.
E-mail: mihal.djuris@ihtm.bg.ac.rs
https://doi.org/10.2298/HEMIND230630014D

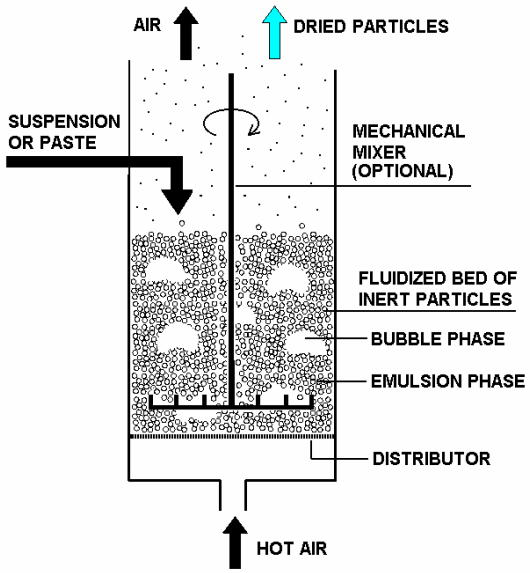

Figure 1. Drying of slurries in a fluidized bed of inert particles

Drying of fungicides and pesticides, other inorganic compounds and complexes was successfully tested in a semi-industrial plant for drying slurries and pastes in a fluidized bed of inert glass spheres [4-9]. Compared to other drying systems, this system can achieve several fold higher specific capacities per unit volume of the unit and thus lower investment costs. Other advantages of this process are continuity, elimination of the subsequent step of grinding of the powdered product, and significantly lower energy consumption per unit of evaporated moisture. The system is stable and very efficient. The efficiency of the system, expressed by the specific evaporation rate, specific heat consumption, and specific air consumption, is higher when the system operates at a larger temperature difference between the incoming air and the bed of inert particles. Due to the intensive mixing of the particles, the temperature of the bed is uniform throughout the volume thus avoiding the risk of local overheating. Stability of the process in terms of product quality (residual moisture) is decisively influenced by the stability of the flow of the input slurry or paste. In this system it is possible to treat all materials that do not stick together with inert particles [5,7].

Drying of slurries in a modified spouted bed with a draft tube is an attractive solution for drying of various organic and biological materials, which are generally sticky. For stable operation of the system, it is extremely important to achieve conditions where the slurry film on the surface of inert particles is completely dry after passing through the draft tube, as otherwise the inert particles in the annular zone may stick together and the bed may sinter. A drying model was developed based on a one-dimensional hydrodynamic model of a turbulent two-phase gas-mass particle flow in the acceleration zone, combined with mass and heat transfer balances along the draft tube. Such a model provides useful information for the design of dryers and for the simulation of drying processes [8,9].

A model was established previously to predict the particle circulation rate in a dryer with a spouted bed of inert particles and a central tube [10]. The proposed model was verified experimentally. Three quantities are known in the calculation algorithm (input parameters): gas velocity through the draft tube, the static pressure value in the draft tube, and the pressure gradient in the annular zone. The particle circulation velocity is calculated by using continuity and momentum balance equations for turbulent two-phase fluid-particle flow.

In previous studies, influences of the initial composition and nature of the slurry and thermal parameters of drying on continuity of the process were studied by observing accumulation of the dried material in a bed of inert particles over time and changes in fluid dynamic parameters [11,12]. Based on these investigations, a technical solution for a plant for drying slurries and pastes in a fluidized bed of inert material was created, *i.e.* an industrial prototype with an evaporation capacity of 650 kg_{H_2O} h^{-1} was realized, which has been in operation since March 2003.

Drying in a fluidized bed of inert particles is continually investigated due to its broad applications, possibilities for process optimization, improved quality, and achievement of energy efficiency. These studies contribute to further

understanding and development of this important industrial process [13-16]. Specific details and effectiveness of a spouted bed of inert particles drying system with draft tube depend on the specific application, type of inert particles used, process conditions, and other factors. Therefore, these systems are still being studied in detail to properly implement this drying process [17,18].

Hold-up in fluidized bed drying refers to the amount of material that is retained as a coating of inert particles within the bed during the drying process. It represents a fraction of the total dry powder that remains within the fluidized bed rather than being carried away by the drying air. The hold-up is influenced by various factors, including properties of the material being dried, such as particle size, density, and surface characteristics, as well as by operating parameters of the fluidized bed dryer.

Measuring and understanding hold-up dependence relations in fluidized bed drying is important for process optimization, as it helps determining the efficiency of the drying process and the extent of drying achieved. It also aids in designing and sizing the equipment, as well as evaluating the potential for material loss or carryover in the system.

Although there iwerextensive literature covering applications of fluidized bed of inert particles in drying of inorganic slurries and pastes and efficiencies of the process, there are only a few papers in which the influence of process parameters on the material hold-up on inert particles was investigated [11,12]. This information can be of great importance as it provides insights into potential optimal conditions under which the process can be operated.

In this paper, influences of the inert particle size and the bed temperature on the hold-up of $NaHCO_3$ in a fluidized bed dryer were investigated. The experiments were performed for two different particle sizes and four drying temperatures. The $NaHCO_3$ slurries of two different concentrations were used.

2. EXPERIMENTAL

Drying of $NaHCO_3$ slurries was performed in an experimental set-up schematically shown in Figure 2.

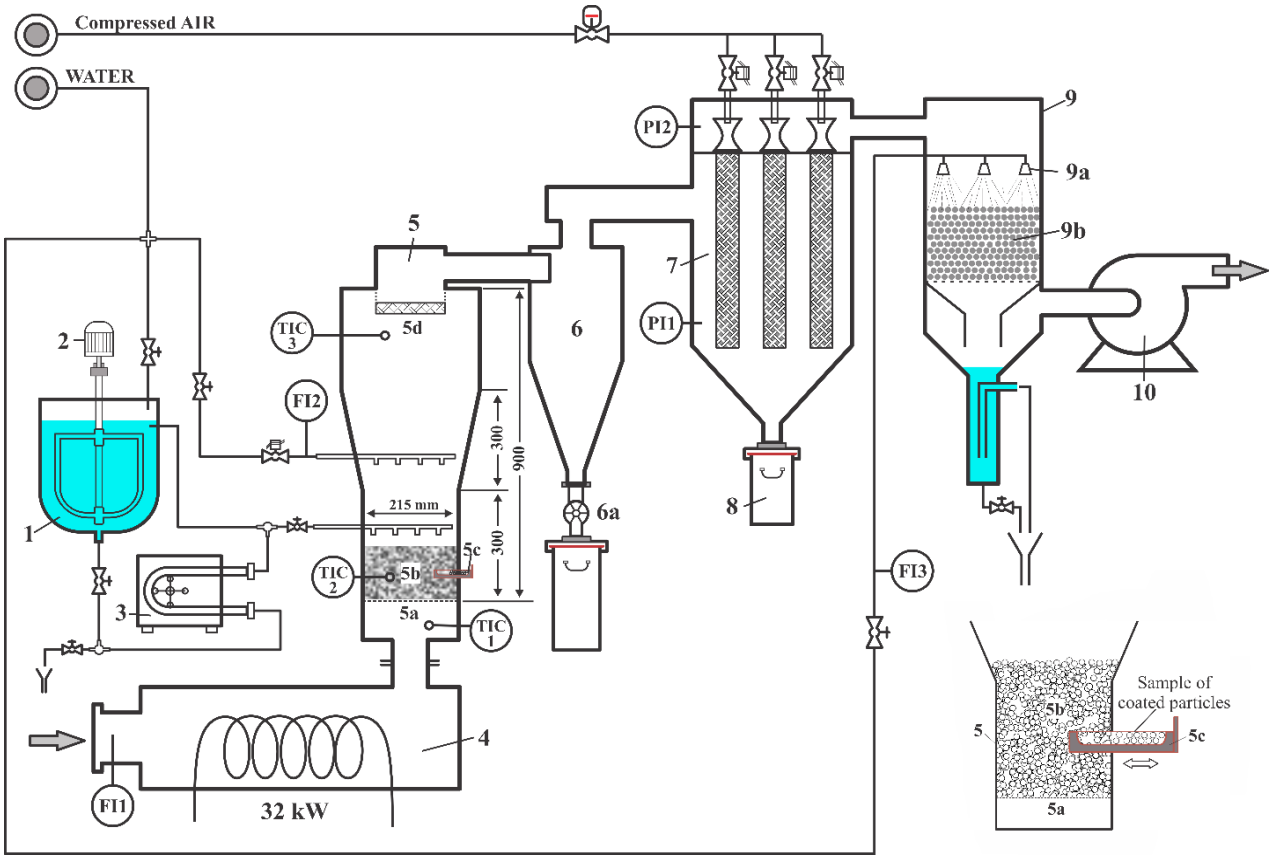

Figure 2. Fluidized bed dryer experimental set-up: 1-tank, 2-agitator, 3-pump, 4-air heater, 5-fluidization column, 5a-distributor, 5b-inert particles, 5c-scoop, 5d-deflector, 6-cyclone, 6a-rotary valve, 7-bag filter, 8-product containers, 9-scrubber, 9a-nozzle, 9b-packing, 10-blower

The main parts of the experimental set-up are fluidized bed of inert particles in which the drying process takes place, agitated slurry tank (1) with slurry pump (3), inlet air heater (4) and air blower (10). The fluidized bed column consisted of a cylindrical and a conical part (5). Dimensions of the cylindrical column are D_c = 215 mm i.d. and H = 300 mm, while the height of the conical section was 300 mm. An air blower is located at the end of the line in order to prevent material loss through fittings (the whole set-up operates under vacuum conditions). After the drying process, the powder is separated from the hot air stream by using a cyclone (6) and a bag filter (7). Before leaving the system, the exhaust air passes through a packed bed scrubber (9) in order to remove any residual particles. Besides these main elements, the set-up contains temperature probes, temperature indicators and controls, and flowrate and pressure indicators.

Temperature controller TIC1 maintains the inlet air temperature at the desired level. Temperature controller TIC2, which is located 0.7 m above the distributor plate and connected to a feeding device, keeps the outlet air temperature constant (T_{ge}). Temperature controller TIC3, which is also placed 0.7 m above the distributor plate, is set at a temperature 20°C above the outlet air temperature. Its role is to prevent overheating of the bed, in the case of feeding device failure, by introducing pure water into the system. During the experiments, the inlet and outlet air temperatures were continuously recorded by using a data acquisition system.

The cylindrical drying section of the fluidized bed was equipped with a specially designed scoop (5c) in order to allow for the extraction of coated inert particles at different time points during the experiment. At these occasions, a sample of 20 to 30 g of particles was taken out of the fluidization column at time intervals of 10 minutes. It was assumed that the mass of the removed particles is negligible as compared to the total mass of the fluidized bed. The removed coated particles were precisely weighted, and then were thoroughly cleaned of the dry material and rinsed in a fine mesh to reduce the possibility of particle loss. The hold-up of the material on the particle surfaces was calculated based on the mass difference between the coated and washed particles. In the experimental investigations, 2 types of inert glass spherical particles were used (Table 1). The minimum fluidization velocity of the particles used was determined in our previous work [19]. The experiments were performed using $NaHCO_3$ slurry concentrations of 10 and 20 wt.%. The inlet air temperature (T_{gi}) was maintained at 200 °C in all experiments, whereas the outlet air temperature (T_{ge}), which is the same as the bed temperature in the fluidized bed dryer was in the range 80 to 140 °C. The slurry flow rate was regulated so as to keep the bed temperature constant.

Table 1. Characteristics of the two types of inert glass particles

Inert particles	**d_p / mm**	**ρ / kg m^{-3}**	**U_{mF} /m s^{-1}[19]**
A	1.94	2640	1.114
B	1.20	2460	0.785

The experimental conditions are shown in Table 2.

Table 2. Experimental conditions in drying of $NaHCO_3$ slurries

Exp. No	Slurry concentration, wt.%	T_{gi} / °C	T_{ge} / °C	ΔT / °C	t / min	G_{sus} / kg h^{-1}
Particles A; d_p=1.94 mm, M_{bed}=5.00 kg						
1	10	200	60	140	135	15.70
2	10	200	80	120	160	13.53
3	10	200	100	100	170	11.57
4	10	200	120	80	165	8.98
5	20	200	60	140	126	16.59
6	20	200	80	120	147	14.45
7	20	200	100	100	135	11.17
8	20	200	120	80	194	9.33
Particles B: d_p = 1.20 mm, M_{bed} = 5.50 kg						
9	10	200	60	140	130	16.18
10	10	200	100	100	168	10.72
11	10	200	120	80	208	8.72
12	20	200	60	140	145	16.51
14	20	200	100	100	154	11.71
15	20	200	120	80	209	8.61

The mass flow rate of the slurry, G_{sus}, depended on the driving force ΔT, *i.e.* the temperature difference between T_{gi} and T_{ge}. ΔT was in the range between 80 and 140 °C.

General parameters of $NaHCO_3$ slurry drying in the fluidized bed of inert particles were determined: product residual moisture content and specific water evaporation rate.

The product residual moisture content was determined by drying the sample of the product from each run to the constant mass, and then determining the mass difference of the initial sample and final, completely dried powder. The specific water evaporation rate was calculated by the Equation (1):

$$w_{H_2O} = \frac{G_{H_2O}}{A_c} \tag{1}$$

Assuming that the bulk density of the material surrounding the inert particles is an arithmetic mean between the densities of the slurry and the dry powder, it is possible to estimate the thickness of the film surrounding the inert particles.

The Equations (2) and (3) used to this aim are the following [19]:

$$\delta_f = 1000\frac{d_p}{2}\left(\sqrt[3]{1+\frac{h}{100}\frac{\rho_p}{\rho_f}}-1\right) \tag{2}$$

where

$$h = 100\frac{\text{Mass of the coating}}{\text{Mass of the coated particles}} \tag{3}$$

Figure 3 illustrates a coated particle with a film of $NaHCO_3$ slurry, which has a thickness denoted as δ_f.

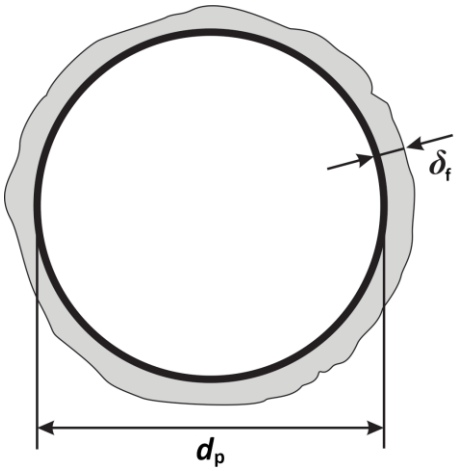

Figure 3. Illustration of a coated inert glass particle

The material hold-up can be also expressed as the mass of the product in contained the bed divided by the unit area of inert particles, kg m^{-2}, φ_p:

$$\varphi_p = \frac{M_{bed}h}{100A_p} \tag{4}$$

All experiments were performed in triplicate and the average values of these measurements are presented in the study.

3. RESULTS AND DISCUSSION

3. 1. General parameters of $NaHCO_3$ slurry drying in the experimental fluidized bed of inert particles

Product moisture content as a function of the drying temperature T_{ge} is shown in Figure 4 for all performed experiments. As expected, the dried powder moisture content decreases with the increase in the bed temperature and it was in the interval from 3 to 30 wt.%. The lowest values were achieved for T_{ge} = 120°C, which is the highest drying temperature used. The lower moisture content of the product at higher drying temperatures (T_{ge}) is explained by the

fact that the driving drying force (ΔT) is lower and therefore the mass flow of the suspension is also lower (*i.e.* the amount of water introduced into the drying column is lower), which affects the final moisture content in the product.

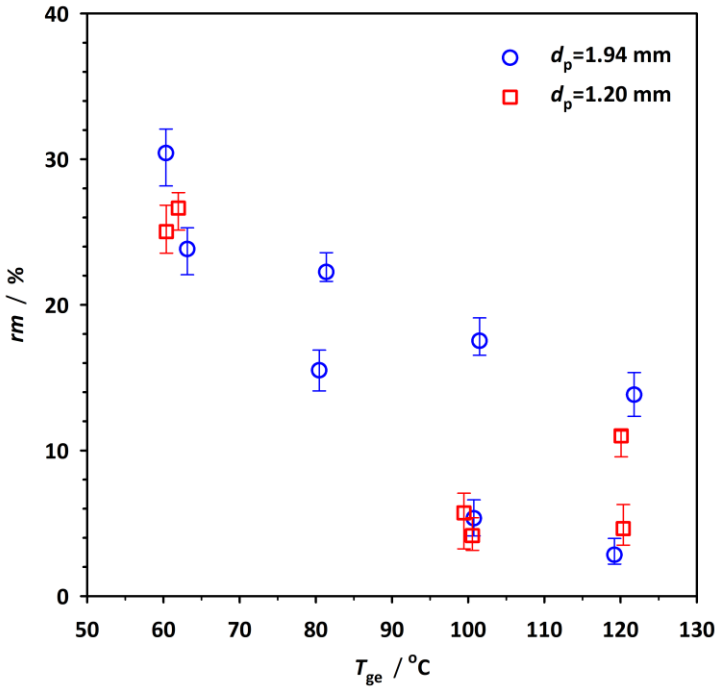

Figure 4. Product moisture content as a function of drying temperature T_{ge} for the two inert particle types used

Specific water evaporation rate ($kg_{H_2O}\ m^{-2}\ h^{-1}$) was calculated according to the Equation (1) as the mass of evaporated water per unit of cross-sectional area and time. Dependence of this parameter on the drying temperature T_{ge} at constant inlet air temperature T_{gi} is shown in Figure 5, for all experimental runs. As can be seen, the specific water evaporation rate is in the range from 190 to 420 kg $m^{-2}\ h^{-1}$ for both types of inert particles used without visible influence of the particle type.

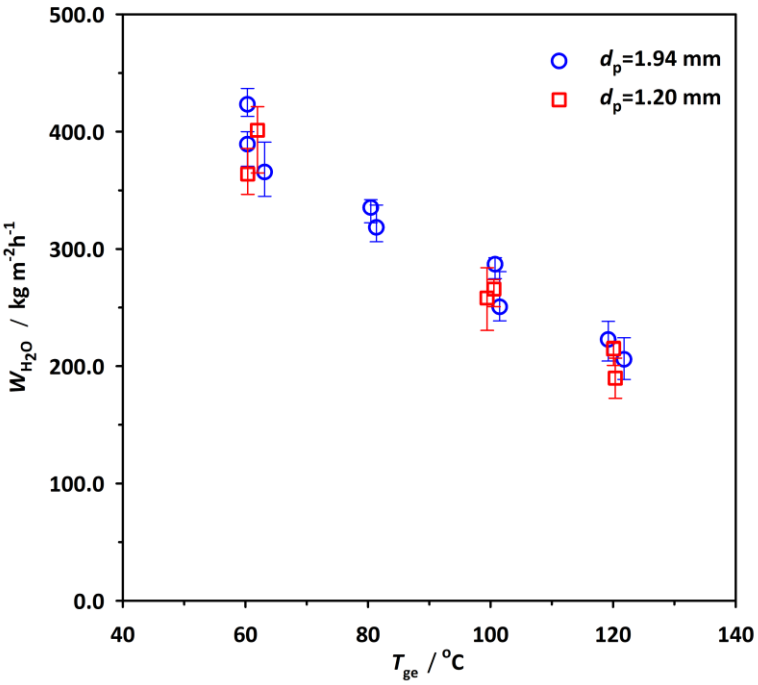

Figure 5. Specific water evaporation rate as a function of drying temperature T_{ge} for the two inert particle types used

3. 2. Material holdup analysis

For each experimental run shown in Table 2, dynamics of the film formation on surfaces of the inert particles were experimentally investigated. In all of the runs, the inlet air temperature was set to T_{gi} = 200 °C, while the outlet temperatures varied in the range T_{ge} = 60 to 120 °C.

Figure 6 shows the film thickness on inert particles A (d_p=1.94 mm) as a function of time, for four different ΔT and for both slurry concentrations.

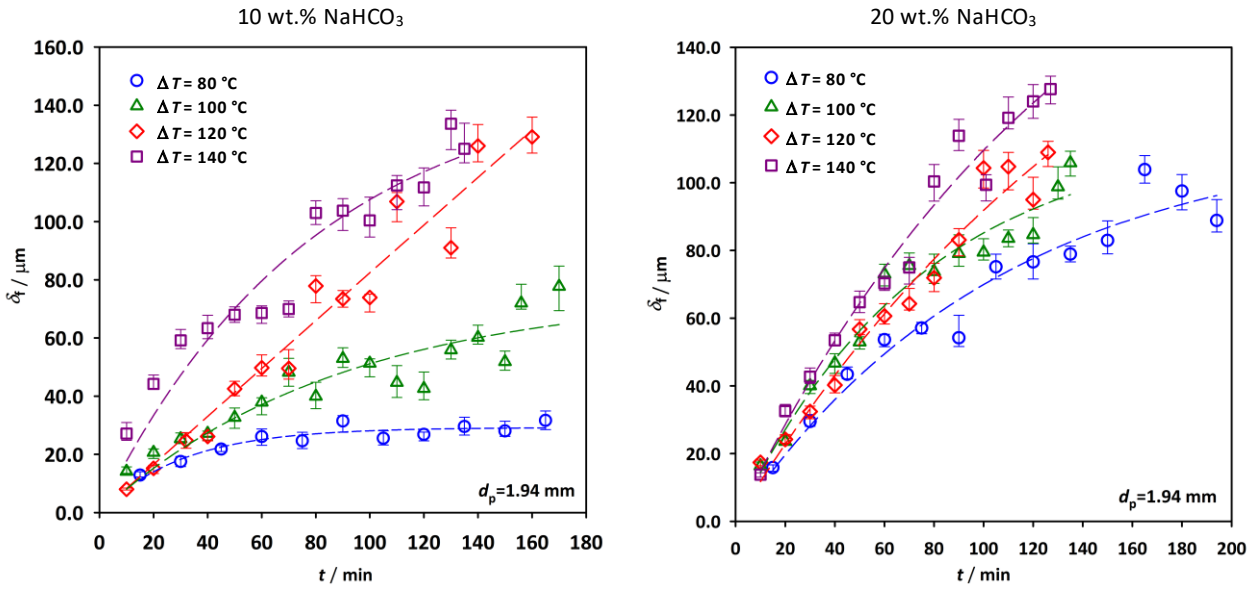

Figure 6. Dependence of the film thickness δ_f on drying time for inert particles A (d_p = 1.94 mm) (symbols; experimental data, lines: exponential model, Equation. (5) predictions)

As it can be seen in Figure 6, the film thickness on inert particles gradually increased with time. It is also evident that with the increase in ΔT, the film thickness increases more rapidly. During drying of the 10 wt.% slurry at ΔT = 80 °C, the film thickness increased from 15 to 22 μm during the time of 180 min, while at ΔT = 140 °C, the increase in film thickness is larger: for the same time of 180 min, the film thickness increased from 24 to 130 μm.

The greater increase in the film thickness with increasing T can be explained by the fact that the mass flow of slurry to be dried increases with higher ΔT, therefore, a larger amount of $NaHCO_3$ comes into the contact with surfaces of the inert particles.

Therefore, due to the larger mass flow of the slurry, a larger amount of $NaHCO_3$ is introduced into the layer of inert particles. Figure 6b shows dependence of the film thickness on drying time for 20 wt.% $NaHCO_3$ slurry. Due to the larger amount of $NaHCO_3$, a greater increase in the film thickness is noticeable, and regarding all experiments performed, the maximal film thickness of $\delta_f \approx$ 90 to 130 μm is reached faster compared to the experiment with 10 wt.% $NaHCO_3$. At ΔT = 8 °C, the film thickness increases from 15 to 25 μm during a time period of about 180 min for 10 wt.% slurry, while under the same conditions for 20 wt.% slurry, the film thickness increases to about 100 μm.

Analysis of the obtained results and dependences of the film thickness δ_f on drying time leads to the conclusion that the film thickness increases exponentially with time and can be described by a two-parameter equation:

$$\delta_f = a(1-e^{-bt}) \quad (5)$$

The results were adjusted to show the trend of growth and changes in the film thickness over time during the drying process. Figure 6 shows that the proposed two-parameter equation represents the experimental data well in all cases except for 10 wt.% $NaHCO_3$ at 120 °C, in which case the film thickness increases linearly. This can be explained by various reasons, such as the fact that under certain conditions the adhesiveness (stickiness) of sodium bicarbonate increases, which influences the drying process and the drying kinetics. The concentration of $NaHCO_3$ can also influence the viscosity and surface tension of the slurry, resulting in its unique impact on the drying process. Also, there could be experimental

errors or deviations in data collection for this experiment that led to the apparent deviation. Further experimental investigations and mathematical modeling are planned for future work in which this finding will be investigated in detail.

Figure 7 shows the film thickness on the inert particles as a function of time, for inert particles B (d_p = 1.20 mm) for three different ΔT and for both slurry concentrations.

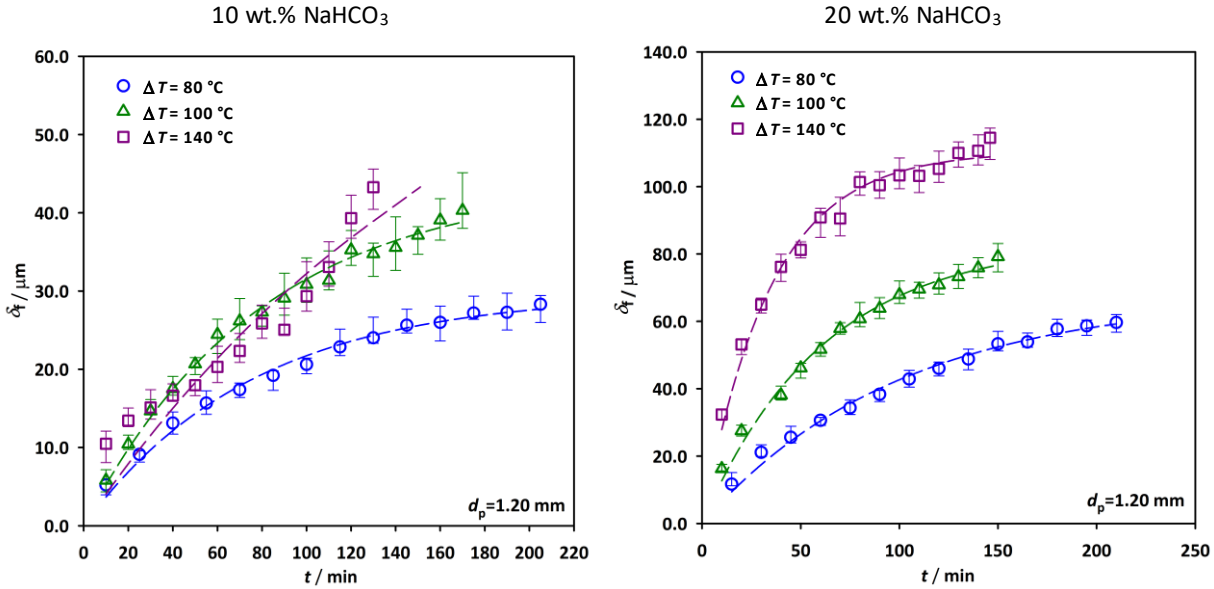

Figure 7. Dependence of film thickness δ_f from drying time for d_p = 1.20 mm (symbols: experimental data, line: exponential model, Equation (5) predictions)

A similar dependence can be observed for 1.2 mm particles: with an increase in the slurry flow rate, *i.e.*, at higher ΔT values, the rate of film thickness formation increases over time. During drying of the 10 wt.% slurry at ΔT = 80 °C, the film thickness increases from 5 to 28 μm during a time period of 205 min, while at ΔT = 140 °C, the increase in film thickness is larger: for a time period of 130 min, the film thickness increases from 10 to 43 μm. Due to the larger amount of $NaHCO_3$ (20 wt.% $NaHCO_3$ slurry), a greater increase in the film thickness is noticeable, and for all experiments performed, the maximal film thickness of $\delta_f \approx$ 60-115 μm is reached faster compared to the experiments with 10 % w/w $NaHCO_3$. At ΔT = 80 °C, the film thickness increases from 12 to 60 μm during a time of about 210 min for 20 wt.% slurry.

Figure 8 provides the comparison of the material hold-up for slurry concentrations of 10 and 20 wt.%. It can be seen that the hold-up is notably higher for the more concentrated slurry, when the rest of the conditions are the same.

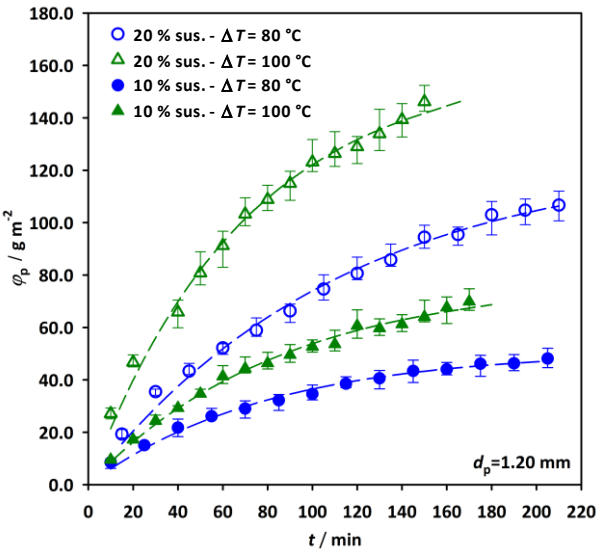

Figure 8. Comparison of the material hold-up for different slurry concentrations

Future research will include additional experimental measurements to investigate the influence of the process parameters on the film thickness and the moisture content in the end-product as well as to derive appropriate mathematical models.

4. CONCLUSIONS

Drying of solutions, suspensions and pastes in a fluidized bed of inert particles is a very effective technique for drying materials whose physical properties are such that the dried material can be easily separated from the particle surface after adhesion to the particle surface. The adhesion of the materials can be expressed numerically by the material hold-up and the film thickness on the surface of the inert particles. Knowing the hold-up of the particular material is very important for process optimization, as it helps determining efficiency of the drying process and the extent of drying that can be achieved in this type of system. In this paper, influences of the process parameters on the material hold-up in the fluidized bed dryer with inert particles for $NaHCO_3$ slurry drying were investigated. It was concluded that there is a strong dependence of the material hold-up on the initial slurry concentration as well as on the drying temperature. The material hold-up increased with the increase in the slurry initial concentration and with the increase in the ΔT. The rate of the material film coating formation is quicker at higher drying temperatures. The product moisture content was in the interval from 3 to 30 %. The lowest values were achieved for T_{ge}=120 °C, which is the highest drying temperature used. The results presented in this paper for $NaHCO_3$ slurry drying have shown that a fluidized bed dryer can be efficiently used for this material, while the established dependences are relevant for development of fluidized bed drying processes for other materials.

5. NOMENCLATURE

Latin symbols

A_c / m^2 - Cross-sectional area of the column at distributor plate
d_p / m - Inert particle diameter
D_c / m - Column diameter (at distributor plate)
G_{dm} / kg s^{-1} - Mass flowrate of dry matter
G_{H_2O} / kg s^{-1} - Water mass flowrate
G_{sus} / kg s^{-1} - Suspension mass flowrate
h / % - Material hold-up
M_{bed} / kg - Mass of the bed
rm / % - Product moisture content
T_{gi} / °C - Inlet air temperature
T_{ge} / °C - Outlet air temperature
T_0 / °C - Ambient temperature
U_{mF} / m s^{-1} - Minimum fluidization velocity at distributor plate
W_{H_2O} / kg m^{-2}s^{-1} - Specific water evaporation rate (G_{H_2O}/A_c)
x / kg kg^{-1} - Water content in the suspension (G_{H_2O}/G_{sus})

Greek symbols

δ_f / m - Material film thickness on inert particles
φ_p / kg m^{-2} - Mass of the product hold-up per inert particle surface
ρ_f / kg m^{-3} - Water density
ρ_p / kg m^{-3} - Particles density

Acknowledgements: This work was financially supported by the Ministry of Science, Technological Development and Innovation of the Republic of Serbia (Grant No. 451-03-66/2024-03/200026 and Grant No. 451-03-65/2024-03/200135).

REFERENCES

[1] Mujumdar AS. *Handbook of Industrial Drying*. 4th ed., New York, NY: Marcel Dekker; 2014 https://doi.org/10.1201/b17208.
[2] Kudra T., Mujumdar AS. Advanced Drying Technologies. 2nd ed., New York, NY: Marcel Dekker; 2009. ISBN 9781420073874.
[3] Romankov PG. *Drying*. In: Davidson JF, Harrison D, eds. Fluidization. London: Academic Press; 1971:569-598. ISBN 0122055500.

[4] Hadžismajlović DžE, Povrenović DS, Grbavčić ŽB, Vuković DV, Littman HA. *Spout-Fluid Bed Drier for Dilute Solutions Containing Solids*. In: Grace JR, Shemilt LW, Bergougnou MA, eds. Fluidization VI. New York, NY: Engineering Foundation; 1989:277-283. ISBN 0816904596, 9780816904594.

[5] Grbavcic ZB, Arsenijevic ZLJ, Garic-Grulovic RV. Drying of slurries in fluidized bed of inert particles. *Drying Technol.* 2004; 22:1793-1812. https://doi.org/10.1081/DRT-200032742.

[6] Đuriš MM, Kaluđerović Radoičić TS, Jaćimovski DR, Arsenijević ZLJ. High Efficiency Disperse Dryer - an innovative process for drying of solutions, suspensions and pastes in a fluidized bed of inert particles. *Hem Ind*. 2019; 73:213-222. https://doi.org/10.2298/HEMIND190626021D.

[7] Grbavcic ZB, Arsenijevic ZLJ, Garić-Grulovic RV. Drying of Suspension and Pastes in Fluidized Bed Inert Particles. *J Serb Chem Soc.* 2000; 65(12):963-975. https://www.shd.org.rs/JSCS/Vol65/No12-Pdf/JSCS12-13.pdf.

[8] Arsenijevic ZLJ, Grbavcic ZB, Garic-Grulovic RV. Drying of Suspensions in the Spouted Bed with Draft Tube. *Can J Chem Eng.* 2004; 82(3):450-464. https://doi.org/10.1002/cjce.5450820305.

[9] Arsenijevic ZLJ, Grbavcic ZB, Garic-Grulovic RV. Drying of Solutions and Suspensions in the Modified Spouted Bed with Draft Tube. *Thermal Science.* 2002; 6(2):47-70. https://doi.org/10.2298/TSCI0202047A.

[10] Arsenijevic ZLJ, Grbavcic ZB, Garic-Grulovic RV. Prediction of the particle circulation rate in the draft tube spouted bed suspension dryer. *J Serb Chem Soc.* 2006; 71(4):401-412. https://doi.org/10.2298/JSC0604401A.

[11] Arsenijevic ZLJ, Grbavcic ZB, Garic-Grulovic RV. The Material Hold-up and Residence Time in Fluidized Bed of Inert Particles Slurry Dryer. In: *Proceedings of 5th South East European Symposium on Research, Development and Implementation of New Energy Efficient and Ecologically Acceptable Technologies Applied to Energy Production, Chemical and Environmental Engineering*. Sunny Beach, Bulgaria, 2005, pp. 83-94.

[12] Kaluđerović Radoičić TS, Đuriš MM, Arsenijević ZLJ. Drying Of Suspensions And Solutions In Fluidized Bed Of Inert Particles – Material Hold-Up And Energy Efficiency Study. *Annals of the Faculty of Engineering Hunedoara – International Journal of Engineering* 202; XVIII(1): 137-142. https://annals.fih.upt.ro/pdf-full/2020/ANNALS-2020-1-20.pdf.

[13] Majumder P, Deb B, Gupta R, Sablani SS. A comprehensive review of fluidized bed drying: Sustainable design approaches, hydrodynamic and thermodynamic performance characteristics, and product quality. *Sustain. Energy Technol Assess*. 2022. 53: 102643. https://doi.org/10.1016/j.seta.2022.102643.

[14] Tatemoto Y, Mizukoshi R, Ehara W, Ishikawa E. Drying characteristics of food materials injected with organic solvents in a fluidized bed of inert particles under reduced pressure. *J Food Eng*. 2015; 158: 80–85. https://doi.org/10.1016/j.jfoodeng.2015.03.006.

[15] Kanga DH, Kimb S, Chunb WP, Lee DH. Drying characteristics of fine powders in an inert medium circulating fluidized bed with binary inert media. *J Ind Eng Chem*. 2017; 45: 266–276. https://doi.org/10.1016/j.jiec.2016.09.034.

[16] Tasirin SM, Puspasari I, Lun AW, Chai PV, Lee WT. Drying of kaffir lime leaves in a fluidized bed dryer with inert particles: Kinetics and quality determination. *Ind Crops Prod.* 2014. 61:19–201. https://doi.org/10.1016/j.indcrop.2014.07.004.

[17] Barros JPAA, Ferreira MC, Freire JT. Spouted bed drying on inert particles: Evaluation of particle size distribution of recovered, accumulated and elutriated powders. *Drying Technol.* 2020; 38(13): 1709-1720. https://doi.org/10.1080/07373937.2019.1656644.

[18] Huang D, Huang W, Huang S, Zhou F, Gong G, Li L, Sunden B. Applications of spouted bed technology in the drying of food products. *Drying Technol.* 2023. 182: 114880. https://doi.org/10.1016/j.lwt.2023.114880.

[19] Arsenijević Z., Sušenje suspenzija u industriji, Zadužbina Andrejević, Biblioteka Dissertatio, str. 1-100, Beograd, 2008. ISBN 978-86-7244-720-0 (in Serbian)

Zadržavanje materijala na inertnim česticama prilikom sušenja u fluidizovanom sloju

Mihal M. Đuriš[1], Zorana Lj. Arsenijević[1] i Tatjana S. Kaluđerović Radoičić[2]

[1]Univerzitet u Beogradu, Institut za hemiju tehnologiju i metalurgiju, Institut od nacionalnog značaja, Beograd, Srbija
[2]Univerzitet u Beogradu, Tehnološko-metalurški fakultet, Beograd, Srbija

(Naučni rad)

Izvod

U ovom radu ispitivan je uticaj procesnih parametara na zadržavanje materijala (engl. *hold-up*) u sušnici sa fluidizovanim slojem inertnih čestica. Eksperimenti su izvedeni u pilot postrojenju sa cilindričnom kolonom za sušenje prečnika 0,215 m i visine 1,2 m, uz korišćenje staklenih sfera prečnika 1,20 mm i 1,94 mm kao inertnih čestica. Materijal korišćen za sušenje je bila suspenzija $NaHCO_3$ dve različite koncentracije, 10 i 20 mas.%. Eksperimentalno je ispitana dinamika formiranja sloja materijala na inertnim česticama za četiri različite temperature sušenja, koje su se kretale od 60 do 120 °C, uzimanjem uzoraka obloženih čestica tokom procesa sušenja i merenjem njihove mase sa i bez formiranog filma materijala. Dobijeni rezultati su pokazali da postoji izražena zavisnost zadržavanja materijala od koncentracije suspenzije, kao i od temperature sušenja. Zadržavanje materijala se povećava sa povećanjem koncentracije suspenzije, a takođe i sa povećanjem temperature sušenja. Brzina formiranja filma materijala na inertnim česticama je veća na višim temperaturama sušenja.

Ključne reči: sušenje; suspenzija; praškaste materije; procesni parametri; koncentracija; temperatura

Local mass transfer and flow visualization around a cylinder in a liquid-solid fluidized bed

Nevenka M. Bošković-Vragolović[1], Danica V. Brzić[1], Katarina S. Šućurović[2], Rada V. Pjanović[1], Darko R. Jaćimovski[2] and Radmila V. Garić-Grulović[2]

[1]*University of Belgrade, Faculty of Technology and Metallurgy, Belgrade, Serbia*
[2]*University of Belgrade, Institute of Chemistry, Technology and Metallurgy - National Institute of the Republic of Serbia, Belgrade, Serbia*

Abstract

Adsorption method has been used for flow visualisation and determination of the local and average mass transfer coefficients around a horizontal cylinder in a liquid-solid fluidized bed. The obtained concentration fields on the adsorbent (silica-foils) represent a clear qualitative flow pattern around the cylinder. By comparison of the concentration fields around the cylinder in the single-phase flow and in the fluidized bed, a significant disturbance of the boundary layer by fluidized particles can be observed. Local mass transfer coefficients were shown to be dependent on the angular position around the cylinder with the maximum determined at the angle 140° (measured from the stagnant point 0°). Selected correlations were applied to predict the average mass transfer coefficients and the two best have shown deviations from the experimental data up to 5 %.

Keywords: Mass transfer coefficients; adsorption method; flow past cylinder; concentration fields.

Available on-line at the Journal web address: http://www.ache.org.rs/HI/

ORIGINAL SCIENTIFIC PAPER

UDC: 544.552.11:676.026.1

Hem. Ind. **78(3)** 147-159 (2024)

1. INTRODUCTION

Liquid-solid fluidized beds (FB) have extensive applications in chemical, biochemical, food and environmental industries. Most of the processes, which are performed in liquid-solid FBs involve mass transfer, like: adsorption/de-sorption, ion-exchange, chromatographic separations and heterogeneously catalyzed reactions. Fields of application of liquid-solid FBs expand continuously, especially in biotechnological processes where they are used as bioreactors [1] as well as in processes for water and waste-water treatment [2]. In design and operation of liquid-solid FBs, accurate determination of mass transfer rates plays a key role.

Investigations of mass transfer in FB refer commonly to the measurements of mass transfer coefficients (MTC) leading to numerous empirical correlations. One very good review of those correlations has been given by Kalaga *et al.* [3]. Most of the investigators have measured particle-to-liquid MTCs, presenting average MTCs over the surface of the particles [4,5,6]. Some of the correlations have been determined based on the mass transfer between an immersed object and liquid [7,8,9,10] or the column wall and liquid [11,12,13]. In these studies, both local and average values of MTC can be considered. Determination of local MTCs around an immersed object has both phenomenological and practical significance. The values of the local MTCs around the immersed object can help understanding the complex two-phase flow pattern in the vicinity of the object surface. On the other hand, local MTCs are important for processes in liquid-solid FBs with internals, like membrane FBs [14] or electrochemical FB reactors [15].

Local MTCs around an immersed cylinder have been reported in literature for gas-solid fluidized beds [16,17]. However, studies of local MTCs around a cylinder in liquid-solid FBs are lacking.

Adsorption method [18] has already been shown as a very convenient technique for flow visualization [19] and mass transfer studies [20]. The method is based on measurements of the concentration of an adsorbate (an organic dye) on

Corresponding authors:Katarina S. Šućurović, University of Belgrade, Institute of Chemistry, Technology and Metallurgy, National Institute of the Republic of Serbia, Njegoševa 12, 11000 Belgrade, Serbia
Paper received: 23 October 2023; Paper accepted: 9 September 2024; Paper published: 24 September 2024.
E-mail: katarina.sucurovic@ihtm.bg.ac.rs
https://doi.org/10.2298/HEMIND231023018B

the adsorbent surface after being shortly exposed to adsorption from a very dilute solution in the regime of mass transfer control. Previous studies on mass transfer around a cylinder in the single phase (liquid) flow by the adsorption method [21], have shown that the concentration boundary layer can be clearly visualized as well as separation of the boundary layer and formation of the wake.

In this work, mass transfer to the horizontal cylinder in a liquid-solid fluidized bed has been studied experimentally by the adsorption method. Visualisation of flow pattern has been used to evaluate the existence of the boundary layer around the cylinder and the extent of its erosion by fluidized particles, by comparison with the flow pattern for the single-phase flow. Local MTCs around the cylinder have been determined for different particle diameters and liquid velocities. Average MTCs have also been determined and compared with the values predicted by selected literature correlations.

2. EXPERIMENTAL

The experimental system is shown in Figure 1. The experiments were conducted in a column of a rectangular cross-section of 140×10 mm and height of 200 mm. A short cylinder with a diameter of 30 mm and a length of 10 mm, was placed horizontally in the column so that it touched the walls. Silica-gel foils (HPTLC LiChrospher Silica gel, Merck, Germany) with a thickness of 0.3 mm, were wrapped around the cylinder body and placed on the flat walls of the column. Particles used for fluidization were glass beads whose properties are given in Table 1. The initial height of the bed was 80 % of the column height. A diluted water solution of methylene blue (c_0 = 2.5 mg dm^{-3}, D_{AB} (20 °C) = 5.84·10^{-10} m^2 s^{-1}) was recirculated through the column by a pump. The flowrate was regulated by a valve and measured by a flowmeter. Duration of the experiments was determined experimentally in order to fulfill the condition of the pure diffusional regime [18], and it was 7 min in the single-phase flow and 5 min in the fluidized bed. After each experiment, the silica gel foils were dried for 24h in dark and subsequently scanned. The scanned images were processed by using the "Sigma Scan Pro 5" software (SigmaScan Software, Jandel Scientific, USA), providing color intensities on the foils.

Table 1. Characteristics of the particles

d_p / mm	ρ_p / kg m^{-3}	U_{mf} / m s^{-1}	U_t / m s^{-1}	ε_{mf}
1.2	2922	0.017	0.172	0.42
2.1	2484	0.027	0.313	0.45

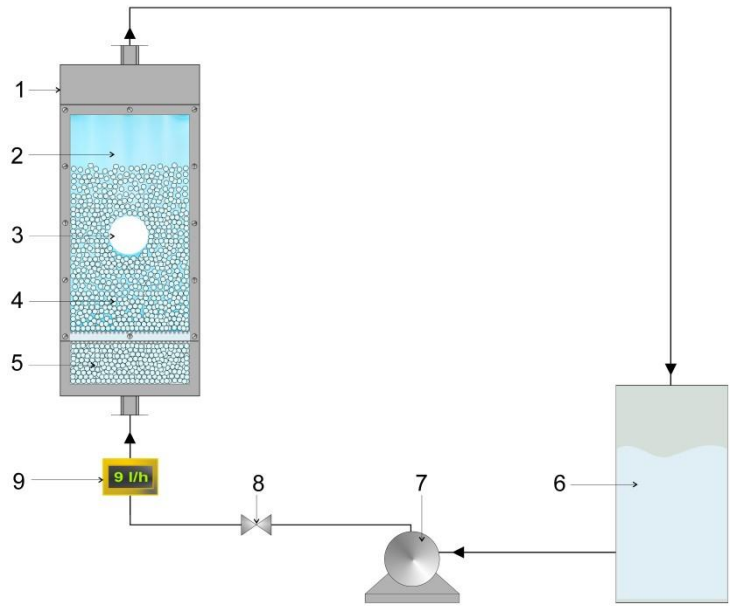

Figure 1. Schematic representation of the experimental set-up: 1 - column, 2 - silica-gel foils, 3 - cylinder, 4 -fluidized bed, 5 - distributor, 6 - tank, 7 - pump, 8 - valve, 9 - flow meter

As it has already been shown in theory of the adsorption method [18], the mass transfer coefficient can be calculated by Equation (1):

$$k = \frac{c_p}{c_0 t} \tag{1}$$

where c_0 is the bulk concentration of the adsorbate, t is the exposure time and c_p is the surface concentration.

The bulk concentration in the aqueous solution of methylene blue c_0 was determined by measuring the intensity of transmitted light at a wavelength of 665 nm by a spectrophotometer (MAPADA UV-3100, China) using a previously determined standard line. The surface concentration c_p was calculated based on the color intensity of the foils by using the previously determined standard line, which represents the function of the surface color intensity on the known surface concentration. The local mass transfer coefficients were determined by using Equation (1) based on the color intensity point by point, while the average mass transfer coefficients were calculated based on the color intensity of the whole surface of the foil.

By previous examination of the expansion of the fluidized bed, dependencies for determining the porosity were defined Equations (2) and (3):

$$\frac{U}{U_t} = 0.61\varepsilon^{1.92} \quad \text{(for } d_p = 1.2 \text{ mm)} \tag{2}$$

$$\frac{U}{U_t} = 0.50\varepsilon^{2.04} \quad \text{(for } d_p = 2.1 \text{ mm)} \tag{3}$$

Ranges of operating conditions in the experiments are shown in Table 2. Total of 17 experiments were performed, while each experiment was performed at least twice for assuring reliability of the measurements.

Table 2. Ranges of operating conditions in the experiments

	$\dot{V}$ / dm^3 min^{-1}	Re_c	Re_p	ε
Single phase flow	0.73-7.7	270-290 0	/	/
Fluidized bed	1.8-9.42	680-3600	20-240	0.44-0.85

3. RESULTS AND DISCUSSION

3. 1. Flow visualization

Application of the adsorption method provided determination of the concentration fields on silica-foils, where the colour intensity is directly proportional to the adsorbate concentration. Figures 2, 3 and 4 show chromatograms that correspond to the concentration fields in two views - the first is a scanned foil, and the second is a foil with marked fields of the same colour intensity. Figure 2 represents comparison of the concentration fields on the column wall for the single-phase flow around the cylinder and in the fluidized bed at almost the same liquid velocity.

In the single-phase flow, the concentration field provides a clear visualization of the flow pattern, which represents a typical discontinuous boundary layer around an immersed object indicated by a lighter blue colour (Fig. 2a). Separation of the boundary layer occurs at the angle of approximately 90° measured from the stagnant point 0° and indicated by widening of the darker blue zone. The obtained result is in accordance with the literature value for the experimental regime (Re_c = 1000-200,000) [22]. The formation of the wake and the reverse flow are visualized above the cylinder.

In the fluidized bed at the almost the same Re_c number (Fig. 2b), the concentration field is considerably more uniform and only a week radial pattern around the cylinder can be observed. It can be concluded that movements of the particles in the fluidized bed significantly disturb formation and separation of the boundary layer. However, certain variations in the colour intensity indicates local distribution of mass transfer rates around the cylinder, which will be further analyzed by means of the values of local MTCs (Section 3.2).

Figures 3 and 4 show chromatograms during fluid flow around the cylinder in the presence of particles with a diameter of 1.2 mm and 2.1 mm, respectively.

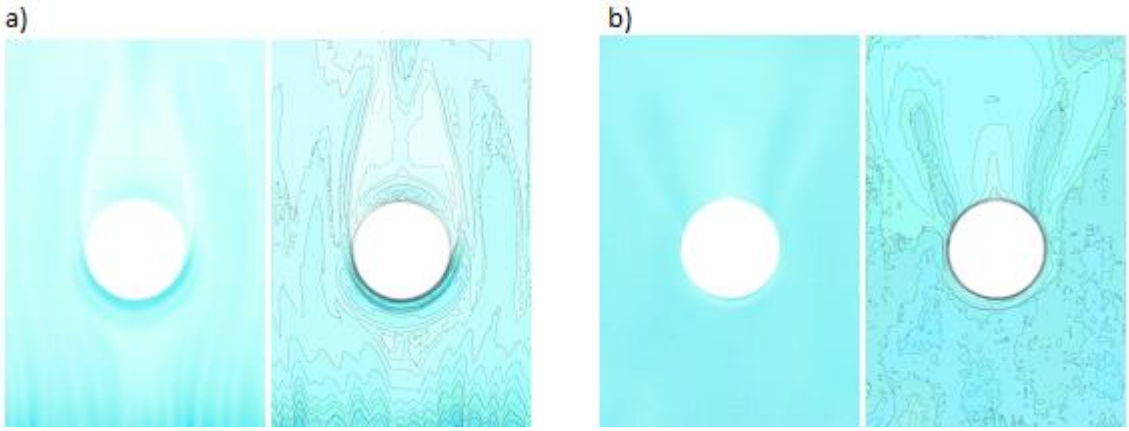

Figure 2. Scanned foils and chromatograms of concentration fields for: a) single phase flow (U = 0.053 m s^{-1}, Re_c = 1699), b) fluidized bed, d_p = 1.2 mm (U = 0.05 m s^{-1}, Re_c = 1612)

Figure 3a shows the flow around a cylinder in a packed bed of particles at the superficial velocity of 0.65·U_{mf}. It is noted that the presence of the cylinder affects acceleration of the flow around it and that the individual particles which started to move even at that velocity, cannot be visually observed. Outside the zone close to the cylinder, stagnant particle s are clearly visible with local staining around each individual particle. Figures 3b, 3c, and 3d show chromatograms in fluidized beds. At velocities slightly higher than the minimum fluidization velocity (Figure 3b, U/U_{mf} = 1.2), different staining can be observed around the cylinder, lighter at the bottom and the top of the cylinder and slightly darker on the sides. The lighter areas indicate lower mass transfer rates and lower flow velocities, which is especially pronounced at the top of the cylinder where the particles were in the packed state. With the increase in the superficial velocity (Fig. 3c, U/U_{mf} = 2.9; Fig. 3d, U/U_{mf} = 4.2) colour differences on the cylinder surfaces are less pronounced.

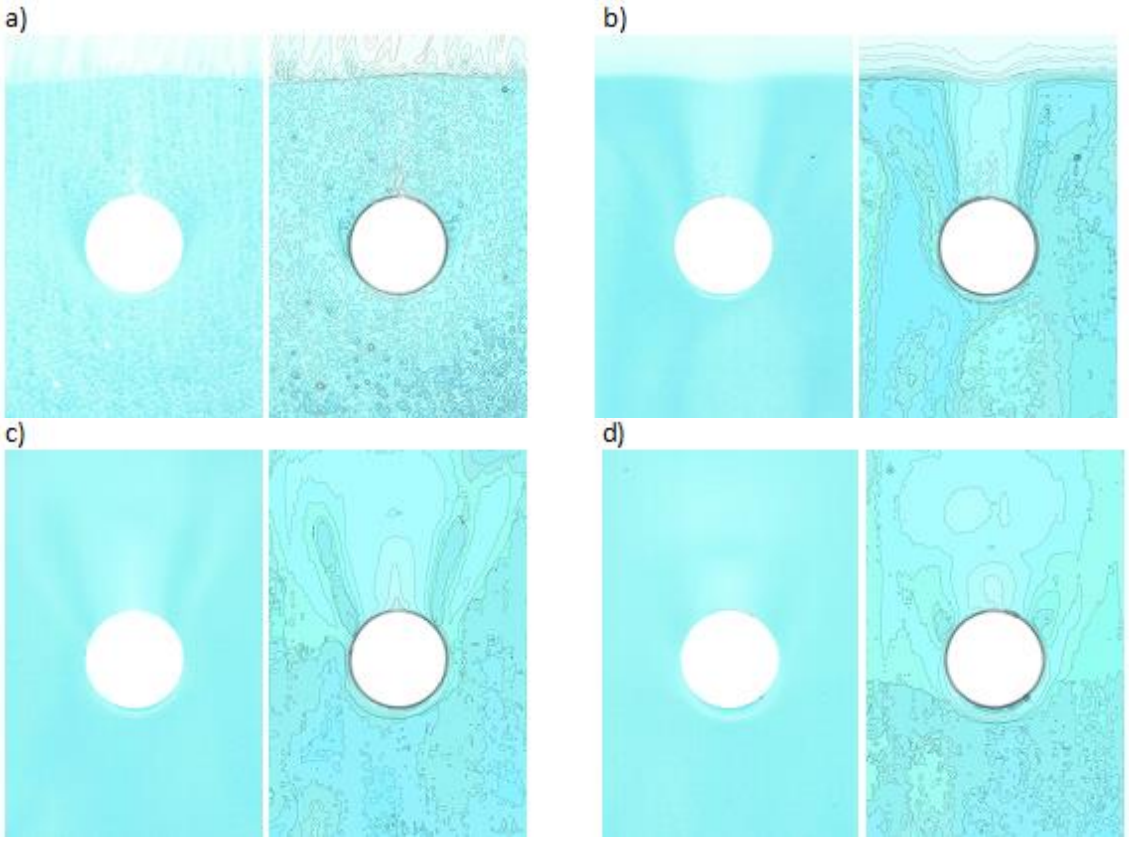

Figure 3. Scanned foils and chromatograms of concentration fields, d_p = 1.2 mm: a) packed bed (U = 0.011 m s^{-1}, U/U_{mf} = 0.65) and fluidized beds: b) U = 0.021 m s^{-1}, U/U_{mf} = 1.20, c) U = 0.05 m s^{-1}, U/U_{mf} = 2.9, d) U = 0.071 m s^{-1}, U/U_{mf} = 4.2

Figure 4 shows chromatograms obtained in the presence of particles of 2.1 mm in diameter at fluid velocities in the range U/U_{mf} = 0.67-4.1 regarding the minimum fluidization velocity. At a velocity lower than the minimum fluidization velocity (Fig. 4a), the influence of the cylinder on the movement of the particles has not been observed. All particles are in the packed bed, and the intensity of mass transfer and local flow around each particle can be clearly seen. At velocities higher than the minimum fluidization velocity (U/U_{mf} = 1.4, Fig. 4b), packed particles remain on the top of the cylinder. An approximately uniform staining of the surface can be observed at a velocity that is 2.6-fold of the minimum fluidization velocity (Fig. 4c). By further increasing the flow velocity (U/U_{mf} = 4.1, Fig.4d) variations in the colour intensity appear again.

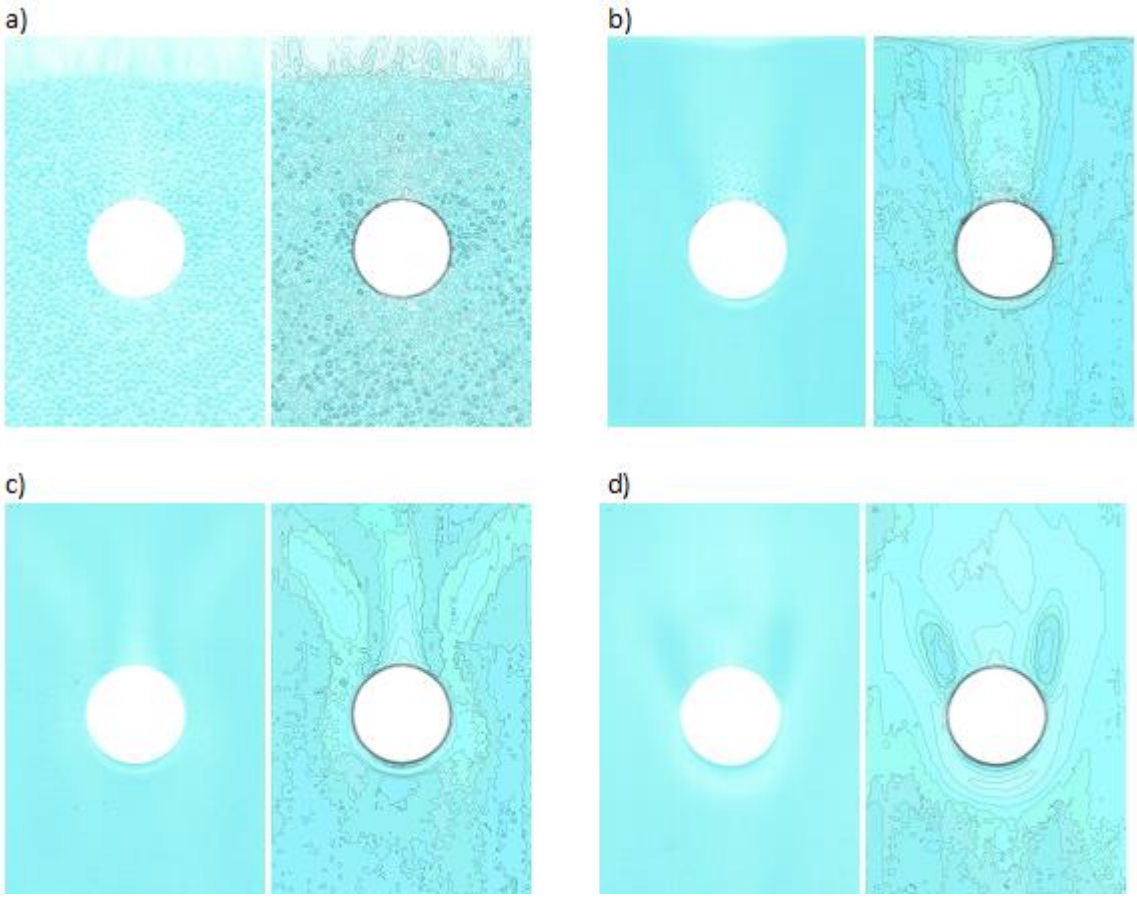

Figure 4. Scanned foils and chromatograms of concentration fields, d_p=2.1 mm: a) packed bed (U = 0.018 m s^{-1}, U/U_{mf} = 0.67) and fluidized beds: b) U = 0.039 m s^{-1}, U/U_{mf} = 1.4, c) U = 0.064 m s^{-1}, U/U_{mf} = 2.6, d) U = 0.112 m s^{-1}, U/U_{mf} = 4.1

3. 2. Local mass transfer coefficients

Local values of the mass transfer coefficient were obtained by analyzing foils at the surface of the cylinder. The appearance of the foils after the performed experiments is shown in Figure 5. The foil obtained in the single-phase flow is shown in Figure 5a while the foils obtained in the fluidized beds of particles of two investigated sizes are shown in Figures 5b and 5c at fluid velocities of about 0.05 m s^{-1}.

Based on the foils shown in Figure 5, by determining local color intensity values at each point with a step of 1°, local mass transfer coefficient values were determined, shown in Figure 6. In specific, Figure 6 represents the local MTCs around the cylinder as a function of the angular position (stagnant point is angle 0°) for the single-phase flow and for fluidized beds at almost the same superficial liquid velocity 0.05 m s^{-1}.

In the single phase flow the highest values of MTCs close to $6 \cdot 10^{-5}$ m s^{-1} are observed at the bottom of the cylinder in the region between 0 and 40°. The zone between 40° and 90° is characterized by a sharp decrease of the MTCs down to the minimum of 0.2×10^{-5} m s^{-1} which has been attributed to the separation of the boundary layer [21]. In the zone between 90° and 180° a weak increase of MTCs has been observed.

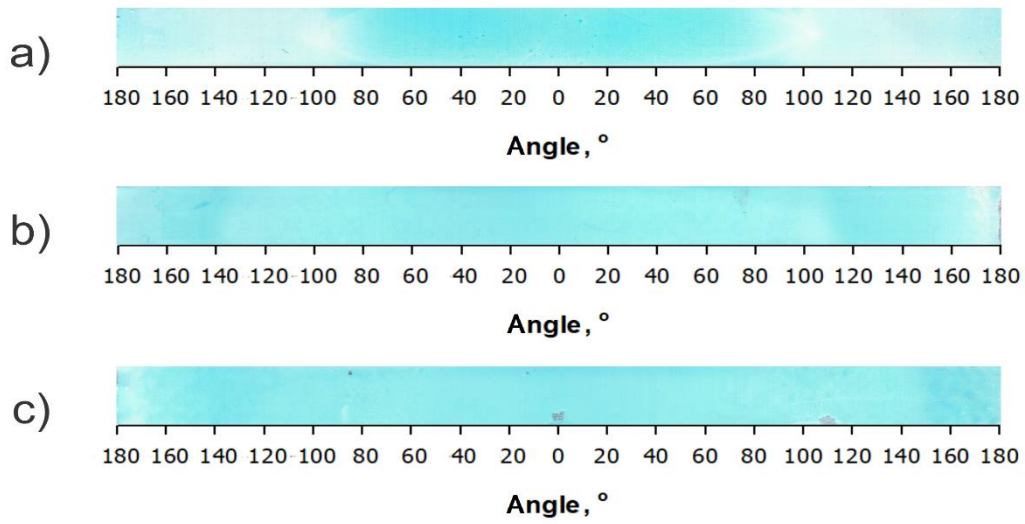

Figure 5. The appearance of foils at the surface of the cylinder in the single-phase flow (a) and in fluidized layers with particles with a diameter of 1.2 mm (b) and 2.1 mm (c). Angles are measured from the stagnant point 0°

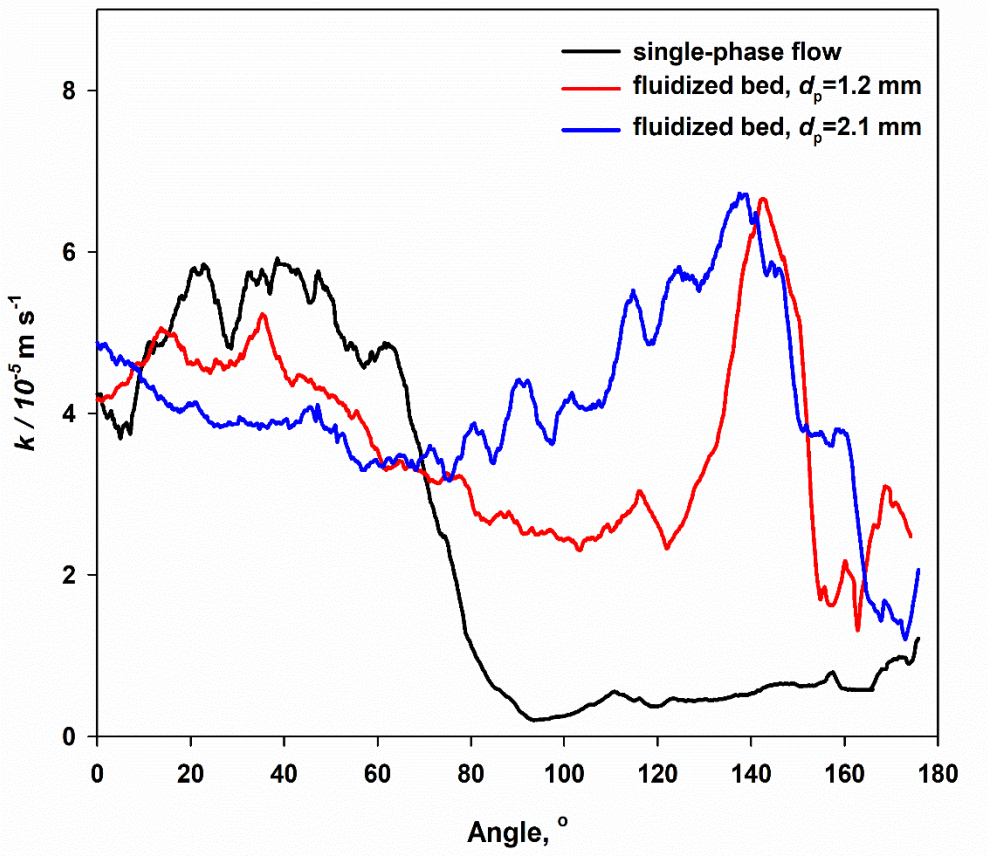

Figure 6. Local mass-transfer coefficient (k) around the cylinder for the superficial velocity of 0.05 m s^{-1} for the single phase flow and fluidized beds of two particle sizes

In the fluidized bed the local distribution of MTCs around the cylinder differs significantly from that in the single-phase flow. For the angular positions from 0 to 40° the values of MTCs are 20 to 30 % lower than in the single-phase flow. The minimum is not as pronounced as in the single-phase flow and occurs at the angle of 70° for 2.1 mm diameter particles and 100° for the 1.2 mm diameter particles. In the range 120 to 150° the values of MTCs in the fluidized bed are significantly higher than those in the single-phase flow and exhibit a sharp maximum at 140°. This maximum may be explained by intensified mixing of the particles in the region of angles 120-150°, which is caused by the increase in the particle

concentration and interstitial velocity (due to the presence of the cylinder) from one side and the reverse flow from another side. On the top of the cylinder (at angles 170 to 180°) the values of MTCs are low, but still slightly higher than those in the single-phase flow. The profiles of local MTCs for fluidized particles of the two investigated sizes (*i.e.* 1.2 and 2.1 mm in diameter) are quite similar, exhibiting a maximum at 140° in both cases.

Figure 7 represents the influence of the superficial liquid velocity on the local MTCs around the cylinder in the fluidized bed of 2.1 mm diameter particles. It can be observed that for the higher superficial velocities the values of MTCs are lower for all angular positions. It can be also clearly seen that for the higher velocities the minimum MTC is becoming more pronounced. That can be explained by the fact that for higher velocities particle concentration is lower and the separation of the boundary layer is less disturbed by particles. On the top of the cylinder the values of local MTCs are low for all tested superficial velocities.

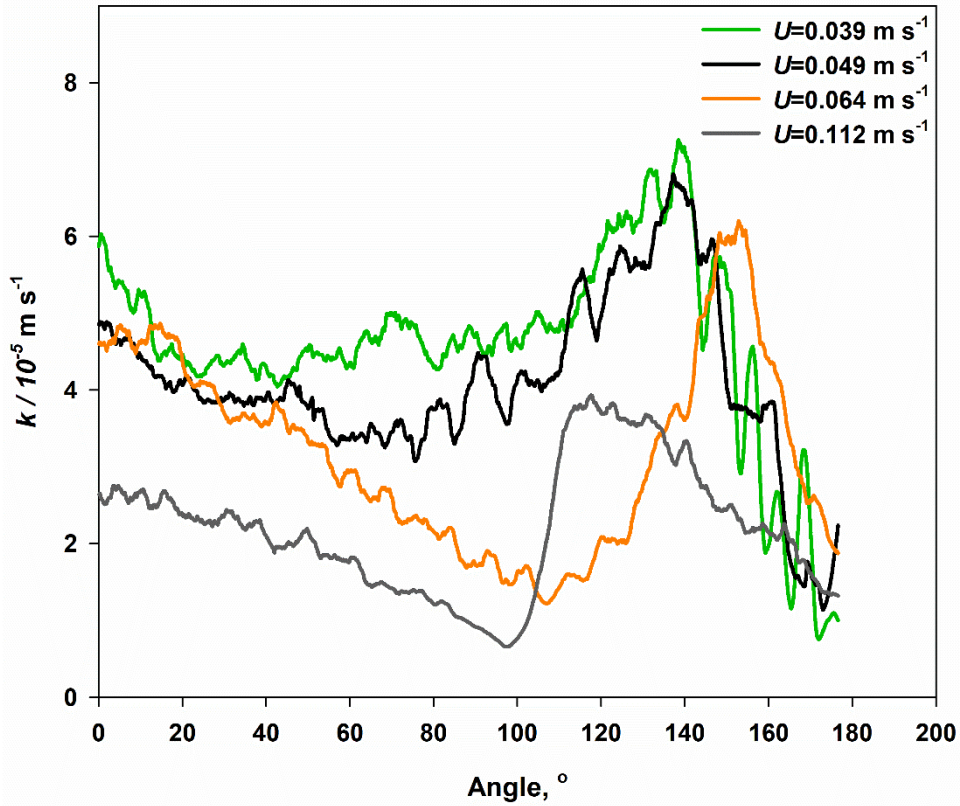

Figure 7. Influence of the superficial liquid velocity on local mass transfer coefficients around the cylinder (d_p = 2.1 mm)

Local values of the Sherwood number for particle (Sh_p) were determined based on local MTC values, Figure 8 shows the local Sh_p values depending on the angular position for mass transfer in fluidized beds of particles with a diameter of 2.1 mm and at superficial velocities of 0.064 and 0.112 m s^{-1}. It could be observed that the local values of the Sh_p number decrease slightly up to the angle of about 90°, *i.e.* on the front half of the cylinder and increase sharply on the back half of the cylinder. Around the last point at the angle of about 180°, the Sh_p number values decrease.

3. 3. Average mass transfer coefficient

Based on the colouring intensity in foils at the cylinder surface, the average values of the mass transfer coefficients in single-phase flow and fluidized beds were calculated (Fig. 9). The results indicate that mass transfer coefficients increase with the increase in the superficial velocity for the single-phase flow. In fluidized beds, the trend is different, i.e. with the increase in the superficial velocity, the values of mass transfer coefficients slightly decrease. The largest difference in the coefficient values between the single-phase flow and the fluidized beds is at velocities close to the minimum fluidization velocity because at that point the particle concentration is the highest affecting mass transfer

better. However, differences in mass transfer intensities in the fluidized beds with particles of different sizes were not observed. It can be also seen in Figure 9 that at higher velocities when the porosity of the fluidized beds is high, the mass transfer coefficients are similar to that in the single-phase flow.

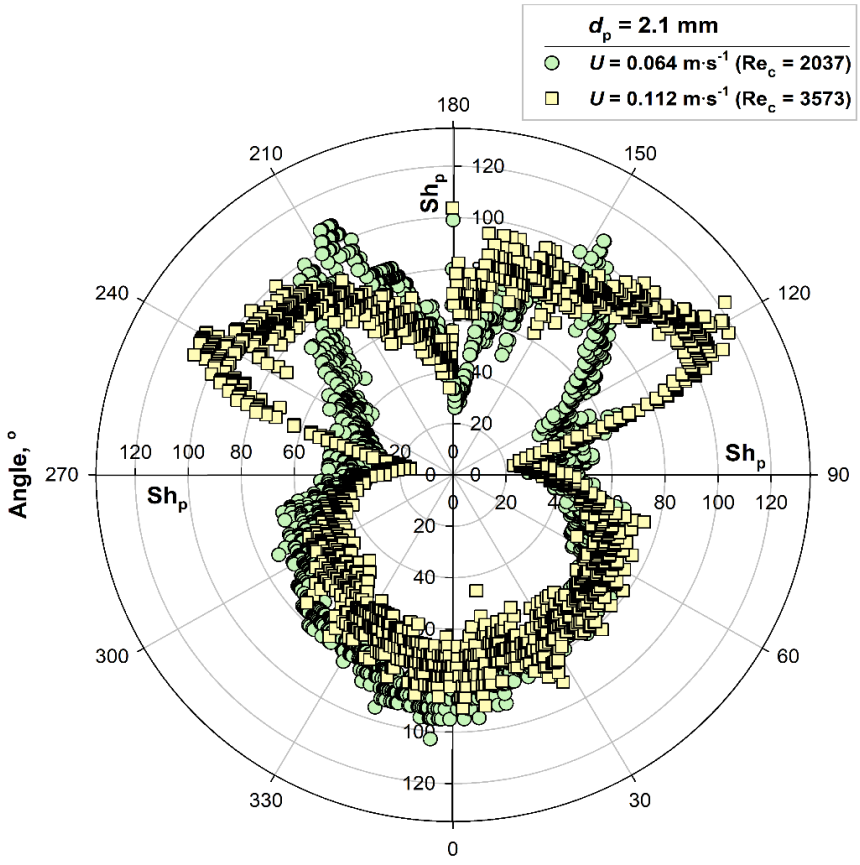

Figure 8. Local Sh_p number as a function of angular position in the fluidized bed of 2.1 mm particles at two fluid velocities

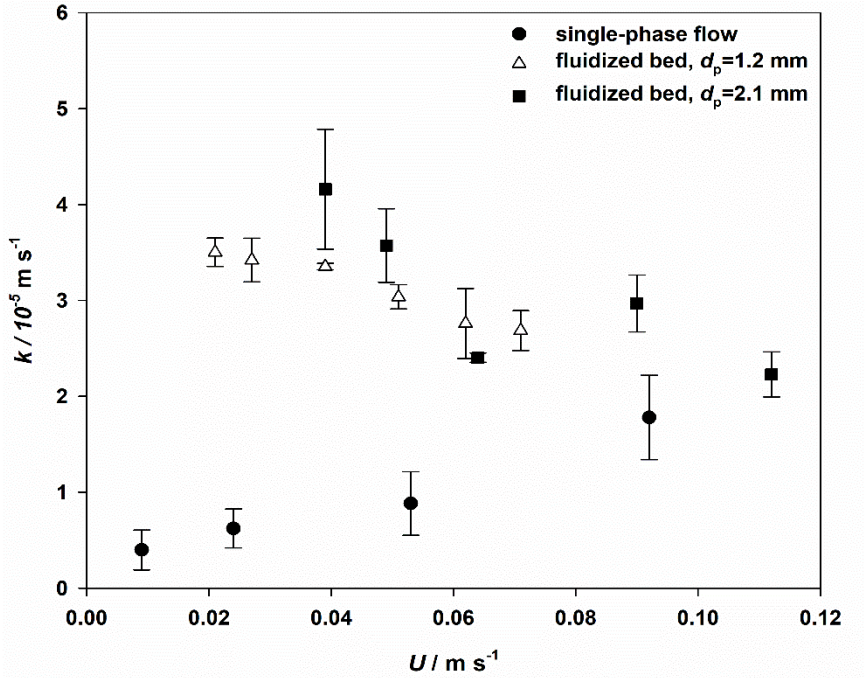

Figure 9. Average values of mass transfer coefficients as functions of the superficial fluid velocity in the single-phase flow and in fluidized beds of particles of two different sizes

3. 4. Comparison of experimental data with calculated values by literature correlations

Selected correlations (Table 3) were applied to calculate the dimensionless mass transfer factor in the range of experimental operating conditions (Table 2) and compare with the experimental data for average MTCs. The selected correlations are empirically derived from data obtained by different experimental techniques. Table 3 also shows average deviations between the experimental and calculated data. It could be seen that for the majority of correlations the calculated values are higher compared to the experimental values. Also, it could be noted that there are significantly smaller deviations for correlations obtained for the immersed object-fluid mass transfers, which is expected due to similar flow conditions. Two correlations of Storck and Vergnes [7] and Riba et al. [8] provided very good agreements with the experimental results.

Table 3. Selected literature correlations for calculation of the dimensionless mass transfer factor for immersed object-fluid and wall-fluid in the range of experimental operating conditions

Equation	Deviation / %	Ref.
Immersed object-fluid		
$j_D = 0.59\left(\frac{Re_p}{1-\varepsilon}\right)^{-0.44}$	5.0	[7]
$j_D = 0.264\,Re_p^{-1.11}\,Ga^{0.36}$	-3.5	[8]
$j_D = 0.261\,Ga^{0.324}\,Re_p^{-0.97}$	-30.3	[9]
$j_D = 0.64\left(\frac{Re_p}{1-\varepsilon}\right)^{-0.4}$	-28.3	[10]
Wall-fluid		
$j_D = 0.6\left(\frac{Re_p}{1-\varepsilon}\right)^{-0.5}$	30.4	[11]
$j_D = 0.4\,Re_p^{-0.4}$	-26.8	[12]
$j_D = 0.14\,Re_p^{-2/3} + 0.13\,Re_p^{-4/3}\,Ar^{2/3}\,\frac{1-\varepsilon}{1-\varepsilon_0}$	-54.5	[13]

Comparisons of experimental and calculated values of the dimensionless mass transfer factor for the fluidized bed with 1.2 mm diameter particles are shown in Figure 10. As can be seen, the trend of dependence of j_D on the Re_p number is the same for experimental and calculated values and deviations between experimental and calculated values are larger for smaller Re_p numbers.

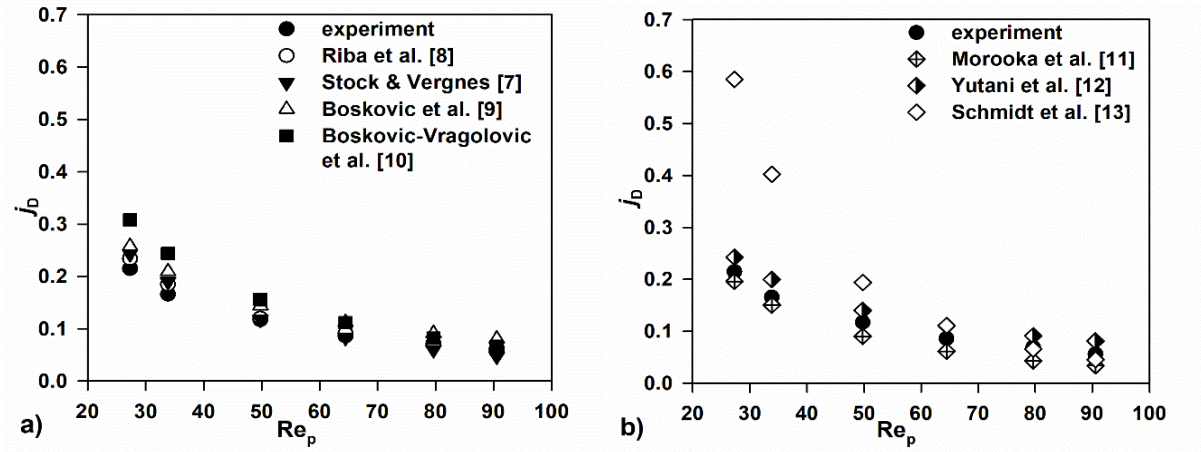

Figure 10. Comparison of experimental and calculated values of the mass transfer factor for the fluidized bed with 1.2 mm diameter particles

4. CONCLUSION

In this paper, mass transfer was experimentally investigated for the flow around a horizontal cylinder in the single-phase flow and in fluidized beds of particles of two sizes. Local and average values of mass transfer coefficients (MTCs) between the fluid and the immersed cylinder were determined by application of the adsorption method.

The local MTCs in the fluidized bed are higher than those in the single-phase flow for the angular positions 70 to 180°. Intensification of the mass transfer in the fluidized bed is especially pronounced at cylinder surfaces at the angular positions between 120 and 150°, with a sharp maximum at around 140°. Fluidized particles significantly disturb the structure of the boundary layer around the cylinder. Local MTCs in the fluidized bed have similar angular profiles for particles 1.2 and 2.1 mm in diameter. At higher superficial velocities the local MTCs in the fluidized bed are lower for all angular positions.

Values of the average mass transfer coefficients in fluidized beds did not depend on the particle diameter and decreased with the increase in the superficial velocity. The mass transfer coefficient in the fluidized bed is approximately 4-fold higher than that in the single-phase flow at the minimum fluidization velocity, while this difference decreases with the increase in fluid velocity, i.e. porosity of the fluidized bed.

Comparison of experimental values of mass transfer factors with values calculated by literature correlations of Storck and Vergnes [7] and Riba *et al.* [8] showed very good agreements with a mean deviation of 5 and -3.5 %, respectively.

The performed study showed the applicability of the adsorption method, novel results of local mass transfer coefficients on the immersed object and the suitability of certain tested correlations. It has also demonstrated the importance of optimizing the superficial fluid velocity as it has positive effects on particle mixing but negative effects on the mass transfer coefficient. The results and approach presented in this paper could be extended to other fluidized bed systems with immersed objects.

5. NOMENCLATURE

Ar	Archimedes number, ($g\ d_p\rho_f\ (\rho_f - \rho_p)/\ \mu^2$)
c_0 / kg m^{-3}	bulk concentration of methylene blue
c_p / kg m^{-2}	surface concentration of methylene blue on adsorbent layer
d_p / m	particle diameter
D / m	single cylinder diameter
D_{AB} / m^2 s^{-1}	the diffusion coefficient of the reactant
Ga	Galileo number, ($g\ d_p^3\rho_f^3\ /\ \mu^2$)
G / m s^{-2}	gravitational acceleration
j_D	dimensionless mass transfer factor, ($k\ Sc^{2/3}$ / U)
k / m s^{-1}	mass transfer coefficient
Re_p	Reynolds number for particle, ($U\ d_p\rho_f\ /\ \mu$)
Re_c	Reynolds number for single cylinder, ($U\ D_p\rho_f\ /\ \mu$)
Sc	Schmidt number, ($m\ /\ \rho_f\ D_{AB}$)
Sh_p	Sherwood number for particle, ($k\ d_p\ /\ D_{AB}$)
t / s	exposure time
U / m s^{-1}	superficial fluid velocity
U_{mf} / m s^{-1}	minimum fluidization velocity
U_t / m s^{-1}	particle terminal velocity in a stagnant fluid
$\dot{V}$ / dm^3 min^{-1}	fluid flowrate
Greek letters	
ε	bed porosity
ε_0	packed bed porosity
ε_{mf}	bed porosity at minimum fluidization velocity
μ / mPa s	fluid viscosity
ρ_f / kg m^{-3}	fluid density
ρ_p / kg m^{-3}	particle density

Acknowledgements: This work was financially supported by the Ministry of Science, Technological Development and Innovation of the Republic of Serbia (Grant No. 451-03-65/2024-03/200135 and Grant No. 451-03-66/2024-03/200026).

REFERENCES

[1] Rasoulnia P, Hajdu-Rahkama R, Puhakka JA. High-rate and -yield continuous fluidized-bed bioconversion of glucose-to-gluconic acid for enhanced metal leaching. *Chem Eng J*. 2023; 462: 142088 https://doi.org/10.1016/j.cej.2023.142088

[2] Gui L, Yang H, Huang H, Hu, C, Feng Y, Wang X. Liquid solid fluidized bed crystallization granulation technology: Development, applications, properties, and prospects. *J Water Process Eng*. 2022; 45: 102513 https://doi.org/10.1016/j.jwpe.2021.102513

[3] Kalaga DV, Dhar A, Dalvi SV, Joshi JB. Particle-liquid mass transfer in solid-liquid fluidized beds. *Chem Eng J.* 2014; 245: 323-341 https://doi.org/10.1016/j.cej.2014.02.038

[4] Evans GC, Gerald CF. Mass transfer from benzoic acid granules to water in fixed and fluidized beds at low Reynolds numbers. *Chem Eng Progr*. 1953; 49: 135-140; ISSN: 0360-7275

[5] Upadhyay SN, Tripathi G. Liquid phase mass transfer in fixed and fluidized beds of large particles. *J Chem Eng Data*. 1975; 1: 20-26 https://doi.org/10.1021/je60064a001

[6] Shen GC, Geankoplis CJ, Brodkey RS. A note on particle-liquid mass transfer in a fluidized bed of small irregular-shaped benzoic acid particles *Chem Eng Sci*. 1985; 40: 1797-1802 https://doi.org/10.1016/0009-2509(85)80046-4

[7] Storck A, Vergnes F. Transfert de Matiere entre un Electrolyte et une Paroi Cylindrique Immergee dans un Lit Fluidise Liquide-Solide: Influence de la Masse Volumique des Particules Fluidisees. *Powder Techn*. 1975; 12209-2013 https://doi.org/10.1016/0032-5910(75)85019-4

[8] Riba, JP, Routie R, and Couderc JP. Mass transfer from a fixed sphere to liquid in a fluidized bed. In: *Fluidization: Proceedings of the Second Engineering Foundation Conference.*Trinity College, Cambridge, England, 1978. pp 157-162

[9] Bošković N, Grbavčić BŽ, Vuković VD, Marković-Grbavčić M. Mass Transfer between Fluid and Immersed Surfaces in Liquid Fluidized beds of Coarse Spherical Inert Particles. *Powder Techn*. 1994; 79: 217-225 https://doi.org/10.1016/0032-5910(94)02826-5

[10] Bošković-Vragolović N, Brzić D, Grbavčić Ž. Mass Transfer between Fluid and Immersed Object in liquid-solid packed and fluidized beds. *J Chem Soc*. 2005; 70: 1273-1379 https://doi.org/10.2298/JSC0511373B

[11] Morooka S, Kusakabe K, Kato Y, Mass Transfer Coefficient at Wall of Rectangular Fluidized Beds for Liquid — Solid and Gas—Liquid—Solid Systems. *Kagaku Kogaku Ronbunshu*. 1979; 5 (2): 162-166 .https://doi.org/10.1252/kakoronbunshu.5.162

[12] Yutani N, Ototake N, Fan LT. Statistical Analiysis of Mass Transfe in Liquid-Solid Fluidized Beds. *Ind Eng Chem Res.* 1987;26: 343-347 https://doi.org/10.1021/ie00062a028

[13] Schmidt S, Buchs J, Born C, Biselli M, A New Correlation for the Wall-to-Fluid Mass Transfer in Liquid-Solid Fluidized Beds. *Chem Eng Sci.* 1999; 54: 829-839 https://doi.org/10.1016/S0009-2509(98)00284-X

[14] Kim J, Kim K, Ye H, Lee E, Shin C, McCarty PL, Bae J. Anaerobic Fluidized Bed Membrane Bioreactor for Wastewater Treatment. *Env Sci Tech.* 2011; *45* (2): 576-581 https://doi.org/10.1021/es1027103

[15] Perry SC, De Leon CP, Walsh FC. Review—The Design, Performance and Continuing Development of Electrochemical Reactors for Clean Electrosynthesis. *J Electrochem Soc.* 2020; 167: 155525; https://doi.org/10.1149/1945-7111/abc58e

[16] Garim MM, Freire JT, Goldstein RJ. Local mass transfer coefficients around a cylinder in a fluidized bed. Powder Technol. 1999; 101 (2): 134-141https://doi.org/10.1016/S0032-5910(98)00164-8

[17] Di Natale F, Nigro R. A critical comparison between local heat and mass transfer coefficients of horizontal cylinders immersed in bubbling fluidized beds. *Int. J Heat Mass Tran*. 2012; 55 (25-26): 8178-8183https://doi.org/10.1016/j.ijheatmasstransfer.2012.08.002

[18] Končar-Đurđević S. Application of a new adsorption method in the study of flow of fluids. *Nature*.1953; 172: 858 https://doi.org/10.1038/172858a0

[19] Mitrović M. Transport phenomena in multiphase systems. *J Serb Chem Soc*. 1996; 61: 233- 251, ISSN: 0352-5139

[20] Bošković-Vragolović N, Garić-Grulović R, Grbavčić Ž, Pjanović R. Mass transfer in heterogeneous systems by adsorption method. *CI CEQ*, 2009; 15 (1): 25-28 https://doi.org/10.2298/CICEQ0901025B

[21] Bošković-Vragolović N, Garić-Grulović R, Pjanović R, Grbavčić Ž. Mass transfer and fluid flow visualization for single cylinder by the adsorption method. *Int. J. Heat Mass Trans.* 2013; 59: 155-160 https://doi.org/10.1016/j.ijheatmasstransfer.2012.11.077

[22] Welty RJ, Wicks EC, Wilson ER, Rorrer G. *Fundamentals of Momentum, Heat, and Mass Transfer*. 5th ed., Copyright 2008 John Wiley & Sons, Inc. ISBN: 13 978-0470128688

Lokalni prenos mase i vizualizacija toka oko cilindra u fluidizovanom sloju tečno-čvrsto

Nevenka M. Bošković-Vragolović[1], Danica V. Brzić[1], Katarina S. Šućurović[2], Rada V. Pjanović[1], Darko R. Jaćimovski[2] i Radmila V. Garić-Grulović[2]

[1]Univerzitet u Beogradu, Tehnološko-metalurški fakultet, Beograd, Srbija
[2]Univerzitet u Beogradu, Institut za hemiju, tehnologiju i metalurgiju – Institut od nacionalnog značaja za Republiku Srbiju, Beograd, Srbija

(Naučni rad)

Izvod

U ovom radu je primenjena adsorpciona metoda za vizualizaciju strujanja i određivanje lokalnih i srednjih koeficijenata prenosa mase na horizontalni cilindar u tečno-čvrsto fluidizovanom sloju. Dobijena polja koncentracije na adsorbentu (folije silika gela) predstavljaju kvalitativnu sliku strujanja oko cilindra. Poređenjem koncentracionih polja oko cilindra u jednofaznom toku i u fluidizovanom sloju, uočeno je da fluidizovane čestice značajno ometaju formiranje i odvajanje graničnog sloja. Lokalni koeficijenti prenosa mase su značajno zavisili od ugaonog položaja tačke na površini cilindra i pokazali su maksimum pri uglu 140° (mereno u odnosu na zaustavnu tačku koja predstavlja ugao od 0°). Odabrane korelacije su primenjene za predviđanje prosečnih vrednosti koeficijenata prenosa mase, a dve najbolje su pokazivale odstupanja od eksperimentalnih podataka do 5 %.

Ključne reči: koeficijent prenosa mase; adsorpciona metoda; opstrujavanje cilindra; koncentraciona polja

A note on a transverse magnetic field controlled co-current bubble column

Jordan Y. Hristov[1] and Radojica D. Pešić[2]

[1]*Department of Chemical Engineering, University of Chemical Technology and Metallurgy, Sofia, Bulgaria*
[2]*University of Belgrade, Faculty of Technology and Metallurgy, Department of Chemical Engineering, Belgrade, Serbia*

Abstract

An experimental study has been carried out investigating the fluidization behavior of a bubble column with a bottom magnetic particle bed controlled by an external transverse magnetic field. The magnetization-first/gas-scanning mode was applied, at up to 45 kA m^{-1} field intensity, with liquid superficial velocities of up to 20 mm s^{-1} and with a gas flowrate of up to 8 m^3 h^{-1}. Particle fractions of two different sizes of up to 1 mm were used. The focus has been both on the three-phase magnetic particle bed expansion playing the role of a gas distributor and the gas holdup of the abovepositioned two-phase section, as well as related column parameters. Piezometric measurements have been performed that provided detection of the position of the interface between the two column sections without visual observation, as well as the gas holdup in the two-phase zone. The bed expansion was strongly affected by the bed state created by the initially established liquid flow rate. The results showed that the intensity of the field applied to the magnetic solids allows control both of bed expansion and internal bed structure, so the applicability of magnetically assisted three-phase beed as a gas distributor in bubble column seems promising.

Keywords: Three-phase magnetic particle bed; bed expansion; gas holdup.

Available on-line at the Journal web address: http://www.ache.org.rs/HI/

ORIGINAL SCIENTIFIC PAPER

UDC: 66.096.5:53.082.78

Hem. Ind. **78(3)** 161-172 (2024)

1. INTRODUCTION

Process control by application of a magnetic field is a technology for effective regulation of the motion of solids and pertinent heat and mass transfer in fluidized beds (see [1] and the related parts of this series of systematic analyses). Studies on this attractive approach to controlling fluidized beds have been performed applying various field intensities, while most of the reported results have been on gas-fluidized systems due to the simpler design of experimental set-ups than the liquid ones [1]. However, there have been studies on liquid-solid [2] and gas-liquid fluidization [3-7] allowing efficient control of heat and mass transfer processes [8,9].

In the past decade of the 21st century, there have been some studies mainly concentrated on gas and liquid fluidization of admixture of magnetic and non-magnetic particles [10-12], porous electrodes for electrochemical reactors [13,14], pharmaceutical and biotechnological applications [15,16] but reports on three-phase (gas-liquid-solid) beds are practically missing. Moreover, all recent studies mentioned above applied axial magnetic fields (parallel to the column axis and the fluid flow), while studies applying transverse fields are missing.

This article reports experiments on a bubble column, with a bottom bed of ferromagnetic solids, controlled by an external transverse magnetic field. The bed expansion, its role as a gas distributor, gas holdup, and relations of these parameters to existing fluidization regimes are the focus of the study. This report is in tribute to the memory of the late Professor Zeljko Grbavcic, a colleague and friend.

The specific aim of the study refers to the possibility of using a magnetically assisted particle bed as a gas distributor in a bubble column by application of an external (steady state) transverse magnetic field. This solution avoids supporting grids (meshes) or porous plates, commonly used in bubble columns, and allows applications to cases when gases contaminated by fine solids are used. The measurements are focused on the magnetized bed expansion upon conditions

Corresponding authors: Jordan Y. Hristov, Department of Chemical Engineering, University of Chemical Technology and Metallurgy, Sofia, Bulgaria
Paper received: 21 June 2023; Paper accepted: 23 May 2024; Paper published: 24 June 2024.
E-mail: jordan.hristov@mail.bg; jyh@uctm.edu
https://doi.org/10.2298/HEMIND230621010H

imposed by the Gas-scanning mode [7], the gas holdup in the two-phase section, and piezometric measurements along the entire column. A specific point coming from the piezometric measurements addresses the detection of the position of the interface between the magnetic bed and the two-phase section.

The application of a transverse magnetic field rather than the common use of axial-oriented ones [7] is motivated by the fact that such an orientation of the field lines allows for avoidance of channeling and the possibility offered by saddle coils magnetic system [1,5,7,8,17] to cover volumes larger than in the case when an axial magnetic field is applied [3,4,5].

It should be noted that bubble sizes and distribution are not considered a topic too common in studies on bubble columns since there was no bubble breakage by floating particle aggregates; such studies in magnetically assisted beds are systematically analyzed in [7,8]

2. EXPERIMENTAL

2. 1. Experimental set-up

The experimental set-up shown in Figure 1 consists of a transparent perplex column (1.95 m in height and 0.1 m inner diameter) with an assigned bottom conical section and a top-located degassing section (conical in shape) containing a droplet separation plate. The bottom section is filled with lead spheres (3 mm in diameter and non-magnetic) playing the role of a static mixer for gas and liquid flows supplied to the upper magnetic section of the column. The magnetic field for controlling fluidization of the ferromagnetic solids was generated by a saddle-coils magnetic system with a maximum field intensity of 45 kA m^{-1} (see more details in [17]). The field orientation, transverse to the column axis and the gas-liquid flow allows efficient control of the motion of the magnetic particles, breakage of the particle aggregates, effective gas bubble breakage (bubble size reduction by mechanical contacts with solids) and avoids channeling. It should be noted that in the case of the axial field *i.e.* parallel to the column axis and particle chains are oriented in the same direction, there is a strong flow bypass through the bed.

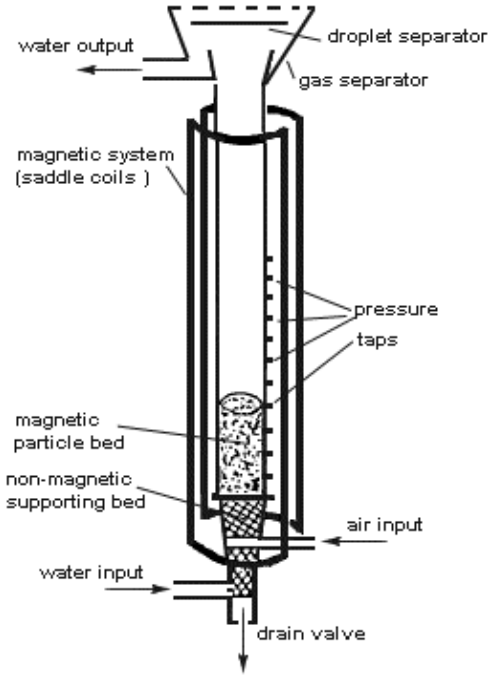

Figure 1. Experimental set-up

A set of vertical glass tube manometers with accessing points (pressure taps) located equidistantly (11 points with a 10 cm distance) along the column was used to measure hydrostatic pressures of the gas-solid-liquid and gas-liquid sections (see the description of the experiment in the sequel), and further used to calculate the gas holdup and solid phase concentration (controlled by the external magnetic field). A measuring scale mounted along the column for measurement of the bed height and the length of different sections of the fluidized systems was used.

2. 2. Materials used

The experiments were performed with air (supplied by a compressor) and water, at room temperature (20-22 °C) as fluidizing agents. The upper limit of the gas supply flow was about 8 m^3 h^{-1} allowing to study all possible fluidization regimes and measuring the related system parameters. Liquid superficial velocities varied up to 25 mm s^{-1}.

Two sieve fractions of artificial (synthetic) magnetite with alumina doping (Catalyst Haldorf Topsoe, KM-1, Denmark), commonly used for ammonia synthesis, of 0.8 to 1 and 0.3 to 0.4 mm, with a density of 5100 kg m^{-3} were used as magnetic solids. The minimum fluidization velocities concerning the liquid phase were, in the absence of a magnetic field, determined visually from the point where the bed was completely fluidized (almost homogeneous unrestricted motions of all solids through the entire bed volume).

Table 1. Magnetic solids used

Material	Sieve fraction, mm	Density, kg m^{-3}	Magnetization at saturation, kA m^{-1}	U_{min} / m s^{-1}	
				U_{l0}	U_{g0}
Catalyst Haldorf	0.8 - 1 .0	5100	236.4	0.0203	0.309
Topsoe KM-1	0.3 – 0.4	5100	236.4	0.0038	0.158

U_{min} - minimum fluidization velocities in the absence of a field; U_{l0} and U_{g0} - minimum fluidization velocities by liquid and by gas

2. 3. Operating modes

The experiments were carried out following the Magnetization-first (corresponding to Fluidization-last) mode [1,7] where the magnetic field is applied on an initially static particle bed, and fluidization starts after that. The fluidization was by the Gas-scanning mode [7], where the liquid flow is established first and then the gas flow is increasing incrementally.

3. CORRELATIONS FOR DETERMINATION OF PHASE HOLDUPS

Here we present the main correlations between the phase holdups in three-phase bubble columns as a base for comparisons and what are the differences when the magnetic particle bed is undergoing fluidization by a gas-liquid flow. Moreover, the focus is on how the piezometric measurements, as a common approach in such studies, can be used to obtain the required information.

3. 1. Conventional relationships for three-phase systems (when a magnetic field is not applied)

From the measurements of the pressure along the column wall, at a given distance h from the magnetic bed base, in the absence of a field, we have Equation (1):

$$P_h - P_{bed\text{-}base} = hg\,(\rho_s\varepsilon_s + \rho_L\varepsilon_L + \rho_g\varepsilon_g) \quad (1)$$

where h is the distance measured from the bed base, P_h is the pressure, $P_{bed\text{-}base}$ is the pressure at bad base, ε_s, ε_L and ε_g are solids, liquid and gas phase holdups, respectively.

Bearing in mind that the phase holdups are related as in Equation (2):

$$\varepsilon_s + \varepsilon_L + \varepsilon_g = 1 \quad (2)$$

we can define these holdups by Equations (3) to (5):

$$\varepsilon_g = \frac{1}{\rho_l - \rho_g}\left(\rho_l - \frac{\Delta P}{hg}\right) \quad (3)$$

$$\varepsilon_s = \frac{M_{solids}}{\rho_s h_{bed} A} \quad (4)$$

$$\varepsilon_L = \frac{1}{\rho_l - \rho_g}\left(\frac{\Delta P}{hg} - \rho_g\right) + \varepsilon_s\frac{\rho_s - \rho_g}{\rho_l - \rho_g} \quad (5)$$

Here, ΔP is the pressure drop between two points at a distance h, M_{solids} is the mass of the magnetic solid phase, A is the cross-section area of the bed (equal to the column cross-section area), and ρ_l and ρ_g are the density of the liquid (water, with ρ_l = 1000 kg m^{-3}) and gaseous agent (air, with ρ_g= 1.24 kg m^{-3}), respectively.

3. 2. Specific conditions imposed by the measurement results when a magnetic field is applied

The above Equations (2)-(5) would be valid if the magnetic field does not affect the magnetic bed structure and the particle mobility. In such a case, Equations (2)-(5) are valid and the relation (4) can be used to estimate the initial bed porosity before the magnetic field application. Upon the action of the magnetic field and the induced interparticle forces, we may use only the solid mass M_{solids} conservation relation, Equation (6):

$$M_{solids} = \rho_s A h_{b0} \varepsilon_{s0} = \rho_s A h_{b0} \varepsilon_{s0} \rightarrow \varepsilon_s = (h_{b0} / h_b) \varepsilon_{s0} \quad (6)$$

where the solid mass in the initial fixed bad is given on the left side of the Equation (6), and the solid mass in the expanded bed is given on the right side of the Equation (6). In Eq. (6) h_{b0} *and* h_b are the initial bed height and the height of the expanded solids under fluidization conditions, respectively, with the corresponding solid phase holdups, ε_{s0} and ε_s.

Moreover, in such cases, it is impossible to define separately the liquid holdup (ε_l) and gas holdup (ε_g), but only the overall void fraction (*i.e*. overall porosity) ε_{gl}, Equation (7):

$$\varepsilon_{gl} = \varepsilon_g + \varepsilon_l = 1 - \varepsilon_s \quad (7)$$

This is a consequence of the fact that only the solid mass (and volume) remains constant during all regimes of the bed upon fluidization, as expressed by Equation (6).

When the magnetized bed plays the role of a gas distributor and only the two-phase section above it is considered, then Equation (1) can be reformulated as in Equation (8):

$$P_h - P_{bed\text{-}top\ surface} = hg(\rho_L \varepsilon_L + \rho_g \varepsilon_g) = hg(\rho_L(1-\varepsilon_g) + \rho_g \varepsilon_g) = hg(\rho_L - \varepsilon_g (\rho_L - \rho_g)) \quad (8)$$

Equation (8) indicates a negative slope, almost linear, of the pressure drop profiles along the column wall that could be verified experimentally.

Playing the role of a gas distributor the magnetized bed keeps a fixed structure, resembling a porous medium, and therefore, measurements of the hydraulic pressure drop along its height are proportional to the density of the gas-solid mixtures $\rho_L (1-\varepsilon_g)$ in its free volume without any effects of the solid phase (it is not suspended by the fluid and does not affect the pressure drop measurements). That is, upon the fixed liquid and gas velocities, and field intensity, the pressure drop is determined by Equation (9):

$$P_{h\text{-}top} - P_{bed\text{-}base} = h_b g \rho_L (1-\varepsilon_g) \quad (9)$$

Thus, we may expect almost linear pressure drop profiles along the magnetized bed (see further in section 4.1.).

3. 3. A conjecture pertinent to the detection of the bed top surface

Therefore, to close this point and related explanations, we expect to get from measurements two almost linear pressure drop profiles corresponding to two different physical behaviors of the column sections. Since, the boundary between these sections is the magnetic bed top surface, the conjecture used in this work and experimentally verified is that the linear approximations of these two pressure drop profiles would allow detecting the magnetic bed top surface position even in cases when the column wall is not transparent.

Thus, as follows from the above explanations, the aim was to demonstrate the role of a magnetized bed as a gas-distributor for a two-phase column making such a construction more flexible when dusty gases, for instance, are used, where porous plates, metallic grids, and perforated tubes face problems with clogging, as it was briefly mentioned in section 2. 1. Additionally, studies on bubble breakage by particle aggregates are lacking, while systematic information about hydrodynamic effects are available in [7] and mass transfer related issues are analyzed in [8]. We guess that this remark provides enough additional information so that misinterpretations of the following experimental results are avoided.

4. RESULTS AND DISCUSSION

4. 1. Initial bed expansion in the liquid fluidization mode

The particle bed pressure drop exhibits a strong hysteresis with increases/decreases in the liquid velocity as a sole fluidizing agent. The area of the hysteresis loop depends on the field intensity and is strongly related to the particle aggregations and their field-aligned orientation transverse to the fluid flow (see Figs. 2 and 3). Moreover, the particle

strings are induced by magnets, and the repulsive forces between them increase the apparent bed porosity, if the porosity of the aggregates is not considered [1]. This increased free bed volume, allows better gas-liquid mixing with an increased gas flow rate once the gas-scan mode was applied, due to increased bed voids and particle aggregates induce a turbulent fluid flow. The upper limit of the fixed bed defined by the minimum liquid fluidization velocity depends on the field intensity applied, which in general increases as the magnetic field intensity is increased (see Fig. 4). All these preliminary measurements are important to understand the behavior of magnetized solids.

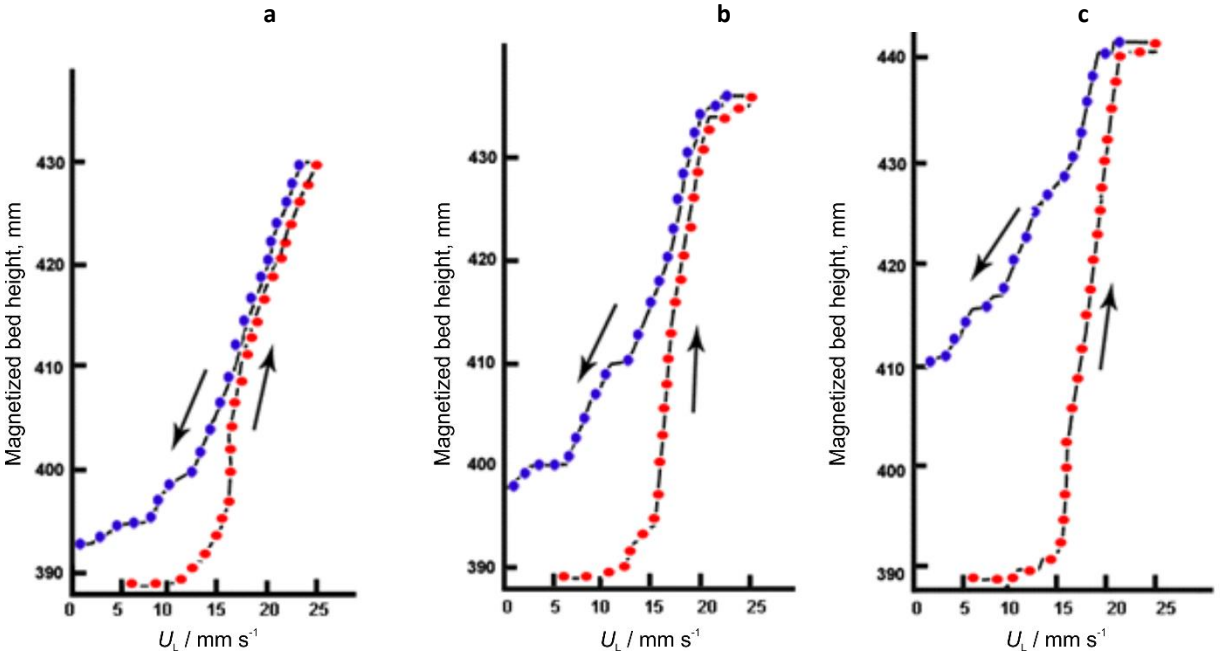

Figure 2. Magnetized bed expansion hysteresis (i.e. bed height) as a function of increasing and decreasing liquid flow at different field intensities: a) H = 4200 A m^{-1} b) H = 8400 A m^{-1} c) H = 12600 A m^{-1}. Particle fraction 0.8-1.0 mm

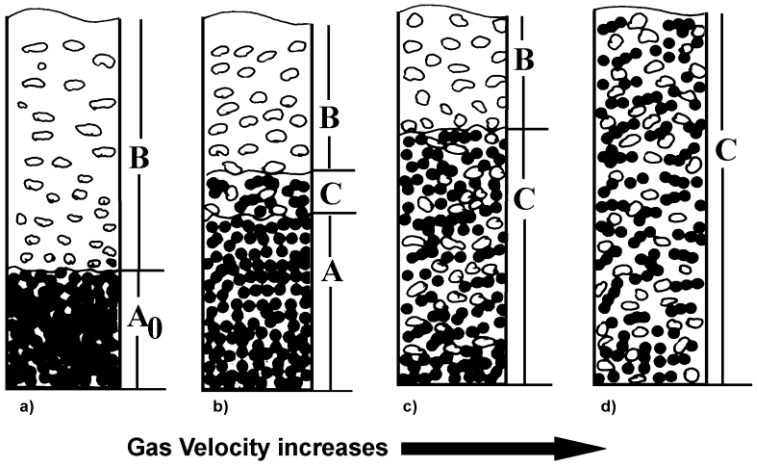

Figure 3. T*he overall picture of magnetized bed expansion and the definitions of the column sections: a) A_0 - initial fixed bed; b) A - magnetically stabilized bed (MSB); B - two-phase (bubbling) section; C - lean unstable bed at the interface with the two-phase section; c) C - three-phase fully fluidized bed; d) C - complet column three-phase fluidized bed*

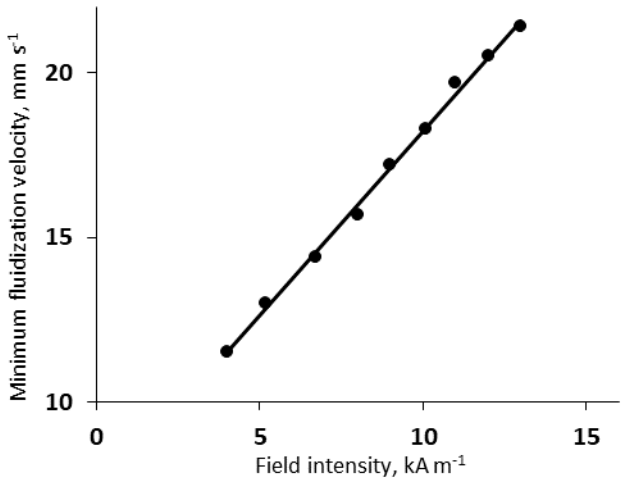

Figure 4. Minimum fluidization velocity concerning the liquid flow as a function of the field intensity applied. Particle fraction 0.8 to 1.0 mm

For the particular case shown in Figure 4, the data could be correlated by a power law, Equation (10):

$$U_{LO} = aH^b \quad (10)$$

The parameters were determined as $a = 1.05\times10^{-3}$ m^2 A^{-1} s^{-1}, and $b = 6.339$, which is a dimensionless exponent, with $R = 0.9995$, a standard error of 2.007×10^{-6}, estimated by SigmaPlot software (Grafiti LLC, CA). The units of U_{L0} and H are as in Figure 4.

4. 2. Magnetized bed expansion

As can be seen in schematic representation of magnetized bed expansion (Fig. 3), two major sections in the column are distinct at some magnetic field intensity applied. The lower part of the column consists of a three-phase (gas-liquid-solids) section and the upper part of the column consists of a two-phase (gas-liquid) section. Since the upper section is practically similar to the freeboard region in the classic bubble column, the lower section is of particular interest, as different bed structures are established due to the application of gas-liquid flow and the external magnetic field. When the liquid velocity is lower than the minimum liquid fluidization velocity and the gas velocity is lower than the minimum gas fluidization velocity, at some magnetic filed intensity, the three-phase section is in the initial fixed (unfluidized) bed regime (Fig. 3a). By increasing the gas velocity, the bed expandes slowly, without unrestricted mixing motions of particles, indicating the beginning of stabilization of the bed by the action of the magnetic field. Thus, it demonstrates the well-known behaviour of magnetically stabilized bed (MSB). At some higher gas velocity, on the top of the MSB, there is a small lean unstable three-phase fluidized bed at the interface with the two-phase section (Fig. 3b). The upper limit of MSB is its breakdown at the fluidization onset, *i.e.* minimum gas fluidization velocity. Three phase section become a fully gas-liquid-solid fluidized bed (Fig. 3c). When the gas velocity is high enough, the two-phase section evolves into a complete column three-phase fluidized bed (Fig. 3d).

Upon the simultaneous action of the external magnetic field and the incrementally increasing gas superficial velocity from 0.124 m s^{-1}, the bed expansion (see Figure 5) is strongly affected by the "background" created by the initially established liquid flow rate (below the minimum fluidization point concerning the liquid-solid bed). The plots in Figure 5 correspond to the height of the interface between the the three-phase and the two-phase sections in the magnetized bed (see Fig. 3) *i.e.* each of these lines separates the diagrams in Figs. 5a and 5b into areas. At lower gas velocities the magnetized bed height is constant, so the areas below the bed expansion lines correspond to initial fixed beds at some field intensity applied, while beyond these lines there are bubbling sections. At higher gas velocities magnetized bed height increases with increasing gas velocities and the areas below the bed expansion lines are corresponding to MSBs, while beyond these lines there are fluidized beds where the section A in Fig. 3 disappears and only sections C (fluidized three-phase bed) and section *B* (two-phase gas-solid section) remain.

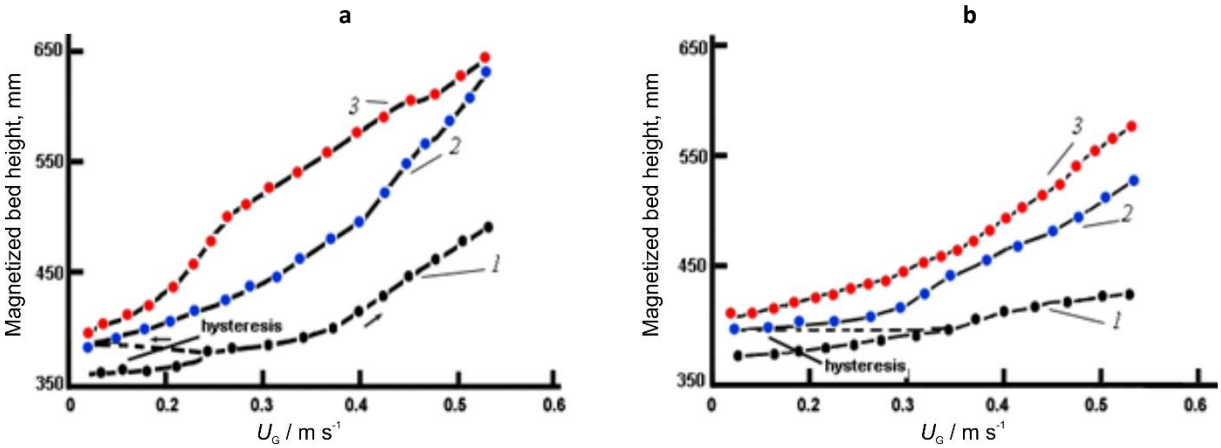

Figure 5. *Magnetized bed expansion in the gas-scanning mode at three different liquid velocities (below the minimum fluidization point concerning the liquid-solid bed) and two distinct field intensities: a) H = 8400 A m^{-1} and b) H = 21000 A m^{-1}; liquid superficial velocity: 1 – U_L=4.246 m s^{-1}; 2 – U_L =10.615 m s^{-1}; 3 – U_L =16.982 m s^{-1}; fraction 0.3 – 0.4 mm.*

4. 3. Minimum gas fluidization velocity

The minimum gas fluidization velocity of the magnetized solids, in general, decreases with the increase in the liquid velocity (see Fig. 5). The plots in Figure 5 reveal the field intensity effect, that is, increased minimum fluidization velocity as the field intensity is increased, an expected and physically clear effect due to increased interparticle forces and formation of particle aggregates. Besides, with an increase in the magnetic field intensity at a constant liquid velocity bellow minimum fluidization velocity for liquid solely, the height of liquid-solid bed increses (see Fig. 2) and the liquid holdup increases, the particles are more firmly connected in strings and thus the hydraulic resistance of the bed decreases. This has the consequence that once gas is introduced into the system (gas-scanning mode), a higher gas velocity is required in order to break the fixed structure of the bed thus formed and fluidization to be developed.

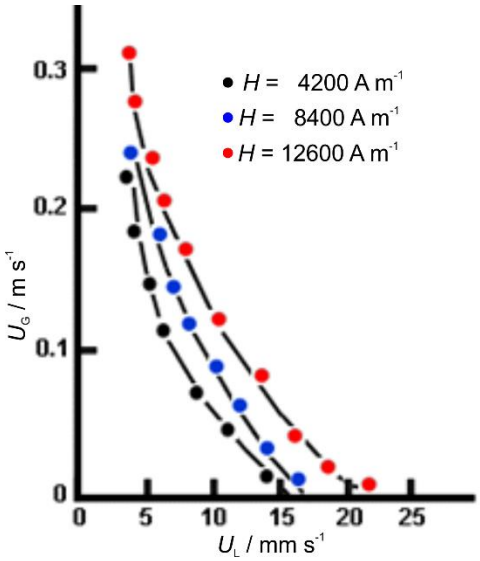

Figure 6. Minimum fluidization velocity concerning the gas flow as a function of the liquid velocity (below the minimum fluidization point concerning the liquid-solid bed) and three intensities of the applied magnetic field. Particle fraction 0.8-1.0 mm

For the plots in Figure 6, the general behaviour of the relationship $U_{G\text{-}mf} = f(U_L, H)$ is to a greater extent exponentially decaying and can be presented as:

$$U_{G\text{-}mf} = k_H \exp(-bU_L) \quad (11)$$

where the pre-factor k_H and the rate coefficient b depend on the field intensity applied (see Table 2 - data correlation carried out by the software package SigmaPlot).

Table 2. Data correlations of the minimum gas fluidization velocity related to the plots in Figure 6 and correlated by Eq. (11)

H / kA m^{-1}	k_H / m s^{-1}	b / s m^{-1}	Standard error	R
4200	0.4763	0.2163	0.0306	0.901
8400	0.4865	0.170	0.0252	0.923
12600	0.5442	0.448	0.0252	0.923

4. 4. Piezometric measurements

Next, the focus was on the data obtained by measurements of the pressure drop profiles along the column axis as commented earlier. This allows us to address: the indirect measurements of the magnetized bed height, the magnetized bed porosity, and the gas holdup in the two-phase section.

4. 4. 1. Magnetized bed height

The piezometric measurements provide creation of useful pressure drop profiles and comparison of the results thereof with visual bed expansion measurements, precisely the position of the interface separating the three-phase and the two-phase sections of the column. The background used in the data treatment was explained in detail in section 3.

As it is shown in Figure 7 the pressure drop lines change their slopes at the points corresponding to this interface, as suggested by the conjecture in section 3.3. Comparison with the visual observations (see Fig. 8) reveals that there is a satisfactory correspondence between the graphically and the visually determined magnetized bed heights, especially for low and medium field intensities. For the high-field intensity, the discrepancy may reach 10 %. The utility of this result is that piezometric measurements and determination of the specific point of the change in pressure drop slopes allow determination of the interface between the two major zones of the column, even in cases when the column wall is not transparent.

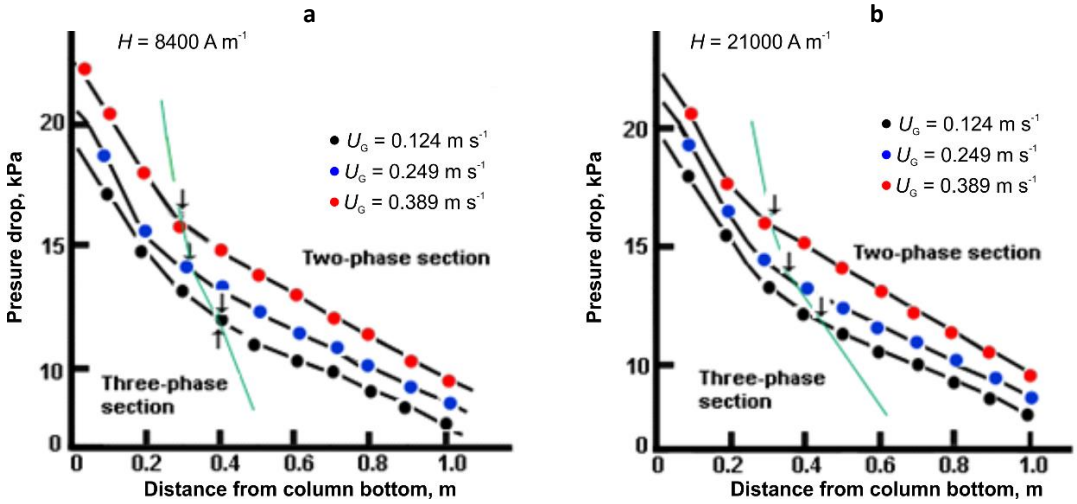

Figure 7. Pressure drop profiles along the vertical column axis determined by the piezometric measurements. The solid lines approximate only the tendency in the pressure drop changes and are not related to any analytic data fittings. The green line shows the points where the pressure drop lines change their slopes, thus indicating the position of the interface B-C (see Fig. 3). Particle fraction 0.8 to 1.0 mm.

4. 4. 2. Phase holdups

The overall porosity of the magnetized bed (see Fig. 9) increases almost linearly (the approximate green lines) with the gas velocity beyond the minimum fluidization point with a strong effect of the applied field intensity. That is, the stronger the field intensity, the higher the magnetized bed porosity. Since the magnetized bed plays the role of a gas distributor, generating bubbles for the above two-phase section, the increase in the gas velocity yields an increase in the gas holdup, which is an expected result. The measurements, as can be seen from the plots in Figure 10 reveal that the effects of the field intensity are not strong, even though there is a slight increase in ε_g with the increase in the field intensity. This could be attributed to the fact that stronger fields create stronger (stable) magnetic particle structure, and this results in finer gas bubbles generated at the magnetized bed top interface.

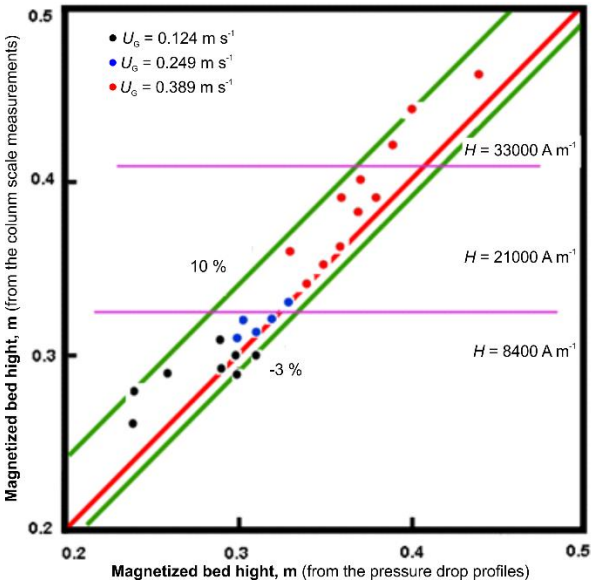

Figure 8. A parity plot between the position of the B-C interface, obtained from pressure drop measurements and the visual measurements at the column wall. Particle fraction 0.8 to 1.0 mm.

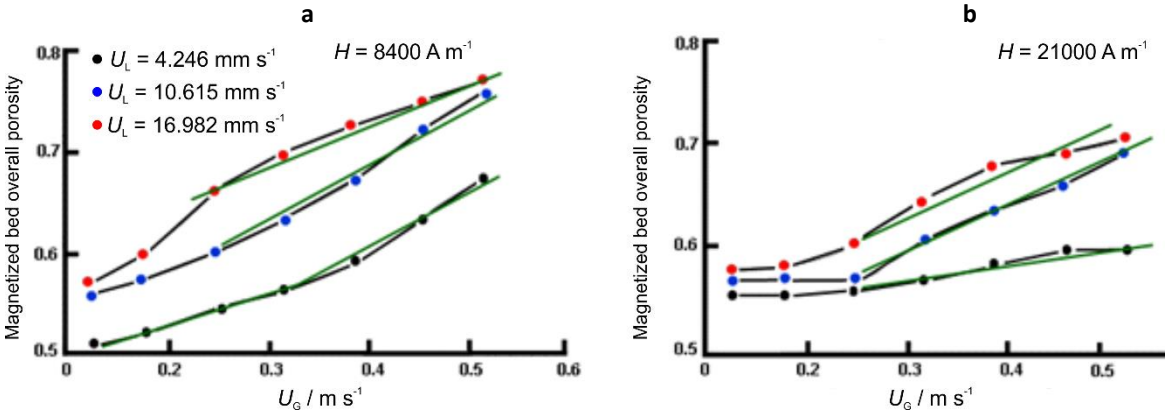

Figure 9. Magnetized bed overall porosity ε_{gl} (combined gas and liquid holdups) as a function of the gas superficial velocity at two distinct intensities of the magnetic field applied. The green solid lines only show almost linear behavior but are not the results of data fittings. Particle fraction 0.3 to 0.4 mm

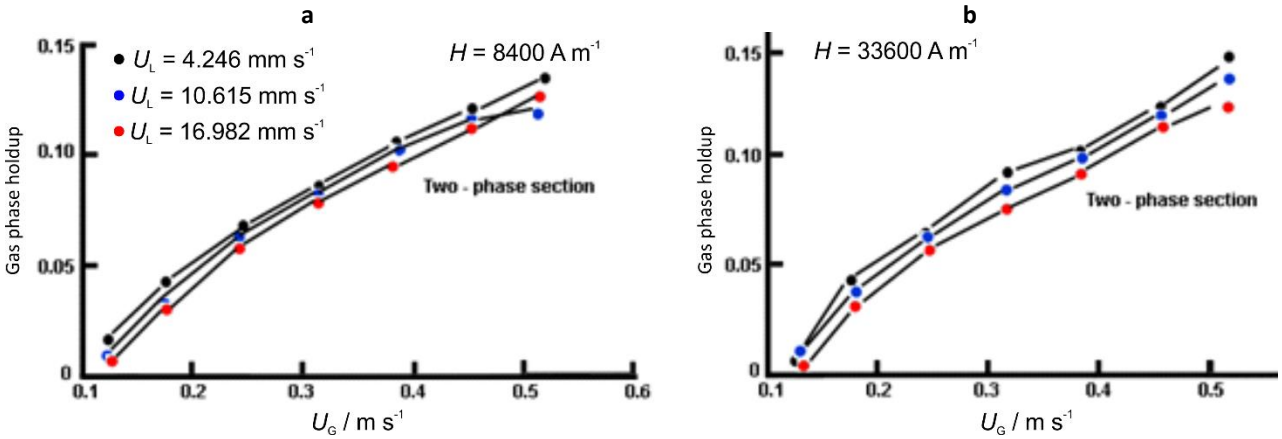

Figure 10. Gas holdup in the two-phase section (when the magnetized bed plays the role of a gas distributor) as a function of the gas velocity. Particle fraction 0.3-0.4 mm.

4. 5. Outlining of the main results

The presented study concerning a bubble column with a magnetized particle bed as a gas distributor is unique even though there are many studies with applications of transverse magnetic fields [1,2,6,7,8,17]. It can be considered as an

upgrade of the research in this field, knowing that there is no literature evidence about three-phase systems under transverse magnetic field.

The main results and contributions can be outlined as follows:

1. It has been demonstrated that a magnetic particle bed can be used as a gas distributor with a structure preliminarily determined by the simultaneous action of both the applied magnetic field and the liquid velocity,
2. The magnetic field intensity allows control of the interparticle forces, thus the bed internal structure and the hydraulic resistance are under remote control,
3. Successful applications of piezometric measurements taking into account the specific conditions due to the imposed magnetic field allowed to create an approach to detect the position of the interface between the magnetized bed and the two-phase section.

5. CONCLUSIONS

This note presented experimental results on a bubble column with a bottom-placed bed of magnetic solids, controlled by an external magnetic field oriented transversely to the column axis. The field orientation and the magnetic system design as saddle coils allow an extended zone of the magnetic bed expansion and control of the bubbles generated at its surface and consequently the gas holdup in the two-phase section above. The pressure drop curves taken from piezometric measurements allowed us to determine the phase holdups in both in the three-phase and two-phase sections as well as the position of the interface between them. The obtained results and the used approach indicate potential benefits for wider applications of transverse magnetic fields in three-phase systems.

NOMENCLATURE

A / m^2	Cross-sectional area of the bed
b / s m^{-1}	Rate coefficient in Eq. (11)
g / m s^{-2}	Gravity acceleration
h / m	Distance from the magnetic bed base
h_{b0} / m	Initial bed height upon the action of the magnetic field
h_b / m	Expanded bed height upon the action of the magnetic field
H/ A m^{-1}	Magnetic field intensity
k_H / ms^{-1}	Pre-factor in Eq. (12)
M_s / Am^{-1}	Magnetization at saturation
M_{solids} / kg	Mass of magnetic solid phase
P_h / Pa	Pressure at distance h
$P_{h\text{-}top}$ / Pa	Pressure at the top of the bubble column
$P_{bed\text{-}base}$ / Pa	Pressure at bed base
$P_{bed\text{-}top\ surface}$ / Pa	Pressure at bed top surface
U_G / m s^{-1}	Gas superficial velocity
U_L / m s^{-1}	Liquid superficial velocity
$U_{G\text{-}mf}$ / m s^{-1}	Gas superficial minimum fluidization velocity in the presence of a magnetic field

GREEK LETTERS

ε_g	Gas phase holdup
ε_l	Liquid phase holdup
ε_{gl}	Magnetized bed overall porosity
ε_s	Solid phase holdup
ε_{s0}	Solid phase holdup in initial bed
ΔP / Pa	Pressure drop between two points;
ρ_g / kg m^{-3}	Density of the gas phase
ρ_l / kg m^{-3}	Density of the liquid phase
ρ_s / kg m^{-3}	Density of the solid phase

REFERENCES

[1] Hristov JY. Magnetic field assisted fluidization-A unified approach. Part 1. Fundamentals and relevant hydrodynamics. *Rev Chem Eng.* 2002; 18: 295-509. https://doi.org/10.1515/REVCE.2002.18.4-5.295

[2] Hristov JY. Magnetic field assisted fluidization-A unified approach. Part5. A Hydrodynamic Treatise on Liquid-solid fluidized beds. *Rev Chem Eng.* 2006; 22: 195-375. https://doi.org/10.1515/REVCE.2006.22.4-5.195

[3] Sajc L, Jovanovic Z, Vunjak-Novakovic G, Jovanovic G, Pesic R, Vucovic D. Liquid dispersions in a magnetically stabilized fluidized bed (MSFB). *Trans Ichem E.* 1994; 72: 236-240.

[4] Sajc L, Pesic R, Bursac P, Vunjak-Novakovic G, Bugarski B, Vukovic D. Liquid dispersion in a magnetically stabilized two and three-phase fluidized bed bioreactors. In: *Fluidization VIII: Proceedings of the Eighth Engineering Foundation Conference on Fluidization*. Tours, France, 1995, pp. 425-432.

[5] Sajc L, Jovanovic G, Jovanovic, Z, Bugarski B. Liquid dispersions in a magnetically stabilized fluidized bed (MSFB). In: Cheremisinoff NP. ed. *Encyclopedia of Fluid Mechanics*, Houston, TX: Gulf Publishing Company.1996, pp. 713-740.

[6] Hristov JY, Hadzisavas K. Gas-liquid-magnetic solid beds: A classification of the operating modes and a hydrodynamic study in a transverse magnetic field. In: *Proceedings of 2nd European Conference on Fluidization*. Bilbao, Spain, 1997, pp. 565-572.

[7] Hristov JY. Magnetic field assisted fluidization - A unified approach. Part 6. Topics of Gas-Liquid-solid Fluidized bed Hydrodynamics. *Rev Chem Eng.* 2007; 23: 373-526. https://doi.org/10.1515/REVCE.2007.23.6.373

[8] Hristov JY. Magnetic field assisted fluidization - A unified approach. Part 7. Mass Transfer: Chemical reactors, basic studies and practical implementations thereof. *Rev Chem Eng*. 2009; 25: 1-254. https://doi.org/10.1515/REVCE.2009.25.1-2-3.1

[9] Hristov JY. Magnetic field assisted fluidization - a unified approach. Part 8. Mass transfer: magnetically assisted bioprocesses. *Rev Chem Eng*. 2010; 26: 55-128. https://doi.org/10.1515/REVCE.2010

[10] Zhu Q, Huang Q, Yang C. Hydrodynamic review on liquid–solid magnetized fluidized bed. *Rev Chem Eng*. 2020; 37: 827-861. https://doi.org/10.1515/revce-2019-0033

[11] Zhu Q, Li H, Zhu Q, Li J, Zou Z. Hydrodynamic study on magnetized fluidized beds with Geldart-B magnetizable particles. *Pow Tech.* 2014; 277: 269-285. https://doi.org/10.1016/j.powtec.2014.08.019

[12] Zhu Q, Hao W, Liang P. Magnetic intensification of mass transfer between fluidizing gas and Geldart-B nonmagnetizable particles: Property effects of added magnetizable particles. *Chem Eng Res Des.* 2021; 175: 25-36. https://doi.org/10.1016/j.cherd.2021.08.034

[13] Tschöpe A, Franzreb M. Influence of non-conducting suspended solids onto the efficiency of electrochemical reactors using fluidized bed electrodes. *Chem Eng J.* 2022; 424: 130322. https://doi.org/10.1016/j.cej.2021.130322

[14] Klaiber M, Tschöpe A, Cu K, Waibel I, Heißler S, Franzreb M, Joerg Lahann J. Multifunctional Core–Shell Particle Electrodes for Application in Fluidized Bed Reactors. *ACS Appl Eng Mater.* 2023; 1: 325–333. https://doi.org/10.1021/acsaenm.2c00072

[15] Rakoczy R, Kordas M, Markowska-Szczupak A, Konopacki M, Augustyniak A, Jabłońska J, Paszkiewicz O, Dubrowska K, Story G, Story A, Zietarska K, Sołoducha D, Borowski T, Roszak M, Grygorcewicz B, Dołegowska B. Studies of a mixing process induced by a rotating magnetic field with the application of magnetic particles. *Chem Proc Eng*. 2021; 42: 157–172. https://doi.org/10.24425/cpe.2021.138922

[16] Grygorcewicz B, Rakoczy R, Roszak M, Konopacki M, Kordas M, Piegat A, Serwin N, Cecerska-Hery´c E, El Fray M, Dołegowska B. Rotating Magnetic Field-Assisted Reactor Enhances Mechanisms of Phage Adsorption on Bacterial Cell Surface. *Curr Iss Mol Biol.* 2022; 44: 1316–1325. https://doi.org/10.3390/cimb4403008

[17] Hristov JY. External Loop Airlift with Magnetically Controlled Liquid Circulation. *Pow Tech*. 2005; 149: 180-194. https://doi.org/10.1016/j.powtec.2004.11.005

Barbotažna kolona sa istostrujnim tokom faza u transferzalnom magnetnom polju

Jordan Y. Hristov[1] i Radojica D. Pešić[2]

[1]Katedra za hemijsko inženjerstvo, Tehnološko-metalurški univerzitet u Sofiji, Sofija, Bugarska
[2]Univerzitet u Beogradu, Tehnološko-metalurški fakultet, Katedra za hemijsko inženjerstvo, Beograd, Srbija

(Naučni rad)

Izvod

U radu je dat prikaz eksperimentalnih rezultata dobijenih u barbotažnoj koloni sa magnetnom čvrstom fazom smeštenom na dnu kolone, kao raspodeljivačem dvofaznog toka gas-tečnost, pod dejstvom poprečnog magnetnog polja. Najpre je obezbeđen protok tečnosti kroz pakovani sloj čestica, zatim je takav sloj podvrgnut dejstvu magnetnog polja, a na kraju je uspostavljen protok gasa kroz sloj, koji je obezbedio uspostavljanje fluidizovanog sloja čestica. Eksperimenti su izvedeni pri intenzitetima polja do 45 kA m^{-1}, površinskim brzinama tečnosti do 20 mm s^{-1} i protocima gasa do 8 m^3 h^{-1}. Korišćene su frakcije čestica dva različita opsega prečnika, do 1 mm. Fokus je bio na ekspanziji trofaznog sloja magnetnih čestica, koji igra ulogu distributora gasa, kao i na zapreminskom udelu gasa u dvofaznoj sekciji kolone koja se nalazi iznad trofaznog sloja, a takođe i na drugim odgovarajućim parametrima sistema. Izvršena piezometarska merenja su pokazala da je na osnovu njih moguće odrediti poziciju granice između dve sekcije u koloni bez vizuelne detekcije te pozicije, kao i određivanje sadržaja gasa u dvofaznoj sekciji kolone. Na ekspanziju sloja snažno je uticalo stanje sloja stvoreno inicijalno uspostavljenim protokom tečnosti. Rezultati su pokazali da intenzitet polja primenjenog na magnetne čestice omogućava kontrolu kako ekspanzije sloja tako i unutrašnje strukture sloja, na osnovu kojih se prepoznaje potencijalna primenljivost magnetno stabilisanog trofaznog sloja kao distributora gasa u barbotažnoj koloni.

Ključne reči: Trofazni magnetno stabilisani sloj; ekspanzija sloja; zapreminski udeo gasa

Combustion of waste solids in a fluidized bed to generate sustainable energy

Milica R. Mladenović, Biljana S. Vučićević, Ana D. Marinković and Jovana Z. Buha Marković

University of Belgrade, Vinča Institute of Nuclear Sciences – National Institute of the Republic of Serbia, Laboratory for Thermal Engineering and Energy, Belgrade, Serbia

Abstract

Exploring alternative options to address the impending global energy crisis while taking into account environmental concerns and climate change mitigation and addressing the sky-rocketing energy demand has become urgently essential. This need is further highlighted by the significant reliance of the Republic of Serbia on imported energy sources so that the focus of its energy sector strategy is rational use of energy resources, use of renewable energy sources (RES), and waste management with satisfying environmental regulations. The use of low-calorific and waste materials in conjunction with fluidized bed combustion technology is a method to achieve all the above goals synergistically. This paper presents experimental results of combustion of several solid wastes (coal mining waste from the "RB Kolubara" complex, Serbia, paper sludge and hazelnut shells), conducted in an industrial prototype and experimental bubbling FB boiler (capacity up to 500 kW). Burning these wastes has a variety of advantages, including recovering substantial energy remaining in the waste and minimizing the overall waste volumes. The work focused on determination of furnace temperature profiles, composition of the flue gas at the furnace outlet as well as fluidization air and fuel flowrates, the minimum fluidization rate, fluidization number, maximum heat output and the transferred heat of the tested fuels. Based on the obtained results, potentials of FBC of waste fuels and the possibility of utilization of their energy potential are evaluated.

Keywords: Low-grade fuels, biomass; paper sludge; coal, hazelnut shells; bubbling fluidized bed combustor.

Available on-line at the Journal web address: http://www.ache.org.rs/HI/

ORIGINAL SCIENTIFIC PAPER

UDC: 662.992.82: 621.8.036: 502.174.3

Hem. Ind. **78(3)** 173-185 (2024)

1. INTRODUCTION

Rational use of limited energy resources is becoming increasingly essential, and the use of waste, low-value and non-conventional fuels holds a special place. Transition to "cleaner" combustion technologies while maintaining economic profitability is the most difficult task in the use of such fuels. In these contexts, the fluidized bed combustion (FBC) technology is highly recommended. This technology enables combustion of materials with high ballast contents and very uneven compositions while emitting less pollution [1,2]. These benefits over other conventional combustion technologies are derived from FBC properties. Namely, high thermal inertness of the fluidized bed (FB) material enables fuel to combust at temperatures of 760-900 °C with minimal NOx generation and without ash melting to contaminate the heating surfaces [1]. By injecting limestone in the FB, a direct desulphurization (up to 90 %) in the furnace can be carried out [2]. Intensive mixing of gases in the layer prevents formation of CO and unburned hydrocarbons, leading to high combustion efficiency. As drying, devolatilization and combustion processes take place simultaneously, it is not required to prepare the solid fuel in any special manner except for reduction to granulation of up to 35 mm in size. The design of these boilers does not require any movable elements or fireproof materials in the furnace. This fact and the possibility of utilizing low-grade, low-priced fuels, ensure low operational costs.

The Laboratory of Thermal Engineering and Energy of the "Vinča" Institute has decades of experience in the field of FBC and the development of furnaces and boilers of this type [2,3]. As a result of that research, a methodology for

Corresponding authors: Milica R. Mladenović, University of Belgrade, Vinča Institute of Nuclear Sciences – National Institute of the Republic of Serbia, Laboratory for Thermal Engineering and Energy, Belgrade, Serbia

Paper received: 6 June 2023; Paper accepted: 22 May 2024; Paper published: 28 May 2024.

E-mail: mica@vinca.rs

https://doi.org/10.2298/HEMIND230606008M

evaluating suitability of burning a particular fuel in an FB is created. The foundation of the methodology is a combustion test of the subject fuel on a semi-industrial water-heating boiler, with the power of up to 500 kW, in steady-state modes of operation. This paper presents the results of FBC of the following solid waste fuels: coal mining waste from the "RB Kolubara" complex, Serbia, paper sludge and hazelnut shells in order to assess the possibility for combustion of these fuels in industrial-scale FB plants. The text that follows explains why these specific fuels were tested.

Exploitation and mining-geological characteristics of domestic lignite and brown lignite basins inevitably cause fluctuations in coal characteristics. Using out-of-balance coal reserves, such as fine-grained coal with high levels of ballast and low heating value, highlights the need for technology, such as FB boilers, that is less sensitive to uneven and inferior fuel composition while meeting environmental standards.

For the production and processing of paper, there are several domestic factories, including the paper factories in Belgrade, Avala Ada and Umka. One of the by-products of paper processing in these factories is paper sludge of high humidity and uneven composition, which is not suitable for recycling, but can therefore be burned in a FB with the support of a higher calorific fuel.

Finally, the Serbian Ministry of Agriculture estimates that there are 44.9 km^2 (4,479 ha) of hazel tree plantations with an annual output of about 5,000 tons of hazelnuts in shell [4]. Due to the rising demand from the confectionery industry and subsidies from the relevant Ministry of Agriculture for new, intensive hazelnut plantations with modern cultivation technology, there are ambitious plans for a multiple increase in this production. Furthermore, hazelnut shell was characterized as a solid biomass fuel with the best biomass quality index (BQI) [5]. Low moisture content due to dry processing in hazelnut production, low trace elements and ash contents as well as high carbon content and high calorific value are responsible for the best BQI of this biomass. Therefore, this paper encourages the use of this waste biomass as an exceptional fuel, as it is a natural pellet that is clean, easily stored, and doses into a furnace similarly to wood pellets.

2. EXPERIMENTAL SECTION

2. 1. Description of the experimental facility

Combustion experiments were performed in a FBC facility shown in a simplified scheme in Figure 1, along with locations of the measurement-regulation points. More about the shown bubbling fluidized bed combustor (BFBC) can be also found in [6,7].

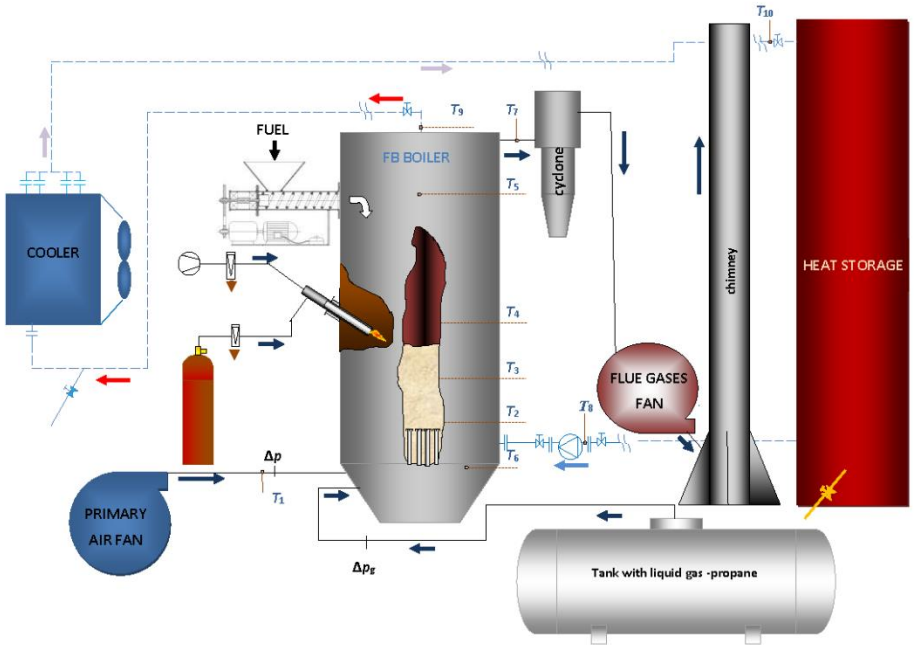

Figure 1. Scheme of the semi-industrial experimental FB facility

Vertical construction of the boiler has been adopted to stop the precipitation of flying solids [7]. Flying solids could originate from the ash or worn-out inert material flown away from the FB furnace. The experiment was conducted with fuel feeding onto the FB by a screw feeder with variable speed. The start-up burner, cooled by water, uses the piezo effect to spark a mixture of liquid gas and air. Flue gases are burned up in the vertical cylindrical space above the FB and then introduced into the vertical tubes of the 1st and 2nd set of flue pipes, which are immersed in the flue gases cooler. During the transfer from the 1st set of the tubes, a part of the flying ash is removed from the flue gas stream due to inertia. After leaving the 2nd set of tubes, flying ash removal is finished in the particle separator - cyclone. To enable experiments in long-term steady state regimes in the FB facility a heat storage unit has been added. Four ports (2 - 5) are used for thermocouples to measure temperature along the furnace height. The thermocouple positions along the gas tract (Fig. 1) are:

- T_1- air temperature on the air distributor inlet,
- T_2 - 5 cm above the air distributor nozzles (in the bed),
- T_3 - 20.5 cm above T_2 (in the bed),
- T_4 - 40 cm above T_3 (above the bed),
- T_5 - 97 cm above T_4 (above the bed),
- T_6 - flue gas temperature in the transition from the first to the second draft, and
- T_7 – flue gas temperature at the combustion chamber exit.

In addition to the temperatures mentioned, the temperatures T_8 - water entering the pump, T_9 - water leaving the boiler and T_{10} - entering the heat storage are also measured (see Fig. 1). The continuous temperature measurement system consists of the thermocouples mentioned above and the KEITHLEY recording device (a Tektronix company, USA). The flue gas composition (CO, NO_x, SO_2, O_2) was measured at the boiler outlet using the MRU Airfare Varioplus industrial gas analyzer (MRU Instruments, Germany) with associated equipment.

2. 2. Fuel characterization

The solid waste fuels tested for their suitability for combustion in a fluidized bed came from: Coal waste (KCW) from the Kolubara Basin, paper sludge (PS) from the Umka factory and hazelnut shells (HSh) from a 0.14 km^2 (14 ha) plantation in Ašanje, AP Vojvodina. Prior to the experimental investigation proximate and ultimate analyses of the subjected fuel have been performed (Table 1) to calculate the adiabatic combustion temperature (T_{adiab}), as the foundation for facility adjustment (defining the fuel and air flow to obtain a steady state on the designed combustion temperature).

Moisture and ash contents of tested fuels were determined by a thermogravimetric analyzer LECO TGA 701 (LECO, USA). The proximate analysis was done according to the standard methods [8-10]. All measurements were done in triplicate. The instrument LECO CHN 628 Series (LECO, USA) was applied to determine the total N, C, and H content in fuels the standard methods [11-13], while O content was calculated [14].

Due to the high ballast content and thus low calorific value (NCV) of the Kolubara waste coal and paper sludge, their combustion was assisted by liquid petroleum (LG) gas (propane or a mixture of propane and butane). Therefore, the composition of the equivalent fuel is also given in Table 1, calculated based on the mass fractions of primary fuel and LG, *i.e.* on the basis of their measured mass flow rates during the combustion test itself in FB.

In addition, finely granulated coal was used in combination with LG right at the beginning of the experiment with paper sludge (PS) in order to stabilize the heating process and achieve stationary parameters for the introduction of the PS into the fluidized bed (constant air flow for fluidization and reaching the bed temperature of 800 °C). After reaching the steady state, the coal was no longer used, and the measurements were performed with continuous dosing of PS and LP to support combustion.

On the other hand, hazelnut shells have a heat value that does not require the support of additional fuel; what's more, 2 kg of these shells is almost energetically equivalent to 1 m^3 of natural gas.

Ash melting temperatures (Table 2) were also determined according to standard methods [15, 16] as a part of fuel characterization in order to prevent the tested fuel's ash from sintering with the bed's inert material, which would eventually cause the fluidized bed to "fall". The only issue in this regard is the combustion of hazelnut shells. The low sintering temperature of ash from hazelnut shells [5,17] is due to their high alkali content [18]. The process of

periodically refreshing the sand (replacement or cleaning, *etc.*) overcomes the problem. At temperatures of combustion around the sintering point, however, problems related to "falling" of a bed should not be expected, especially if the procedure of sand refresh is foreseen.

Table 1. Characterization of fuel - partial proximate and ultimate analyses of subject fuels and calculated adiabatic combustion temperature as a function of excess air (λ)

	Content (as received), wt.%				
	Kolubara coal waste		Paper sludge		Hazelnut shells
	Primary fuel composition	Equivalent fuel[1]	Primary fuel composition	Equivalent fuel[2]	Primary fuel composition
Moisture	36.74	35.62	46.09	35.56	12.84
Ash	39.13	37.94	13.94	10.76	1.89
Volatile matter	14.28	16.89	39.35	53.6	66.65
Char	48.98	47.49	14.56	10.9	20.51
C	15.69	17.71	15.99	31.16	45.09
H	1.78	2.28	2.68	6.08	6.53
O	6.28	6.09	20.46	15.79	33.32
N	0.22	0.21	0.73	0.56	0.22
S	0.16	0.16	0.12	0.09	0.11
NCV[3], MJ kg^{-1}	5.21	6.46	4.8	14.26	16.13
λ			T_{adiab} / °C		
1.00	1274	1386	1211	1750	1764
1.15	1186	1285	1135	1602	1605
1.30	1110	1198	1068	1479	1473
1.45	1042	1122	1008	1374	1363
1.60	984	1055	955	1284	1268
1.75	931	996	908	1205	1188
1.90	883	944	865	1135	1116
2.05	841	897	826	1074	1053
2.20	802	855	791	1019	996
2.35	767	816	758	970	947
2.50	735	781	728	925	902

[1]Calculated based on the mass fraction of liquid gas (LG) and Kolubara's coal (on the basis of their measured flows during the combustion test in FB, 0.03 : 0.97) and their elemental compositions; [2]Calculated based on the mass fraction of LG and paper sludge (0.23 : 0.77) and their elemental compositions; [3]Net calorific value

Table 2. Ash melting temperatures in an oxidizing atmosphere

	T / °C		
	Kolubara coal waste	Paper sludge	Hazelnut shells
Sintering point	960	950	845
Softening point	1130	1060	990
Semi sphere point	1280	1280	1250
Melting point	1340	1420	1270

Granulometric analysis of Kolubara waste coal small fractions (Table 3) was also performed according to standard methods [19].

Table 3. Sieve analysis of the Kolubara coal waste used in the study

Particle size, μm		Tare	Gross	Net	M / %	M / % ↓[1]	M / % ↑[2]
	3150	289.07	300.68	11.61	11.58	88.42	11.58
- 3150	+2000	270.02	274.97	4.95	4.94	83.48	16.52
-2000	+1000	418.14	431.23	13.09	13.06	70.42	29.58
- 1000	+ 710	213.82	218.65	4.83	4.82	65.60	34.40
- 710	+ 500	215.01	220.43	5.42	5.41	60.19	39.81
- 500	+200	255.16	303.27	48.11	48.01	12.18	87.82
-200	0	175.56	187.77	12.21	12.18	0.00	100.00
Σ					100		
Average size 940							

[1]The portion of the granulate that has passed through the sieve; [2]The portion of the granulate remaining on the sieve

2. 3. Experimental procedure

After starting the installation by combustion of liquid gas and reaching temperatures of FB required for the beginning of combustion of the examined fuel, it is gradually dosed. Empirically, based on numerous in-house tests on a semi-industrial installation with FB (Fig. 1), the temperature for the start of dosing the subjected fuel depends on the fuel quality. Thus, high-calorific value fuels such as hazelnut shells or dry wood chips can start with gradual dosing already at temperatures of approx. 600 °C, while low-calorific ones, such as PS and KCW, generally require a bed temperature of ≈ 800 °C. Once the combustion is self-sustaining, the liquid gas supply is gradually reduced and if it is possible to independently burn the primary fuel, it is shut off. By adjusting the flows of fuel and air (by frequency regulators), stationary operation of installation with pre-defined performance parameters is achieved. Temperatures along the combustor are monitored and recorded continuously.

Experiments on the BFB installation in long-term operation were performed in several operating regimes, for each of the tested fuels. The paper presents representative regimes for each of the fuels in the aforementioned range of combustion temperatures.

Quartz sand was used as the inert bed material for all fuels and regimes, with the fixed bed parameters given in Table 4.

Table 4. Summary overview of fixed bed properties (without fluidization)

Fuel	d_p / mm	ρ_b / kg/m³	*Ho* / mm	Liquid gas	
				For start-up	For flame support
KCW	0.79	1475	290	propane	
PS	0.96	1380	325	propane/butane mixture	
HSh	0.76	1548	254	propane	-

d_p - average send diameter calculated on the basis of granulometric analysis of quartz sand; ρ_b - bulk density of fixed bed; *Ho* - fixed bed height.

The expressed volatility and the ballast content of the paper sludge determined the choice of the highest *Ho*, while on the other hand the low ballast content and the high calorific value of HSh determined the choice of the lowest *Ho*. The particle diameter and bulk density of the fixed bed are values determined according to standard methods [19,20] on quartz sand supplied for each test.

3. RESULTS OF MEASUREMENTS IN STEADY REGIMES OF OPERATION

After achieving steady-state conditions in the experimental FBC, measurements of flue gas composition and flow rates of fuel and air are taken (Table 5). Figures 2, 4, and 6 in the following text show temperature profiles of the flue gases in the BFB combustion chamber, while Figures 3, 5 and 7 show the measured gas concentrations during the combustion of the tested fuels. All tests were conducted at fluidized bed temperatures of 850-861 °C, which corresponds to the average operating temperature range of industrial-scale facilities [21]. These are optimal temperatures both from the aspect of reduced concentrations of NOx compounds and from the aspect of efficiency of desulfurization with limestone if it turns out that its use is necessary. During the test, a sufficient heat sink was achieved through the heat exchanger and heat storage, so that the experiment was not time-limited.

Table 5 shows the fluidization parameters and flue gas compositions for all three tested fuels, which are as follows:

- $T_{avr} = T_{2\,avr} + T_{3\,avr}$ - measured fluidized bed average temperature (see Fig. 2, 4 and 6),
- $\dot{m}_{air}$ and $\dot{m}_{fuel}$ - measured fluidization air and fuel flows
- v_{mf} - minimum fluidization velocity calculated accordingly to [22],
- $N = v_f / v_{mf}$ - fluidization number, where v_f is measured fluidization velocity (calculated from the measured air flow for fluidization ($\dot{m}_{air}$) divided by the cross-section of the FB combustion chamber),
- $P_{max} = \dot{m}_{fuel}$ NCV- maximum power output and
- $Q_w = \dot{m}_w C_w \Delta T_w$, the heat transferred to the boiler working fluid (water), where are:
  - $\Delta T_w = T_8 - T_9$ = 16.72, 11.11 and 17.00 K, for KCW, PS and HSh, respectively
  - specific heat capacity of water C_w = 4.18 kJ/kg K and measured flow of working fluid-water - $\dot{m}_w$ = 12000, 10000 and 12000 kg/h for KCW, PS and HSh, respectively

- H_{exp} - expanded bed height, *i.e.* expanded splash zone calculated according to the equations from the paper [22].

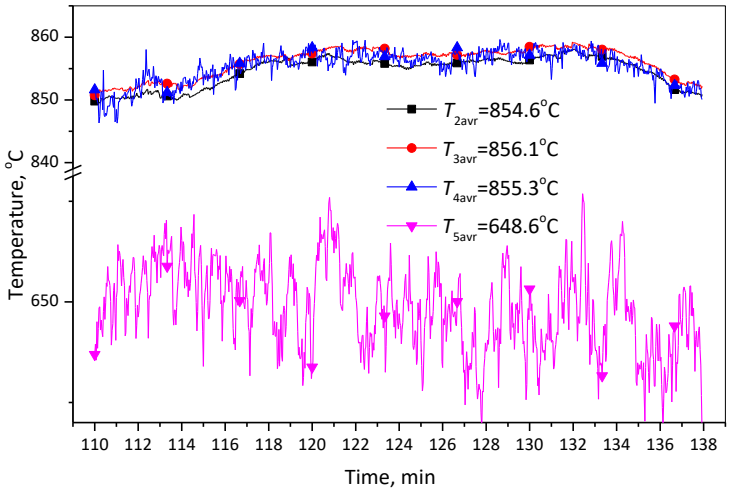

Figure 2. The temperature profile in the furnace in the KCW combustion regime

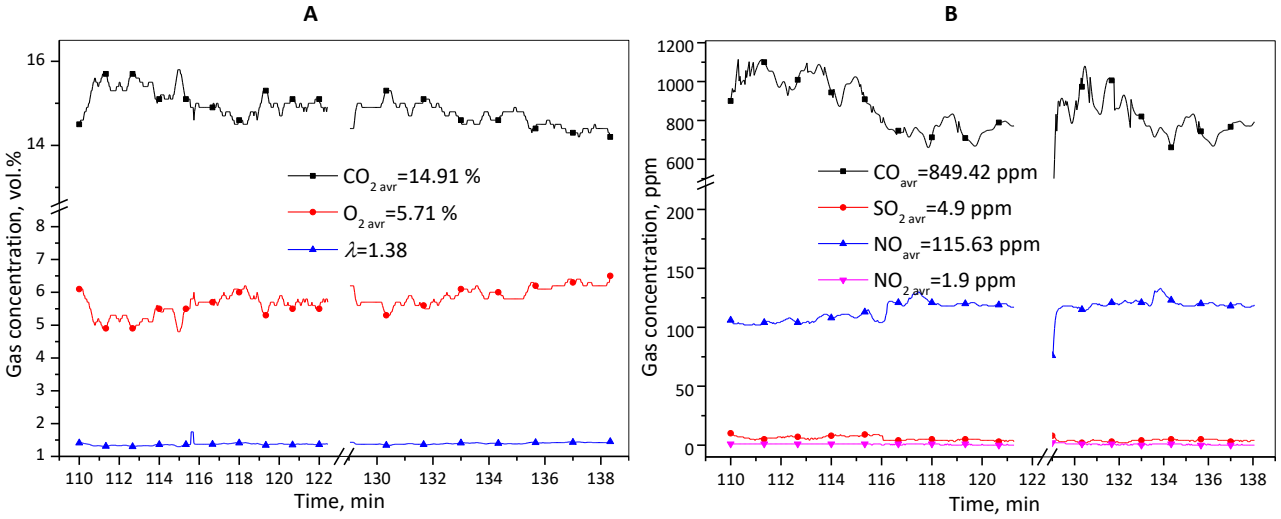

Figure 3. Gas composition in the flue gas during the KCW combustion regime expressed in A - vol.% and B - ppm

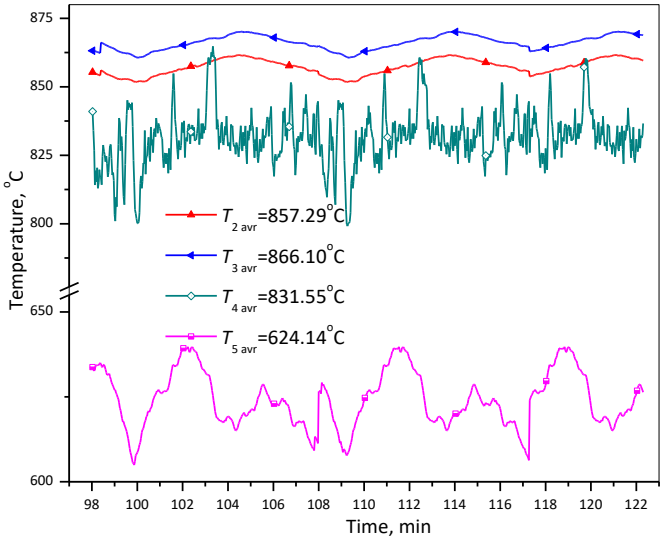

Figure 4. The temperature profile in the PS combustion regime

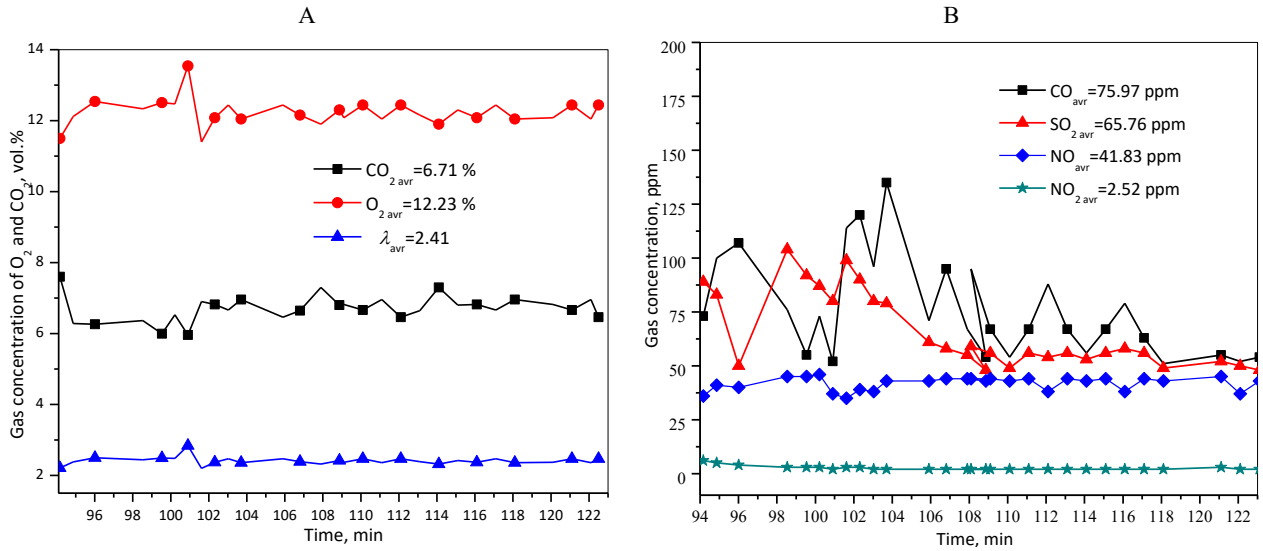

Figure 5. Gas concentration in the flue gas during the PS combustion regime

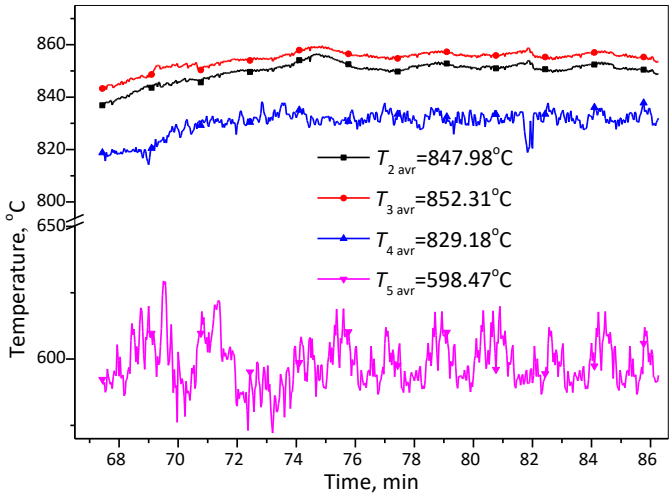

Figure 6. The temperature profile in the furnace in the HSh combustion regime

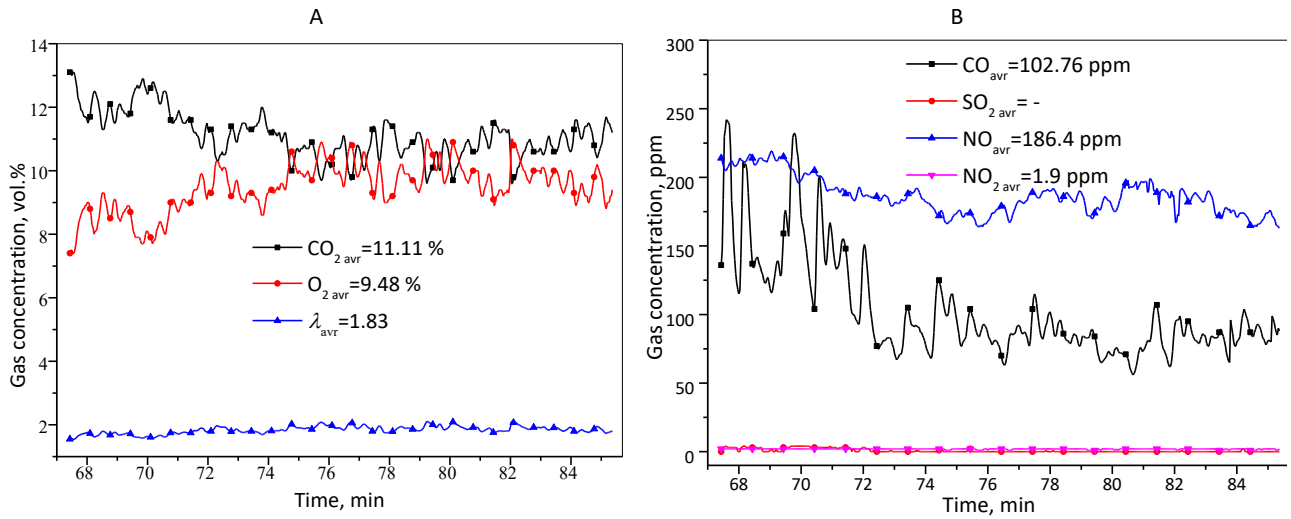

Figure 7. Gas concentration expressed in A - vol.% and B - ppm in the flue gas in the HSh combustion regime

According to the Regulations in the Republic of Serbia [23], CO_{ref}, $SO_{2\,ref}$ and $NO_{x\,ref}$ are the contents of flue gas components calculated on the reference value of oxygen - $O_{2\,ref}$, for small combustion plants. Namely, the volume share of oxygen in the waste gas for existing small combustion plants that use coal, briquettes and coke from coal is 8 %, and when using other solid fuels the $O_{2\,ref}$ is 13 %. In Table 5, the measured values of CO, SO_2 and NO_x (Figs. 3, 5 and 7 right) for the reference value O_2 are converted into CO_{ref}, $SO_{2\,ref}$ and $NO_{x\,ref}$ in accordance with the Regulations [23]. The fluidization parameters were obtained at uniform combustion (bed) temperatures for each of the tested fuels.

Table 5. Fluidization parameters and flue gas composition for all three tested fuels

Fuel	FB operating parameters							
	T_{avr} / °C	$\dot{m}_{air}$ / kg h^{-1}	v_{mf} / m s^{-1}	N	H_{exp} / mm	$\dot{m}_{fuel}$ / kg h^{-1}	P_{max} / kW	Q_w / kW
KCW	855	699	0.31	7.1	551	144.40	258	233
PS	861	632	0.46	4.4	480	75.17	297	129
HSh	850	582	0.30	6.0	471	54.60	245	237
	$O_{2\,ref}$ content, %	Content, mg m^{-3}						
		CO	CO_{ref}	SO_2	$SO_{2\,ref}$	NO_x	$NO_{x\,ref}$	
KCW	8	1059.79	900.84	13.99	11.89	238.36	202.61	
PS	13	94.78	86.47	187.66	172.63	90.87	77.24	
HSh	13	128.21	89.04	-	-	385.87	328.00	

To illustrate the zone of intensive combustion, Figure 8 shows the change of average measured temperatures along the furnace height for all tested fuels.

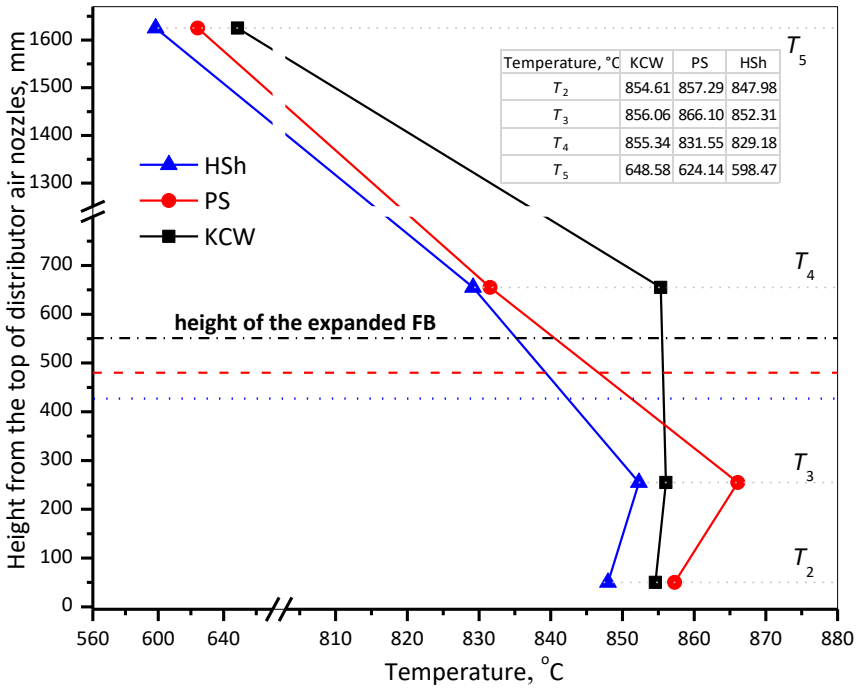

Figure 8. Measured temperature gradients along the furnace height

4. DISCUSSION

Due to the pronounced content of ballast in the fuel composition and consequently low heating values (NCV), the KCW and PS combustion experiments took place with the support of supplementary fuel (Table 1). The energy share of propane during the combustion of KCW was 22 %, and the propane-butane mixture during the combustion of PS was 74 %, so the latter process effectively was the incineration of paper sludge in a fluidized bed. The combustion process in all regimes was encompassed by the heat exchange with the water-cooled furnace surface (Q_w, Table 5), so the measured combustion temperatures in the fluidized bed (T_2 + T_3 = T_{avr}) are considerably lower than the theoretical adiabatic combustion

temperatures for the measured excess air and the composition of the tested fuel. The adiabatic combustion temperatures calculated based on the ultimate analysis (Table 1) of the equivalent fuel for KCW and PS and the measured excess air were 1157 °C (λ = 1.38) and 953 °C (λ = 2.41), respectively. For HSh, this value was 1150 °C (λ = 1.83).

The consequence of that is also a temperature drop from the layer surface to the top of the furnace of 207 °C for KCW and PS, and 231°C, for HSh, (Fig. 8). The highest measured temperatures in the combustion chamber are the temperatures in the bed: T_2 and T_3 (Fig. 8), which indicates that the process was carried out in a way that the zone of intensive combustion was in the bed itself, at temperatures which avoid sintering of the bed inert material. The literature [24, 25] has shown that this indicates a good organization of combustion in the fluidized bed. From the same diagram it can be noticed that the difference between the temperature in the bed and above it ($\Delta T_{34} = T_3 - T_4$) increases directly with decreasing the degree of fluidization - N (Table 5), as a direct consequence of reducing the height of the expanded bed. Furthermore, a very low ΔT_{34} = 0.72 °C was recorded during KCW combustion also as a result of the removal and combustion of the predominant finer coal particles (Table 3) above the fluidized bed.

The FBC facility where the combustion experiments were performed belongs to small combustion facilities [23]. According to [23], section 29, for small combustion plants that use solid fuels in a fluidized bed, the highest prescribed limit values for solid fuels from Annex 3 of this regulation are applied, when they alternately or simultaneously use two or more types of fuel, which is practically presented in Table 6.

Table 6. Emission limit values (ELV) for small combustion facilities (150-500 kW of thermal power) [23]

Polluting matter	Type of fuel	ELV, mg m^{-3}	
		existing[1]	new[2]
CO	coal, wood, briquettes or wood pellets	2000	1000
	all gaseous fuels	100	100
NO_x	liquefied petroleum gas	200	150

[1]article 3 no. 13 of regulation [23]: an **existing** small combustion plant is a combustion plant which has a use permit issued before the entry into force of this regulation and, in the absence of a use permit, a building permit or which was put into operation before the entry into force of this regulation.
[2]article 3 no. 14 of regulation [23]: a **new** small combustion plant is a combustion plant which has a use permit issued after the entry into force of this regulation and, in the absence of a use permit, a building permit or which has been put into operation after the entry into force of this regulation.

Tables 5 and 6, as well as the fact that the limit value of SO_2 is not prescribed for small combustion plants, indicate that the emission limits have not been exceeded in any of the tests performed.

When KCW is combusted, high CO emissions must be observed regardless of whether they are within the permitted limits. This is due to a combination of factors, including high concentrations of small particles that partially burned in the space above the bed, where the temperature drops to 650 °C - insufficient for complete oxidation to CO_2, insufficient height, and a lack of insulation in the space above the bed. Following the same fuel combustion experiments, only 19.5 % of the expected amount of ash (based on the material balance) was captured in the particle separator (cyclone, Fig. 1). About 70 % of the captured ash had granulation greater than 200 μm, with a combustible content of 4.6 %. Given that the sand level was not increased due to the ash remaining in the layer, this means that 80 % of the finest ash particles were brought out of the bed, confirming the previous assertion that their after-burning and combustion occurred under unfavorable conditions above the fluidized bed. At the same time, the SO_2 emission is very low, which is logical considering the KCW composition. Given the mass participation of propane of only 3 % (energy-wise 22 %), it is a matter of burning solid fuel, so the value of $NO_{x\ ref}$ is not subject to restrictions even though it is also relatively low.

Combustion of paper sludge resulted in very low CO and NOx emissions, but an unexpectedly high SO_2 emission, considering the composition of the used PS. This is because, for this experiment, coal with a significantly higher sulfur content than PS was used to stabilize the flame during the boiler startup, so residual sulfur in the bed was included in the overall average SO_2 emission value. This is visible in Figure 5 (B). Considering the high N content in both the primary fuel (PS) and the equivalent (Tab. 1), low NOx emissions have to be noted. This suggests that the lowest degree of fluidization (N) and the highest initial bed height (Ho) in all three experiments, provided sufficient mixing in the bed to achieve the catalytic effects of ash, char and water [6,26] on reduction of nitrogen oxides.

HSh, superior to the other two used fuels in terms of its fuel characteristics (Table 1), is the only fuel that burned without the support of another fuel. At the same time, the measured emissions were below the legal limits, even though

the concentration of SO_2 was at the detection limit of the gas analyzer, so this emission value is not listed in Table 5. Although the N content in the fuel is identical to that in KCW, a higher NOx emission was recorded, which is justified by the lower content of ash and char, as NOx reduction catalysts, compared to KCW.

Based on the tests carried out and the analysis of the test results, it can be concluded that combustion of both PS and HSh can be successfully carried out in an industrial plant with a similar concept to the FBC facility where the tests were performed, while a modified concept is proposed for the combustion of KCW. Namely, due to possible large variations in the quality of KCW and the effort to avoid the use of higher quality supplementary fuel, a FB boiler with an adiabatic two-part combustion chamber could be proposed. The adiabatic combustor enables the combustion of fuel whose NCV is even below 5 MJ kg^{-1}, while the two-part combustor enables a greater range of boiler powers. Adiabatic furnaces are also very important from the aspect of reducing the output concentration of CO because combustion above FB would take place at temperatures of 800 to 850 °C, which is significantly higher than the temperature obtained in our boiler during the experiments. Another solution could be the combustion of KCW in a circulating fluidized bed (CFB) [28]. In the CFB, the majority of solids leaving the furnace are captured by the gas-solid separator and recirculated back to the FB at a sufficient rate to cause a minimum degree of solids refluxing in the furnace. In this way, it is possible to completely burn particles and gases in the return loop, but with more complex fluidization dynamics and higher fluidization velocities .

The question also arises as to whether it is economically justified to dry KCW or PS first and then combust these fuels later with a lower moisture content. To answer that question, a simple analysis has been performed, defining the power of the furnace when the moisture content in the used samples decreases by 20 % (Table 7 and Fig. 9).

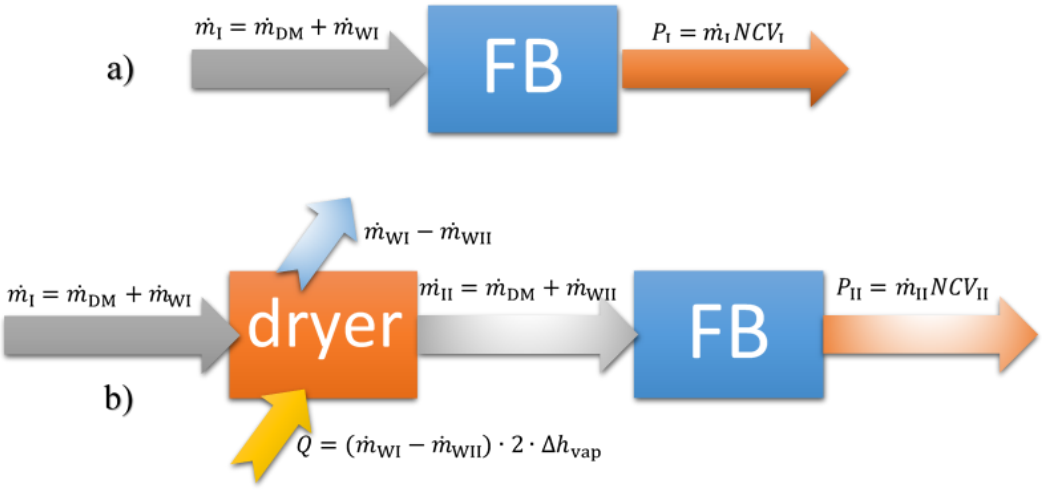

Figure 9. Scheme of the simplified analysis: a) the fuel enters the FB directly without drying; b) the fuel is first dried by removing 20 % of the original moisture (W) and then enters the FB after drying

For simplicity's sake, it is assumed that the fuel can be burned without the support of the auxiliary fuel, and that the flows of the undried fuel directly dosed into the FB and the fuel inserted first into the dryer, are the same (see Fig. 9). It is also assumed that the energy of drying is at least twice as high as the latent heat of water vaporization, Δh_{vap} =2,500 kJ kg^{-1}.

The example shows that combustion of the undried tested fuel saves 14 and 5 % of the required energy (for PS and KCW, respectively). However, in the literature it could be found that the drying energy is 3 to 20 MJ kg^{-1} of the evaporated water [27], thus the drying energy consumption could be significantly higher. The higher the moisture content in the fuel, the greater the energy savings during its direct combustion in the fluidized bed compared to the drying pre-treatment. It is crucial to note that the dryer investment and operating costs have not been considered in this straightforward analysis.

Table 7. Comparative overview of the calculated maximum power of the furnace, with non-dried and pre-dried (20 % reduced moisture content) test fuel without the auxiliary fuel use

Calculation parameters		PS		KCW	
		Non-dried (I)	Pre-dried (II)	Non-dried (I)	Pre-dried (II)
W / %		46.09	26.09	36.74	16.74
Content of dry matter, %		53.91	73.91	63.26	83.26
NCV, kJ/kg		4825	7547[1]	5217	8137[1]
Fuel flow at the FB inlet, kg h^{-1}	$\dot{m}_{I}$	58		140	
	$\dot{m}_{II}$		42.31		106.37
Flow of dry matter ($\dot{m}_{DM}$), kg h^{-1}		31.27	31.27	88.56	88.56
Amount of water removed from the pre-dried fuel ($\dot{m}_{WI} - \dot{m}_{WII}$), kg h^{-1}		15.69		33.63	
Maximum power of furnace obtained from non-dried fuel (P_I), kW		77.74		202.98	
maximum power of furnace obtained from pre-dried fuel minus drying energy ($P_{II} - Q$), kW		66.89		193.72	
Savings[2], $\left(1-\frac{P_{II}-Q}{P_I}\right)100$, %		14		5	

[1]Calculated based on the fuel composition; [2]Achieved by direct combustion in FB

6. CONCLUSION

The investigation of the suitability of the tested waste solid fuels (coal mining waste from the "RB Kolubara" complex, paper sludge and hazelnut shells) for fluidized bed combustion was focused on the combustion quality, *i.e.* combustion efficiency, and the combustion stability, as well as on the fulfilment of the environmental protection criteria.

From the point of view of combustion organization, PS and HSh are burned with an intensive combustion zone in the bed, while combustion of the finest KCW fractions took place above the bed. As far as compliance with environmental norms is concerned, they were not exceeded in any test. However, high CO emissions were also detected during the combustion of KCW, although these were within the permissible limits. It can therefore be concluded that the combustion of both PS and HSh can be successfully carried out in an industrial plant with a comparable concept to the FBC facility in which the tests were carried out, while a modified concept is recommended for the combustion of KCW.

Aside from successfully combusting fuel with a high ballast content with the support of more calorific fuel, a simple analysis revealed that combusting wet fuel directly in a fluidized bed is more cost-effective than drying it first and then combusting it.

The paper demonstrated that by burning the investigated and similar waste materials in a fluidized bed, the principles of sustainability are realized - the waste issue is solved through their energy utilization (economic benefits), while meeting environmental standards.

Acknowledgements: *This work was supported by the Ministry of Science, Technological Development and Innovation of the Republic of Serbia; grant number 451-03-66/2024-03/200017. Also, this research was supported by the Science Fund of the Republic of Serbia, #Grant No 2929, Sustainable deployment of biomass catalytic gasification technology to increase the utilization of renewable energy in the Serbian industry- STABILISE.*

REFERENCES

[1] Leckner B. Fluidized Bed Combustion. In: *Reference Module in Chemistry, Molecular Sciences and Chemical Engineering*. J. Reedijk (Ed.), Elsevier; 2016:

[2] Mladenović MR. *Research of thermomechanical proces during decomposition of high density liquid fuel in the fluidized bed* (in Serbian), Ph.D. Thesis, University of Belgrade, Faculty of Mechanical Engineering, 2013.

[3] Grubor BD, Dakić DV, Nemoda SD, Mladenović MR, Paprika MJ, Oka SN. Research of the fluidized bed combustion in the laboratory for thermal engineering and energy: Part A: Achievements in targeted fundamenal research. *Therm Sci*. 2019; 23: S1637-S1653 https://dx.doi.org/10.2298/TSCI180725289G.

[4] Ministry of Agriculture, Forestry and Water Management of the Republic of Serbia, Information on hazelnuts, 2019, http://www.minpolj.gov.rs/download/informacija-o-lesniku-2019/
[5] Rocha S, Candia O, Valdebenito F, Flavio Espinoza-Monje J, Azócar L. Biomass quality index: Searching for suitable biomass as an energy source in Chile. *Fuel*. 2020; 264: 116820 https://doi.org/10.1016/j.fuel.2019.116820.
[6] Mladenović MR, Dakić DV, Nemoda SĐ, Paprika MJ, Komatina MS, Repić BS, Erić AM. The combustion of biomass - The impact of its types and combustion technologies on the emission of nitrogen oxide. *Hem Ind.* 2016; 70: 287-298 https://dx.doi.org/10.2298/HEMIND150409033M.
[7] Mladenović M, Nemoda S, Dakić D, Milijana P, Đurović D, Repić B. Mogućnosti sagorevanja kontaminirane zrnaste biomase i drugih ostataka poljoprivredne proizvodnje u fluidizovanom sloju. *Cont. Agr. Engng*. 2013; 39: 213-220
[8] ISO 1822:2015, Solid Biofuels - Determination of Ash Content, International Organization for Standardization (2015)
[9] ISO 18134-1:2015, Solid Biofuels - Determination of Moisture Content - Oven Dry Method - Total Moisture - Reference Method (2015)
[10] ASTM D7582-12: Standard test methods for proximate analysis of coal and coke by macro thermogravimetric analysis (2012)
[11] ISO 16948: 2015 Solid Biofuels - Determination of Total Content of Carbon, Hydrogen and Nitrogen (2015)
[12] ASTM D5373-14: Standard test methods for determination of carbon, hydrogen and nitrogen in analysis samples of coal and carbon in analysis samples of coal and coke (2014)
[13] ASTM D5016-08: Standard test method for total sulfur in coal and coke combustion residues using a high-temperature tube furnace combustion method with infrared absorption (2008)
[14] ASTM D3176-09: Standard practice for ultimate analysis of coal and coke (2009)
[15] ISO 540:2008, Hard coal and coke – Determination of ash fusibility (2008)
[16] SRPS EN ISO 21404:2020, Solid biofuels - Determination of ash melting behaviour
[17] Demirbaş A. Fuel Characteristics of Olive Husk and Walnut, Hazelnut, Sunflower, and Almond Shells. *Energy Sources*. 2002; 24: 215-221 https://doi.org/10.1080/009083102317243601.
[18] Bakisgan C, Dumanli AG, Yürüm Y. Trace elements in Turkish biomass fuels: Ashes of wheat straw, olive bagasse and hazelnut shell. *Fuel*. 2009; 88: 1842-1851 https://doi.org/10.1016/j.fuel.2009.04.[027.
[19] ISO 1953:1994: Hard Coals - Size Analysis (1994)
[20] SRPS B.H8.340:1988, Determination of bulk density in a small container
[21] Yin, C., 5 - Biomass co-firing, in Biomass Combustion Science, Technology and Engineering, L. Rosendahl, Editor. 2013, Woodhead Publishing. p. 84-105. https://doi.org/10.1533/9780857097439.2.84
[22] Mladenović MR, Dakić DV, Nemoda SDJ, Mladenović RV, Erić AM, Repić BS, Komatina MS. Combustion of low grade fractions of Lubnica coal in fluidized bed. *Therm Sci*. 2012; 16: 297-311 https://dx.doi.org/10.2298/TSCI1201297M.
[23] *Regulation on limit values of emissions of pollutants into the air from combustion plants ("Official Gazette of RS", no. 6/2016 and 67/2021)*,
[24] Caillat, S. and E. Vakkilainen, 9 - Large-scale biomass combustion plants: an overview, in Biomass Combustion Science, Technology and Engineering, L. Rosendahl, Editor. 2013, Woodhead Publishing. p. 189-224. https://doi.org/10.1533/9780857097439.3.189
[25] Moradian, F. (2016) Ash Behavior in Fluidized-Bed Combustion and Gasification of Biomass and Waste Fuels : Experimental and Modeling Approach. PhD dissertation. Högskolan i Borås. Available at: https://urn.kb.se/resolve?urn=urn:nbn:se:hb:diva-9563
[26] Mladenović M, Paprika M, Marinković A. Denitrification techniques for biomass combustion. *Renew Sustain Energy Rev*. 2018; 82: 3350-3364 https://dx.doi.org/10.1016/j.rser.2017.10.054.
[27] Baker CGJ, McKenzie KA. Energy Consumption of Industrial Spray Dryers. *Drying Technol.* 2005; 23: 365-386 https://doi.org/10.1081/DRT-200047665.
[28] Oka S. *Fluidized Bed Combustion*, (Ed.), CRC Press; 2003.

Sagorevanje čvrstih otpadnih materija u fluidizovanom sloju za generisanje održive energije

Milica R. Mladenović, Biljana S. Vučićević, Ana D. Marinković i Jovana Z. Buha Marković

Univerzitet u Beogradu, Institut za nuklearne nauke "Vinča"-Institut od nacionalnog značaja za Republiku Srbiju, Laboratorija za termotehniku i energetiku, Beograd, Srbija

(Naučni rad)

Izvod

Istraživanje alternativnih opcija za rešavanje aktuelne globalne energetske krize uzimajući u obzir zabrinutost za životnu sredinu i klimatske promene, kao i rešavanje naglo rastuće potražnje za energijom postaje suštinska neophodnost. Ova potreba je dodatno naglašena značajnim oslanjanjem Republike Srbije na uvozne energente i strateškim fokusom njenog energetskog sektora, koji podrazumeva racionalno korišćenje energetskih resursa, korišćenje obnovljivih izvora energije i upravljanje otpadom uz zadovoljavanje ekoloških propisa. Upotreba niskokaloričnih i otpadnih materijala u kombinaciji sa tehnologijom sagorevanja u fluidizovanom sloju je metod za sinergijsko postizanje svih gore navedenih ciljeva. U radu su prikazani eksperimentalni rezultati sagorevanja više vrsta čvrstog otpada (kolubarski otpadni ugalj, papirni mulj i ljuske lešnika), sprovedeni u industrijsko-demonstracionom i eksperimentalnom kotlu sa fluidizovanim slojem (kapaciteta do 500 kW). Spaljivanje ovog otpada ima niz prednosti, uključujući iskorišćenje značajne preostale energije u otpadu i minimiziranje ukupne količine otpada. U radu su određeni temperaturni profili u fluidizovanom sloju u ložištu, sastav dimnih gasova na izlazu iz ložišta, kao i protoci vazduha za fluidizaciju i goriva, minimalna brzina fluidizacije, stepen fluidizacije, maksimalna snaga ložišta i predata toplota, za ispitivana goriva. Na osnovu ovih rezultata data je procena kvaliteta sagorevanja otpadnih goriva u fluidizovanom sloju i mogućnosti iskorišćenja njihovog energetskog potencijala.

Ključne reči: goriva lošeg kvaliteta, biomasa; papirni mulj; ugalj; ljuske lešnika; ložište sa mehurastim fluidizovanim slojem

Reciprocating plate column – fundamental research and application in Serbia from 1970 to 2020

Vlada B. Veljković[1,2], Ivana B. Banković Ilić[1] and Dejan U. Skala[3]

[1]*University of Niš, Faculty of Technology, Leskovac, Serbia*
[2]*Serbian Academy of Sciences and Arts, Belgrade, Serbia*
[3]*University of Belgrade, Faculty of Technology and Metallurgy, Belgrade, Serbia*

Abstract
In the group of multiphase contactors and reactors, an important place belongs to reciprocating plate columns (RPCs), which consist of a set of perforated plates fixed on a carrier (the so-called reciprocating or vibrating agitator) moving periodically up and down through a column. This construction maximizes the positive effects of mechanical agitation and minimizes or eliminates the adverse effects characteristic of column-type contactors and reactors. In RPCs, the highest dispersed-phase holdup is achieved at a lower dispersed-phase velocity due to the influence of mechanical agitation on the bubble or drop comminution. Therefore, this device can be the most acceptable contactor or reactor for performing complex actions in multiphase systems. The paper reviews the fundamental research and application of RPCs in Serbia in the last fifty years, from 1970 to 2020. Hydrodynamic and mass-transfer characteristics are analyzed, such as the pressure variation at the column bottom, power consumption, dispersed-phase holdup, axial dispersion, liquid mass transfer coefficient, specific interfacial area, and volumetric mass transfer coefficient. The use of RPCs as reactors in bioprocesses and biodiesel production processes is also discussed.

Keywords: Reciprocating plate agitator, pressure variation, power consumption, dispersed-phase holdup, axial dispersion, volumetric mass transfer coefficient

Available on-line at the Journal web address: http://www.ache.org.rs/HI/

REVIEW PAPER

UDC: 602.42-7+624.073.13

Hem. Ind. **78(3)** 187-203 (2024)

1. INTRODUCTION

Various mechanical agitation methods improve mass transfer in multiphase contactors and reactors. Mechanical agitation is often performed using a rotating agitator (stirred vessels) or perforated plates fixed on a reciprocating (vibrating) plate carrier moving up and down through a column (so-called reciprocating plate columns, RPCs). Compared to bubble columns, a significantly higher gas holdup and larger specific interfacial area can be achieved in RPCs [1,2]. Additional advantages of RPCs over bubble columns are reduced backmixing [3], a prolonged bubble residence time in the dispersion, and a greater contact area between the phases [4]. Moreover, RPCs are characterized by ease of maintenance, simple construction, the possibility of applying large fluid flows, and a simple scale-up procedure [4].

The axial reciprocating motion of a set of perforated plates through a column was patented in 1935 [5]. However, this device remained unused until 1959, when Karr developed an extraction RPC with perforated plates of a large free surface area [6]. Since then, the application of RPCs as extractors has increased because a uniform dispersion, with little axial mixing, is achieved with a relatively little external energy input. Since the 1960s, RPCs with different reciprocating elements (Table S-1, Supplementary Material) have been studied as absorption columns. In the 1980s, 'pure' liquids were used, while later, the gassed systems (gas-liquid and gas-liquid-solid particles) were tested. Newtonian liquids, most frequently water, were mainly used as the liquid phase, while spherical particles and Raschig rings were used as the solid phase.

The first tests of Karr-type RPCs as liquid-liquid extractors in Serbia were conducted on the pressure variation at the column bottom (PVCB) and power consumption [7,8]. Then, studies of gas-liquid [3,9] and gas-liquid-solid phase [10-16] systems were conducted to understand the hydrodynamic and oxygen mass transfer phenomena. After that, RPCs were

Corresponding authors:Ivana B. Banković Ilić, University of Niš, Faculty of Technology in Leskovac, Serbia
E-mail: ivanabank@yahoo.com
Paper received: 20 March 2023; Paper accepted: 5 November 2023; Paper published:21 November 2023.
https://doi.org/10.2298/HEMIND230320028V

tested as reactors for biodiesel production [17-20]. Table S-2 overviews the previous research on hydrodynamics, mass transfer, and applications of RPCs in Serbia.

This paper reviews the fundamental research and application of RPCs in Serbia in the last fifty years, from 1970 to 2020. Both hydrodynamic and mass-transfer characteristics are analyzed, such as the PVCB, power consumption, dispersed-phase holdup, axial dispersion, liquid mass transfer coefficient, specific interfacial area, and volumetric mass transfer coefficient. The analysis mainly focuses on 'pure' liquid, gas-liquid, and gas-liquid-solid systems, although some liquid-liquid systems are also discussed. In addition, the use of RPCs as reactors in bioprocesses and biodiesel production processes is also discussed.

2. HYDRODYNAMICS OF RPCS

The studies of the RPC hydrodynamics include regime and flow models, PVCB, power consumption, dispersed phase holdup, bubble size, and axial dispersion. Knowledge of PVCB is an additional requirement for large-scale device construction of equipment. Power consumption is essential for appraising the mechanical driving mechanism and the operating cost. Dispersed phase holdup is crucial for the dispersed phase retention time and specific gas-liquid interfacial area. Bubble size determines the interfacial area and the mass transfer rate, while axial dispersion is essential for the efficacy of RPCs.

2. 1. Flow regime and models

When a set of reciprocating plates moves through the column filled with a liquid, a characteristic flow develops between two perforated plates [21]. As the plates move upwards, liquid jets are induced in the plate openings, which are directed downwards; a ring vortex surrounds each jet. By changing the plate movement direction, the fluid flow direction in jets and ring vortices changes but not the fluid circulation inside vortices. During the plate movement, the liquid is exchanged between neighboring interplate spaces in the vertical direction due to the jet movement as well as in the horizontal direction due to the creation, destruction, and recreation of ring vortices, thus inducing an intensive liquid mixing in interplate spaces. The mixing intensity is enhanced by turbulence due to the shear forces at the jet and vortex interface. In multiphase RPCs, the flow is dependent on plate movement, superficial gas and liquid velocities, and solid particle type and content. In gas-liquid systems, when the direction of the jet is changed (twice in one cycle), gas bubbles are forced to move with the liquid, resulting in periodic repetition of coalescence and dispersion [21]. Visual examination of a gas-liquid dispersion shows several characteristic dispersion states depending on the reciprocating intensity and superficial gas velocity [22]: segregated (mixer-settler), homogeneous, cellular, and slug bubble dispersion.

The liquid flow through an RPC is usually described by the quasi-steady-state flow model [23]. It supposes the fully developed liquid flow, steady-state changes of the pressure at the column bottom and power consumption equal to the mean values over a long-time interval. This model is confirmed when the reciprocating amplitude exceeds 1 cm [24]. Therefore, for smaller reciprocating amplitudes, an alternative 'acoustic' flow model was developed [25], which assumes most of the external energy dissipation near the plates.

2. 2. The PVCB and power consumption

Several forces influence the PVCB [26]: inertia (because of the reciprocating plate movement and a part of the liquid near the plates), friction (which occurs in all mechanical contacts of plates with the column wall and liquid contacts with moving and stationary parts of the column), gravity, and buoyancy. The energy of mechanical agitation is determined based on the quasi-steady-state flow model [23]. The PVCB and power consumption depend on the amplitude and frequency of reciprocating movement, the system's physical properties, the solid particle type and concentration, the column's geometry, and the hydrodynamic flow conditions [27], as can be seen in Table 1.

The instantaneous PVCB depends on inertial and frictional components of the pressure variation [28]:

$$(p_2 - p_1) - \rho_l g(z_2 - z_1) = \rho_l n_p s_e \frac{1-\varepsilon}{\varepsilon}\left(\frac{\mathrm{d}u_s}{\mathrm{d}t}\right) + n_p \rho_l \frac{1-\varepsilon^2}{2C_0^2\varepsilon^2} u_s |u_s| \quad (1)$$

while the instantaneous power consumption is equal to the product of the cross-sectional column area, instantaneous plate movement speed, and PVCB:

$$P = A_c \left| \Delta p u_s \right| = n_p \rho_l A_c \frac{1\text{-}\varepsilon^2}{2C_0^2 \varepsilon^2} u_s^2 \left| u_s \right| \quad (2)$$

Adopting the assumptions of the quasi-steady-state flow model, the instantaneous PVCB and power consumption in RPCs filled with a 'pure' liquid are [28]:

$$\Delta p = n_p \rho_l \frac{1-\varepsilon^2}{2C_0^{\ 2} \varepsilon^2} u_s \left| u_s \right| \quad (3)$$

$$P = n_p \rho_l A_c \frac{1-\varepsilon^2}{2C_o^{\ 2} \varepsilon^2} u_s^{\ 2} \left| u_s \right| \quad (4)$$

The average and total PVCB (Δp and Δp^*) and power consumption ($\bar{P}$ and P^*) are as follows [28]:

$$\Delta \bar{p} = n_p \rho_l \frac{1-\varepsilon^{\ 2}}{2C_0^2 \varepsilon^2} (2\pi A f)^2 \left(\frac{1}{2} + \frac{4s}{3\pi} + \frac{s^2}{8} \right) \quad (5)$$

$$\Delta p^* = n_p \rho_l \frac{1-\varepsilon^2}{C_0^2 \varepsilon^2} (2\pi A f)^2 \quad (6)$$

$$\bar{P} = \frac{16\pi^2}{3} n_p \rho_l A_c \frac{1-\varepsilon^2}{C_0^2 \varepsilon^2} (Af)^3 \left(\frac{3}{5} s^2 + 1 \right) \quad (7)$$

$$P = A_c \Delta p^* u_{s,m} = 8\pi^3 n_p \rho_l A_c \frac{1-\varepsilon^2}{C_0^2 \varepsilon^2} (Af)^3 \left[\left(\sin 2\pi f t (1 + s \cos 2\pi f t \right) \right]_{max} \quad (8)$$

Rational physical models for gas-liquid and gas-liquid-solid systems in RPCs do not exist. For these systems, the empirical correlations assume proportionality of the PVCB and power consumption on $(Af)^n(1-\varepsilon_g)$ (Table 1), which are based on theoretical equations corrected for the liquid holdup $(1-\varepsilon_g)$, where ε_g is the gas holdup; the exponent n is dependent on the flow regime [22,28].

Rheological properties of the liquid significantly affect the PVCB and power consumption that increase with the increase in the liquid viscosity due to more intense friction between the liquid and the reciprocating plates [11,28-30]. In the case of Newtonian liquids in the turbulent flow (Re >50), the PVCB and power consumption are about proportional to $(Af)^2$and $(Af)^3$, respectively [11,30]. This indicates the applicability of the quasi-steady-state flow model and suggests that frictional losses determine the PVCB. For non-Newtonian liquids, there is a deviation from the model, which is more significant if the solution is more pseudoplastic. In the laminar flow regime, for Re <10, the PVCB and power consumption are approximately proportional to Af and $(Af)^2$, respectively [11].

The PVCB and power consumption for gas-liquid systems are smaller compared to those in 'pure' liquids, regardless of the column diameter and the type of liquid [9,11,22,28-35]. It is ascribed to a lower dispersion density and a weaker interaction between reciprocating plates and gas-liquid systems. A decrease in the superficial gas velocity increases the pressure change in the two-phase system despite the rheological properties of the liquid [11,30]. With increasing the reciprocating intensity, the PVCB increases linearly or reaches a maximum and then decreases in the unstable operation regime [11,22,28]. The critical reciprocating intensity at which the PVCB shows a maximum is dependent on the superficial gas velocity, the reciprocating amplitude, the number of perforated plates [22], and the liquid rheological properties [11]. Up to a critical reciprocating intensity, the average PVCB is proportional to $(Af)^n$, where the value of the exponent is 1.67 to 2.10 [11,30] and 1.2–1.3 [11,29] for Newtonian and viscous non-Newtonian fluids, respectively. A decrease in the exponent indicates a change from turbulent to laminar flow.

Regardless of the solid particle type placed in the interplate spaces (spheres or Raschig rings), the PVCB and power consumption for liquid-solid systems are greater if the solid phase fraction is larger under the same operating conditions and independently of the rheological properties of the liquid [10,11,29,32,33,37]. It results from greater frictional interaction between solid particles, liquid, and plates.

Table 1. Empirical correlations for the PVCB and power consumption in RPCs developed in Serbia

	System	Correlation		Ref.
		PVCB	Power consumption	
'Pure' liquid	Water	-	$\overline{P} = 2.688 \cdot 10^{-4} n_p \rho_l (2\pi Af)^3$	[7]
	Water	-	$\overline{P} = 1.742 \cdot 10^{-3} n_p \rho_l (2\pi Af)^3$	[8]
	Distilled water, sucrose solution, and a model dextran fermentation broth	$\Delta p^* \propto n_p \rho_l (Af)^2$	$P^* = 2.567 \cdot 10^{-3} n_p \rho_l (2\pi Af)^3$	[22]
	Water	$\Delta p^* = 0.113 n_p \rho_l (Af)^2$	$P^* = 0.34 n_p \rho_l (Af)^3$	[28]
		$\Delta \overline{p} = 0.0317 n_p \rho_l (Af)^2$	$\overline{P} = 0.0642 n_p \rho_l (Af)^3$	
	Water	$\Delta p^* = 0.082 n_p \rho_l (Af)^2$	$P^* = 5.49 n_p \rho_l (Af)^3$	[11]
		$\Delta \overline{p} = 0.023 n_p \rho_l (Af)^2$	$\overline{P} = 1.157 n_p \rho_l (Af)^3$	
	Water	$\Delta p^* = 657.2 (Af)^{1.57}$		[20]
		$\Delta \overline{p} = 457.8 (Af)^{1.96}$		
	CMC (1 %) solution	$\Delta p^* = 314.5 (Af)^{1.21}$		
		$\Delta \overline{p} = 115 (Af)^{1.2}$		
	Water	$\Delta p^* = 899 (Af)^{1.617}$		[30]
		$\Delta \overline{p} = 615.6 (Af)^2$		
	Sunflower oil (batch)	$\Delta p^* = 2.081 (Af)^{1.35}$	$P^* = 6.840 (Af)^{2.36}$	[17]
		$\Delta \overline{p} = 0.542 (Af)^{1.32}$	$\overline{P} = 1.345 (Af)^{2.33}$	
	Sunflower oil (continuous)	$\Delta p^* = 1.652 (Af)^{1.31}$	$P^* = 5.432 (Af)^{2.32}$	
		$\Delta \overline{p} = 0.591 (Af)^{1.39}$	$\overline{P} = 1.434 (Af)^{2.39}$	
Gas-liquid	Air-distilled water, sucrose solution, and a model dextran fermentation broth	-	$P^* = 1.804 \cdot 10^{-3} n_p \rho_l (1-\varepsilon_g)(2\pi$	[22]
	Air-water		$P^* = 0.310 n_p \rho_l (1-\varepsilon_g)(Af)^3$	[32]
			$\overline{P} = 0.0664 n_p \rho_l (1-\varepsilon_g)(Af)^3$	
	Air-water	$\Delta p^* = 0.0647 n_p \rho_l (1-\varepsilon_g)(Af)^2$	$P^* = 0.199 n_p \rho_l (1-\varepsilon_g)(Af)^3$	[28]
		$\Delta \overline{p} = 0.0176 n_p \rho_l (1-\varepsilon_g)(Af)^2$	$\overline{P} = 0.0403 n_p \rho_l (1-\varepsilon_g)(Af)^3$	
	Air-water	$\Delta p^* = 0.1087 n_p \rho_l (1-\varepsilon_g)(Af)^2$	$P^* = 4.481 n_p \rho_l (1-\varepsilon_g)(Af)^3$	[11]
		$\Delta \overline{p} = 0.0322 n_p \rho_l (1-\varepsilon_g)(Af)^2$	$\overline{P} = 1.034 n_p \rho_l (1-\varepsilon_g)(Af)^3$	
	Air-water	$\Delta p^* = 711.9 (Af)^{1.67}$		[20]
		$\Delta \overline{p} = 425.4 (Af)^{1.93}$		
	Air-CMC (1 %) solution	$\Delta p^* = 321.5 (Af)^{1.14}$		
		$\Delta \overline{p} = 115.1 (Af)^{1.21}$		
	Air-water	$\Delta p^* = 899 (1-\varepsilon_g)(Af)^{1.617}$		[30]
		$\Delta \overline{p} = 615.6 (1-\varepsilon_g)(Af)^2$		
	Air-CMC (0.5 %) solution	$\Delta p^* = 862.3 (1-\varepsilon_g)(Af)^{1.57}$		
		$\Delta \overline{p} = 473.4 (1-\varepsilon_g)(Af)^{1.85}$		
	Air-CMC (1 %) solution	$\Delta p^* = 740.6 (1-\varepsilon_g)(Af)^{1.46}$		
		$\Delta \overline{p} = 390.9 (1-\varepsilon_g)(Af)^{1.71}$		
Liquid-solid	Water-solid (spheres, 8.4 mm, 5 spheres per each second or third interplate space)	$\Delta p^* = 0.279 n_p \rho_l (Af)^2$	$P^* = 0.88 n_p \rho_l (Af)^3$	[32]
		$\Delta \overline{p} = 0.0322 n_p \rho_l (Af)^2$	$\overline{P} = 0.152 n_p \rho_l (Af)^3$	
	Water-solid (spheres, 8 mm, 0.35-3.2 %)	$\Delta p^* = 699.7 (Af)^{1.56}$		[20]
		$\Delta \overline{p} = 458.4 (Af)^{1.95}$		
	CMC (1 %) solution -solid (0.35-3.2 %)	$\Delta p^* = 248.4 (Af)^{0.93}$		
		$\Delta \overline{p} = 92.3 (Af)^{1.0}$		

	System	Correlation		Ref.
		PVCB	Power consumption	
Liquid-solid	Water-solid (spheres: 8.4 mm, 3.8 %)	$\Delta p^* = 610.7(Af)^{1.31}$		[30]
		$\Delta \bar{p} = 324.6(Af)^{1.58}$		
	Water-solid (6.6 %)	$\Delta p^* = 425.5(Af)^{10.97}$		
		$\Delta \bar{p} = 265.4(Af)^{1.29}$		
	CMC (0.5 %) solution-solid (3.8 %)	$\Delta p^* = 683.7(Af)^{1.34}$		
		$\Delta \bar{p} = 419.6(Af)^{1.64}$		
	CMC (0.5 %) solution-solid (6.6 %)	$\Delta p^* = 416.9(Af)^{0.91}$		
		$\Delta \bar{p} = 187.2(Af)^{1.09}$		
	CMC (1 %) solution-solid (3.8 %)	$\Delta p^* = 1276.4(Af)^{1.54}$		
		$\Delta \bar{p} = 676.1(Af)^{1.78}$		
	CMC (1 %) solution-solid (6.6 %)	$\Delta \bar{p} = 255(Af)^{1.18}$		
		$\Delta p^* = 479(Af)^{1.2}$		
Gas-liquid-solid	Water		$\frac{P^* = 0.31 n_p \rho_l (1-\varepsilon_g)(Af)^3}{\bar{P} = 0.0664 n_p \rho_l (1-\varepsilon_g)(Af)^3}$	[32]
	Air-water-solid (spheres, 8 mm, 0.35-3.2 %)	$\Delta p^* = 413.8(Af)^{1.43}$	-	[20]
		$\Delta \bar{p} = 327.5(Af)^{1.84}$		
	Air-CMC (1 %) solution-solid (0.35-3.2 %)	$\Delta p^* = 173(Af)^{0.86}$		
		$\Delta \bar{p} = 70.1(Af)^{0.93}$		
	Air-water-solid (spheres: 8.4 mm, 3.8 %)	$\Delta p^* = 610.7(1-\varepsilon_g)(Af)^{1.31}$		[30]
		$\Delta \bar{p} = 324.6(1-\varepsilon_g)(Af)^{1.58}$		
	Water-solid (6.6 %)	$\Delta p^* = 425.5(1-\varepsilon_g)(Af)^{10.97}$		
		$\Delta \bar{p} = 265.4(1-\varepsilon_g)(Af)^{1.29}$		
	Air-CMC (0.5 %) solution-solid (3.8 %)	$\Delta p^* = 683.7(1-\varepsilon_g)(Af)^{1.34}$		
		$\Delta \bar{p} = 419.6(1-\varepsilon_g)(Af)^{1.64}$		
	Air-CMC (0.5 %) solution-solid (6.6%)	$\Delta p^* = 416.9(1-\varepsilon_g)(Af)^{0.91}$		
		$\Delta \bar{p} = 187.2(1-\varepsilon_g)(Af)^{1.09}$		
	Air-CMC (1 %) solution-solid (3.8 %)	$\Delta p^* = 1276.4(1-\varepsilon_g)(Af)^{1.54}$		
		$\Delta \bar{p} = 676.1(1-\varepsilon_g)(Af)^{1.78}$		
	Air-CMC (1 %) solution-solid (6.6 %)	$\Delta p^* = 947(1-\varepsilon_g)(Af)^{1.20}$		
		$\Delta \bar{p} = 255(1-\varepsilon_g)(Af)^{1.18}$		
Liquid-liquid	Sunflower oil-methanol (1:6 mol: mol)	$\Delta p^* = 1.158(1-\varepsilon_d)(Af)^{1.28}$	$P^* = 3.829(1-\varepsilon_d)(Af)^{2.29}$	[17]
		$\Delta \bar{p} = 0.428(1-\varepsilon_d)(Af)^{1.37}$	$\bar{P} = 1.393(1-\varepsilon_d)(Af)^{2.48}$	

2. 3. Gas holdup

The gas holdup remains unchanged [39,40] or decreases [22,28,41] with increasing the reciprocating intensity at specific superficial gas and liquid velocities due to the superimposition of gas bubbles and reciprocating plate speed, which leads to bubble coalescence. The 'critical' $(Af)_{cr}$ at which the gas holdup reaches its minimum value depends little on the superficial gas velocity [22]. After reaching the minimum value, the gas holdup in the gas-liquid system increases almost linearly with a further enhancement in reciprocating intensity due to the bubble comminution [22]. By adding solid particles (spheres or Raschig rings), the gas holdup in the 2.54 and 9.2 cm i.d. RPCs increases with an increase in reciprocating intensity and superficial gas velocity because bubble comminution intensifies by shear forces [11,36,42-46]. However, in a 16.6 cm i.d. RPC, a higher gas holdup is observed at a High superficial gas velocity

and a smaller solid particle fraction resulting from the change in the liquid flow regime through the plate openings because of the reduced free cross-sectional plate area [15].

Usually, empirical equations for the gas holdup in RPCs involve maximum or average power consumption and superficial gas velocity (Table 2):

$$\varepsilon_g = k(P_g)^a u_g^b \quad (9)$$

The power consumption P_g has a lower influence on gas holdup than the gas flow energy because mechanical energy dissipation occurs only near the plates ($a < b$).

Table 2. Empirical equations for the dispersed phase holdup in RPCs developed in Serbia.

Column type[a]	System	Special conditions	Correlation	Ref.
RPC1	Air-water, Air-sucrose solution	Segregated dispersion	$\frac{u_r}{1-\varepsilon_g} = 0.436 u_g^{0.22} \exp(-0.122 \bar{P} \varepsilon_g u_g^{0.88})$	[56]
		Homogeneous dispersion	$\varepsilon_g = 1.38 P^{*0,25} u_g^{0.6}$	
RPC2	Air-water-spheres	$Af > 0.03$ ms^{-1}	$\varepsilon_g = 2.515 P^{*0.29} u_g^{0.83}$	[33]
RPC2	Air-water, Air-sucrose solution	Segregated dispersion	$\varepsilon_g = 7.4 P^{*(-0.05)} u_g$	[28]
		Homogeneous dispersion	$\varepsilon_g = 6.2 P^{*0.2} u_g$	
			$\varepsilon_g = 44.55 (Af)^{0.6} u_g$	
RPC2, RPC3	Air-water	$Af > 0.03$ ms^{-1}	$\varepsilon_g = 1.38 P^{*0.27} u_g^{0.73}$	[11]
RPC3	Air-CMC solution (0.5 and 1 %)-spheres (8 mm)	Polymerization degree: 200	$\varepsilon_g = 0.043 \bar{P}^{0.39} u_g^{0.53}$	[36]
		Polymerization degree: 1000	$\varepsilon_g = 0.043 \bar{P}^{0.31} u_g^{0.44}$	
RPC3	Air-water-Raschig rings (8 mm)	$Af > 0,03$ ms^{-1}	$\varepsilon_g = 1.145 \bar{P}^{0.428} u_g^{0.662}$ $\varepsilon_g = 0.393 P^{*0.495} u_g^{0.628}$ $\varepsilon_g = 1.06 P_t^{0.456} u_g^{0.663}$	[42]
RPC2, RPC3	Air-water		$\varepsilon_g = 1.369 u_g^{0.962} D_c^{-0.483} + 172.26 u_g^{0.33} D_c^{0.453} (Af)^{2.21}$	[57]
	Air-water-Raschig rings (8 mm)		$\varepsilon_g = 1.369 u_g^{0.962} D_c^{-0.483} + 66.942 u_g^{0.294} D_c^{0.268} (Af)^{1.693} \varepsilon_s^{0.238}$	
RPC3	Air-CMC solution (0.5, 1, and 2 %)-spheres	$Af > 0.04$ ms^{-1}, polymerization degree: 50	$\varepsilon_g = 0.053 \bar{P}^{0.39} u_g^{0.605}$	[51]
		$Af > 0.04$ ms^{-1}, polymerization degree: 200	$\varepsilon_g = 0.041 P^{0.4} u_g^{0.54}$	
RPC3	Air-water, air-water-Raschig rings (12 mm)	$\varepsilon = 0.454$	$\varepsilon_g = 1.991 \bar{P}^{0.404} u_g^{0.787}$	[16]
	Air-CMC solution (1 %)	$\varepsilon = 0.319$	$\varepsilon_g = 0.335 \bar{P}^{0.291} u_g^{0.527}$	
	Air-CMC solution (1 %), air-CMC solution (1 %) - Raschig rings (12 mm)	$\varepsilon = 0.319$	$\varepsilon_g = 0.441 \bar{P}^{0.259} u_g^{0.567}$	
RPC2	Methanol-sunflower oil	$Af < 0,05$ ms^{-1}	$\varepsilon_d = 4.67 \cdot 10^{-5} (Af)^{0.67} u_d^{-1.22}$	[17]
		$Af > 0,05$ ms^{-1}	$\varepsilon_d = 4.87 \cdot 10^{-6} (Af)^{0.67} u_d^{-1.24}$	

[a]RPC1: D_c= 0.025 m, l_c = 1.875 m; RPC2: D_c= 0.025 m, l_c= 2 m, RPC3: D_c= 0.092 m, l_c= 1.05 m

The effect of the superficial gas velocity on the gas holdup is very pronounced, regardless of the type of system and column geometry. At $u_g < 3$ cm s^{-1}, the gas holdup increases proportionally with the increased superficial gas velocity due to increased resistance to the gas flow through the plate openings [2,11,22,28,33,39-43,47-53]. At higher superficial gas velocities, gas slugs appear in the RPC, and the gas holdup reaches its maximal value and does not change when the superficial gas velocity further increases [28,45].

There are conflicting opinions about the effect of superficial liquid velocity on the gas holdup in two-phase systems. Some researchers believe that superficial liquid velocity does not affect the gas holdup [40,41,54,55], while others believe that it increases with the increase in the superficial liquid velocity [2,22,39] if $u_l > 1.2$ cm s^{-1} [3]. In three-phase systems, the superficial liquid velocity does not significantly affect the gas holdup [43,45].

By increasing the plate opening, the gas holdup decreases in the segregated regime, while the effect is insignificant in the homogeneous regime. Increasing the number of plates increases the gas holdup due to a reduced mean bubble diameter and increased resistance to bubble movement [2,22,39,41]. Independently of the liquid rheological properties and the presence of a solid phase, the gas holdup increases with decreasing the fractional free plate surface due to favoring gas dispersion and making gas and liquid flow through the plate openings difficult [16].

Solid particles have multiple effects on gas-liquid dispersion. The solid particles, forced to move due to the reciprocating plate movement, affect the equalization of the field of turbulent forces in the interplate spaces, prevent coalescence and favor the bubble reduction. By their movement, solid particles reduce the intensity of backmixing and stabilize the column operation [43]. Consequently, the gas holdup is larger in three-phase RPCs than in two-phase RPCs under the same working conditions. This difference is greater at higher reciprocating intensities. Raschig rings disperse gas more efficiently than spheres of approximately the same diameter in RPCs of the same geometry [49].

Physical properties of the liquid affect the gas holdup. It was reported to be higher in *n*-butanol, glycerol, and sodium sulfite solutions than in water [11]. The highest gas holdup is achieved in the *n*-butanol solution due to the prevented coalescence of bubbles. In non-Newtonian solutions of CMC, gas holdup is dependent on the solution concentration and the molar mass of CMC [36].

Among two-phase column contactors, a much higher gas holdup is achieved in a Prochazka RPC [2]. The gas holdup is 50-60 % higher than that in pulsed bubble columns and about 25 % higher than that in vibrating disc columns under similar working conditions. Gas holdup in RPCs is higher than those in stirred vessels, bubble columns, and air-lift rectors, especially at lower superficial gas velocities [11]. At the same specific power consumption and superficial gas velocity, gas holdup was reported to be approximately the same in three RPCs with similar geometric characteristics [52].

2. 4. Bubble size

The state of dispersion depends on the relationship between gas bubble formation, dispersion, and coalescence processes [55]. Bubble formation depends on instabilities in the gas flow through plate openings. Bubble dispersion results from external power dissipation and is dependent on the ratio of surface tension forces, stabilizing the bubbles, and local shear forces, which break up the bubbles. If the dynamic forces do not take action evenly over the entire bubble surface, the bubble first deforms and then disintegrates. The maximum size of a stable bubble, which can be maintained in an existing turbulent field, according to the Kolmogoroff's model of isotropic turbulence, depends on the liquid surface tension, σ, and density, ρ, as well as on the specific dissipated energy P/V_l [27]:

$$d_{3,2} = k\frac{\sigma^{0.6}}{\rho^{0.2}\left(\frac{P}{V_l}\right)^{0.4}} \tag{10}$$

The measured Sauter-mean bubble diameter $d_{3,2}$ agrees with that estimated by Eq. (10) for water and glycerol solutions. In contrast, the agreement is relatively poor for *n*-butanol and sodium sulfite solutions. This correlation was also proved for a methanol-to-oil emulsion where the Sauter-mean drop diameter was proportional to the specific power consumption (average power consumption P divided by the emulsion mass) on the power of -0.4, *i.e.* $d_{3,2} \propto (\overline{P}/m_e)^{-0.4}$ [17].

With increasing the reciprocating intensity, as a consequence of the contribution of external energy input to the comminution, the mean bubble diameter decreases in RPCs [2,3,11,40,55,58]. When the total power consumption is lower than a critical value, the Sauter-mean bubble diameter is not dependent on the agitation intensity. However, it decreases when the power consumption exceeds the critical value [58]. The decrease in bubble size with increasing reciprocating intensity is more pronounced in the presence of coalescence inhibitors [9].

The superficial gas velocity affects the bubble size due to a facilitated coalescence [2,11,40,58], but this effect is significant only at low superficial gas velocity [2]. Bubble size is not affected by the superficial liquid velocity [2,39,41] or it decreases with increasing the superficial liquid velocity [58] because of turbulent forces created in plate openings [40]. Compared to that in water, bubble size is smaller in liquids that favor bubble reduction by viscous forces (*e.g.* aqueous glycerol solution) or prevent bubble coalescence (*e.g.* aqueous *n*-butanol and sodium sulfite solutions).

The plate geometry significantly affects the Sauter-mean bubble diameter in RPCs. In the segregated regime, it is controlled by the plate opening diameter, and in the homogeneous regime, by the bubble dispersion process. The Sauter-mean bubble diameter is reduced by increasing the plate opening and decreasing the fractional free plate surface area [55]. In three-phase systems, it increases with increasing the solid phase fraction [45]. Also, it is reduced with the increase in the reciprocating intensity and the decrease in the superficial gas velocity.

2. 5. Axial mixing

In real column-type multiphase contactors, fluids do not flow in an ideal plug flow due to channeling, recirculating, or creation of stagnant zones. Most often, the non-ideality of the flow is expressed by axial or radial mixing coefficients. Axial mixing does not exist in the ideal plug flow, and the axial mixing (dispersion) coefficient D_l equals zero. In contrast, the axial dispersion coefficient is maximal for the flow with ideal mixing. In smaller-diameter columns, radial mixing is usually neglected. However, when designing column-type reactors with the countercurrent flow of the phases, axial dispersion is desirable to maintain the maximal concentration difference (driving force) in the axial direction.

The dispersion (diffusion) model is most frequently used for describing the flow through multiphase RPCs. Depending on the turbulence intensity in the column, this model, as limit values, defines the cases of the ideal plug flow and the flow with ideal mixing. In RPCs, large mass transfer rates and relatively low axial dispersion can be achieved. In the literature, there is a large amount of data on axial dispersion for 'pure' liquids, resulting from researching this contactor as an extraction column [27]. However, the findings of different researchers are often contradictory, which is difficult to explain. For example, the axial dispersion coefficient was reported to increase [59,60] or decrease [61,62] with increasing the interplate space. Similarly, it was reported to increase [60] or decrease [63] with the increase in the plate opening size. However, it was found not to depend [59,64] or to depend weakly [65] on the column diameter.

Conversely, the axial dispersion coefficient increases approximately linearly with the reciprocating intensity [50,60-62]; the increase in amplitude seems to increase axial dispersion [50]. In gas-liquid systems, the axial dispersion coefficient increases with the superficial gas velocity, especially at higher superficial gas and liquid velocities, as well as with the increase in the superficial liquid velocity due to favored backmixing resulting from increased resistance to the flow through the plate openings and the liquid jets intensifying mixing in interplate spaces [66]. In addition, turbulent fluid flow in interplate spaces and circulation due to gas bubbles increase axial mixing compared to a 'pure' liquid [67]. Finally, in three-phase systems, solid particles influence the axial dispersion coefficient more significantly than the superficial gas velocity, especially at low reciprocating intensities [57]. However, axial dispersion coefficient is decreased with an increase in reciprocating intensity independently of the superficial gas velocity [57].

Empirical correlations for determining the axial dispersion coefficient are given in Table 3.

Table 3. Empirical correlations for axial dispersion coefficient in RPCs (D_c = 2.54 cm) developed in Serbia

System	Operating conditions	Correlation	Ref.
Water ↓	A = 0–1.4 cm f = 0–10 Hz u_l = 0.1–1.1 ms^{-1}	$\ln D_l = \ln\left(D_L\right)_{l=0} + \left(Af\right)^{0.56} \exp\left(-1.44u_c + 0.912\right)$ $\left(D_l\right)_{l=0} = 5.15 \cdot u_l^{0.471}$	[70]
Air-water ↓↑	A = 0.65–1.5 cm f = 0.5–6.18 Hz u_l = 0.38–1.2 ms^{-1} u_g = 0.8–3.2 ms^{-1}	$D_l = 90.5u_R^{-0.964}$; $D_l = 81.47 \cdot u_l^{0.627} u_R^{-075+0.19u_l}$ with $u_R = \frac{u_g}{\varepsilon_g} + \frac{u_l}{1-\varepsilon_g} + 2Af$	[3]
Water ↓	A= 1 and 2.35 cm f = 2–4.5 Hz u_l = 0.24–0.87 ms^{-1} u_g = 0–1.48 ms^{-1}	$D_l = 0.49\left(Af\right)^{1.11} u_l^{0.31}$	[66]
Air-water ↓↑		$D_l = 3.37\left(Af\right)^{0.17} u_l^{0.38} u_g^{0.07}$	
Water ↓ - spheres (8.3 mm)		$D_l = 1.26\left(Af\right)^{1.42} u_l^{0.51} \varepsilon_S^{0.23}$	
Air-water ↓↑ - spheres (8.3 mm)		$D_l = 1.39\left(Af\right)^{0.47} u_l^{0.42} u_g^{0.03} \varepsilon_S^{-0.26}$	

Application of these correlations is limited to the liquid (continuous) phase and specific columns used in the axial dispersion studies [62]. Discrepancies between correlations result from different geometries of RPCs and operating condition ranges. Axial dispersion in RPCs is less intensive than in bubble columns [68] but more intensive than in packed columns [69].

3. MASS TRANSFER IN RPCS

Efficiency of multiphase RPCs is dependent on the interfacial mass transfer rate of the reactant per unit dispersion volume, i.e., on the volumetric mass transfer coefficient in the liquid phase ($k_l a$), which is a product of the liquid mass transfer coefficient (k_l) and the specific interfacial area (a). The liquid mass transfer coefficient and specific interfacial area in RPCs depend on the reciprocating intensity (Af), *i.e.* power consumption, superficial gas and liquid velocities, properties of the phases, column geometry, and bubble size. Many researchers investigated the influence of reciprocating intensity and superficial gas and liquid velocities on the volumetric mass transfer coefficient, liquid mass transfer coefficient, and specific interfacial area in RPCs. Table 4 overviews correlations for the mass transfer characteristics of RPCs developed by Serbian researchers.

Table 4. Correlations for the liquid mass transfer coefficient, specific interfacial area, and volumetric mass transfer coefficient in RPCs developed in Serbia

Phase flow	D_c / cm	n_p	d_o / mm	ε	ε_s / %	Special condition	k_l / m s^{-1}; a / m^2 m^{-3} $k_l a$ / s^{-1}	Ref.
Batch	2.54	65, 33	8, 7	0.51, 0.41	0	$P_g^* > P_{g,cr}^*$ [a]	$k_l = 2.94 \cdot 10^{-4} P_g^{*0.25}$ $a = 1783 P_g^{*0,3} u_g^{0,6}$	[9,56]
						$P_g^* < P_{g,cr}^*$	$k_l = 2.62 \cdot 10^{-4} P_g^{*-0.05}$	
							$k_l = 0.0564 d_{3,2}$ $a = 1583 u_g^{0,6}$	
							$k_l a = 0.467 P_g^{*0.25} u_g^{0.6}$	
Batch	2.54	65, 15	8	0.51, 0.454	0 to 6.6	u_g< 1.5 cm s^{-1}	$k_l = 20.24 d_{3,2}^{1.743}$ $a = 18883 \overline{P}^{0,31} u_g^{0,97}$ $k_l a = 0.719 \overline{P}^{0.74} u_g^{0.63}$	[11,71,72]
Batch	16.6	15	8	0.466	3.8	u_g< 1.5 cm s^{-1}	$k_l a = 2.33 \left(\frac{\overline{P}}{V_l}\right)^{0.803} u_g^{0.572}$	[15,84]
					6.6		$k_l a = 0.6 \left(\frac{\overline{P}}{V_l}\right)^{0.572} u_g^{0.316}$	
Batch	9.2	33	8	0.454	0.35 to 3.2	u_g< 1.5 cm s^{-1}	$k_l a = 0.995 \left(\frac{\overline{P}}{V_l}\right)^{0.776} u_g^{0.854}$	[16]
Counter-current	2.54	63	8	0.51	0	Methanol-sunflower oil	$a = 3.3 (Af)^{0.74} u_d^{-1.2}$	[43]

[a] $P_{g,cr}^* = 4.2(1-\varepsilon_{g,cr}) u_g^{0.25}$

The correlations developed by others can be found elsewhere [27]. As with other contact devices with mechanical agitation, these mass transfer characteristics in RPCs can be correlated with the power consumption (total, average, or specific), *i.e.* reciprocating intensity, superficial gas and liquid velocities, and geometric characteristics of the column. Aeration more significantly affects the specific interfacial area than agitation. At the same superficial gas velocity, the specific interfacial area and volumetric mass transfer coefficient in gas-liquid systems are greater in RPCs than in stirred vessels, bubble columns, and air-lift reactors due to larger gas holdup and smaller bubble size resulting from a more intensified bubble dispersion [71,72].

If $P_g^* < P_{g,cr}^*$, where $P_{g,cr}^*$ is the critical value of the maximum power consumption, P_g^*, in the gassed RPC, then $k_l \propto (P_g^*)^{0.25}$ [58]. However, when $P_g^* > P_{g,cr}^*$, then $k_l > (P_g^*)^{0.05}$ and $k_l \propto d_{3,2}$, where $d_{3,2}$ is the Sauter-mean bubble diame-

ter [58]. Similar dependencies were found for other RPCs [73], vibrating disc columns [74], and stirred vessels [75]. The dependence of the liquid mass transfer coefficient on the Sauter-mean bubble diameter has been confirmed for vibrating disc columns [74], pulsating columns [76], stirred vessels [77], and bubble columns [78]. Change of the specific interfacial area with reciprocating intensity is dependent on the flow regime in column [58]. At $Af < 2$ cm s^{-1} [40], the specific interfacial area either increases due to the decrease in bubble size [79] or remains unchanged because the gas holdup and bubble size do not change [3,40,58]. The specific interfacial area increases at higher reciprocating intensities, while the liquid mass transfer coefficient decreases with increasing reciprocating intensity because of increased gas holdup and decreased bubble size [11,58]. The volumetric mass transfer coefficient increases with increased reciprocating intensity because of greater power consumption and intensified gas bubble size reduction [3,52,67,71,73,79-81]. This increase is insignificant at lower and significant at higher reciprocating intensities, $Af > 5$ cm s^{-1} [3,79].

The liquid mass transfer coefficient decreases with increased superficial gas and liquid velocities [73,79]. Increasing the superficial gas velocity increases the gas holdup, whereas increasing the superficial liquid velocity decreases the bubble size. Both decrease the liquid mass transfer coefficient and the relative velocity between the liquid and gas phases [79]. The effect of the superficial gas velocity on the specific interfacial surface is particularly significant at low reciprocating intensities when increasing reciprocating intensity helps the bubbles to comminute, thus increasing the interfacial area [11,22]. At larger superficial gas velocities, bubbles increase in size and pack densely, which favors their coalescence [3], but the specific interfacial area may increase due to the increased gas holdup [2,40,58,79]. According to some researchers [58], the superficial liquid velocity negligibly affects the specific interfacial area due to a weak influence on bubble size and gas holdup, while others [1,2,40,79] reported the increased specific interfacial area with increasing the superficial liquid velocity because of a decrease in bubble size. As the superficial gas velocity increases, the volumetric mass transfer coefficient increases to a maximum due to the higher energy that the gas is transferring to the liquid. Then, a larger gas holdup is observed in the RPC, and reduction in the bubble size is enhanced when the gas passes through the plate openings. Some researchers reported constants volumetric mass transfer coefficient with increasing the superficial liquid velocity [79] or ignored this influence [9,81], while the other group found an increase in this coefficient with increasing the superficial liquid velocity [69,73].

The RPC geometry influences the liquid mass transfer coefficient, specific interfacial area, and volumetric mass transfer coefficient. Increasing the opening diameter and the fractional free plate surface reduces the gas holdup, specific interfacial area, liquid mass transfer coefficient, and volumetric mass transfer coefficient. These changes were experimentally observed, although the bubble size decreases insignificantly with increasing the opening diameter [7,80]. In addition, the specific interfacial area and volumetric mass transfer coefficient are higher in cocurrent than in countercurrent flow due to a higher gas holdup [79].

The liquid mass transfer coefficient decreases, and the specific interfacial area increases by adding Raschig rings (2.5 vol.%) to each interplate space [76], while spheres do not affect the specific interfacial area [11]. In a 9.2 cm i.d. RPC, the specific interfacial area is greater with a greater solid phase fraction than in the two-phase (gas-liquid) system [11]. Increasing the reciprocating intensity and superficial gas velocity in a three-phase system increases the volumetric mass transfer coefficient because a higher power consumption favors the bubble size reduction [11,15]. The volumetric mass transfer coefficient is higher in a three-phase system than in a two-phase system due to a more efficient mixing and the influence of the solid phase. However, increasing the solid phase fraction does not significantly affect the volumetric mass transfer coefficient.

Dependence of the volumetric mass transfer coefficient on the liquid properties is complex since they influence the liquid mass transfer coefficient and the specific interfacial area. For example, adding a non-electrolyte (alcohol) at a small concentration increases the volumetric mass transfer coefficient [83]. Conversely, for the liquids with close surface tensions and densities, the volumetric mass transfer coefficient decreases with increased viscosity [9].

4. APPLICATION OF RPCS IN SERBIA

RPCs were investigated regarding potential applications as reactors for various aerobic bioprocesses and biodiesel production. RPCs are applied worldwide in the chemical and pharmaceutical industries, hydrometallurgy, biotech-

nology, and wastewater treatment (Table S-3). For example, they are used for aerobic wastewater treatment [85], biosynthesis of pullulan [86,87], dextran [88], antibiotics [89], lemon acid [21], ethanol [13,21], and enzymes [9,88], as well as in biodiesel production [17,19,20]. Due to their favorable hydrodynamic properties and efficient oxygen mass transfer, RPCs are classified as new-generation bioreactors [90].

RPCs have been used in Serbia to study biosyntheses of dextransucrase, dextran [9, 88], and ethanol [13] as well as biodiesel production [17-20,91] at laboratory and pilot levels.

An RPC (2.54 cm i.d.) was used as a bioreactor for alcoholic fermentation of a glucose medium (40 g dm^{-3}) using a commercial yeast *Saccharomyces cerevisiae* immobilized on macroporous polymer particles (ε_s = 0.236) at 30 °C and a liquid flow rate of about 1.2 dm^3 day^{-1} [13]. The dispersion model was verified by comparing predicted and measured glucose concentrations at the exit of the bioreactor. With the zero-order reaction rate law, axial dispersion did not affect the glucose conversion degree. However, with the Monod kinetics, axial dispersion positively influenced the glucose conversion degree and ethanol yield. Furthermore, biosynthesis of dextransucrase by a *Leuconostoc mesenteroides* Zdravlje S-P strain was investigated at a laboratory level in an RPC (2.5 cm i.d.), a bubble column and a stirred vessel, at 25 °C [9,88]. The maximum power consumption was calculated from the maximum PVCB (Table 1) [22], while the volumetric oxygen mass transfer was determined by a dynamic method during aerobic microbial growth (Table 4) [56]. Among the tested bioreactors, the RPC had the highest aeration capacity for the same total specific power consumption and at a much lower superficial gas velocity [88]. Still, it was higher than the optimal one needed for the maximum enzyme biosynthesis. Therefore, the aerated, stirred tank bioreactor was selected for microbial dextransucrase production [9,88].

Continuous KOH-catalyzed biodiesel production from various oily feedstocks (sunflower oil, rapeseed oil, and waste pig-roasting lard) and methanol was performed in RPCs of different diameters [17-20,91]. Hydrodynamics of a cocurrent two-phase upflow in an RPC (2.5 cm i.d.) was investigated for the KOH-catalyzed methanolysis of sunflower oil [17]. Plug flow of the continuous phase (sunflower oil) through the column was confirmed for the flow at the 1 mm reciprocating amplitude. Also, the flow regime through the column and plate openings was laminar and laminar to transitional. The PVCB and power consumption depended on the reciprocating intensity, while the Sauter-mean drop diameter was dependent on the specific power consumption. The dispersed phase (methanol) holdup and the specific interfacial area were correlated with the reciprocating intensity and the superficial dispersed phase velocity (Tables 2 and 4, respectively). Therefore, the hydrodynamic study showed that RPCs offer benefits of plug flow, effective two-phase mixing, and fast reaction of two immiscible reactants, such as sunflower oil and methanol, at room temperature along with the simple scale-up method accepted for Karr type RPCs [17]. Next, the effects of tetrahydrofuran (THF) as a cosolvent on hydrodynamics and kinetics were studied [19]. The THF addition positively affected the drop size of the dispersed phase and the triacylglycerol (TAG) conversion degree. The plug flow through the RPC and simple kinetic models were verified. The mass transfer limitation was observed in the initial part of the reactor (only for THF contents of $\leq$10 %), whereas the chemical reaction-controlled regime was in the upper reactor part, which included a fast irreversible second-order reaction and/or reversible second-order reaction (only at the THF content of 30 %). The TGA content of around 80 % at the reactor exit indicated that the overall biodiesel production process should be conducted in a series of two RPCs with the separation of glycerol after each reactor. This process configuration was patented nationally in 2014 [91]. A 98–100 % TAG conversion was achieved at the exit of the second reactor. However, a TAG purity of 96.2 % was obtained in the same RPC using KOH (1 % of the oil loading), waste pig-roasting lard, and methanol (1:4.5 mol mol^{-1}) at 60 °C, a retention time of 10 min, and a capacity of 120 kg day^{-1} [20]. In this case, the first-order model for both the reaction and the mass transfer and the model of the changing reaction mechanism and TAG mass transfer were proved. Continuous KOH-catalyzed methanolysis of rapeseed oil at 30 °C was performed in a cocurrent upflow RPC of 2.5 cm or 16.6 cm diameter and a gravitational separator providing the TAG conversion degrees at the exit of the plant of 98 % [92,93]. Residence times of the reaction mixture in the reactors and separators were 13 min and about 3 h, respectively.

5. CONCLUSION

Reciprocating plate columns (RPCs) have been investigated and applied in Serbia from 1970 to 2020 at the laboratory level as contactors and reactors. Hydrodynamic and mass-transfer characteristics of RPCs are reviewed, such as the

PVCB, power consumption, dispersed-phase holdup, axial dispersion, volumetric oxygen mass transfer coefficient, liquid mass transfer coefficient, and specific interfacial area. Serbian researchers have used RPCs as multiphase contactors for liquid-liquid extraction and gas absorption, bioreactors in alcoholic fermentation, polysaccharide and enzyme biosyntheses, and reactors for biodiesel production.

Nomenclature

a / m^{2}m^{-3}	specific interfacial area
A / m	amplitude of reciprocating motion
A_c / m^2	cross-sectional column area
Af / m s^{-1}	reciprocating intensity
C_0	orifice coefficient
D_l / m^2 s^{-1}	axial dispersion coefficient
D_c / m	column diameter
d_o / m	plate opening diameter
$d_{3,2}$ / m	Sauter-mean bubble diameter
f / Hz	frequency of reciprocating motion
g / m s^{-2}	gravitational acceleration
k_l / m s^{-1}	liquid mass transfer coefficient
k_la / s^{-1}	volumetric mass transfer coefficient
L / m	length of the tie-rod
l_c / m	column length
m_e / kg	emulsion mass
n_p	number of plates
p / Pa	instantaneous pressure
p_1, p_2 / Pa	pressures at the top and bottom of the column, respectively
$\Delta\overline{p}$, ΔP / Pa	average and maximum pressure variation at the column bottom, respectively
P / W	instantaneous power consumption
$\overline{P}$, P^* / W	average and maximum power consumption, respectively
P_g^* / W	maximum gassed power consumption
$P_{g.cr}^*$ / W	critical maximum gassed power consumption
s	the ratio of the radius (equal to the amplitude of reciprocating motion *A)* of the disk to the length of the tie-rod, (A / L)
s_e / m	equivalent plate length
t / s	time
u_c / m s^{-1}	superficial continuous phase velocity
u_d / m s^{-1}	superficial dispersed phase velocity
u_g / m s^{-1}	superficial gas velocity
u_l / m s^{-1}	superficial liquid velocity
u_s / m s^{-1}	velocity of the plate stack, = $A\,\omega \sin[\omega t\,(1 + s\cos\omega t)]$
$u_{s,m}$ / m s^{-1}	maximum plate stack velocity
u_R / m s^{-1}	slip velocity
V_l / m^3	liquid volume
z_1 and z_2 / m	top and bottom of the column, respectively

Greek symbols

ε	fractional free plate area
ε_d	dispersed phase holdup
ε_g	gas holdup
ε_s	solid phase content
ρ_L / kg m^{-3}	liquid density
σ / N m^{-1}	liquid surface tension
ω / s^{-1}	angular frequency ($2\pi f$)

Abbreviations

i.d.	internal diameter

SUPPLEMENTARY MATERIAL

Additional data are available electronically at https://www.ache-pub.org.rs/index.php/HemInd/article/view/1110, or from the corresponding author on request.

Acknowledgements: *This work was supported by the Serbian Academy of Sciences and Arts (SASA, Project F-78), the SASA Branch in Niš (Project 0-14-18), and the Republic of Serbia – Ministry of Science, Technological Development, and Innovation of Serbia, Programs for Financing Scientific Research Work (Project No. 451-03-47/2023-01/200133 assigned to the Faculty of Technology, Leskovac, University of Niš, Research group III 45001).*

REFERENCES

[1] Al Taweel AM, Landau J, Boyle J, Gomaa HG. Operational characteristics of a novel reciprocating plate multiphase contactor. *Trans Inst Chem Eng*. 1995; 73: 707–712.
[2] Gomaa HG, Landau J, Al Taweel AM. Gas-liquid contacting in reciprocating plate columns: I. Hydrodynamics. *Can J Chem Eng*. 1991; 69: 228–239. https://doi.org/10.1002/cjce.5450690127
[3] Skala D. Analiza sistema gas-tečnost u koloni sa vibracionom mešalicom. Doktorska disertacija, Univerzitet u Beogradu, Tehnološko-metalurški fakultet, Beograd; 1980 (in Serbian).
[4] Lo TC, Prochazka J. *Reciprocating plate extraction columns*. In: Lo TC, Baird MHI, Hanson C. eds. *Handbook of solvent extraction.* New York, NY: John Wiley & Sons; 1983: 373–389. ISBN 0-471-04164-5.
[5] Van Dijck WJD. Process and apparatus for intimately contacting fluids. US Patent 2,011,186; 1935. https://patentimages.storage.googleapis.com/6d/ac/4c/65e173f0fd9eba/US2011186.pdf
[6] Karr AE. Performance of reciprocating plate extraction columns. *AIChE J*. 1959; 5: 446–452. https://doi.org/10.1002/aic.690050410
[7] Pavasović V. Ispitivanje hidrodinamike u vibracionom ekstraktoru. Doktorska disertacija, Univerzitet u Beogradu, Tehnološko-metalurški fakultet, Beograd; 1975 (in Serbian).
[8] Kažić N. Proučavanje promene pritiska u cilju definisanja hidromehaničkih sila u vibracionom ekstraktoru. Magistarska teza, Univerzitet u Beogradu, Mašinski fakultet, Beograd; 1979 (in Serbian).
[9] Veljković V. Ispitivanje hidrodinamičkih i maseno-prenosnih karakteristika različitih reaktora i izbor optimalnog tipa za biosintezu dekstran-saharaze. Doktorska disertacija, Univerzitet u Beogradu, Tehnološko-metalurški fakultet, Beograd; 1985 (in Serbian).
[10] Banković-Ilić I. Ispitivanje snage mešanja i sadržaja gasa u trofaznoj koloni sa vibracionom mešalicom. Magistarska teza, Univerzitet u Beogradu, Tehnološko-metalurški fakultet; Beograd; 1993 (in Serbian).
[11] Banković-Ilić I. Hidrodinamika i prenos mase u sistemima gas-tečnost-čvrsto u koloni sa vibracionom mešalicom. Doktorska disertacija, Univerzitet u Nišu, Tehnološki fakultet, Leskovac; 1999 (in Serbian).
[12] Naseva O. Uticaj reoloških osobina tečne faze na snagu mešanja u bioreaktoru sa vibracionom mešalicom, Magistarska teza, Univerzitet u Nišu, Tehnološki fakultet, Leskovac; 2002 (in Serbian).
[13] Nikolić Lj. Povratno mešanje tečne faze i kinetika procesa alkoholne fermentacije u trofaznom bioreaktoru sa vibracionom mešalicom. Doktorska disertacija, Univerzitet u Nišu, Tehnološki fakultet, Leskovac; 2003. http://doiserbia.nb.rs/phd/fulltext/NI20031003NIKOLIC.pdf (in Serbian)
[14] Stamenković I. Uticaj reoloških osobina tečne faze na sadržaj gasa i promenu pritiska na dnu reaktora sa vibracionom mešalicom. Magistarska teza, Univerzitet u Nišu, Tehnološki fakultet, Leskovac; 2005 (in Serbian).
[15] Vasić Lj. Brzina prenosa mase kiseonika kao kriterijum za povećanje razmere kolone sa vibracionom mešalicom. Magistarska teza, Univerzitet u Nišu, Tehnološki fakultet, Leskovac; 2006 (in Serbian).
[16] Aleksić M. Hidrodinamičke i maseno-prenosne karakteristike višefaznog reaktora sa vibracionom mešalicom. Doktorska disertacija, Univerzitet u Nišu, Tehnološki fakultet, Leskovac; 2006 (in Serbian).
[17] Stamenković IS, Banković-Ilić IB, Jovanić PB, Veljković VB, Skala D. Hydrodynamics of a cocurrent upflowliquid-liquid reciprocating plate reactor for homogeneously base-catalyzed methanolysis of vegetable oils. *Fuel.* 2010; 89: 3971–3984. http://www.doi:10.1016/j.fuel.2010.06.026
[18] Stamenković I. Kontinualna homogena bazno katalizovana alkoholiza biljnih ulja u reaktoru sa vibracionom mešalicom. Doktorska disertacija, Univerzitet u Nišu, Tehnološki fakultet, Leskovac; 2014 (in Serbian).
[19] Banković-Ilić IB, Todorović ZB, Avramović JM, Veličković AV, Veljković VB. The effect of tetrahydrofuran on the base-catalyzed sunflower oil methanolysis in a continuous reciprocating plate reactor. *Fuel Process Technol*. 2015; 137: 339–350. http://dx.doi.org/10.1016/j.fuproc.2015.03.023
[20] Miladinović MR, Stojković IS, Veličković AV, Stamenković OS, Banković-Ilić IB, Veljković VB. Optimization and kinetic modeling of waste lard methanolysis in a continuous reciprocating plate reactor. *Chin J Chem Eng*. 2019; 27: 2481–2490. https://doi.org/10.1016/j.cjche.2019.02.019

[21] Brauer H. Growth of fungi and bacteria in the reciprocating jet bioreactor. *Bioprocess Eng*. 1990; 6: 1–15. https://doi.org/10.1007/BF00369272
[22] Veljković V, Skala D. Hydrodynamic investigation of gas-liquid contacting in a reciprocating plate column. *Can J Chem Eng*. 1986; 64: 906-914. https://doi.org/10.1002/cjce.5450640604
[23] Jealous AC, Johnson HF. Power requirements for pulse generation in pulse column. *Ind Eng Chem*. 1955; 47: 1159–1166 https://doi.org/10.1021/ie50546a021
[24] Baird MHI, Rama Rao NV, Stonestreet P. Power dissipation and holdup in a gassed reciprocating baffle-plate column. *Trans Inst Chem Eng*. 1996; 74: 463–470. https://doi.org/10.1002/cjce.5450730401
[25] Baird MHI, Stonestreet P. Energy dissipation in oscillatory flow within a baffled tube. *Trans Inst Chem Eng*. 1995; 73A**:** 503–511.
[26] Hafez M, Baird MHI. Power consumption in a reciprocating plate column. *Trans Inst Chem Eng*. 1978; 56: 229–238.
[27] Banković-Ilić I, Veljković V, Skala D. Hidrodinamičke i masenoprenosne karakteristike kolone sa vibracionom mešalicom za sisteme gas-tečnost i gas-tečnost-čvrsta faza – monografija. Univerzitet u Nišu, Tehnološki fakultet, Leskovac; 2009. ISBN 978-86-82367-80-2 (in Serbian).
[28] Banković-Ilić IB, Veljković VB, Lazić ML, Skala DU. Power consumption and gas holdup in a gas-liquid reciprocating plate column. *Chem Eng Comm*. 1995; 134: 17–32. https://doi.org/10.1080/00986449508936320
[29] Aleksić M, Veljković VB, Banković-Ilić IB, Lazić ML, Skala DU. Uticaj Rašigovih prstenova i reoloških osobina tečnosti na promenu pritiska na dnu kolone sa vibracionom mešalicom. *Hem Ind*. 2002; 56: 409–414. https://doi.org/10.2298/HEMIND0210409A (in Serbian)
[30] Vasić Lj, Banković-Ilić IB, Lazić ML, Veljković VB, Skala DU. The effects of operating conditions on the pressure variation at the bottom of a 16.6 cm i.d. reciprocating plate column. *Chem Ind Chem Eng Q.* 2005; 11: 195–202. https://doi.org/10.2298/CICEQ0504195V
[31] Aleksić M, Veljković VB, Banković-Ilić IB, Lazić ML, Skala DU. Uticaj Rašigovihi reoloških osobina tečnosti na promenu pritiska na dnu kolone sa vibracionom mešalicom. *Hem Ind*. 2003; 57: 107–113. https://doi.org/10.2298/HEMIND0210409A (in Serbian)
[32] Banković-Ilić IB, Veljković VB, Lazić ML, Skala DU. Hydrodynamics of a gas-liquid-solid reciprocating plate column. In: *11th International Congress of Chemical and Process Engineering*, Prague, Czech Republic, 1993, E4.27.
[33] Banković-Ilić IB, Veljković VB, Lazić MB, Skala DU. Power consumption and pressure fluctuation at the column base in gas-liquid-solid reciprocating plate columns. In: *12th International Congress of Chemical and Process Engineering.* Prague, Czech Republic, 1996, P3.89.
[34] Banković-Ilić IB, Veljković VB, Lazić ML, Skala DU. Influence of liquid properties on power consumption in reciprocating plate columns. I. Newtonian fluids. In: *13th International Congress of Chemical and Process Engineering.* Prague, Czech Republic, 1998, P3.37 (CD-ROM of full texts 0195.pdf).
[35] Banković-Ilić I. Stamenković I, Stamenković O, Lazić M, Veljković V, Skala D. Pressure variation at the bottom of a reciprocating plate reactor filled with non-newtonian liquids. In: *18th Congress of Chemists and Technologists of Macedonia.* Ohrid, Republic of Macedonia, 2004, CD ROM of Extendent abstracts, CHE-Bankovic-IlicIvana-effects-e.pdf.
[36] Naseva OS, Stamenković IS, Banković-Ilić IB, Lazić ML, Veljković VB, Skala DU. Sadržaj gasa u bioreaktoru sa vibracionom mešalicom – tečna faza je njutnovski fluid. *Hem Ind*. 2002; 56: 198–203. https://doi.org/10.2298/HEMIND0205198N (in Serbian)
[37] Stamenković I, Stamenković O, Banković-Ilić I, Lazić M, Veljković V, Skala DU. The pressure variation at the bottom of a reciprocating plate bioreactor filled with non-newtonian liquids. In: *16th International Congress of Chemical and Process Engineering.* Prague, Czech Republic, 2004, CD ROM of Full Texts 0763.pdf.
[38] Vasić LS, Banković-Ilić IB, Lazić ML, Veljković VB, Skala DU. Snaga mešanja nenjutnovskih tečnosti u višefaznoj koloni sa vibracionim mešanjem prečnika 16,6 cm. In: *19. Kongres o procesnoj industriji Procesing 2006*, *Zbornik rezimea radova.* Beograd, Srbija, 2006, CD verzija punog rada (in Serbian).
[39] Rama Rao NV, Baird MHI. Characteristics of a countercurrent reciprocating plate bubble column. I. Holdup, pressure drop and bubble diameter. *Can J Chem Eng*. 1988, 66: 211–221. https://doi.org/10.1002/cjce.5450660205
[40] Yang NS, Shen ZQ, Chen BH, McMillan AF. Pressure drop, gas holdup and interfacial area for gas-liquid contact in Karr-columns. *Ind Eng Chem Proc Des Dev*. 1986; 25: 660–664. https://doi.org/10.1021/i200034a011
[41] Rama Rao NV, Srinivas NS, Varma YBG. Dispersed phase holdup and drop size distributions in reciprocating plate columns. *Can J Chem Eng*. 1983; 61: 168–177. https://doi.org/10.1002/cjce.5450610204
[42] Aleksić M, Veljković VB, Banković-Ilić IB, Lazić ML, Skala DU. Gas holdup in a gassed reciprocating plate column with Rashig rings placed in interplate spaces. *Can J Chem Eng*. 2002: 80: 485–490. https://doi.org/10.1002/cjce.5450800318
[43] Skala D, Veljković V. Zadržavanje gasa u trofaznoj koloni sa vibracionom mešalicom. In: *II Jugoslovenski kongres za hemijsko inženjerstvo i procesnu tehniku sa međunarodnim učešćem*, *Zbornik radova II.* Dubrovnik, Jugoslavija, 1987, pp. 56–59 (in Serbo-Croation).
[44] SkalaDU, Veljković VB. Gas holdup in three-phase reciprocating columns. In: Cheremisinoff NP, ed. *Mixed-flow hydrodynamics: advances in engineering fluid mechanics*. Houston: Gulf Publ. Co; 1996: 803-810. ISBN 0-88415-256-1.
[45] Skala DU, Veljković VB, Janjić VV, Lazić M, Banković-Ilić IB. Gas holdup in a gas-liquid-solid reciprocating plate column. *Can J Chem Eng*. 1993; 71: 817–820. https://doi.org/10.1002/cjce.5450710521

[46] Veljković VB, Banković-Ilić IB, Lazić ML, Skala DU. Gas holdup in three-phase reciprocating plate columns. In: *12th International Congress of Chemical and Process Engineering*. Prague, Czech Republic, 1996, P3.90.
[47] Aleksić M, Veljković V, Banković-Ilić I, Lazić M, Skala D. The Effects of operating conditions on the gas holdup in a multiphase reciprocating plate column with Rashig rings placed in interplate spaces. In: *16th International Congress of Chemical and Process Engineering.* Prague, Czech Republic, 2004, CD ROM of Full Texts 0755.pdf.
[48] Banković-Ilić I, Veljković V, Skala D. Gas holdup in a three phase reactors of the bubble column type. *Hem Ind*. 1994; 48: 397–402.
[49] Banković-Ilić I, Aleksić M, Veljković V, Lazić M, Skala D. Effects of size of Rashig rings placed in interplate spaces and fractional plate free area on the gas holdup in a reciprocating plate reactor. In: *18th Congress of Chemists and Technologists of Macedonia*. Ohrid. Republic of Macedonia, 2004, CD Rom of Extendent abstracts, CHE-11-Bankovic-IlicIvana-effects-e.pdf.
[50] Lounes M, Thiboult J. Hydrodynamics and oower consumption of a reciprocating rlate gas-liquid column. *Can J Chem Eng*. 1993; 71: 497-506.
[51] Stamenković IS, Stamenković OS, Banković-Ilić IB, Lazić ML, Veljković VB, Skala DU. The gas holdup in a multiphase reciprocating plate column filled with carboxymethylcellulose solutions. *J Serb Chem Soc*. 2005; 70: 1533–1544. https://doi.org/10.2298/JSC0512533S
[52] Vasić LJ, Banković-Ilić IB, Lazić ML, Veljković VB, Skala DU. Sadržaj gasa u koloni sa vibracionom mešalicom prečnika 16,6 cm. *Hem Ind*. 2005; 59: 263–266. https://doi.org/10.2298/HEMIND0510263V
[53] Vasić LS, Banković-Ilić IB, Lazić ML, Veljković VB, Skala DU. The gas holdup in a 16.6 cm i.d. multiphase reciprocating plate column. In: *5th International Conference of the Chemical Societies of the Southeast European Countries.* Ohrid, Republic of Macedonia, 2006, p. 238.
[54] Chen BH, Yang NS, McMillan AF. Gas holdup and pressure drop for air-water flow through plate bubble columns. *Can J Chem Eng*. 1986; 64: 387–392. https://doi.org/10.1002/cjce.5450640305
[55] Sundaresan A, Varma YBG. Dispersed phase holdup and bubble size distributions in gas-liquid cocurrent upflow and countercurrent flow in reciprocating plate column. *Can J Chem Eng*. 1990; 68: 560–568. https://doi.org/10.1002/cjce.5450680405
[56] Skala D, Veljković V. Gas holdup in a Karr reciprocating plate column. In: *9th International Congress of Chemical and Process Engineering*. Prague, Czech Republic, 1987.
[57] Nikolić LB, Nikolić VD, Veljković VB, Skala DU. Gas holdup in a three-phase reciprocating plate column. *J Serb Chem Soc*. 2005; 70: 1363–1371. https://doi.org/10.2298/JSC0511363N
[58] Veljković V, Skala D. Mass transfer characteristics in a gas-liquid reciprocating plate column. II. Interfacial area. *Can J Chem Eng*. 1988; 66: 200–210. https://doi.org/10.1002/cjce.5450660203
[59] Kagan SZ, Veisbein BA, Trukhanov VG, Musychenko LA. Longitudinal mixing and its effect on mass transfer in pulsed-screen extractor. *Int Chem Eng*. 1973; 13: 217–219.
[60] Miyauchi T, Oya H. Longitudinal dispersion in pulsed perforated-plate columns. *AIChE J*. 1965; 11: 395–402. https://doi.org/10.1002/aic.690110307
[61] Kim SD, Baird MHI. Axial dispersion in a reciprocating plate extraction column. *Can J Chem Eng*. 1976; 54: 81–89. https://doi.org/10.1002/cjce.5450540112
[62] Stevens GW, Baird MHI. A model for axial mixing in reciprocating plate columns. *Chem Eng Sci*. 1990; 45: 457–465. https://doi.org/10.1016/0009-2509(90)87032-N
[63] Mar BW, Babb AL. Longitudinal mixing in a pulsed sieve-plate extraction column. *Ind Eng Chem*. 1959; 51: 1011–1014. https://doi.org/10.1021/ie51396a032
[64] Kim SD, Baird MHI. Effect of hole size on hydrodynamics of a reciprocating perforated plate extraction column. *Can J Chem Eng*. 976; 54: 235–237. https://doi.org/10.1002/cjce.5450540320
[65] Karr AE, Gebert W, Wang M. Axial mixing and scale-up of reciprocating plate columns. *Can J Chem Eng*. 1987; 65: 373–381. https://doi.org/10.1002/cjce.5450650304
[66] Nikolić LB, Nikolić VD, Veljković VB, Lazić ML, Skala DU. Axial dispersion of the liquid phase in a three-phase Karr reciprocating plate column. *J Serb Chem Soc*. 2004; 69: 581–599. https://doi.org/10.2298/JSC0407581N
[67] Baird MHI, Rama Rao NV. Axial mixing in a reciprocating plate with very small density gradients. *AIChE J*. 1988; 37: 1019–1026. https://doi.org/10.1002/aic.690370707
[68] Baird MHI, Rice RG. Axial dispersion in large unbaffled column. *Chem Eng J*. 1975; 9: 171–174. https://doi.org/10.1016/0300-9467(75)80010-4
[69] Sater VE, Levenspiel O. Two-phase flow in packed beds. *Ind Eng Chem Fundam*.1966; 5: 86–92. https://doi.org/10.1021/i160017a015
[70] Skala D. Ispitivanje aksijalnog mešanja u Karrovoj koloni, Magistarski rad, Univerzitet u Beogradu, Tehnološko-metalurški fakultet, Beograd, 1976 (in Serbian).
[71] Banković-Ilić IB, Veljković VB, Lazić ML, Skala DU. Mass transfer in a multiphase vibration column. I. The volumetric mass transfer coefficient. *Hem Ind.* 2001; 55: 376–382.
[72] Banković-Ilić IB, Veljković VB, Lazić ML, Skala DU. Mass transfer in a multiphase vibration column. II. Interfacial area. *Hem Ind*. 2001; 55: 383–388.

[73] Yang NS, Shen ZQ, Chen BH, McMillan AF. Axial mixing and mass transfer in gas-liquid Karr columns. *Ind Eng Chem Process Des Dev*. 1986; 25: 776–780.
[74] Miyanami K, Tojo K, Minami I, Yano T. Gas-liquid mass transfer in vibrating disc column. *Chem Eng Sci*. 1978; 33: 601–608. https://doi.org/10.1016/0009-2509(78)80022-0
[75] Yoshida Y, Muira Y. Gas absorption in agitated gas-liquid contactors. *Ind Eng Chem Process Des Dev.* 1963; 2: 263–268. https://doi.org/10.1021/i260008a002
[76] Baird MHI, Garstang JH. Gas absorption in a pulsed bubble column. *Can J Chem Eng.* 1972; 27: 823–833. https://doi.org/10.1016/0009-2509(72)85016-4
[77] Miller DN. Scale-up of agitated vessels gas-liquid mass transfer. *AIChE J*. 1974; 20: 445–53. https://doi.org/10.1002/aic.690200303
[78] Akita K, Yoshida F. Bubble size interfacial area and liquid-phase mass transfer coefficient in bubble columns. *Ind Eng Chem Process Des Dev.* 1974; 13: 84–91. https://doi.org/10.1021/i260049a016
[79] Sundaresan A, Varma YBG. Interfacial area and mass transfer in gas-liquid cocurrent upflow and countercurrent flow in reciprocating plate column. *Can J Chem Eng*. 1990; 68: 951–958. https://doi.org/10.1002/cjce.5450680610
[80] Lounes M, Thibault J. Mass transfer in a reciprocating plate bioreactor. *Chem Eng Comm.* 1994; 127: 169–189. https://doi.org/10.1080/00986449408936231
[81] Skala D, Veljković V. Mass transfer characteristics in a gas-liquid reciprocating plate column. I. Liquid phase volumetric mass transfer coefficient. *Can J Chem Eng*. 1988; 66: 192–199. https://doi.org/10.1002/cjce.5450660203
[82] Rama Rao NV, Baird MHI. Gas-liquid mass transfer in a 15 cm diameter reciprocating plate column. *J Chem Technol Biotech*. 2003; 78: 134–137. https://doi.org/10.1002/jctb.704
[83] Liu CH, Chen BH. Characteristics of reciprocating screen-plate bubble column with dilute alcohol solutions. *Can J Chem Eng*. 1993; 71: 464–467. https://doi.org/10.1002/cjce.5450710318
[84] Vasić LS, Banković-Ilić IB, Lazić ML, Veljković VB, Skala DU. Oxygen mass transfer in a 16.6 i.d. multiphase reciprocating plate column. *J Serb Chem Soc*. 2007; 72: 523–531. https://doi.org/10.2298/JSC0705523V
[85] Brauer H, Sucker D. Biological waste water treatment in a high efficiency reactor. *Ger Chem Eng*. 1979; 2: 77-86.
[86] Audet J, Lounes M, Thibault J. Pullulan fermentation in a reciprocating plate bioreactor. *Bioprocess Eng*. 1996; 15: 209–214. https://doi.org/10.1007/BF00369484
[87] Lounes M, Audet J, Thibault J, LeDuy A. Description and evaluation of a reciprocating plate bioreactors. *Bioprocess Eng*. 1995; 13: 1–11. https://doi.org/10.1007/BF00368758
[88] Veljković VB, Lazić ML, Rutić DJ, Jovanović SM, Skala DU. Selection of a bioreactor and the optimal aerobic conditions for dextransucrase fermentation by *Leuconostoc mesenteroides*. *J Serb Chem Soc*. 1990; 35: 483–490.
[89] Reschke M, Schügerl K. Continuous reactive extraction of penicillin-G in a Karr column. *Chem Eng J*. 1985; 31: B19-B26. https://doi.org/10.1016/0300-9467(85)80061-7
[90] Deshusses MA, Chen W, Mulchandani M. Innovative bioreactors. *Curr Opin Biotechnol*. 1997; 8: 165–168. https://doi.org/10.1016/S0958-1669(97)80096-1
[91] Stamenković I, Stamenković O, Banković-Ilić I, Todorović Z, Lazić M, Veljković V, Skala D. Dobijanje estara masnih kiselina postupkom alkoholize biljnih ulja. RS 52398 B, 2013 (in Serbian).
[92] Stamenković I, Banković-Ilić I, Konstantinović S, Ilić S, Lazić M, Veljković V, Skala D. Laboratorijski kontinualni tehnološki postupak za dobijanje metil estara masnih kiselina repičinog ulja, Univerzitet u Nišu, Tehnološki fakultet, br. 04 536/1, Leskovac, 2010.
[93] Stamenković I, Banković Ilić I, Todorović Z, Lazić M, Veljković V, Skala D. Kontinualna poluindustrijska proizvodnja metil estara masnih kiselina iz ulja repice. *IX Savjetovanje hemičara i tehnologa Republike Srpske.* Banja Luka, Republika Srpska, BiH, 2010, p. 69.

Kolona sa vibracionom mešalicom – fundamentalna istraživanja i primena u Srbiji od 1970. do 2020. godine

Vlada B. Veljković[1,2], Ivana B. Banković Ilić[1] i Dejan U. Skala[3]

[1]Univerzitet u Nišu, Tehnološki fakultet, Leskovac, Srbija
[2]Srpska akademija nauka i umetnosti, Beograd, Srbija
[3]Univerzitet u Beogradu, Tehnološko-metalurški fakultet, Beograd, Srbija

(Pregledni rad)

Izvod

U grupi višefaznih kontaktora i reaktora, značajno mesto zauzima reaktor sa vibracionom mešalicom (RVM) koji se sastoji od niza perforiranih pločica pričvršćenih na zajedničkom vratilu, koje se kreću gore-dole. Ovakva konstrukcija reaktora maksimizira pozitivne efekte mehaničkog mešanja i minimizira ili elimiše negativne efekte karakteristične za kontaktore i reaktore kolonskog tipa. U RVM, najveće zadržavanje dispergovane faze postiže se pri njenoj manjoj brzini strujanja zbog uticaja mehaničkog mešanja na usitnjavanje mehurova ili kapi. Zato ovaj uređaj može biti najprihvatljiviji kontaktor za izvođenje složenih procesa u višefaznim sistemima. U radu su opisana fundamentalna istraživanja i primena RVM u Srbiji u poslednjih pedeset godina, od 1970. do 2020. godine. Analizirane su hidrodinamičke i mesenoprenosne karakteristike, kao što su promena pritiska na dnu reaktora, snaga mešanja, zadržavanje dispergovane faze, aksijalna disperzija, koeficijent prenosa mase u tečnosti, specifična međufazna površina i zapreminski koeficijent prenosa mase. Takođe, opisana je primena RVM kao reaktora u bioprocesima i procesima proizvodnje biodizela.

Ključne reči: povratno-periodično mešanje, promena pritiska, snaga mešanja, zadržavanje dispergovane faze, aksijalna disperzija, zapreminski koeficijent prenosa mase

Continuous reciprocating plate and packed bed multiphase reactors in biodiesel production: Advancements and challenges

Ivana B. Banković-Ilić[1], Marija R. Miladinović[1] and Vlada B. Veljković[1,2]

[1]*University of Niš, Faculty of Technology in Leskovac, Serbia*
[2]*Serbian Academy of Sciences and Arts, Belgrade, Serbia*

Abstract
Biodiesel, a renewable and environmentally friendly alternative to conventional fossil fuels, has gained significant attention over the last two decades. Continuous production of biodiesel offers efficiency, productivity, and scalability advantages. This paper provides a concise overview of continuous reactor systems for biodiesel production, focusing on two specific systems—the reciprocating plate reactor and the packed bed reactor—subjects of the authors' extensive research. A thorough comparison of these reactors, spanning biodiesel yield, reaction kinetics, and conversion efficiency, underscores their advantages. The reciprocating plate reactor demonstrates superior mixing characteristics, which improve mass transfer and reaction kinetics. Conversely, the packed bed reactor offers a higher catalyst-to-feedstock ratio and longer residence time, enhancing conversion efficiency. Both reactors exhibit favourable performance for continuous biodiesel production. This research can contribute to understanding continuous biodiesel production using innovative reactor designs. The comparative analysis between the reciprocating plate and packed bed reactors offers valuable insights for process optimization and reactor selection based on specific requirements such as feedstock availability, reaction kinetics, and economic considerations. These insights pave the way for the implementation of sustainable and efficient biodiesel production processes in the future.

Keywords: Transesterification, methanolysis, hydrodynamics, mass-transfer, continuous reactors.

Available on-line at the Journal web address: http://www.ache.org.rs/HI/

REVIEW PAPER

UDC: 665.75: 330.123.7

Hem. Ind. **78(3)** 205-225 (2024)

1. INTRODUCTION

The rising worldwide interest in clean energy sources has driven extensive research in biodiesel production. Biodiesel, a sustainable and energy-efficient fuel, addresses current energy usage and supply concerns. It can be blended with conventional diesel, offering a safe, non-toxic alternative, significantly reducing carbon dioxide emissions without requiring major engine modifications. Biodiesel production involves transesterification of vegetable and algal oils or animal fats with alcohol in the presence of a catalyst. Various factors, such as reactor type, feedstock and catalyst properties, alcohol-to-oil ratio, temperature, time, and mixing intensity, affect the quality and yield of biodiesel [1].

Traditional batch reactors have limitations like poor heat and mass transfer, high operating costs, long reaction times, variable product quality, and challenges in scaling up production. Continuous reactors have emerged as a viable solution, providing controlled operation, improved kinetics, and enhanced product quality. They allow precise control over process parameters, resulting in higher conversion rates, reduced reaction times, and improved yield. In addition, they facilitate the use of solid catalysts, offering benefits such as reduced waste generation and catalyst reusability. Moreover, continuous reactors optimize contact between reactants and catalyst surfaces, improving overall reaction efficacy. They enable process intensification by integrating multiple steps within a single system, leading to streamlined operations, reduced energy consumption, and increased process efficiency. This integrated approach increases the

Corresponding authors:Ivana B. Banković-Ilić, University of Niš, Faculty of Technology in Leskovac, Serbia
Paper received: 30 June 2023; Paper accepted: 20 May 2024; Paper published: 31 May 2024.
E-mail: ivanabank@yahoo.com
https://doi.org/10.2298/HEMIND230630010B

economic viability of biodiesel production and reduces environmental impact, making continuous reactors highly attractive for large-scale production [2-5].

This paper comprehensively reviews recent advancements in continuous multiphase reactors for biodiesel production, emphasizing their benefits and drawbacks. The review critically analyses existing literature and identifies key challenges and opportunities. It focuses explicitly on reciprocating plate reactors (RPRs) and packed bed reactors (PBRs) as promising multiphase reactors for biodiesel production. Comparing their characteristics and performance will contribute to the knowledge base of continuous reactor technologies. The findings will assist researchers and industry professionals in reactor selection and process optimization, ultimately enhancing the sustainability of biodiesel production.

2. BASIC TYPES OF REACTORS USED IN BIODIESEL PRODUCTION

Biodiesel can be produced through four main steps, which refer to the transesterification reaction between the reactants under defined reaction conditions and then three consecutive separation unit operations [3], *i.e.*:

- the reaction between the reactants,
- product separation by settling, filtration, floatation, decantation, sedimentation, or centrifugation,
- removal of unreacted alcohol and excess water from biodiesel by evaporation or flash distillation and
- separation of undesirable compounds, such as a residual catalyst, soap, moisture, or acylglycerols, using dry or wet washing (purification of biodiesel).

Each of these steps can be implemented in different ways, but the first, main step - chemical reaction, can be performed using one of three available modes for biodiesel production: batch, semi-continuous (semi-batch), or continuous, where each of them has its own advantages and drawbacks (Table 1) [2-5].

Table 1. Classification of reactors for biodiesel production on the basis of the operating mode

Reactor	Advantages	Drawbacks
Batch	Simplicity of design and operation Suitability for variable type and quality of feedstock Good flexibility, versatility, and easy scale-up Good mixing of reactants Easy control of the material inflow and outflow	Low selectivity and production rate Inferior heat and mass transfer High energy consumption, capital, and operating costs Requirement for large reactor volumes Requirement for high amounts of alcohol to shift the reaction forward Biodiesel separation costs Requirement for high water consumption for purification
Continuous	Reduced energy consumption Low capital requirements Uniform product quality Good reactor selectivity and flexibility Suitable for fast reactions and large-scale processes	Complex design and scale-up Low versatility
Semi-continuous (semi-batch)	Suitable for rapid reactions Uniform product quality Good temperature control Good heat transfer Easy monitoring	High operating costs Low production rate High energy consumption Labor intensive process Complex scale-up

According to the mode of operation, the phase numbers, operating conditions, reaction parameters, and the type of mixing, the chemical reactors employed in the production of biodiesel can be grouped into five categories (Table 2) [5,6].

Table 2. Advantages and drawbacks of different categories of reactors applied in biodiesel production [5,6].

Reactor type		Advantages	Drawbacks
Tubular (plug-flow)	Oscillatory flow[c]	High biodiesel yield, high mass and heat transfers, low required alcohol-to-oil molar ratio, and low operating and capital costs	Complicated design for industrial biodiesel production in continuous mode
	Packed (fixed) bed[b, c]	High biodiesel yield, simple and economically favourable processes, possible to realize high pressures and temperatures	Difficult catalyst replacement, difficult heat and temperature control, possible side-reactions
	Trickle bed[b,c]	Low catalyst destruction without the need for separation, simple operation under high temperatures and pressures, continuous separation of products	Channelling and flooding, difficult control of reaction parameters, complex scale-up process
	Fluidized bed[b, c]	High mixing intensity, high heat, and mass transfers, uniform distribution of temperature, and convenient catalyst replacement	High-pressure drop, high catalyst attrition, erosion of the reactor wall, expensive equipment for regeneration, high operating and capital costs
	Micro-channel[c]	Easy control of temperature and phase separation, good energy efficiency	Low contact between phases
Rotating	Stirred tank- batch	Low capital and operating costs, easy to maintain, simple design	Complexity of the reaction kinetics, complex operating conditions, difficult temperature control, non-uniform product quality, large reactor volume, less efficient compared to continuous reactors, high capital and labour costs
	Stirred tank- continuous	Simple temperature control, constant heat release rate	Difficult process control
	Rotating - spinning tube[c]	Improved heat and mass transfers	Energy consumption for rotation
	Rotating - spinning disc[c]	Good control of side reaction, reduced cost of downstream purification	
Microwave [c]		Short reaction time, efficient heat transfer, and clean products	Difficult control of power and temperature, low reproducibility of the process
Cavitational[c]	Ultrasonic	Decreased reaction time, temperature, alcohol-to-oil molar ratio, and catalyst amount	High cost of the downstream process, complex scale-up, particle erosion, cavitational blocking
	Hydrodynamic cavitation	Simple design, operation, maintenance, and scale-up	Lower conversion degree for pressures above the optimal
	Shockwave power	Stable formed emulsion	
Simultaneous reaction-separation	Membrane[c,b,sc]	Small amount of wastewater, membrane resistance to organic solvents, low energy consumption	Plate-and-frame membranes: a possibility of plugging at flow stagnation points, difficult cleaning, high cost: Inorganic membranes: brittleness, complicated sealing at high temperatures, difficult scale-up, low selectivity, high cost
	Reactive distillation[c]	Safe process, low capital and operating costs, low emissions	
	Annular centrifugal contactors[b,c]		Transesterification cannot be completed due to uncontrolled and extremely low residence time

[c]Continuous, [b]batch, and [sc]semi-continuous mode.

2. 1. Tubular reactors

Plug-flow reactors (PFRs) are the simplest chemical reactors utilized in continuous flow reactions, where reactants enter at one end and exit at the other. Their design ensures turbulent, constant-velocity flow through a narrow, tubular channel without back-mixing. PFRs, often incorporating a fixed-bed catalyst, promote uniform reaction progress and

allow for radial mixing of immiscible fluids, enhancing efficiency. Suitable for steady-state flow, high pressure, and small solid particles, PFRs are scalable from laboratory to industrial scales. Advantages include simple construction, easy cleaning, and uniform product quality, but challenges include a large length-to-diameter ratio, slow mixing, and high dispersed phase holdup, requiring careful consideration of kinetics, mass transfer, and pressure drop in design and operation.

2. 1. 1. Oscillatory flow reactors

Oscillatory flow reactors (OFRs) use periodic reactant oscillation for enhanced mixing and improved reaction efficiency. Whether horizontal or vertical, tubes with pistons or diaphragms generate oscillatory flow. Baffles inside create vortex mixing, turning interbaffle spaces into stirred tanks, resembling an ideal plug flow reactor (PFR). This motion enhances mixing and mass transfer and improves reaction kinetics and conversion. RPCs, a type of OFRs, will be discussed further in Chapter 3.1. OFRs boost biodiesel production through improved mixing, enhanced mass transfer, and reduced reaction times. Oscillatory motion enhances reactant dispersion, promoting contact with the catalyst for higher reaction rates and conversion. This design allows for scalability from lab to industry, but energy consumption must be balanced with efficiency and conversion benefits.

In recent decades, OFRs have been investigated in continuous biodiesel production as a potential alternative to conventional batch or continuous flow reactors [7-12]. Highina *et al.* [9] achieved a 96 % yield using Jatropha oil and methanol in a continuous oscillatory baffled reactor. Palm fatty acid distillate yielded 94.2 % under optimized conditions [10]. Solar-powered rotating flask OFR produced 93.7 % yield from coconut waste cooking oil [11]. Zheng *et al.* [12] obtained similar conversion in batch and continuous mesoscale OFRs. Azhari *et al.* emphasized the importance of mixing, heat, and mass transfer to scale OFRs [7]. García-Martín *et al.* [8] found a higher yield (72.5 %) in batch OFR compared to STR (63.5 %) using a blend of waste cooking and olive/sunflower oil. The composition of fatty acid methyl esters (FAME) and physicochemical properties were similar in both reactors.

It is clear that OFRs can potentially improve biodiesel production, but their practical implementation and commercial viability are still being researched. More studies are needed to understand their benefits and limitations in large-scale production.

2. 1. 2. Packed-bed reactors

Packed-bed reactors (PBRs), known as fixed-bed reactors, consist of a column filled with solid catalyst particles or a combination of catalyst particles and an inert support material. The reactants flow through the packed bed, allowing the transesterification reaction. The structure and size distribution of catalyst and inert particles determine the transport phenomena, the surface area, and the interparticle space. The process of particle packing is determined by the physical properties of the solid particles that do not require any downstream separation process and treatment method. High oil conversion and favourable economic process variables are the most important advantages of PBR for its application in biodiesel production. The use of PBRs in biodiesel production will be described in more detail in Chapter 3.2.

2. 1. 3. Trickle-bed reactors

Trickle-bed reactors (TBRs) consist of a tube with a sieve plate or wire mesh as a support for a packed bed near the bottom and can be used for biodiesel production due to its flexibility and simple operation. This configuration provides intimate contact between the liquid reactants and the solid catalyst. The liquid phase trickles through the catalyst bed downward in the form of drops or film based on pressure or gravity forces, while the gas phase can flow concurrently or countercurrent through the reactor, which operates in continuous or semi-continuous mode.

TBRs are not extensively utilized in biodiesel production but have been explored for certain aspects [13-15]. The advantages of TBRs for biodiesel production are high liquid-solid contacting area due to the trickling flow, facilitating the efficient mass transfer and reaction kinetic rate, reduced catalyst requirements due to high contact efficiency, and lowering the cost of the overall process. However, the choice of catalyst is critical for achieving its high activity and

stability in TBRs. In addition, proper reactor design, including the selection of packing material, reactor dimensions, and flow distribution devices, is essential to ensure uniform flow distribution, avoid channelling, and maximize contact between the reactants and the catalyst. Further research and development are needed to explore the full potential of trickle-bed reactors in biodiesel production and optimize their performance for large-scale implementation.

2. 1. 4. Fluidized-bed reactors

Fluidized-bed reactors (FBRs) are column-type reactors where an upward liquid flow fluidizes a bed of solid particles. The temperature inside the reactor is more uniform, and the heat and mass transfers are greater than in PBRs. Chen *et al.* [16] obtained a 91.8 % biodiesel yield from waste cooking oil in an FBR using *Pseudomonas mendocina* cells as a biocatalyst immobilized in magnetic microspheres. The catalyst showed good reusability (87.5 % biodiesel yield after 10 cycles).

2. 1. 5. Microchannel reactors

Microchannel reactors (MCRs) are small-scale reactors with millimetre-sized interconnected channels, operating based on microfluidic principles for controlled and efficient chemical reactions. Their high surface area-to-volume ratio enhances heat and mass transfers, allowing for precise control of reaction conditions. MCRs can be scaled up for continuous, high-throughput biodiesel production by stacking or parallelizing multiple channels. However, short diffusion paths necessitate micro-mixers for the improved liquid contact. Specialized fabrication techniques and careful handling are required to prevent blockage or damage. Oily feedstock properties may also require pretreatment for smooth operation.

There are several studies in the literature about biodiesel production in MCRs with high achieved yields (higher than 95 %) by using various raw oil materials (sunflower, palm, cotton seed, soybean oils, or pork lard), methanol, and homogeneous or solid catalysts (KOH, NaOH, H_2SO_4, CaO, or enzyme) [17-21]. Further studies are needed to optimize the reactor design, catalyst selection, and process conditions to maximize possibilities for the use of microchannel reactors for efficient biodiesel production.

2. 2. Rotating reactors

2. 2. 1. Stirred-tank reactor

Stirred-tank reactors (STRs) are cylindrical vessels with a central shaft containing one or multiple impellers. They can operate in batch or continuous mode. To enhance mixing, especially in large multiphase reactors, it is recommended to use vertical baffles on the inner wall or different types of stirrers, such as turbine, impeller, monolithic, and foam.

Batch stirred-tank reactors (BSTR) are commonly used for industrial biodiesel production, with reactor productivity linked to conversion time. Continuous STRs offer advantages for large-scale production due to perfectly mixed flow, simpler temperature control, and consistent heat release rate, conversion rate, and selectivity. While most biodiesel literature focuses on batch processes, CSTRs have gained attention in the last three decades. Studies on homogeneously-catalysed oil transesterification and the use of CaO as a solid catalyst have shown promises. However, a single CSTR may not achieve the same biodiesel yield as a BSTR, suggesting the need for a series of continuous reactors, particularly for large-scale plants with glycerol separation as a byproduct.

2. 2. 2. Rotating/spinning tube reactors

Rotating/spinning tube reactors (R/S-TR) can be categorized into 3 groups that are rotating-tube reactors (RTRs), rotating-bed reactors (RBRs), and spinning tube-in-tube reactors (STTRs). These centrifugal reactors use rotation to induce centrifugal forces, thus enhancing mixing and mass transfer, and providing turbulent flow for improved reaction kinetics and conversion of oil and alcohol. They are versatile for use in laboratories as well as in industrial-scale biodiesel production.

RTRs have such a cylinder geometry so to provide low shear stresses, improving heat and mass transfer. RBRs, on the other hand, use a rotating bed for micromixing and improved mass transfer, depending on parameters like rotating

speed, which affects efficiency. Concentric rotating tubes in STTRs enhance micromixing and interfacial contact, reducing reaction time. Lodha *et al.* [25] achieved a 97.6 % biodiesel yield with the use of RTR. RBR demonstrated high yields (over 973 %) in continuous biodiesel production using homogeneous (KOH) [26] or solid (K/γ-Al_2O_3) [27] catalysts. The COSTELLO Company utilized an STTR reactor for industrial biodiesel production [28].

2. 2. 3. Spinning-disc reactors

Spinning-disc reactors (SDRs) are a distinctive class of reactors in which the reactants are introduced into a dynamically rotating disc or a series of stacked discs. The radius and thickness of the liquid film in the reactor are controlled by a defined rotating speed, generating strong shear stresses and turbulence, leading to enhanced mass transfer and reaction kinetic rates. This reactor type provides excellent control of side reactions, increases the product yield, reduces further purification costs, and shows significant advantages of good heat and mass transfers. Soybean oil was converted with methanol (methanol-to-oil molar ratio of 6:1) into biodiesel (97 % yield within 2 to 3 s) in an SDR using NaOH (1.5 %) as a catalyst at 60 °C and 2400 rpm [29].

2.3. Microwave reactors

Microwave reactors (MRs) use microwave energy to generate heat directly within the reaction mixture, enabling rapid and uniform heating. Microwaves selectively interact with polar molecules, such as water and certain organic compounds, leading to efficient heating.

Microwave irradiation can effectively produce biodiesel *via* two main routes: extraction of oil from raw materials and transesterification of oil into biodiesel. Continuous MRs were applied for the ethanolysis of soybean [30] and cottonseed oils [31] using microwave powers of 1000 W and 270 W when 84 and 99.5 % ester yields were obtained, respectively. Microwave irradiation was combined with ultrasound for the *in situ* transesterification of microalgae over a KF/CaO catalyst, providing a biodiesel yield of 93 % [32].

2. 4. Cavitational reactors

Cavitational reactors utilize the cavitation phenomenon to enhance chemical reaction rates, by forming and collapsing vapor-filled cavities or bubbles in a liquid and generating intense localized conditions of high temperatures and pressures that can improve the reaction efficiency. Generally, in this reactor type acoustic (ultrasonic reactors, URs) or flow energy (hydrodynamic cavitation reactors, HCRs) or shockwave power (shockwave power reactor, SPR) are used to intensify the transport process, i.e., mixing intensity *via* micro eddies, acoustic liquid microcirculation, or shock waves. Thus, during the alcoholysis of oils, a very fine emulsion of two immiscible reactants is generated due to cavitational collapse near the liquid interface. The reaction rate was increased due to the increase in surface area between the reactants and the catalyst.

2. 4. 1. Ultrasonic (sonochemical) reactors

Acoustic cavitation is based on changes in the pressure (positive or negative) of the bubbles due to their expansion or constriction during the passage of sound waves, which intensifies the chemical reaction. Three main steps make up every ultrasound-assisted reaction: converting electrical energy into mechanical energy, transmitting acoustic energy into medium, and converting energy to the final form (chemical transformation). Batch [33,34] or continuous [35,36] ultrasonic reactors (URs) are usually applied for biodiesel production. However, the continuous mode is more suitable when large amounts of vegetable oil have to be processed in a relatively small reactor volume [37].

2. 4. 2. Hydrodynamic cavitation reactors

Hydrodynamic cavitation reactors (HCRs) use pressure changes generated by a pump and a constriction channel with some orifice, valve, or vent. This specific geometry causes cavity formation in a flowing liquid, induces intense mixing and localized high temperatures and pressures, and increases the reaction rate. Many cavities are formed when the pressure drops below the vapor pressure in the liquid at the reaction temperature. Compared to conventional reactors,

HCRs are a more efficient alternative due to reduced energy consumption. Batch HCRs were used for transesterification of non-edible oils from Thumba (*Citrullus colocyntis*) [38] and *Nagchampa* [39], achieving 80 and 92.1 % biodiesel yield, respectively, while Javadikia *et al.* [40] transesterified sunflower oil into biodiesel with 88 % yield in a continuous HCR.

2. 4. 3. Shockwave power reactors

Shockwave power reactors (SPRs) are rotating hydrodynamic reactors with spinning rotors with dead-ended cavities and a low-pressure zone at the bottom of the cavities. They utilize shockwaves generated by the rapid compression and expansion of gases. The resulting shockwaves propagate through the liquid medium, inducing intense mixing and enhancing reaction rates (shockwaves process). Hydro Dynamics, Inc. offers different models of SPRs for continuous biodiesel production with a capacity of 3 to 495 kt/year [41].

2. 5. Simultaneous reaction-separation reactors

A simultaneous reaction-separation reactor, called a reactive separation reactor, combines chemical reaction with product extraction from unreacted reactants in a single step. It is incredibly convenient for applications in equilibrium reactions, such as transesterification reactions so that the separation of products shifts the reaction in the direction of product formation. Several reactor designs can fulfil his task.

2. 5. 1. Membrane reactors

Membrane reactors (MRs) combine chemical reactions with membrane separation and integrate a reaction chamber with a selectively permeable membrane in a single unit. The membrane continuously separates the products from the reactants, allowing selective transport of specific components while retaining others, thus enhancing reaction kinetic rates and improving product separation. Due to feedstock impurities or reaction byproducts and potential membrane degradation over time, membrane fouling can affect the reactor performance inducing the requirement of periodic cleaning or replacement.

The membrane type depends on various parameters, such as the separation method, membrane cost, and reaction conditions. This reactor design is a relatively new concept in biodiesel production, although a higher biodiesel quality can be provided compared with conventional methods. MRs can be divided into inert, where the membrane is physically separated from the catalyst and does not participate in the reaction, and catalytic, where the membrane acts as a catalyst, or the catalyst is dispersed in the membrane. The first reactor type with a tubular ceramic TiO_2 membrane was used for continuous methanolysis of palm [42] and canola [43] oils. In the latter, an agarose membrane was used in batch biodiesel production from *Eruca sativa* Gars oil [44], while a polypropylene nonwoven fabric membrane was used in continuous biodiesel production from soybean oil [45].

2. 5. 2. Reactive distillation reactors

Reactive distillation reactors (RDRs) combine the reaction and distillation steps in a single unit, enabling improved reaction efficiency, product purity, and simplified process flow. They contain catalysts or reactive packing materials that facilitate the desired reactions while allowing simultaneous separation of reaction products by distillation. The reactive distillation process is appropriate if the boiling points of the reactants and products differ.

Petchsoongsakul *et al.* [46] used two solid catalysts as a packed bed, Amberlyst-15 at the top and CaO/Al_2O_3 at the bottom of an RDR, for the continuous production of biodiesel from used cooking oil through a combination of esterification and transesterification processes. Similarly, Noshadi *et al.* [47] used an RDR for continuous methanolysis of used cooking oil to biodiesel (94 % yield) over 12-tungestophosphoric acid hexahydrate as a catalyst under optimal operating conditions (67.9:1 methanol-to-oil molar ratio and 10 % of the catalyst).

2. 5. 3. Annular centrifugal contactors

Annular centrifugal contactors (ACCs), or annular centrifuges, are separation devices that perform liquid-liquid extraction or reaction processes, using centrifugal force to separate immiscible liquids based on their density difference.

The device consists of an annular channel or rotor, where the two immiscible liquids are introduced through two separate inlets at the top of the ACC. They flow through narrow annular spaces between the casing wall and the rotating rotor, where chemical reactions occur, and are separated due to the rotational motion and centrifugal forces acting on them.

By using a continuous ACC, a 98 % biodiesel yield was obtained *via* ethylation of Jatropha oil catalysed by sodium ethoxide at optimal conditions (6:1 ethanol-to-oil molar ratio, 1 % C_2H_5ONa, and 60 °C) [48]. Although the biodiesel yield was 57 %, which was lower than the yield achieved in a batch reactor under optimized conditions, this process was appropriate for small-scale units.

3. SPECIFIC CONTINUOUS REACTORS FOR BIODIESEL PRODUCTION

Several reviews on continuous-flow biodiesel production technologies *via* transesterification processes can be found in the literature, focusing on reactor type, operation conditions, reactant sources, catalyst type, and reaction mechanisms [4,28,49,50]. Different authors have divided continuous reactors into about 20 types in different manners. Many of these types were described in Section 2. However, the present study is directed toward exploring two continuous reactor types employed in biodiesel production, RPRs and PBRs. Both reactors are tubular, consisting of a column that contains a set of reciprocating plates or a fixed bed of solid particles, respectively. Generally, the configurations of these reactors are designed to enhance biodiesel production in terms of biodiesel yield, improved separation of final products with increased purity, and optimized energy consumption. The ensuing analysis delves into a detailed examination of the performance of these 2 reactor types.

3. 1. Biodiesel production in RPRs

Reciprocating plate reactors (RPRs) occupy an important place in the group of multiphase contactors, characterized by relatively low energy consumption and a high interfacial mass transfer rate. This column-type reactor can be classified in the subgroup of oscillatory flow reactors due to the reciprocating motion, *i.e.* periodically moving up and down the vibration set consisting of a number of perforated plates that are equally spaced and attached to a vertical carrier connected to the driving motor. An experimental system with an RPR is shown in Figure 1.

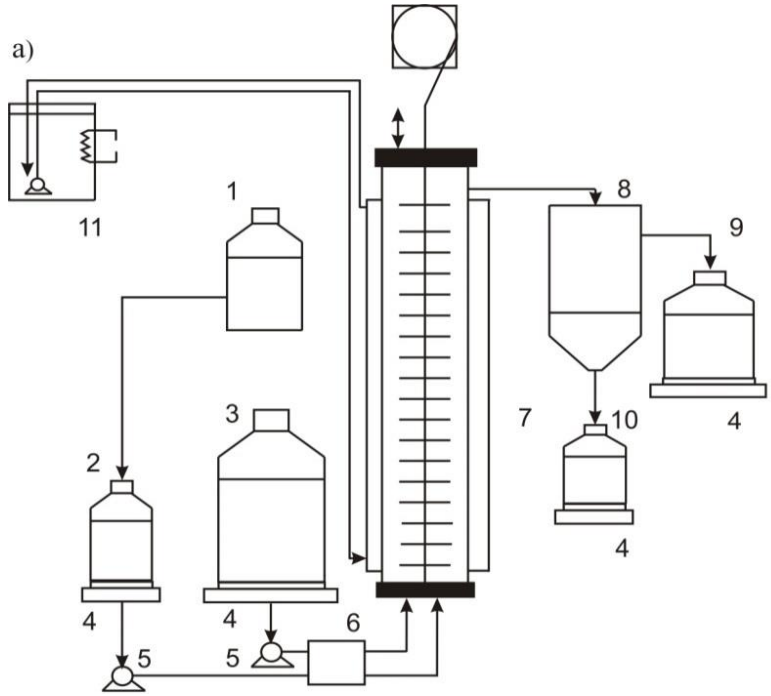

Figure 1. Experimental setup containing an RPR for laboratory-scale biodiesel production: 1 - vessel for preparing a catalyst solution in alcohol, 2 - tank for the catalyst solution in alcohol, 3 - tank for vegetable oil, 4 - scales, 5 - peristaltic pumps for transporting the vegetable oil and the catalyst solution in alcohol, 6 - oil and alcohol preheater, 7 - RPR, 8 - gravity separator, 9 - oil-ester phase tank, 10 - glycerol-alcohol phase tank, and 11 - water bath with recirculation.

In such a simple construction, the positive effects of mechanical mixing are maximized, and the adverse effects are minimized. In addition, several advantages of RPRs over the other column-type reactors can be noted such as a large and frequent renewal contact area between the phases, the radial and axial uniformity of dispersion [51], reduced axial mixing [52], and simple scale-up [51]. Small drops with long retention times in the liquid-liquid system are created by the energy of reciprocating motion.

Studies of hydrodynamic characteristics of the RPRs were mainly based on investigations of the pressure variation at the column bottom (PVCB), power consumption, flow regime, drop size, dispersed phase holdup, and axial dispersion [53-62]. Also, mass-transfer characteristics in RPCs, such as the specific interfacial area (SIA) and the liquid volumetric mass transfer coefficient (LVMTC), have been investigated in many studies [57,63-70]. The PVCB value is needed to know how to size the device for liquid transport, while the power consumption value is required to size the driving motor and calculate operating column costs. The axial dispersion coefficient has an important effect on RPR productivity. The interfacial mass transfer rate and the design of RPRs depend on the dispersed phase holdup and drop size, which influence the interphase mass transfer rate of the reactants per unit volume of dispersion, *i.e.* the LVMTC.

Due to their beneficial hydrodynamic and mass-transfer properties, RPRs have been investigated over the last three decades for commercial use as multiphase extractors or reactors in the chemical, petrochemical, and pharmaceutical industries. For instance, two immiscible reactants, like vegetable oil and alcohol, in biodiesel production can readily react with a relatively low energy input due to a maximized interfacial surface area [71-74].

3. 1. 1. Hydrodynamic characteristics of RPRs

Pressure variations at the column bottom (PVCB) result from the influences of inertia, friction, gravity, and buoyancy forces [58,75]. The first two forces appear due to the reciprocating plate movement, their mechanical contact with the reactor wall, and the contact of the liquid phase with moving and stationary column parts. A quasi-steady-state flow model was the base for calculating the PVCB value and power consumption [76].

These values in single- and multiphase systems in RPRs depend on the column geometry (height, diameter, plate number, and free fraction plate area), operating conditions (amplitude and frequency of reciprocating movement, temperature, and superficial velocities of continuous and dispersed phases), physical properties of the phases, the type and concentration of solid particles, and hydrodynamic flow conditions. In addition, power consumption depends on the liquid flow regime through the plate openings, which changes with the change in the viscosity of the liquid.

Applications of RPRs in the alcoholysis of edible or non-edible oils in producing biodiesel have been rarely investigated [73,77]. These studies focused on some hydrodynamic (PVCB, power consumption, mean drop size, drop size distribution, and dispersed phase holdup) and mass-transfer (SIA) properties of a continuous concurrent RPR in the case of the KOH-catalysed methanolysis of commercial sunflower oil. The obtained results can be crucial for designing continuous RPRs in producing biodiesel from vegetable oils. The influences of the vibration intensity and reaction conditions (reaction temperature and methanol-to-oil molar ratio) on the performance of the RPR in both non-reactive (sunflower oil as the continuous phase and methanol as the dispersed phase) and reactive (methanol-sunflower oil-KOH) systems were studied.

Investigations of PVCB and power consumption related to single-phase (sunflower oil) and two-phase (methanol/sunflower oil without catalyst) systems showed their increase with increased vibration intensity due to increased frictional losses. Decreases in density and viscosity of the dispersion with a temperature increase from 20 to 30 °C for the same methanol-to-oil molar ratio reduced the time-averaged and total PVCB and power consumption values. Also, a change in the methanol-to-oil molar ratio from 3:1 to 6:1 at a constant temperature affected the physical properties of the dispersion and reduced the PVCB and power consumption.

Gas holdup, as a crucial hydrodynamic characteristic of multiphase reactors, determines the mean gas retention time and the specific gas-liquid interfacial area. There is a 'critical' vibration intensity at which the gas holdup reaches its minimum value, depending on the type of plates, physical properties of the liquid, and the gas velocity, after which it increases. The gas holdup increases proportionally with the increased gas velocity up to the 'critical' value due to the increased resistance to the gas flow through the plate openings [56,62,78]. At a gas velocity of 3 cm s^{-1}, the gas holdup

reaches its maximal value and does not further change with the increase in the gas velocity [60]. The physical properties of the liquid phase affect the gas holdup. Comparing the gas holdup in different solutions of *n*-butanol, glycerol, and sodium sulphite, the lowest value was determined in water and the highest value in the *n*-butanol solution due to the prevented coalescence of bubbles. In non-Newtonian solutions of carboxymethyl cellulose (CMC), the gas holdup depended on the CMC molar mass and concentration in the solution as a result of changes in the rheological properties of the liquid phase [57].

The dispersed phase holdup for a non-reactive system (methanol/sunflower oil) in RPR with a diameter of 2.54 cm and 63 perforated plates was found to be independent of operating temperature, but it was greater at a higher methanol-to-oil molar ratio (6:1 *vs.* 3:1) [73,77]. In this case, the effect of increasing the vibration amplitude (from 1 to 2.35 cm) and frequency (from 2 to 3 Hz) on dispersed holdup was not observed. However, it increased nonlinearly with an increase in the vibration intensity up to 5 cm/s due to the intensification of drop breakage and then remained almost constant due to a slight drop size reduction.

With increasing the vibration intensity, the size of drops formed in RPRs depends on the energy input for their dispersion, so it reduces with increasing the total power consumption above the critical value [70]. This reduction is greater if the liquid flow is higher due to the effect of the turbulent force field on the dispersion process. The Sauter-mean drop diameter (SMDD) in non-reactive systems reduces with increasing the vibration amplitude and frequency due to the drop breakage [73,77]. The SMDD for the reactor's upper part (more than half of the height) is correlated with the time-average power consumption. It is higher than that in the reactive system (methanol-KOH/sunflower oil) under the same operating conditions due to the stabilization of small drops by emulsifiers, such as soaps, monoglycerides, and diglycerides, formed during the methanolysis reaction [79]. Drop size distributions in a reactive system are narrower and shift to smaller drop sizes along the reactor height. Also, they have higher peaks of drop size distributions at smaller drop sizes than non-reactive systems, where they are uniform in the whole reactor at vibration frequencies of 3 and 4 Hz and only in the upper part of the reactor at the vibration frequency of 2 Hz. The drop size distribution shape and peaks position are not affected by the methanol-to-oil molar ratio [73,77].

The effect of tetrahydrofuran (THF) as a co-solvent on biodiesel production by the continuous sunflower oil methanolysis catalysed by KOH was investigated in a continuous concurrent up-flow RPR [71]. THF effectively transforms non-reactive and reactive heterogeneous systems into stable homogeneous emulsions. For all co-solvent concentrations (up to 30 %) and both systems, the SMDD decreased along the reactor height in its lower part. In this zone, without the reaction between the phases, the initially large drops break up, passing through the plate perforations, while the occurrence of the reaction presents another factor in reducing the drop size. The SMDD remains constant in the upper part of the reactor, where a stable homogeneous dispersion of small drops is formed. Mainly, at any location in the reactor under the same operating conditions, the SMDD is smaller in the reactive than in the non-reactive system. The increase in the THF concentration reduces the SMDD due to the influence of THF on the drop breakage and the solubility of the reactants. The drop size distribution along the reactor is unimodal for both systems, *i.e.* with one peak located in the small drop size range for all the applied THF concentrations, and it became narrower along the reactor height. THF shifts the system into a homogeneous emulsion of small drops [71].

3. 1. 2. Mass-transfer characteristics in RPRs

The LVMTC and the interphase mass transfer rate of the reactant per unit volume of dispersion affect the efficiency of multiphase reactors, while the SIA is a significant parameter for achieving maximum reactor productivity.

The LVMTC, $k_l a$, increases with increasing vibration intensity as a result of greater power consumption and intensified reduction of gas bubbles [61,65-67,80-82], especially at higher vibration intensities [82]. The LVMTC increases to a maximum value as the gas flow rate increases due to higher energy transferred from the gas to the liquid. By adding Raschig rings (2.5 vol.%) in each interspace between the plates, the LVMTC increases by 30 % due to the effect of the solid phase on the bubble-breaking process [66]. The geometrical characteristics of an RPR affect the LVMTC. With an increase in the number of reciprocating plates under the same conditions of aeration and mixing, the LVMTC increases [68] due to more intensive energy dissipation, preventing bubble coalescence [65]. As the hole diameter and

free area of the plates increase, the VMTC decreases, probably due to the reduced power consumption [65,66]. The LVMTC in RPRs can be correlated with power consumption, *i.e.* vibration intensity, gas or liquid velocities, and geometric characteristics of the reactor [57].

The SIA depends on fluid-dynamic conditions in the multiphase reactor as well as on the properties of the phases. Variation of the SIA with the vibration intensity depends on the fluid flow regime in the reactor [70], so at low vibration intensities, either it increases due to the decrease in bubble size [66] or remains unchanged at constant bubble size and gas holdup [70,83]. At higher vibration intensities, SIA increases with increasing vibration intensity due to the increased gas holdup and reduced bubble size. The effect of gas velocity on the SIA depends on the flow regime. At low gas velocities, SIA increases with the increase in the vibration intensity due to the enhanced bubble break up. At higher gas velocities and larger amounts of gas in the column, gas bubbles increase in size and become densely packed, which favors their coalescence and increases the SIA due to the increased gas holdup [62,66,70,83]. Raschig rings (2.5 vol.%) placed in the interplate spaces increased the SIA by about 30 % [66], while the addition of spheres in the interplate spaces did not have any effect [57]. Geometric characteristics of the column, such as the hole diameter and the fractional free area of the plates, also affect the SIA. With their increase, the SIA decreases [66]. Correlations proposed in the literature for SIA estimation in RPRs include dependences on power consumption and gas velocity [57]. The SIA value in a 2.54 cm i.d. RPR filled with mixtures of methanol and sunflower oil (molar ratios 3:1 and 6:1) increased with increasing the methanol-to-oil molar ratio and vibration intensity, as a consequence of the influence of these parameters on the SMDD and the dispersed phase holdup.

3. 1. 3. Effects of operating conditions on FAME yields and reaction kinetics in RPRs

Stamenković et al. [77] examined the sunflower oil methanolysis with KOH as a catalyst (1 % of the oil weight) in a continuous reactor under atmospheric pressure. Optimal conditions for single-step (one reactor and one separator) and two-step (two reactor-separator in series) reactor systems were determined: vibration amplitude of 1 cm, vibration frequency of 2 Hz, temperature of 30 °C, and methanol-to-oil molar ratio of 6:1. Residence time in each reactor of both system was 13 minutes. The results obtained in the laboratory-scale experiments were successfully implemented in a semi-industrial plant for methanolysis of rapeseed oil achieving a 98 % biodiesel yield at the separator outlet. Overall, this investigation shed light on the optimal operating conditions for the sunflower oil methanolysis catalysed by KOH and demonstrated the scalability of the process for industrial application.

FAME concentrations at several THF concentrations were below 10 % in the initial part of the reactor because of the mass-transfer limitation [71]. At the reactor exit and low THF concentrations, the maximum FAME concentration reached about 80 % when the reaction approached the equilibrium. At the THF concentration of 30 % of the oil mass, the FAME concentration increased quickly along the reactor height due to negligible mass transfer limitations. In the upper reactor part, the FAME concentration achieved the maximum at the exit. The reaction also approached equilibrium, indicating that the reactor height could be lower. Thus, the overall biodiesel production process should be conducted in two RPRs in a series.

At lower THF concentrations (0, 1, and 10), FAME concentration varied in a sigmoid manner along the reactor height indicating different kinetic regimes along the reactor [71]. The overall triacylglycerol (TAG) reaction rate is controlled by the rate of mass transfer in the lower and by the chemical reaction in the upper part of the reactor, *i.e.* the lower region was TAG mass transfer controlled followed by the region controlled by the irreversible second-order reaction. At the highest THF concentration (30 %), the curve becomes exponential, indicating the reaction-controlled regime without mass transfer limitations, *i.e.* the irreversible and reversible second-order reaction kinetics can be used to describe the process in this case. By simulating the methanolysis process and comparing the developed kinetic models with the experiment, three equations were suggested for the TAG conversion degree calculation for the mass transfer-controlled regime, the reaction-controlled regime with the irreversible pseudo-second-order reaction, and the reaction-controlled regime with the reversible second-order reaction. The study of Banković-Ilić *et al.* [71] was the first attempt to investigate the kinetics of methanolysis of vegetable oils in the presence of a co-solvent in a continuous up-flow RPR

and presented a good basis for studying alcoholysis of cheap oily raw materials (non-edible oils, used cooking oils, waste animal fats, etc.) in the presence of homogeneous base catalysts.

Further research into this trend was performed by Miladinović *et al.* [84], who conducted biodiesel production from a waste pig-roasting lard using methanol as a reactant and KOH as a base catalyst at 60 °C in a continuous RPR (diameter: 2.54 cm, height: 200 cm, 63 plates). The influential process factors, such as the methanol-to-lard molar ratio (4.5:1 to 7.5:1), catalyst loading (0.5 to 1.0 %, based on the lard mass), and height of the reactor column (13 to 192 cm) were optimized with respect to the FAME content in the ester phase using the response surface methodology (RSM). The optimal methanol-to-lard molar ratio and catalyst amount at the reactor exit (corresponding to the retention time of 10 min) were 4.5:1 and 0.9 % of waste lard, respectively. Also, the transesterification reaction kinetics models that defined the variation of TAG and FAME concentrations along the height of the RPR were determined indicating two models, namely the irreversible pseudo-first-order reactions or the reactions involving a changing mechanism and TAG mass transfer.

3. 2. Biodiesel production in PBRs

Packed bed reactors (PBRs) play a crucial role in the methanolysis of vegetable oil, which involves a three-phase system of methanol, vegetable oil, and a solid catalyst. When considering the choice of the reactor type for this process, several factors should be taken into account and PBRs are preferred for several reasons. These reactors are relatively easy to design and construct, typically comprising a column filled with catalyst pellets or beads (Fig. 2). They are widely used due to the low operating costs and ease of operation, particularly in separating the final products from the catalyst. In a PBR, the reactants are continuously fed into the reactor while the product continuously flows out, leaving the catalyst behind. As a result, high-purity biodiesel and glycerol can be obtained as final products. When using solid catalysts with poor mechanical properties, PBRs are clearly advantageous over CSTRs in which aggressive agitation can lead to the catalyst destruction and leaching of active species, contaminating the final products.

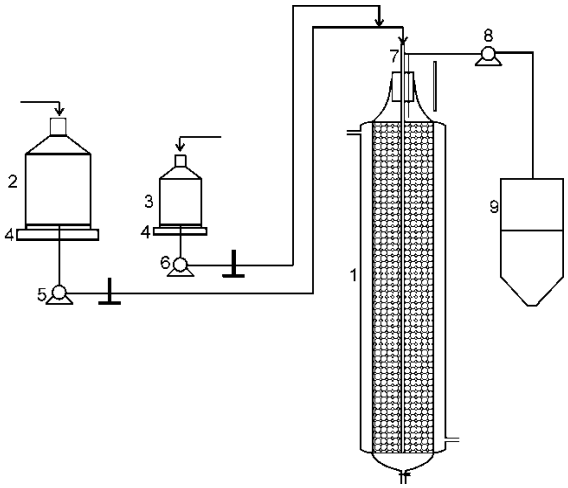

Figure 2. Experimental setup containing a PBR for laboratory-scale biodiesel production: 1 - PBR with catalyst particles, 2,3 - tanks for vegetable oil and alcohol, 4 - scales, 5,6 - pumps for transporting the reactants, 7 - glass tube for introducing and thermostating reactants, 8 - pump for transporting the reaction mixture from the reactor, and 9 - gravity separator

Different types of PBRs have been employed for oil methanolysis, including rotating PBRs, packed bed membrane reactors (PBMRs), TBRs, PBRs with a recycle, and MCRs. For example, a rotating PBR was used for the methanolysis of soybean oil [26] providing enhanced mixing and mass transfer by centrifugal acceleration and resulting in shorter reaction times, higher FAME yields, and greater production capacity. However, it should be noted that a rotating PBR is not recommended for oil methanolysis with solid catalysts with low mechanical strength, as centrifugal acceleration can cause catalyst leaching [27].

A PBMR was employed to obtain high-quality FAMEs [42] using the advantages of a dual-functionality membrane that acts as both a reactor and a separator, thereby increasing the reaction rate and yield. The small molecules of FAMEs,

methanol, and glycerol can permeate through the membrane pores, while the permeation of larger TAG molecules is prevented. Removal of the products through the membrane shifts the reaction equilibrium towards product formation. The selective permeation FAMEs and exclusion of unreacted TAGs and other impurities lead to high-quality FAMEs that do not require further purification. In one study, a ceramic membrane (TiO_2/Al_2O_3) packed with KOH supported on palm shell activated carbon was an efficient catalyst for transesterifying soybean oil with methanol in a PBMR [42]. PBMRs have also been investigated using shaped KF/Ca−Mg−Al hydrotalcite [85] and KF/Ca-Mg-Al hydrotalcite/honeycomb ceramic monolithic [86] catalysts.

Another type of three-phase reactor explored in oil methanolysis is TBR, in which gas and liquid phases flow concurrently or countercurrent through a packed bed of catalyst particles. Methanol is typically heated to its vapor temperature and used as a continuous upward gas phase, while oil and condensed methanol flow downwards by gravity through the catalyst bed. This arrangement enhances the contact area between methanol and oil, promoting the methanolysis reaction on the catalyst surfaces. Oil methanolysis has been investigated in conventional [13,14] or modified [14] TBRs. A 98 % biodiesel yield was achieved by countercurrent transesterification of sunflower oil with vaporized methanol above the boiling point and CaO particles in a packed bed [13]. Similarly, Meng *et al.* [14] obtained a 94.5 % biodiesel yield using a packed bed of base heterogeneous Ca/Al composite oxide catalyst to convert rapeseed oil and methanol at the boiling point and atmospheric pressure. Also, a countercurrent TBR with palm oil methanol vapor and a CaO-based extrudate catalyst produced a 92.3 % biodiesel yield [15].

PBRs with a recycle offer advantages regarding product stream division and improved mass transfer rates. Hernández-Montelongo *et al.* [87] conducted esterification of FFA in canola oil with methanol using cation exchange resins in a PBR with recycling to produce biodiesel. This configuration involved recycling the reaction mixture to the feed stream and approximating the PBR to a CSTR by ensuring a high volumetric ratio of the recycling flow to the reactor inflow. This setup facilitated a higher methanol concentration within the reactor that shifted the reaction equilibrium towards the products.

MCRs have also been investigated for heterogeneously catalysed methanolysis, offering enhanced biodiesel production through improved conversion, reduced reaction time, and improved biodiesel quality [21]. Chueluecha *et al.* [88] conducted palm oil methanolysis in a micro-channel reactor using CaO as a catalyst achieving a high FAME content of 99 % at the methanol-to-oil molar ratio of 24:1, a short retention time of 8.9 min, and 65 °C. Another study [17] explored iso-propanol as a co-solvent in micro-channel reactors. The addition of a co-solvent (14.5 %) reduced the methanol-to-oil molar ratio to 20:1 and the retention time to 6.5 min while maintaining the same high FAME content as in the previous study.

3. 2. 1. Flow regime and external mass transfer limitations in PBRs

Analysis of heterogeneously catalysed oil methanolysis in PBRs involves consideration of various phenomena, primarily focusing on mass transfer between phases and liquid phase flow. At a steady-state operation, catalytic PBRs typically exhibit ideal plug flow behaviour under specific conditions that have to be met [89]. These conditions include ensuring that the reactor diameter and the catalyst bed length are at least ten-fold and several hundred-fold higher than the catalyst particle diameter, respectively, for low flow rates. In addition to the reactor geometry and dimensions, operational conditions significantly influence the abovementioned phenomena. Parameters such as bed height, feed flow rate (reactants), residence time, molar ratio, and catalyst size and amount all have an impact [90].

Given that heterogeneously catalysed oil methanolysis in a PBR involves a liquid-liquid-solid system, it is essential to consider the possibility of external mass transfer limitations. Marinković *et al.* [91] conducted experimental investigations on a PBR using a methanol-to-oil molar ratio of 18:1 at 60 °C. They measured the FAME content at various heights within the catalyst bed and volumetric flow rates of the reaction mixture while maintaining a constant retention time of 4.2 h, corresponding to a weight hourly space velocity (WHSV) of 0.10 h^{-1}. By varying the volumetric flow rate from 0.05 to 0.16 $cm^3\ min^{-1}$, they achieved a constant FAME content (97.8 %) at the reactor outlet. This observation indicated that the external diffusion did not limit the rate of oil methanolysis. Miladinović *et al.* [92] ensured a constant ratio of catalyst mass to the liquid flow rate by increasing the catalyst mass proportionally with the liquid flow rate, thus

maintaining the same retention time for the reactants. They observed that the FAME content at the reactor outlet remained independent of the liquid flow rate within the range of 1.75 to 3.5 cm^3 min^{-1}, corresponding to retention times from 1.0 h to 2.0 h and different ratios of the liquid flow rate to catalyst mass (*i.e.* different WHSVs). Consequently, external liquid-solid mass transfer limitations could be neglected.

3. 2. 2. Effects of operating conditions on FAME yields and process optimization in PBRs

Residence time in a reactor is inversely proportional to the flow rate of reactants. According to the literature [93], reducing the flow rate of linseed oil resulted in an increased oil residence time and a higher FAME yield (methanol-to-oil molar ratio 7.5:1, co-solvent (diethyl ether)-to-methanol molar ratio 1.25:1, and 30 °C). Similarly, a prolonged residence time of waste cooking oil in the bed of agglomerated Zr-SBA-15 catalyst led to a higher FAME yield [94]. However, when increasing the feed flow rate from 0.6 to 1.2 cm^3 min^{-1}, there was an initial rise in the FAME content from 85.5 to 95.2 %, while a further increase from 1.2 to 1.7 cm^3 min^{-1} resulted in a decline in the FAME content from 95.2 to 70.5 % [95].

The relationship between the feed flow rate and the volume or mass of the catalyst bed can be described by the liquid hourly space velocity (LHSV) [96] and the WHSV [91,92]. In the study by Zarabudin *et al.* [96], the LHSV was varied from 6 to 30 h^{-1}, corresponding to residence times ranging from 1 to 4 min. The researchers concluded that the highest conversion rate (99.9 %) was achieved at an LHSV of 8 h^{-1}, corresponding to a residence time of 3 min. Miladinović *et al.* [92] observed that decreasing the WHSV led to increased FAME contents. The lowest WHSV (0.188 $kg/kg_{cat}h$) resulted in the longest retention time of 2 h and the highest conversion rate. It allowed for a longer contact time between the catalyst and the feed, enhancing the overall conversion process. Regarding the retention time in a PBR, Bausri *et al.* [97] noted a gradual increase in the FAME yield as the residence time increased from 0.5 to 2.5 h while maintaining a constant catalyst bed length and methanol-to-oil molar ratio. However, Sakthivel *et al.* [98] discovered that the FAME yield initially increased with an increasing retention time up to a specific value, beyond which it started to decline. This result could be attributed to a reverse reaction occurring at longer residence times. These findings highlight the importance of optimizing the residence time concerning the flow rate and catalyst bed characteristics to achieve the desired conversion and FAME yield.

The methanol-to-oil molar ratio is a critical factor influencing the FAME content in a PBR. Various studies have examined the effect of the methanol-to-oil molar ratio in the range from 3:1 to 60:1 [99]. An increased methanol-to-oil molar ratio generally leads to higher FAME contents or TAG conversion due to an increased driving force for methanol adsorption [27]. However, some studies have observed that this positive effect reaches a threshold value of the methanol-to-oil molar ratio, beyond which further increases result in a decrease in the FAME content [95,100]. This decline could be attributed to the generation of glycerol, which dissolves in methanol and inhibits further methanol adsorption on the catalyst active sites. Ren *et al.* [95] found that production of glycerol increased at higher methanol amounts. At methanol-to-oil molar ratios lower than 9:1, glycerol was not detected in the effluent, either due to its low solubility in the reaction system or because it was adsorbed on the catalyst (resin). In the case of resin as a catalyst, it was explained in literature [101] that a high methanol concentration had an inhibitory effect on the FAME production due to easier diffusion of lighter methanol molecules through the catalyst pores compared to heavier TAG molecules. Thus, a high methanol concentration hinders TAG adsorption on the catalyst active sites. Similarly, increasing the pre-added methanol amount up to a particular value positively influenced the ester content. However, the excess of methanol had the opposite effect by occupying the catalyst active sites [14]. Nonetheless, in another study [93] it was argued that a high amount of methanol could mask the effects of other parameters. On the other hand, other authors [99] suggested that a high methanol-to-oil molar ratio is necessary for an efficient transesterification in a PBR at a low flow rate of reactants, where the laminar flow regime limits the mass transfer between the liquid phases and to the solid catalyst. Moreover, a higher excess of methanol increases the polarity of the reaction mixture, which can cause the leaching and dissolution of glycerol and glyceride derivatives from the active sites on the CaO surface. This may explain why the impact of the methanol-to-oil molar ratio on the FAME content is more pronounced at longer retention times [100].

Continuous methanolysis in PBRs is performed at different temperatures and pressures depending on the reaction system (reactants-catalyst). For base catalysts, Miladinović *et al.* [100] observed a significant influence of the reaction temperature on the FAME content within a range of 40 to 60 °C at atmospheric pressure. Bausri *et al.* [102] demonstrated that exceeding 60 °C decreased the biodiesel yield. In the case of methanolysis of waste frying oil catalysed by KOH/fruit shell of *Jatropha curcas* in a PBR at atmospheric pressure, temperatures above 60 °C caused methanol evaporation, reducing the methanol-to-oil ratio and leading to a decline in TAG conversion. Studies employing acid catalysts, such as Zr-SBA-15/bentonite, investigated a higher temperature range (150-210 °C) and pressure (7 MPa) [94]. In a PBR system utilizing resins as catalysts for the interesterification of palm oil and ethyl acetate, Akkarawatkhoosith *et al.* [103] found that temperatures in a range of 80-120 °C affected not only the fatty acid ethyl esters (FAEE) content but also the reaction rate.

Optimization of reaction conditions in PBRs typically involves considering the above-mentioned parameters, that is, the residence time, catalyst bed height, feed flow rate, reaction temperature, and methanol-to-oil molar ratio. These parameters and their interactions on the FAME content/yield are evaluated statistically and optimized using factorial designs. The significance of these parameters varies depending on the reaction system, including the type of oil feedstock, alcohol, and catalyst. For instance, Díaz *et al.* [104] used a Box-Behnken design to evaluate the effects of flow rate, methanol-to-oil molar ratio, and co-solvent/methanol-to-oil molar ratio on the FAME yield when Li/Pumice was used as a catalyst. They found that the methanol-to-oil molar ratio had the most significant effect on the FAME content, while the effects of the other analysed parameters were not significant. Similarly, for the CaO-catalyzed linseed oil methanolysis with diethyl ether as a co-solvent carried out in a PBR, the flow rate and co-solvent-to-methanol molar ratio had the most significant effect on the FAME content [93]. Miladinović *et al.* [92] used a full factorial design (3^3) to evaluate the effect of methanol-to-oil molar ratio, WHSV, and the catalyst bed height on the FAME content. All three factors and their interactions had a significant effect, with the catalyst bed height showing the strongest influence due to its relationship with the retention time. Optimal values were determined as 40 cm the catalyst bed height, 0.188 kg/(kg_{cat} h) WHSV, and 6 : 1methanol-to-oil molar ratio. Sakthivel *et al.* [98] reported that residence time, reaction temperature, and molar flow rate significantly affected the biodiesel yield from *Jatropha curcas* oil. The significance of packed bed height, ethanol-to-oil molar ratio, and volumetric flow rate on the FAEE yield from palm oil catalyzed by radiation-induced Kenaf as a catalyst was also evaluated [105], with optimal values determined as 9.8 cm for the packed bed height, 50:1 for the ethanol-to-oil molar ratio, and 0.38 cm^3 min^{-1} for the volumetric flow rate. In the palm oil methanolysis catalysed by potash/orange peel in a PBR [106] the reaction temperature was found to have a higher significance with respect to the FAME yield than the catalyst amount and the methanol-to-oil molar ratio. RSM optimization proposed an optimum temperature of 60 °C, catalyst loading of 2.5 %, and a methanol-to-oil molar ratio of 12:1, resulting in a 95.6 % biodiesel yield. Conversely, Talha and Sulaiman [107] found that the reaction temperature had an insignificant effect on the FAME yield in the in-situ transesterification of solid coconut waste in a PBR with the CaO/PVA catalyst. The highest biodiesel yield of 95 *%* was achieved with the catalyst loading of ~2.3 % and a methanol-to-solid ratio of 12:1 at 61 °C. Similarly, Zik *et al.* [108] optimized the catalyst loading, temperature, and methanol-to-oil molar ratio for producing biodiesel from used cooking oil over a CaO/nanocrystal cellulose/polyvinyl alcohol catalyst in a PBR. The optimum conditions were determined as 65 °C, 6:1 methanol-to-oil molar ratio, and 0.5 *%* catalyst amount, resulting in a 98.4 % biodiesel yield.

3. 3. Comparison of RPRs and PBRs for biodiesel production

The choice between the RPRs and PBRs for biodiesel production depends on the process conditions, reaction kinetics, feedstock and catalyst characteristics, scalability, and economic considerations. Each reactor type has unique advantages, and the optimal choice can be determined by evaluating these factors in the context of the biodiesel production process. Compared to PBRs, RPRs offer superior mixing efficiency, improved heat and mass transfers, better catalyst utilization, handling different feedstock, including oils of various viscosities, better reaction control, and simple scalability, making them suitable for both small- and large-scale biodiesel production. On the other hand, PBRs require less energy for mixing, promote higher conversion rates, increase biodiesel yield due to providing sufficient reaction times for complete

conversion of the reactants, better stability for solid catalyst particles, convenience for homogeneous feedstock, and often have a smaller footprint than RPRs, making them more suitable for space-constrained environments. Both reactor types can be scaled up for large-scale production, although RPRs have a slight advantage in terms of scalability due to their design. Also, economic considerations (capital and operating costs, maintenance requirements) should be carefully evaluated to determine the appropriate option between the two offered.

To gain a comprehensive assessment and better understanding of the potential of RPRs and PBRs as innovative technologies in the biodiesel production industry, it is crucial to conduct a thorough examination of these reactors using a SWOT analysis (Strengths, Weaknesses, Opportunities, and Threats). It is a practical tool for identifying and assessing the internal and external factors that can impact the successful deployment of either reactor type. Understanding the strengths of these reactor technologies allows for leveraging their unique advantages. Similarly, identifying weaknesses helps in addressing potential challenges and finding strategies to alleviate them. Furthermore, recognizing the opportunities offered by each reactor type enables stakeholders to explore new possibilities for enhancing biodiesel production. Concurrently, identifying potential threats helps to proactively manage risks and ensure the long-term viability of the chosen reactor technology in the industry. As presented in Tables 3 and 4, this analysis provides valuable insights into the advantages and disadvantages of each of the 2 discussed reactor types. By carefully evaluating these factors, stakeholders in the biodiesel production industry can make informed decisions regarding the implementation of these technologies.

Table 3. SWOT analysis of RPRs for biodiesel production

STRENGTHS	**WEAKNESSES**
Efficient mixing	Complex design and operation
Scalability	Susceptible to fouling and plugging
Catalyst utilization	
Heat transfer	
OPPORTUNITIES	**THREATS**
Advancements in materials and manufacturing	Competition from alternative reactor systems
Research and development	Availability and cost of catalysts

Table 4. SWOT analysis of PBRs for biodiesel production

STRENGTHS	**WEAKNESSES**
High catalyst loading	Limited mixing
Longer residence time	Potential pressure drop
Catalyst stability	Potential catalyst fouling
Compact design	Mass transfer limitations
Cost-effectiveness	Process control
Versatility	
OPPORTUNITIES	**THREATS**
Advanced in materials and catalyst	Competing reactor technologies
Process optimization	Feedstock variability
	Evolving regulatory environment

4. CONCLUSIONS

Despite the significant advantages of continuous reactors, their implementation in biodiesel production still poses specific challenges. Reactor design, catalyst selection, reaction conditions, and process optimization are key factors that must be carefully considered to ensure efficient and reliable operation. Furthermore, the scale-up of continuous reactor systems from laboratory to industrial scale requires a comprehensive understanding and optimization of various parameters. Continuous reactors have immense potential for revolutionizing biodiesel production, offering improved

productivity, product quality, and process efficiency. With further research and development, continuous reactor systems can pave the way for a more sustainable and environmentally friendly energy future.

Both reciprocating plate reactors and packed bed reactors show promise for biodiesel production. Their continuous flow operation, improved mass or heat transfer properties, and potential for efficient control over reaction conditions make them attractive options for enhancing the efficiency and scalability of biodiesel manufacturing processes. However, the specific implementation and adoption of these reactor types will depend on various factors, including cost considerations, process optimization, and further research and development.

Acknowledgments: *This work was supported by the Serbian Academy of Sciences and Arts (SASA, Project F-78), the SASA Branch in Niš (Project 0-14-18), and the Republic of Serbia - Ministry of Science, Technological Development, and Innovation, Programs for Financing Scientific Research Work (Project No. 451-03-47/2023-01/200133 assigned to the Faculty of Technology, Leskovac, University of Niš, Research group III 45001).*

REFERENCES

[1] Živković SB, Veljković MV, Banković-Ilić IB, Krstić IM, KonstantinovićSS, Ilić SB, Avramović JA, Stamenković OS, Veljković VB. Technological, technical, economic, environmental, social, human health risk, toxicological and policy considerations of biodiesel production and use. *Renew Sust Energ Rev*. 2017; 79: 222-247. https://doi.org/10.1016/j.rser.2017.05.048

[2] Awogbemi O, Von Kallon DV, Application of tubular reactor technologies for the acceleration of biodiesel production. *Bioengineering*. 2022;9(8): 347. https://doi.org/10.3390/bioengineering9080347

[3] Fonseca FAS, Vidal-Vieira JA, Ravagnani SP. Transesterification of vegetable oils: Simulating the replacement of batch reactors with continuous reactors. *Bioresour Technol.* 2010; 101(21): 8151-8157. https://.doi.org/10.1016/j.biortech.2010.05.077

[4] Gopi R, Thangarasu V, Vinayakaselvi MA, Ramanathan A. A critical review of recent advancements in continuous flow reactors and prominent integrated microreactors for biodiesel production. *Renew Sust Energ Rev*. 2022; 154: 111869.https://doi.org/10.1016/j.rser.2021.111869

[5] Tabatabaei M, Aghbashlo M, Dehhaghi M, Panahi HKS, Mollahosseini A, Hosseini M, Soufiyan MM. Reactor technologies for biodiesel production and processing: A review. *Prog Energy Combust Sci.* 2019; 74: 239-303. https://doi.org/10.1016/j.pecs.2019.06.001

[6] Mohiddin MNB, Tan YH, Seow YX, Kansedo J, Mubarak NM, Abdullah MO, Chan YS, Khalid M, Evaluation on feedstock, technologies, catalyst and reactor for sustainable biodiesel production: A review. *J Ind Eng Chem.* 2021; 98: 60-81. https://doi.org/10.1016/j.jiec.2021.03.036

[7] Ghazi ATIM, Resul MFMG, Yunus R, Yaw TCS. Preliminary design of oscillatory flow biodiesel reactor for continuous biodiesel production from Jatropha triglycerides. *J Eng Sci Technol.* 2008; 2(3): 138-145.

[8] García Martín JF, Barrios CC, Alés Álvarez F-J, Dominguez Sáez A, Alvarez Mateos P. Biodiesel production from waste cooking oil in an oscillatory flow reactor. Performance as a fuel on a TDI diesel engine. *Renew Energy.* 2018; 125: 546-56. https://doi.org/10.1016/j.renene.2018.03.002

[9] Highina BK, Bugaje IM, Ngala GM. Performance evaluation of continuous oscillatory baffled reactor arrangementon production of biodiesel from Jatropha oil using heterogeneous catalyst. *World J Renew Energ Eng*. 2014; 1: 1-7. http://www.scenrp.com/World%20Journal%20of%20Renewable%20Energy%20&%20Engineering/Current%20Issue.php

[10] Kefas HM, Yunus R, Rashid U, Taufiq-Yap YH. Enhanced biodiesel synthesis from palm fatty acid distillate and modified sulfonated glucose catalyst via an oscillation flow reactor system. *J Environ Chem Eng.* 2019; 7: 102993. https://doi.org/10.1016/j.jece.2019.102993

[11] Niyas MM, Shaija A. Biodiesel production from coconut waste cooking oil using novel solar powered rotating flask oscillatory flow reactor and its utilization in diesel engine. *Therm Sci Eng Prog*. 2023; 40: 101794. https://doi.org/10.1016/j.tsep.2023.101794

[12] Zheng M, Skelton RL, Mackley MR. Biodiesel reaction screening using oscillatory flow meso reactors. *Process Saf Environ Prot*. 2007; 85(5): 365-371.https://doi.org/10.1205/psep07030

[13] Son SM, Kusakabe K. Transesterification of sunflower oil in a counter-current trickle-bed reactor packed with a CaO catalyst. *Chem Eng Process.* 2011; 50: 650-654. https://doi.org/10.1016/j.cep.2011.04.001

[14] Meng YL, Tian SJ, Li SF, Wang BY, Zhang MH. Transesterification of rapeseed oil for biodiesel production in trickle-bed reactors packed with heterogeneous Ca/Al composite oxide-based alkaline catalyst. *Bioresour Technol.* 2013; 136: 730-734. https://doi.org/10.1016/j.biortech.2013.03.081

[15] Jindapon W, Ruengyoo S, Kuchonthara P, Ngamcharussrivichai C, Vitidsant T. Continuous production of fatty acid methyl esters and high-purity glycerol over a dolomite-derived extrudate catalyst in a countercurrent-flow trickle-bed reactor. *Renew Energ*. 2020; 157: 626-636. https://doi.org/10.1016/j.renene.2020.05.066

[16] Chen G, Liu J, Yao J, Qi Y, Yan B. Biodiesel production from waste cooking oil in a magnetically fluidized bed reactor using whole-cell biocatalysts. *Energy Conv Manag*. 2017; 138: 556-564. https://doi.org/10.1016/j.enconman.2017.02.036

[17] Chueluecha N, Kaewchada A, Jaree A. Biodiesel synthesis using heterogeneous catalyst in a packed-microchannel. *Energy Conv Manage.* 2017; 141: 145-154. https://doi.org/10.1016/j.enconman.2016.07.020

[18] Santana HS, Tortola DS, Silva JL Jr, Taranto OP. Biodiesel synthesis in micromixer with static elements. *Energy Conv Manag.* 2017; 141: 28-39. https://doi.org/10.1016/j.enconman.2016.03.089

[19] Sun P, Sun J, Yao J, Zhang L, Xu N. Continuous production of biodiesel from high acid value oils in microstructured reactor by acid-catalyzed reactions. *Chem Eng J.* 2010; 162: 364-370. https://doi.org/10.1016/j.cej.2010.04.064

[20] Yamsub A, Kaewchada A, Jaree A. Pork lard conversion to biodiesel using a microchannel reactor. *Korean J Chem Eng.* 2014; 31:2170-2176. https://doi.org/10.1007/s11814-014-0120-5

[21] Natarajan Y, Nabera A, Salike S, Tamilkkuricil VD, Pandian S, Karuppan M, Appusamy A. An overview on the process intensification of microchannel reactors for biodiesel production. *Chem Eng Process: Process Intensif*. 2019; 136: 163-176. https://doi.org/10.1016/j.cep.2018.12.008

[22] Darnoko D, Cheryan M. Continuous production of palm methyl esters. *J Am Oil Chem Soc*. 2000; 77: 1269-1272. https://doi.org/10.1007/s11746-000-0199-x

[23] Kouzu M, Fujimori A, Fukakusa R, Satomi N, Yahagi S. Continuous production of biodiesel by the CaO-catalyzed transesterification operated with continuously stirred tank reactor. *Fuel Process Technol*. 2018; 181: 311-317. https://doi.org/10.1016/j.fuproc.2018.10.008

[24] Sun Y, Zhang J, Sun Z, Zhang L. Biodiesel production using calcium-based catalyst from venus shell: Modeling of startup production in an industrial reactor. *Environ Prog Sustain Energy.* 2019; 38(3): 1-9. https://doi.org/10.1002/ep.13053

[25] Lodha H, Jachuck R, Suppiah Singaram S. Intensified biodiesel production using a rotating tube reactor. *Energ Fuel.* 2012; 26: 7037-7040. https://doi.org/10.1021/ef301235t

[26] Chen YH, Huang YH, Lin RH, Shang NC. A continuous-flow biodiesel production process using a rotating packed bed. *Bioresour Technol.* 2010; 101: 668-673. https://doi.org/10.1016/j.biortech.2009.08.081

[27] Chen YH, Huang YH, Lin RH, Shang NC, Chang CY, Chang CC, Chang CC, Chiang PC, Hu CY. Biodiesel production in a rotating packed bed using K/γ-Al_2O_3 solid catalyst. *J Taiwan Inst Chem Eng.* 2011; 42(6): 937-944. https://doi.org/10.1016/j.jtice.2011.05.007

[28] Qiu Z, Zhao L, Weatherley L. Process intensification technologies in continuous biodiesel production. *Chem Eng Process.* 2010; 49: 323-330. https://doi.org/10.1016/j.cep.2010.03.005

[29] Chen KJ, Chen YS. Intensified production of biodiesel using a spinning disk reactor. *Chem Eng Process.* 2014; 78: 67-72. https://doi.org/10.1016/j.cep.2014.02.009

[30] Scares L, Franca A, Oliveira L. Feasibility of biodiesel production in a continuous flow microwave reactor with static mixing. In: *8th international conference on mechanical and aerospace engineering (ICMAE)*. Prague, Czech Republic: IEEE, 2017. pp. 581-585.

[31] Thirugnanasambandham K, Sivakumar V. Investigation on biodiesel production from cotton seed oil using microwave irradiated transesterfication process. *Environ Prog Sustain Energy.* 2015; 34: 1229-1235. https://doi.org/10.1002/ep.12094

[32] Ma G, Hu W, Pei W, Jiang L, Song M, Mu R. *In situ* heterogeneous transesterification of microalgae using combined ultrasound and microwave irradiation. *Energy Conv Manag.* 2015; 90: 41-46. https://doi.org/10.1016/j.enconman.2014.10.061

[33] Avramović JM, Stamenković OS, Todorović ZB, Lazić ML, Veljković VB. Empirical modeling of ultrasound-assisted base-catalyzed sunflower oil methanolysis kinetics. CI&CEQ. 2012; 18(1): 115-127.https://doi.org/10.2298/CICEQ110705053A

[34] Avramović JM, Radosavljević DB, Veličković AV, Stojković IJ, Stamenković OS, Veljković VB. Statistical modeling and optimization of ultrasound-assisted biodiesel production using various experimental designs. *Zaštita Materijala*. 2019; 60(1): 70-80. https://doi.org/10.5937/zasmat1901070A

[35] Gogate PR, Sutkar VS, Pandit AB. Sonochemical reactors: important design and scale up considerations with a special emphasis on heterogeneous systems. *Chem Eng J.* 2011; 166(3): 1066-1082. https://doi.org/10.1016/j.cej.2010.11.069

[36] Thanh LT, Okitsu K, Sadanaga Y, Takenaka N, Maeda Y, Bandow H. A two-step continuous ultrasound assisted production of biodiesel fuel from waste cooking oils: a practical and economical approach to produce high quality biodiesel fuel. *Bioresour Technol*. 2010; 101: 5394-5401. https://doi.org/10.1016/j.biortech.2010.02.060

[37] Veljković VB, Avramović JM, Stamenkovi OS. Biodiesel production by ultrasound-assisted transesterification: State of the art and the perspectives. *Renew Sust Energ Rev*. 2012; 16: 1193-1209. https://doi.org/10.1016/j.rser.2011.11.022

[38] Pal A, Verma A, Kachhwaha S, Maji S. Biodiesel production through hydrodynamic cavitation and performance testing. *Renew Energy.* 2010; 35(3): 619-624. https://doi.org/10.1016/j.renene.2009.08.027

[39] Gole VL, Naveen K, Gogate PR. Hydrodynamic cavitation as an efficient approach for intensification of synthesis of methyl esters from sustainable feedstock. *Chem Eng Process.* 2013; 71: 70-76. https://doi.org/10.1016/j.cep.2012.10.006

[40] Javadikia H, Nosrati Y, Mostafaei M, Naderloo L, Tabatabaei M. Optimization of hydrodynamic cavitations reactor efficiency for biodiesel production by response surface methods (Case study: sunflower oil). *J Agric Mach.* 2017; 7: 260-269.https://doi.org/10.22067/jam.v7i1.51920

[41] https://www.hydrodynamics.com/cavitation-technology/ (Accessed April 10, 2023.)
[42] Baroutian S, Aroua MK, Raman AAA, Sulaiman NM. A packed bed membrane reactor for production of biodiesel using activated carbon supported catalyst. *Bioresour Technol.* 2011; 102(2): 1095-1102. https://doi.org/10.1016/j.biortech.2010.08.076
[43] Cao P, Dubé MA, Tremblay AY. High-purity fatty acid methyl ester production from canola, soybean, palm, and yellow grease lipids by means of a membrane reactor. *Biomass Bioenergy.* 2008; 32(11): 1028-1036. https://doi.org/10.1016/j.biombioe.2008.01.020
[44] Hou R, Zhang D, Duan X, Wang X, Wang S, Sun Z. Fabrication of $H_3PW_{12}O_{40}$/agarose membrane for catalytic production of biodiesel through esterification and transesterification. *RSC Adv.* 2016; 6: 81794-81801. https://doi.org/10.1039/C6RA17118D
[45] Luo Q, He B, Liang M, Kong A, Li J. Continuous transesterification to produce biodiesel under HTCC/Na_2SiO_3/NWF composite catalytic membrane in flow-through membrane reactor. *Fuel.* 2017; 197: 51-57. https://doi.org/10.1016/j.fuel.2016.12.089
[46] Petchsoongsakul N, Ngaosuwan K, Kiatkittipong W, Aiouache F, Assabum-rungrat S. Process design of biodiesel production: hybridization of ester- and transesterification in a single reactive distillation. *Energy Conv Manag.* 2017; 153: 493-503. https://doi.org/10.1016/j.enconman.2017.10.013
[47] Noshadi I, Amin N, Parnas RS. Continuous production of biodiesel from waste cooking oil in a reactive distillation column catalyzed by solid heteropolyacid: Optimization using response surface methodology (RSM). *Fuel.* 2012; 94: 156-64. https://doi.org/10.1016/j.fuel.2011.10.018
[48] Abduh MY, Van Ulden W, Kalpoe V, Van De Bovenkamp HH, Manurung R, Heeres HJ. Biodiesel synthesis from *Jatropha curcas* L. oil and ethanol in a continuous centrifugal contactor separator. *Eur J Lipid Sci Technol.* 2013; 115: 123-131. https://doi.org/10.1002/ejlt.201200173
[49] Carlucci C. An overview on the production of biodiesel enabled by continuous flow methodologies. *Catalysts,*2022;12: 717. https://doi.org/10.3390/catal12070717
[50] Tran DT, Chang JS, Lee DJ. Recent insights into continuous-flow biodiesel production via catalytic and non-catalytic transesterification processes. *Appl Energy.*2017;185: 376-409. https://doi.org/10.1016/j.apenergy.2016.11.006
[51] Lo TC, Prochazka J. Reciprocating plate extraction columns, in Handbook of solvent extraction (Lo TC, Baird MHI, Hanson C. eds.); New York, NY: John Wiley & Sons; 1983. pp. 373-389. ISBN 0-471-04164-5.
[52] Nikolić LB, Veljković VB, Skala DU. Axial dispersion of the liquid flow in a Karr reciprocating plate column. *Hem Ind.* 2001; 55: 249-254. https://doi/10.2298/JSC0407581N
[53] Aleksić M, Veljković VB, Banković-Ilić IB, Lazić ML, Skala DU. Uticaj Rašigovih prstenova i reoloških osobina tečnosti na promenu pritiska na dnu kolone sa vibracionom mešalicom. *Hem Ind.* 2002; 56:409-414. https://doi.org/10.2298/HEMIND0210409A (in Serbian).
[54] Aleksić M, Veljković VB, Banković-Ilić IB, Lazić ML, Skala DU. Uticaj Rašigovih prstenova i reoloških osobina tečnosti na promenu pritiska na dnu kolone sa vibracionom mešalicom. *Hem Ind.* 2003; 57: 107-113. https://doi.org/10.2298/HEMIND0210409A (in Serbian).
[55] Banković-Ilić I, Veljković V, Skala D. Gas holdup in a three phase reactors of the bubble column type. *Hem Ind*. 1994; 48: 397-402.
[56] Banković-Ilić IB, Veljković VB, Lazić ML, Skala DU. Power consumption and gas holdup in a gas-liquid reciprocating plate column. Chem Eng Comm. 1995; 134: 17-32. https://doi.org/10.1080/00986449508936320.
[57] Banković-Ilić I, Veljković V, Skala D. Hidrodinamičke i masenoprenosne karakteristike kolone sa vibracionom mešalicom za sisteme gas-tečnost i gas-tečnost-čvrsta faza - monografija. Leskovac: Tehnološki fakultet; 2009. ISBN 978-86-82367-80-2 (in Serbian)
[58] Hafez M, Baird MHI. Power consumption in a reciprocating plate column. *Trans Inst Chem Eng*. 1978; 56: 229-238.
[59] Naseva OS, Stamenković IS, Banković-Ilić IB, Lazić ML, Veljković VB, Skala DU. Sadržaj gasa u bioreaktoru sa vibracionom mešalicom - tečna faza je njutnovski fluid. *Hem Ind*. 2002; 56: 198-203. https://doi.org/10.2298/HEMIND0205198N (in Serbian)
[60] Skala DU, Veljković VB, Janjić VV, Lazić M, Banković-Ilić IB. Gas holdup in a gas-liquid-solid reciprocating plate column. *Can J Chem Eng*. 1993; 71: 817-820. https://doi.org/10.1002/cjce.5450710521
[61] Vasić Lj, Banković-Ilić IB, Lazić ML, Veljković VB, Skala DU. Sadržaj gasa u koloni sa vibracionom mešalicom prečnika 16,6 cm. *Hem Ind*. 2005; 59: 263-266. https://doi.org/10.2298/HEMIND0510263V
[62] Veljković V, Skala D. Hydrodynamic investigation of gas-liquid contacting in a reciprocating plate column. *Can J Chem Eng*. 1986; 64: 906-914. https://doi.org/10.1002/cjce.5450640604
[63] Banković-Ilić IB, Veljković VB, Lazić ML, Skala DU. Mass transfer in a multiphase vibration column. I The volumetric mass transfer coefficient. *Hem Ind*. 2001; 55(9): 376-382
[64] Banković-Ilić IB, Veljković VB, Lazić ML, Skala DU. Mass transfer in a multiphase vibration column. II. Interfacial area. *Hem Ind*. 2001; 55(9): 383-388
[65] Lounes M, Thibault J. Mass transfer in a reciprocating plate bioreactor. *Chem Eng Commun*. 1994; 127: 169-189. https://doi.org/10.1080/00986449408936231.

[66] Sundaresan A, Varma YBG. Interfacial area and mass transfer in gas-liquid cocurrent upflow and countercurrent flow in reciprocating plate column. *Can J Chem Eng*. 1990; 68: 951-958. https://doi.org/10.1002/cjce.5450680610

[67] Rama Rao NV, Baird MHII. Gas-liquid mass transfer in a 15 cm diameter reciprocating plate column. *J Chem Technol Biotech*. 2003;78: 134-137. https://doi.org/10.1002/jctb.704

[68] Skala D, Veljković V. Mass transfer characteristics in a gas-liquid reciprocating plate column. I. Liquid phase volumetric mass transfer coefficient. *Can J Chem Eng*. 1988; 66: 192-199. https://doi.org/10.1002/cjce.5450660203

[69] Vasić Lj, Banković-Ilić IB, Lazić ML, Veljković VB, Skala DU. Oxygen mass transfer in a 16.6 i.d. multiphase reciprocating plate column. *J Serb Chem Soc*. 2007; 72: 523-531. https://doi.org/10.2298/JSC0705523V

[70] Veljković V, Skala D. Mass transfer characteristics in a gas-liquid reciprocating plate column. II. Interfacial area. *Can J Chem Eng*. 1988; 66: 200-210. https://doi.org/10.1002/cjce.5450660203

[71] Banković-Ilić IB, Todorović ZB, Avramović JM, Veličković AV, Veljković VB. The effect of tetrahydrofuran on the base-catalyzed sunflower oil methanolysis in a continuous reciprocating plate reactor. *Fuel Process Technol*. 2015; 137: 339-350. http://dx.doi.org/10.1016/j.fuproc.2015.03.023

[72] Stamenković I, Stamenković O, Todorović Z, Banković -Ilić I, Lazić M, Veljković V, *et al.* The production of fatty acid methyl esters by a continuous base catalyzed methanolysis of sunflower oil. In: *The Proceedings of the 1st Conference of the Sustainable Development And Climate Changes*. Niš, Serbia, 2008. p. 251-255.

[73] Stamenković IS, Banković-Ilić IB, Jovanić PB, Veljković VB, Skala D. Hydrodynamics of a cocurrent upflow liquid-liquid reciprocating plate reactor for homogeneously base-catalyzed methanolysis of vegetable oils. *Fuel* 2010; 89: 3971-3984. http://www.doi:10.1016/j.fuel.2010.06.026

[74] Stamenković I, Stamenković O, Banković-Ilić I, Todorović Z, Lazić M, Veljković V, Skala D. Production of fatty acid esters by continuous alcoholysis of vegetable oils. Serbian patent RS 52398 B, 2013 (in Serbian)

[75] Hafez M, Prochazka J. The dynamic effects in a vibrating plate and pulsed extractors I. Theory and experimental technique. *Chem Eng Sci*. 1974; 29: 1745-1753. https://doi.org/10.1016/0009-2509(74)87033-8

[76] Jealous AC, Johnson HF. Power requirements for pulse generation in pulse column. *Ind Eng Chem*. 1955; 47: 1159-1166. https://doi.org/10.1021/ie50546a021

[77] Stamenković I. Kontinualna homogena bazno katalizovana alkoholiza biljnih ulja u reaktoru sa vibracionom mešalicom. Doktorska disertacija, Univerzitet u Nišu, Tehnološki fakultet, Leskovac; 2014 (in Serbian).

[78] Rama Rao NV, Srinivas NS, Varma YBG. Dispersed phase holdup and drop size distributions in reciprocating plate columns. *Can J Chem Eng*. 1983; 61: 168-177. https://doi.org/10.1002/cjce.5450610204

[79] Stamenković OS, Lazić ML, Todorović ZB, Veljković VB, Skala DU. The effect of agitation intensity on alkali-catalyzed methanolysis of sunflower oil. *Bioresour Technol*. 2007; 98: 2688-2699. https://doi.org/10.1016/j.biortech.2006.09.024

[80] Banković-Ilić IB, Veljković VB, Lazić ML, Skala DU. Mass transfer in a multiphase vibration column. I. The volumetric mass transfer coefficient. *Hem. Ind*. 2001; 55: 376-382

[81] Baird MHI, Rama Rao NV. Characteristics of a countercurrent reciprocating plate bubble column. II Axial mixing and mass transfer. *Can J Chem Eng*. 1988; 66: 222-231. https://doi.org/10.1002/cjce.5450660206

[82] Sundaresan A, Varma YBG. Yang NS, Shen ZQ, Chen BH, McMillan AF. Axial mixing and mass transfer in gas-liquid Karr columns. *Ind Eng Chem Proc Des Dev*. 1986; 25: 776-780. https://doi.org/10.1021/i200034a031

[83] Yang NS, Shen ZQ, Chen BH, Mc Millan AF. Pressure drop, gas holdup and interfacial area for gas-liquid contact in Karr-columns. *Ind Eng Chem Pro. Des Dev*. 1986; 25**:** 660-664. https://doi.org/10.1021/i200034a011

[84] Miladinović MR, Stojković IJ, Veličković AV, Stamenković OS, Banković-Ilić IB, Veljković VB. Optimization and kinetic modeling of waste lard methanolysis in a continuous reciprocating plate reactor. *Chin J Chem Eng*. 2019; 27: 2481-2490. https://doi.org/10.1016/j.cjche.2019.02.019

[85] Xu W, Gao L, Wang S, Xiao G. Biodiesel production from soybean oil in a membrane reactor over hydrotalcite based catalyst: An optimization study. *Energ Fuels*. 2013; 27:6738-6742. https://doi.org/10.1021/ef401823z

[86] Xu W, Gao L, Xiao G. Biodiesel production optimization using monolithic catalyst in a fixed-bed membrane reactor. *Fuel*. 2015; 159: 484-490. https://doi.org/10.1016/j.fuel.2015.07.017

[87] Hernández-Montelongo R, García-Sandoval JP, Dochain D, Gonz A. Biodiesel production in a continuous packed bed reactor with recycle: A modeling approach for an esterification system. *Renew Energy*. 2018; 116: 857-865. https://doi.org/10.1016/j.renene.2017.09.030

[88] Chueluecha N, Kaewchada A, Jaree A. Enhancement of biodiesel synthesis using co-solvent in a packed-microchannel. *J Ind Eng Chem*. 2017; 51: 162-171. https://doi.org/10.1016/j.jiec.2017.02.028

[89] Perego C, Peratello S. Experimental methods in catalytic kinetics. *Catal Today*. 1999; 52: 133-145.

[90] Zahan KA, Kano M. Technological progress in biodiesel production: An Overview on different types of reactors. *Energy Procedia*. 2019; 156: 452-457. (https://doi.org/10.1016/j.egypro.2018.11.086

[91] Marinković DM, Miladinović MR, Avramović JM, Krstić IB, Stanković MV, Stamenković OS, Jovanović DM, Veljković VB. Kinetic modeling and optimization of sunflower oil methanolysis catalyzed by spherically-shaped CaO/γ -Al_2O_3 catalyst. *Energy Conv Manag*. 2018; 163: 122-133. https://doi.org/10.1016/j.enconman.2018.02.048

[92] Miladinović MR, Stamenković OS, Veljković VB, Skala DU. Continuous sunflower oil methanolysis over quicklime in a packed-bed tubular reactor. *Fuel*. 2015; 154: 301-307. https://doi.org/10.1016/j.fuel.2015.03.057

[93] Hashemzadeh Gargari M, Sadrameli SM. Investigating continuous biodiesel production from linseed oil in the presence of a Co-solvent and a heterogeneous based catalyst in a packed bed reactor. *Energy*. 2018; 148: 888e895. https://doi.org/10.1016/j.energy.2018.01.105

[94] Melero JA, Bautista LF, Iglesias J, Morales G, Sánchez-vazquez R. Production of biodiesel from waste cooking oil in a continuous packed bed reactor with an agglomerated Zr-SBA-15/bentonite catalyst. *Applied Catal B. Environ*. 2014; 145: 197-204. https://doi.org/10.1016/j.apcatb.2013.02.050

[95] Ren Y, He B, Yan F, Wang H, Cheng Y, Lin L, Feng Y, Li J. Continuous biodiesel production in a fixed bed reactor packed with anion-exchange resin as heterogeneous catalyst. *Bioresour Technol*. 2012; 113: 19-22. https://doi.org/10.1016/j.biortech.2011.10.103

[96] Zabaruddin NH, Mohamed NH, Abdullah LC, Tamada M, Ueki Y, Seko N, Choong TSY. Palm oil-based biodiesel synthesis by radiation-induced kenaf catalyst packed in a continuous flow system. *Ind Crops Prod*. 2019; 136: 102-109. https://doi.org/10.1016/j.indcrop.2019.04.069

[97] Buasri A, Loryuenyong V. Continuous production of biodiesel from rubber seed oil using a packed bed reactor with $BaCl_2$ impregnated CaO as catalyst. 2018; 13(2): 320-330. https://doi.org/10.9767/bcrec.13.2.1585.320-330

[98] Sakthivel S, Halder S, Gupta PD. Optimization of process variables for production of biodiesel in packed bed reactor using response surface methodology. *Int J Ambient Energy*. 2013; 34: 83-91. https://doi.org/10.1080/01430750.2012.740422

[99] Ketcong A, Meechan W, Naree T, Seneevong I. Production of fatty acid methyl esters over a limestone-derived heterogeneous catalyst in a fixed-bed reactor. *J Ind Eng Chem*. 2014; 20(4): 1665-1671. https://doi.org/10.1016/j.jiec.2013.08.014

[100] Miladinović MR, Stamenković OS, Banković PT, Milutinović AD, Jovanovic DM, Veljković VB. Modeling and optimization of sunflower oil methanolysis over quicklime bits in a packed bed tubular reactor using the response surface methodology. *Energy Conv Manag.* 2016; 130: 25-33. https://doi.org/10.1016/j.enconman.2016.10.020

[101] Co CET, Tan MC, Diamante JAR, Yan LRC, Tan RR, Razon LF. Internal mass-transfer limitations on the transesterification of coconut oil using an anionic ion exchange resin in a packed bed reactor. *CatalToday*. 2011; 174(1): 54-58. https://doi.org/10.1016/j.cattod.2011.02.065

[102] Buasri A, Chaiyut N, Loryuenyong V, Rodklum C, Chaikwan T, Kumphan N. Continuous process for biodiesel production in packed bed reactor from waste frying oil using potassium hydroxide supported on *Jatropha curcas* fruit shell as solid catalyst. *Appl Sci.* 2012; 2: 641-653. https://doi.org/10.3390/app2030641

[103] Akkarawatkhoosith N, Kaewchada A, Ngamcharussrivichai C, Jaree A. Biodiesel production via interesterification of palm oil and ethyl acetate using ion-exchange resin in a packed-bed reactor. *BioEnergy Res*. 2020; 13: 542-551. https://doi.org/10.1007/s12155-019-10051-4

[104] Díaz L, Escalante D, Rodríguez KE, Kuzmina Y, Gonz LA. Response surface methodology for continuous biodiesel production from *Jatropha curcas* oil using Li/pumice as catalyst in a packed-bed reactor assisted with diethyl ether as cosolvent. *Chem Eng Process: Process Intensif*. 2022; 179: 109065. https://doi.org/10.1016/j.cep.2022.109065

[105] Zabaruddin NH, Abdullah LC, Mohamed NH, Choong TSY. Optimization using response surface methodology (RSM) for biodiesel synthesis catalyzed by radiation-induced kenaf catalyst in packed-bed reactor. *Processes*. 2020; 8: 1289. https://doi.org/10.3390/pr8101289

[106] Sulaiman S, Mohamed A, Raja S, Shah S, Ehsan R. Potash derived from orange peel supported on PVA as a heterogeneous catalyst for biodiesel production in the packed - bed reactor. *Appl Nanosci*. 2022; 12(12): 3747-3754. https://doi.org/10.1007/s13204-022-02367-z

[107] Talha NS, Sulaiman S. In situ transesterification of solid coconut waste in a packed bed reactor with CaO / PVA catalyst. *Waste Manag*. 2018; 78: 929-937. https://doi.org/10.1016/j.wasman.2018.07.015

[108] Zik N, Sulaiman S, Jamal P. Biodiesel production from waste cooking oil using calcium oxide/nanocrystal cellulose / polyvinyl alcohol catalyst in a packed bed reactor. *Renew Energy*. 2020; 155: 267-277. https://doi.org/10.1016/j.renene.2020.03.144

Kontinualni višefazni reaktor sa vibracionom mešalicom i pakovanim slojem u proizvodnji biodizela: unapređenja i izazovi

Ivana B. Banković-Ilić[1], Marija R. Miladinović[1] i Vlada B. Veljković[1,2]

[1]*University of Niš, Faculty of Technology in Leskovac, Serbia*
[2]*Serbian Academy of Sciences and Arts, Belgrade, Serbia*

(Pregledni rad)

Izvod

Biodizel, obnovljiva i ekološki prihvatljiva alternativa konvencionalnim fosilnim gorivima, privukao je značajnu pažnju u poslednje dve decenije. Kontinualna proizvodnja biodizela ima prednosti u primeni zbog svoje efikasnosti, produktivnosti i mogućnosti uvećanja razmera reaktora. Ovaj rad predstavlja pregled kontinualnih reaktorskih sistema za proizvodnju biodizela sa naglaskom na prinos biodizela, kinetiku reakcije i efikasnost konverzije u reaktorima sa vibracionom mešalicom i pakovanim slojem. Reaktor sa vibracionom mešalicom se odlikuje superiornijim karakteristikama mešanja, boljim prenosom mase i kinetikom reakcije. Suprotno, reaktor sa pakovanim slojem se odlikuje boljim odnosom količine katalizatora i sirovine i dužim vremenom zadržavanja, što poboljšava efikasnost konverzije. Oba reaktora imaju povoljne performanse za kontinualnu proizvodnju biodizela. Ovo istraživanje može doprineti razumevanju kontinualne proizvodnje biodizela primenom inovativnih kostrukcija reaktora. Uporedna analiza reaktora sa vibracionom mešalicom i reaktora sa pakovanim slojem nudi dragocena saznanja u vezi optimizacije procesa i izbora reaktora na osnovu specifičnih zahteva kao što su dostupnost sirovina, kinetika reakcije i ekonomska razmatranja. To sve utire put za implementaciju održivih i efikasnih procesa proizvodnje biodizela u budućnosti.

Ključne reči: transesterifikacija, metanoliza, hidrodinamika, prenos mase, kontinualni reaktori

Photodegradation of thiophanate-methyl under simulated sunlight by utilization of novel composite photocatalysts

Aleksandar A. Jovanović[1], Mladen D. Bugarčić[1], Miroslav D. Sokić[1], Tanja S. Barudžija[2], Vladimir P. Pavićević[3] and Aleksandar D. Marinković[3]

[1]*Institute for Technology of Nuclear and Other Mineral Raw Materials, Belgrade, Serbia*
[2]*University of Belgrade, "VINČA" Institute of Nuclear Sciences - National Institute of the Republic of Serbia, Belgrade, Serbia*
[3]*University of Belgrade, Faculty of Technology and Metallurgy, Belgrade, Serbia*

Abstract

This work aimed to investigate the influence of modified titanium(IV) oxide by different nanosized particles on photocatalytic capacity to decompose the chosen organic pollutant under simulated sunlight. For that purpose, rutile-phased titanium(IV) oxide (r-TiO_2) was decorated with iron vanadate ($FeVO_4$/r-TiO_2) and vanadium-substituted goethite ($Fe_{1-x}V_xOOH$/r-TiO_2). The obtained composites were characterized by field emission scanning electron microscopy, energy-dispersive X-ray spectroscopy, X ray powder diffraction, Brunauer-Emmett-Teller, Fourier transform infrared spectroscopy – attenuated total reflectance and ultraviolet–visible diffuse reflectance spectroscopy techniques. Both synthesized photocatalysts showed higher photoactivity than the base r-TiO_2 for the degradation of the target contaminant - thiophanate-methyl (2.5 h *vs*. 5 h). During the tests, parameters like the irradiation time, catalysts amount, and pesticide concentration were systematically investigated. Furthermore, photocatalysts were applied in multicycle degradation tests for examining their effectiveness during exploitation time. Monitoring of the removal rate was performed both by UV/visible spectrometry and high-performance liquid chromatography (HPLC). In order to prove completion of fungicide degradation chemical oxygen demand was measured in the course of the photocatalytic experiment. The final concentration of the observed contaminant in treated samples was under the prescribed legislative level. The fabricated materials displayed great reliability, durability and photocatalytic activity representing good potentials for implementing this process in real wastewater treatment plants.

Keywords: photocatalysis; titanium(IV) oxide; advanced oxidation process; pesticide pollution; wastewater.

Available on-line at the Journal web address: http://www.ache.org.rs/HI/

ORIGINAL SCIENTIFIC PAPER

UDC: 577.152.3:544.478.3

Hem. Ind. **78(3)** 227-240 (2024)

1. INTRODUCTION

Contamination of the environment with different classes of organic pollutants is constantly increasing [1,2]. Several types of pesticides were employed as agents in agriculture production and preservation [3-5]. One of them is thiophanate-methyl, a fungicide with immense usage predominantly in the area of inhibition of fungal growth and extension of the product life. The induced negative side effects on public health and non-target organisms presented in previous investigations[6-8] made this fungicide forbidden by the legislative [9]. However, it can be still found on the market, and it has been also detected in water sources [10].

Treatment of pesticide-contaminated waters originating from industrial plants or agricultural fields can be performed in many ways [11,12]. The most promising techniques nowadays are advanced oxidative processes (AOPs), where photocatalysis has almost a mandatory role. Different organic and inorganic-based materials are utilized as photocatalysts with the aim to promote the decomposition of various pollutants [13,14]. Rapid production of complex, persistent organic hazardous chemicals has caused an increased demand for enhanced photosensitive materials that can catalyze pollutant decomposition over their surfaces. A predominantly used photocatalyst is TiO_2, with its structural

Corresponding authors:: Aleksandar A. Jovanović, Institute for Technology of Nuclear and Other Mineral Raw Materials, Belgrade, Serbia
E-mail: a.jovanovic@itnms.ac.rs
Paper received: 25 May 2023; Paper accepted: 6 January 2024; Paper published: 25 January 2024.
https://doi.org/10.2298/HEMIND230523004J

modifications [15]. These catalysts provide outstanding potentials for boosting the degradation of organic pollutants in wastewater due to their good physicochemical properties [16].

Heterojuncted materials exhibit exceptional performances as a faster electron/hole separation, great stability, decreased degradation time and lower band gap energy [17,18]. Transition metal oxides contain smaller band gaps, such as vanadium compounds, which can be combined with TiO_2 to create a heterojunction complex. Progress in charge carrier separation can be achieved by minimizing recombination throughout photocatalysis [19]. Recently, iron vanadate was used in the sphere of electrocatalysis, photoluminescence, optical and humidity sensors, *etc.* [20]. It was found that $FeVO_4$ doping with different transition metal cations and commercial TiO_2 P25 truly improve material properties [21,22]. Hence, it is anticipated that adding $FeVO_4$ to rutile TiO_2 will enhance the stability and selectivity of such a novel catalyst. On the other hand, vanadium-substituted goethite ($Fe_{1-x}V_xOOH$) appears as a promising adsorbent in wastewater treatment, but it was not tested as a catalyst. A major disadvantage of application photocatalysis is the price of prepared photocatalysts, mostly due to the usage of costly nanosized photocatalysts.

The purpose of this study was to investigate removal and degradation efficiency of the fungicide thiophanate-methyl from water solutions by photocatalysis under simulated sunlight. Two newly fabricated photocatalysts based on commercial r-TiO_2, *i.e.* $FeVO_4$/r-TiO_2 and $Fe_{1-x}V_xOOH$/r-TiO_2 were structurally analyzed and utilized comparatively as photocatalysts. This study aims to propose the preparation of photoactive and low-cost rutile-based catalysts that possess decent oxidation properties. From the literature review, the abovementioned composites were not yet fabricated and applied in this way.

2. EXPERIMENTAL

2. 1. Materials

In order to develop photocatalysts, various chemicals were utilized. The surface of rutile-phased TiO_2(r-TiO_2, Sigma Aldrich, Germany) was modified by the deposition of oxides and hydroxides in the system water layer around r-TiO_2 and non-solvent medium (xylene, 98 %, Zorka Pharma, Serbia) to perform effective deposition of iron vanadate ($FeVO_4$/r-TiO_2) and vanadium-substituted goethite ($Fe_{1-x}V_xOOH$/r-TiO_2). Pesticide thiophanate-methyl - TPM (purity > 95 %) was acquired from Agrosava, Serbia. Hence, the used chemicals for surface modification were: $Fe(NO_3)_3\times 9H_2O$ (*p. a.* Fisher, UK), NH_4VO_3(*p. a.* Merck, Germany), VCl_3 (*p. a.* Sigma Aldrich, Germany), ethanol (96 %, Reahem, Serbia), KOH (*p. a.* Zorka, Serbia). All solutions were prepared with deionized water (18.2 MΩ cm).

The surfaces of both catalysts were enriched to approximately 5 wt.% of $FeVO_4$ and $Fe_{1-x}V_xOOH$ regarding the initial r-TiO_2 mass.

2. 2. Synthesis of $FeVO_4$/r-TiO_2

In a 50 cm^3 three-necked pyrex flask, equipped with a refluxed condenser, thermometer and air inlet tube, 2.00 g r-TiO_2 and 0.0753 g NH_4VO_3 were added and mixed in 4.00 mL of deionized water. The prepared pasty suspension was overlaid with 12.00 mL of xylene and heated at 70 °C for 1 h. Subsequently, 2 mL of $Fe(NO_3)_3\times 9H_2O$ (m = 0.2602 g) solution was added dropwise to the solution and heated at 70 °C for 1 h without mixing. Thereafter, the obtained composite was rinsed with deionized water and ethanol (2 times), centrifuged, and dried for 6 h. In the last step, the composite was annealed at 520 °C for 4 h.

2. 3. Synthesis of $Fe_{1-x}V_xOOH$/r-TiO_2

r-TiO_2 powder (2.00 g) and 10.00 mL of xylene were added in a 50 mL three-necked flask. Then, a water solution of 0.7503 g of VCl_3 and 0.4289 g $Fe(NO_3)_3\times 9H_2O$ were added together with 2.50 mL of deionized water. The solution was mixed for 1 h at 70 °C. After 1 h, 1.5 mL of a 15 M solution of KOH was added and stirred for an additional hour. The prepared solution was stored in the dark for 15 days to obtain particles with smaller diameters (in contrast to 48 days according to Schwertman & Cornell [23]). Lastly, the stored solution was rinsed with ethanol and deionized water until negative chloride reaction and dried for 2 h at 60 °C.

2. 4. Structural characterization of prepared composites

Presence of crystalline phases in commercial and two modified materials was determined based on measurements using SmartLab Rigaku powder diffractometer (Rigaku, Japan) that works on the principle of Bragg-Brentano geometry, using an X-ray tube with a copper anticathode, *i.e.* using CuKα radiation of wavelength λ = 0.154178 nm. The voltage on the X-ray tube was 40 kV, and the current was 30 mA. Measurements were made in the range of diffraction angles 2 θ from 10 to 80° with a step of 0.02° and a measurement speed of 1° min^{-1}. The Brunauer-Emmett-Teller (BET) technique was utilized to estimate the specific surface area of photocatalysts, by Micrometrics ASAP 2020 (Micromeritics Instrument Corporation, USA). The identification of functional groups in base and modified materials was authenticated by Fourier-transform infrared spectroscopy with Attenuated total reflection (ATR-FTIR) using Nicolet iS 10 FTIR Spectrometer (ThermoFisher Scientific, USA). Spectra were collected in the range 4000 to 400 cm^{-1}. Analysis of particle surface morphology was examined by a Field Emission Scanning Electron Microscope (FE-SEM) TESCAN MIRA 3 (TESCAN ORSAY HOLDING, a.s., Czech Republic). Mapping of photocatalyst surfaces was performed by FE-SEM JSM 7001F (Jeol, Japan) coupled with an energy dispersive spectrometer (EDS) Xplore 15 (Oxford Instruments, UK) operated at accelerating voltage of 20 kV, probe current of 10 nA in high vacuum mode (0.1 mPa). Optical properties of base and fabricated composites were determined by UV-Vis diffuse reflectance spectroscopy (UV-DRS) (Shimadzu UV-Vis UV-2600, Japan). Determination of band gap energies will give a better insight into photocatalytic activity.

2. 5. Photocatalytic tests

A water solution of thiophanate-methyl (TPM) was placed in a 200 mL cylindrically shaped quartz reactor together with a photocatalyst at room temperature. The TPM solution (150 mL) and selected photocatalyst (67 mg L^{-1}) was mixed in the dark for 30 min at 200 rpm on a magnetic stirrer (IKA C-MAG HS7, IKA, China) with the aim to achieve adsorption-desorption equilibrium among the prepared solution and chosen photocatalyst and the reactor was temperature controlled by the feedback loop. Immediately afterward, the source of irradiation (Osram Vitalux, Germany, 300 W, UVA:UVB = 13.6:3) was placed 20 cm above the solution level in the reactor and degradation was initiated. Light intensity of the light source was determined previously [24].

Equation (1) was used to evaluate the degradation or pesticide removal (*PR*):

$$PR = \frac{c_i - c_f}{c_i} 100 \quad (1)$$

where c_i and c_f represent the initial and the final pesticide concentration, respectively. Furthermore, endurance and efficiency of the fabricated materials were estimated in five consecutive cycles. Before each application, catalysts were collected from the solution, rinsed and centrifuged with ethanol and deionized water.

The photocatalytical experiments were performed in triplicates, for attenuating measurement uncertainty.

2. 6. Analytical procedures

Monitoring of fungicide degradation was recorded by UV/Vis spectroscopy (Shimadzu 1800, Japan) and high pressure liquid chromatography (HPLC) (Dionex UltiMate 3000 LC system, Thermo Fisher Scientific, USA with Zorbax Eclipse XDB-C18, 250 × 4.6 mm (i.d.) × 5 µm column, mix of methanol (25 %), acetonitrile (25 %) and water (50 %) as eluent). Every 30 min up to 5 h water aliquots (3.00 mL) were sampled, filtered through a 0.25 µm syringe filter and placed into a cuvette. Further, the kinetic rate constant (*k*) from all degradation reactions was determined together with halftime periods ($t_{1/2}$), by using the pseudo-first order kinetic model:

$$\ln\frac{c_t}{c_i} = -kt \quad (2)$$

$$t_{1/2} = \frac{\ln 2}{k} \quad (3)$$

where c_i and c_t are the initial and the pesticide concentration at some time *t*, respectively. As a check-up, the concentrations were also measured by HPLC.

2. 7. Environmental impact

Evaluation of oxygen consumption of initial molecules and their fractions during the degradation process represents a necessa ry step in the evaluation of the efficiency and eco-friendliness of the implemented treatment process. Chemical oxygen demand (COD) was determined by the EPA [25] standard method. The obtained values were compared with those given in the legal regulations.

3. RESULTS AND DISCUSSION

3. 1. Structural characterization of prepared composites

SEM micrographs of all investigated photocatalysts are presented in Figure 1.

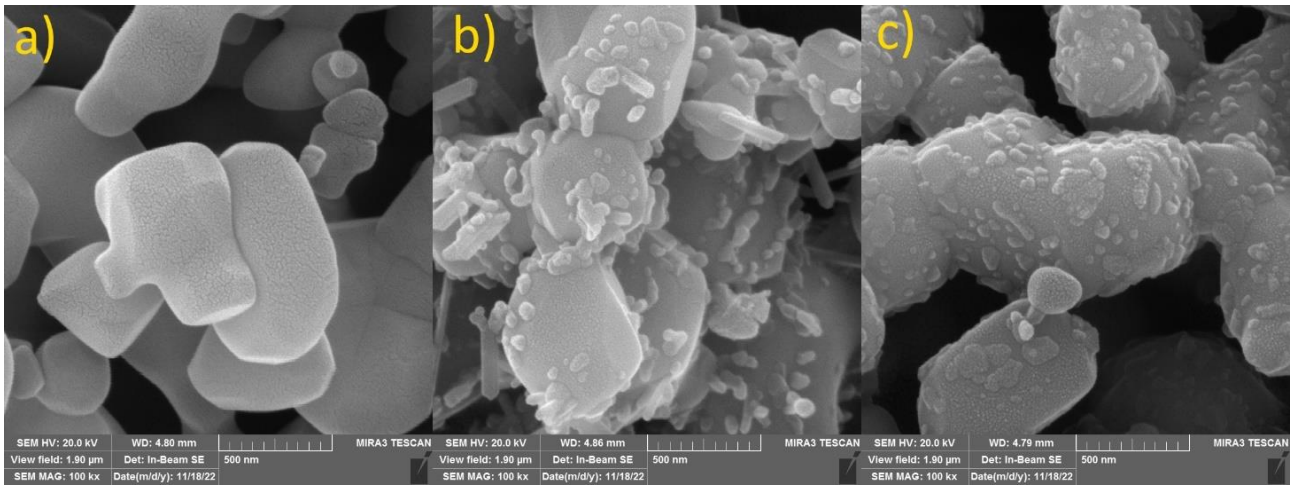

Figure 1. FE SEM micrographs of: a) r-TiO_2, b)$FeVO_4$/r-TiO_2 and c) $Fe_{1-x}V_xOOH$/r-TiO_2 (scale bar = 500 nm)

Particles seen in Figure 1a present the base material which is consistent with the rutile phase TiO_2. The particles have smooth surfaces and uneven shape. The smallest particle diameter is about 0.5 µm, while the largest length is about 5 µm (the data are provided by the manufacturer obtained from sieves analysis).

The material modified with $FeVO_4$ (Fig. 1b) differs from the base one since the surface of rutile TiO_2 is decorated by deposed particles ($FeVO_4$). The iron vanadate particles are mostly rod-shaped (length x diameter = 200 nm × 50 nm) or coerced nanoparticles (mostly cubic with edges ≈ 50 nm) [26,27]. The presence of those particles contributes to a negligible increase in the specific surface area (SSA) from 0.54 $m^2\ g^{-1}$ for r-TiO_2, to 1.70 $m^2\ g^{-1}$ obtained for $FeVO_4$/r-TiO_2. as determined by the BET method.

The presence of V-substituted goethite on the surface of the sample ($Fe_{1-x}V_xOOH$) can be seen in Figure 1c. Those particles are uniformly deposited and are in the shape of flakes, rarely found as sticks. All deposed particles exhibit pox-like surfaces. A similar shape of fabricated oxyhydroxide particles is observed with other transition metals, as reported in literature [28,29]. Dimension of deposited particles is in the range from 50 nm for single particles to 250 nm for coerced flakes, while the sticks are 50 nm in diameter and up to 200 nm in length. The SSA of $Fe_{1-x}V_xOOH$-modified material is 1.82 $m^2\ g^{-1}$.

Surface mapping of fabricated materials is shown in Figures 2 and 3.

SEM-EDS analyses have shown four elements on the surfaces of the prepared photocatalysts. Oxygen, titanium, iron and vanadium constitute both materials in different portions. The ratio of presented elements in Figure 2 are: 32.11 wt.% Ti, 66.64 wt.% O, 0.79 wt.% Fe, 0.47 wt. % V, while in Figure 3 are: 32.41 wt.% Ti , 66.35 wt.% O, 1.06 wt.% Fe, 0.19 wt.% V. The distribution of mentioned elements in Figures 2 and 3 confirms that deposition of nanoparticles on TiO_2 surface is achieved. The calculations verified that the deposited amount of $FeVO_4$ was 5.14 wt.% and $Fe_{1-x}V_xOOH$ was 4.27 wt.%, from scans on Figures 2 and 3.

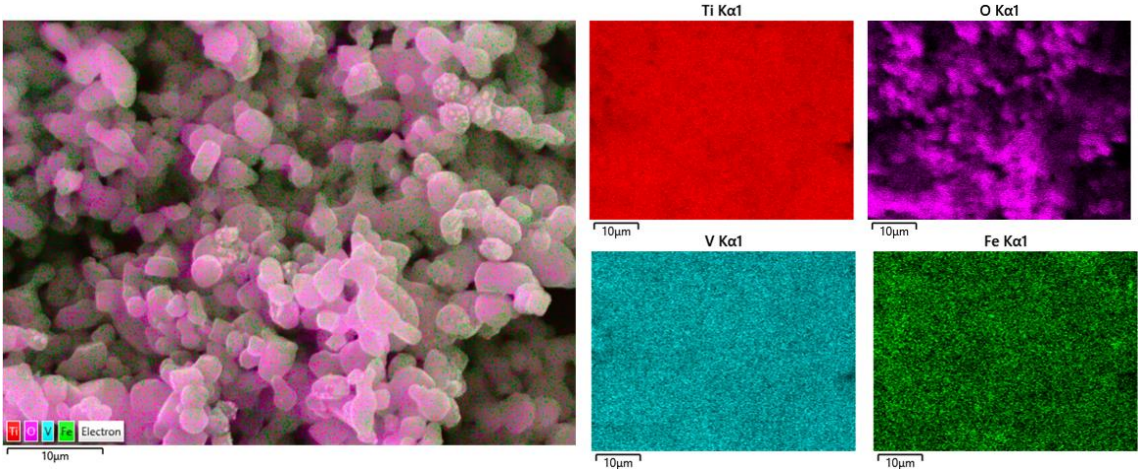

Figure 2. EDS mapping of $FeVO_4$/r-TiO_2 surface (detector for Secondary Electron Imaging, Working Distance 4.80 mm)

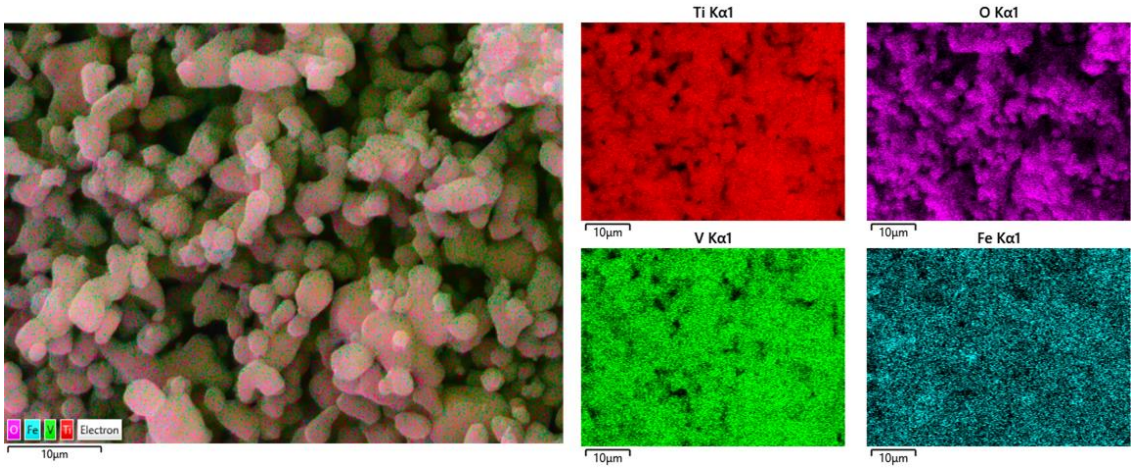

Figure 3. EDS mapping of $Fe_{1-x}V_xOOH$/r-TiO_2 surface (detector for Secondary Electron Imaging, Working Distance 4.80 mm)

The phase compositions of the base and prepared photocatalysts are shown in Figure 4.

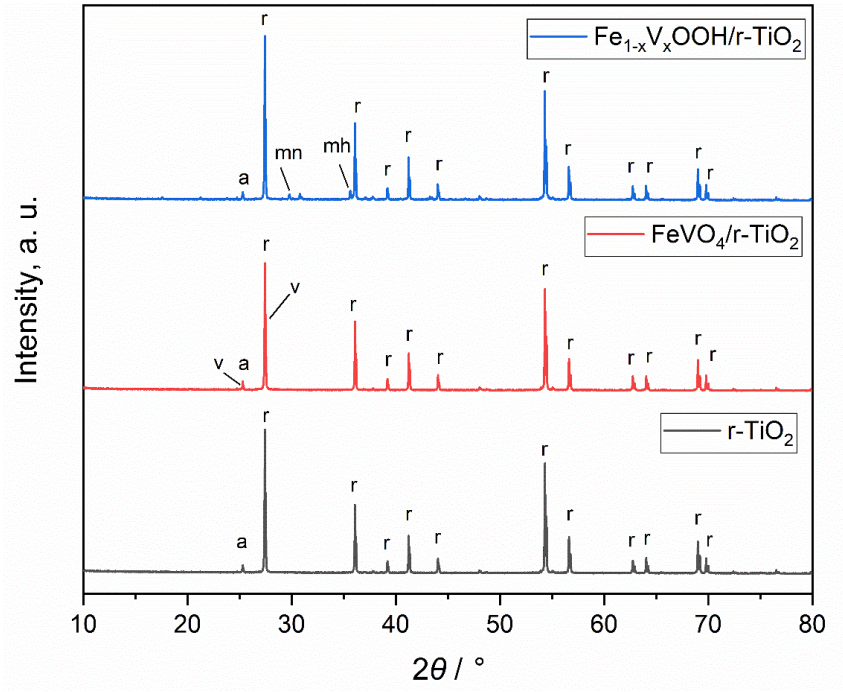

Figure 4. XRPD patterns of r-TiO_2 (bottom line), $FeVO_4$/ r-TiO_2 (middle line) and $Fe_{1-x}V_xOOH$/r-TiO_2 (upper line); r - rutile, a - anatase, mn - magnetite, mh - maghemite, v -iron(III) vanadate

The base material (black line in Fig. 4) is mostly composed of rutile phase TiO_2 particles (observed peaks at 27.4, 36.1, 39.2, 41.2, 44.0, 54.3, 56.6, 62.8, 64.0, 69.0 and 69.8°, PDF No. 03-065-0191) with the small amount of anatase phase (most pronounce peak at 25.3°, PDF No. 01-086-1157). Both fabricated materials have similar peaks as the start material. The XRPD pattern of $Fe_{1-x}V_xOOH/r\text{-}TiO_2$ (upper spectrum in Fig. 4) contains additional diffraction peaks at: 35.6° that could be ascribed to maghemite (PDF No. 01-089-5892), 29.7° that could be ascribed to magnetite (PDF No. 01-089-0951) and 30.8° that could be assigned to brookite (PDF No. 01-076-1934) [30]. The XRPD pattern of $FeVO_4/r\text{-}TiO_2$ (middle spectrum Fig. 4) contains additional small peaks at 25.0 and 27.7° that belong to $FeVO_4$ (PDF No. 00-038-1372) [31] that coincides with the most intensive peak of anatase and rutile phase, respectively [32].

The FT-IR spectra of $r\text{-}TiO_2$, $FeVO_4/ r\text{-}TiO_2$ and $Fe_{1-x}V_xOOH/ r\text{-}TiO_2$ particles are shown in Figure 5.

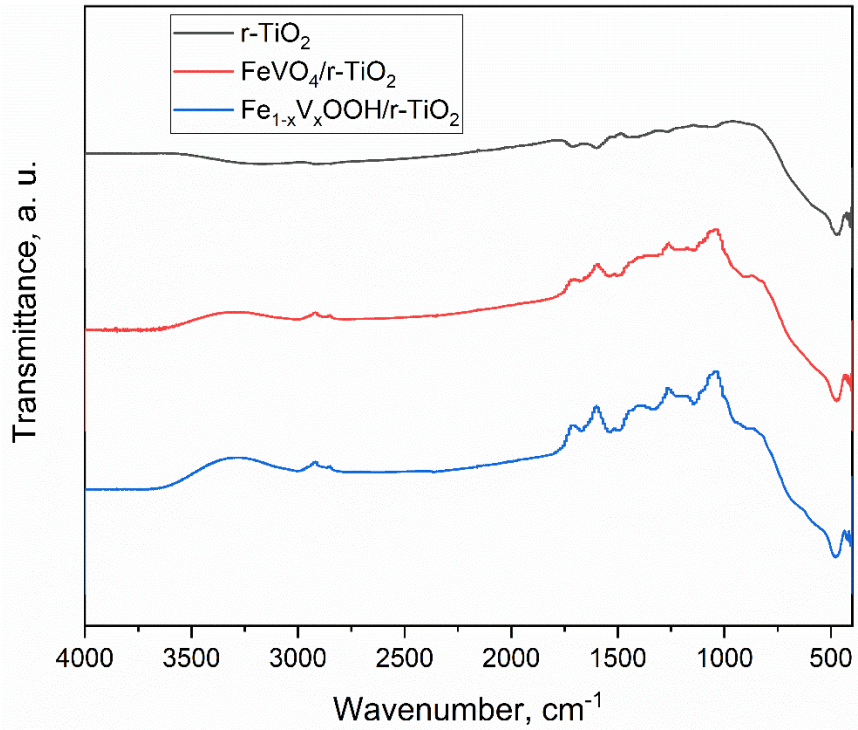

Figure 5. ATR-FTIR spectra of $r\text{-}TiO_2$(upper spectrum), $FeVO_4/ r\text{-}TiO_2$(middle spectrum) and $Fe_{1-x}V_xOOH/r\text{-}TiO_2$ (bottom spectrum)

By observing the FTIR spectra of the two synthesized materials, several new peaks are found. Firstly, a broad peak in a range from 930 to 890 cm^{-1} was attributed to V=O and V-O-V coupled vibrations as well as the stretching of vanadyl (V=O) bonds, respectively [31]. Due to intense Ti-O vibrations in $r\text{-}TiO_2$, combined bridging and stretching of V-O-Fe were overlapped [31]. According to the peak found at 505 cm^{-1}, V-O-V deformation vibration together with Fe-O stretching modes is observed [33].

One of the parameters of utmost significance for improvement of photocatalytic activity is achievement of a lower band gap energy (E_{gap}). The quantity of deposited $FeVO_4$ and $Fe_{1-x}V_xOOH$ (~5 wt.%) and contact between phases caused changes in the material electronic configuration. DRS and Tauc graphics for the two synthesized materials are presented in Figure 6. E_{gap} values were retrieved by Tauc plot, obtained by charting $(F(R)hv)^n$ *vs.* hv, where R is reflectance and $F(R)$ is the so-called remission or Kubelka-Munk function, n = 1/2.

The obtained band gap energies of all investigated materials are listed in ascending order: 2.68, 2.87 and 3.03 eV for $Fe_{1-x}V_xOOH/r\text{-}TiO_2$, $FeVO_4/r\text{-}TiO_2$ and $r\text{-}TiO_2$, respectively. The determined E_{gap} values indicate that the presence of particles on the surfaces of rutile microparticles induces lowering the energy needed for excitation [34]. By decreasing the energy gap in heterojuncted photocatalysts, the surface electron - hole transition is facilitated. This phenomenon induces faster generation of oxidative species and decreases the degradation time.

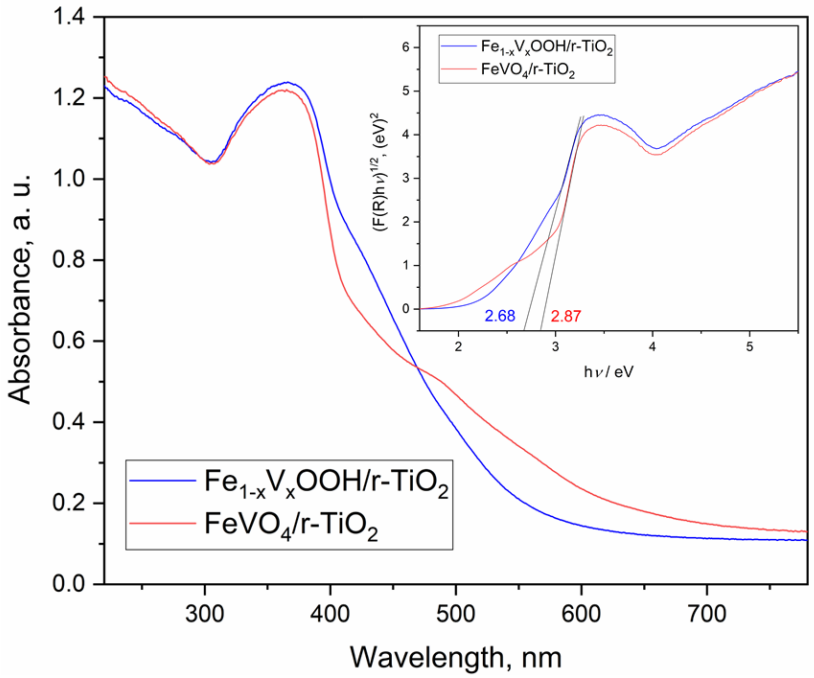

Figure 6. DRS and Tauc plots for $FeVO_4$/ r-TiO_2 and $Fe_{1-x}V_xOOH$/r-TiO_2

3. 2. Photocatalytic assays

Process parameters have to be investigated prior to any possible application of a process on the pilot level. The obtained results in essential tests in this area of engineering are presented in the following lines.

3. 2. 1. Photocatalyst mass

When the mass of the applied catalyst is considered, it should be taken into account that a higher mass does not mean a better result within the observed system. Namely, when the amount of catalyst is very low, the total number of active centers on the surface that could generate electron/hole pair (*i.e.* reactive radicals in solution which participate in degradation of the present pollutant) is not sufficient to perform photodegradation at a satisfactory rate. On the other hand, an excessive amount of catalyst leads to its potential coagulation and precipitation. In addition, a large catalyst amount hinders penetration of radiation into the pollutant and catalyst solution suspension, thereby reducing the efficiency of the process and the inevitable prolongation of the reaction. Effects of catalyst amount on photocatalytic efficiency are shown in Figure 7.

As can be seen in Figure 7, the best results were obtained when the catalyst amount was 10 mg (150 mL)$^{-1}$ (67 mg L^{-1}). This dosage of catalyst (*i.e.* 67 mg L^{-1}) was used in the following tests as the optimal for removal of TPM. In our previous work (Jovanovic et al., 2023), a photolytic test was performed under the same experimental conditions (initial TPM concentration and irradiation time)[35]. The findings indicated that the photolytic degrading efficiency was extremely poor. Namely, the results demonstrated that photocatalytic rates for 5 and 10 mg L^{-1} of TPM was 33 and 23 times higher, respectively, then photolytic decomposition [35]. Furthermore, adsorption tests were conducted in dark, by addition of the chosen photocatalyst in a TPM solution resulting in a slight decrease in the TPM concentration by a maximum of 10 %. The obtained findings implied that adsorption is not the primary process during the complete photocatalysis. Effectiveness of the interaction between TPM and photocatalyst significantly determines the further reaction kinetic. Obviously, the additional obstacle is the cost of the used catalyst, and from that side it is necessary to further optimize the process as much as possible.

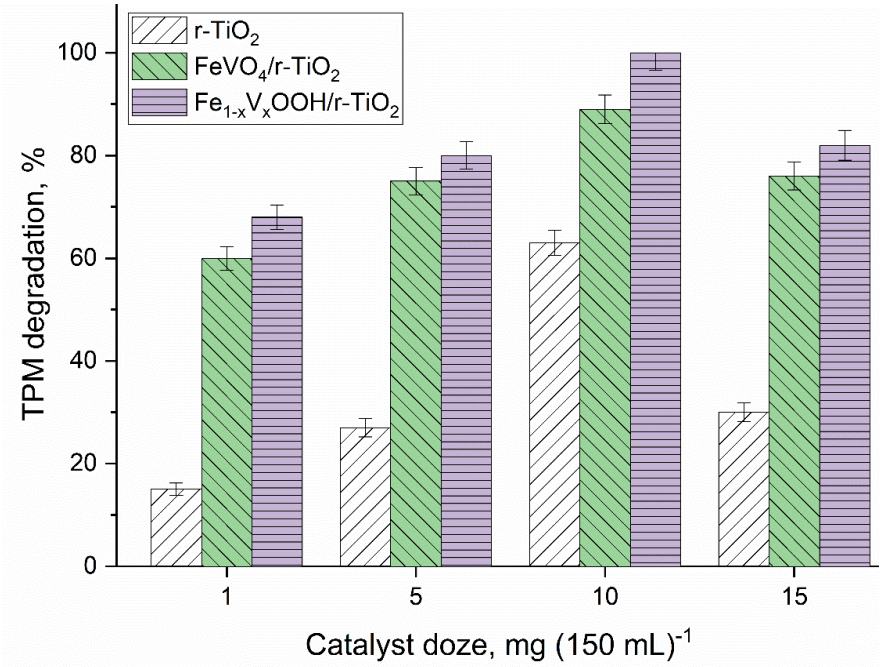

Figure 7. Impact of the catalyst amount on the TPM removal efficiency (c_0 = 5 mg L^{-1}, t = 150 min, 200 rpm; data are the average of n = 3)

3. 2. 2. Initial pollutant concentration

The second factor that directly affects the process rate is the initial TPM concentration. The influence of varied concentrations of TPM on degradation profiles is shown in Figure 8. Low solubility of TPM in water (18.5 mg L^{-1} at 20 °C) defines the upper limit of the fungicide concentration [36]. By observing the TPM degradation curves in the initial concentration range 1 to 15 mg L^{-1}, it can be seen that degradation efficiency gradually decreases. This can be explained by lower free spots on the catalyst surface for the generation of hydroxyl radicals.

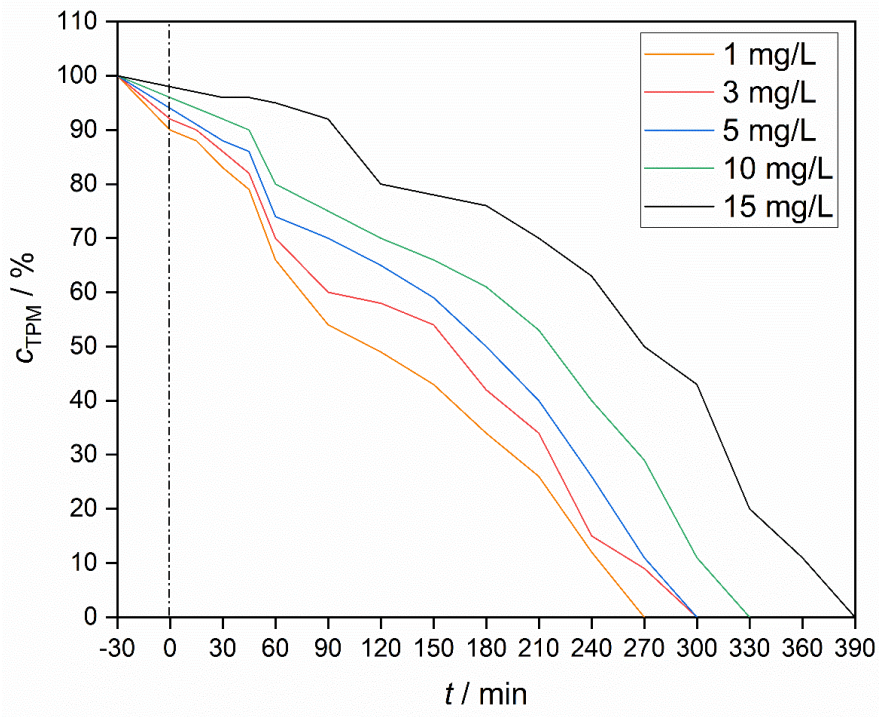

Figure 8. Influence of the initial TPM concentration on the degradation percentage (150 mL of suspension mixing at 200 rpm in the dark for the first 30 min, after that mixing under irradiation using 0.067 g L^{-1} r-TiO_2)

Complete degradation of TPM was accomplished in 5 h for the systems with the initial concentrations of 3 and 5 mg L^{-1}. At the lower initial concentration of 1 mg L^{-1} even a shorter degradation time was obtained. Longer irradiation times were necessary at higher TPM concentrations (10 and 15 mg L^{-1}) to achieve the complete pollutant degradation. It was decided that the optimal initial concentration for the photocatalytic probes was 5 mg L^{-1}, and similar concentration was also detected in riverside, as reported in literature [10].

The calculated values of reaction rate constant (k) and half-time ($t_{1/2}$) for TPM degradation at different initial concentrations are given in Table 1.

Table 1. Estimated kinetic rate constant (k) and degradation half-time ($t_{1/2}$) for TPM

TPM concentration, mg L^{-1}	k±SE* /10^4 min^{-1}	$t_{1/2}$ / min	R^2
1	59.4±3.5	117	0.963
3	45.6±3.5	152	0.939
5	35.9±2.4	193	0.950
10	29.7±1.4	233	0.964
15	18.6±1.0	273	0.939

*SE - standard error; R^2 - coefficient of determination

Values of determined k and $t_{1/2}$show reciprocal dependence on the TPM concentration. Kinetic curves for different TPM concentrations are similarly shaped and follow the pseudo first rate order. From the experimental results can be seen that it takes longer time for the first part of the reaction to take place (reduction of TPM concentration by 50 %), which indicates the persistence of the fungicide.

3. 2. 3. Comparison of catalysts activities

The fabricated materials were utilized as photocatalysts with the aim to help in the degradation of the chosen pollutant. Figure 9 depicts a comparison of photocatalysts efficiencies toward the decomposition of TPM in water solution under simulated solar light.

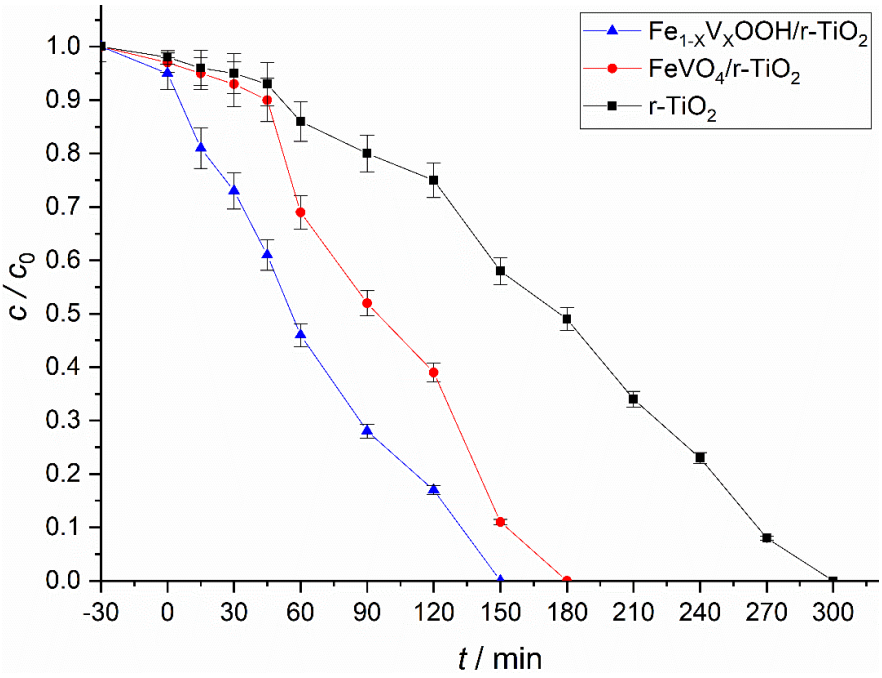

Figure 9. Photocatalytic activity of prepared materials and commercial r-TiO_2 (150 mL of suspension mixing at 200 rpm in the dark for the first 30 min, after that mixing under irradiation using 0.067 g L^{-1} of the selected photocatalyst)

As can be observed, the $Fe_{1-x}V_xOOH$-modified catalyst has shown the best performance. The base material r-TiO_2 shows the weakest ability to advance photodegradation, which justifies the fact that further modification of the surface

was necessary. Worse outcomes can be explained by the fact that TiO_2 absorbs only in the UV area of radiation [37,38]. Contrarily, molecules of vanadium oxide and vanadium oxyhydroxide can be excited by solar radiation. This is the reason for better activity and lower degradation times in cases when this two photocatalysts were employed ($FeVO_4$/r-TiO_2 and $Fe_{1-x}V_xOOH$/r-TiO_2). Increased generation of photoactive species significantly impacted photocatalytic degradation, and this could be another explanation for better catalytic performances of the fabricated materials. Furthermore, it is necessary to put special effort into engineering of materials with the tunable gap energy, so that they can easily surpass all barriers for better charge transfer [39]. Once again it was proven that the band gap energy plays a special role in the field of radiation-assisted photocatalytic reactions.

3. 2. 4. Reusability

Efficiencies of materials in 5 consecutive exploited cycles are shown in Figure 10.

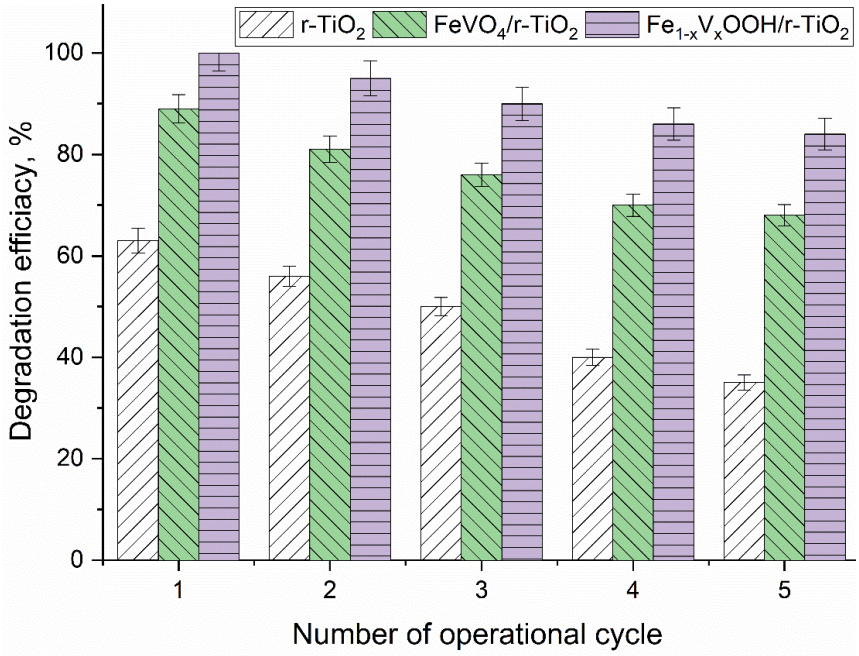

Figure 10. Multicycle efficiencies of catalysts ($c_{0(TPM)}$ = 5 mg L^{-1}, catalyst amount = 0.067 g L^{-1}, solution volume = 150 mL, 200 rpm, the cycle time for each degradation experiment was set to 150 min)

A slightly lower reusability potential of $FeVO_4$/r-TiO_2 with respect to $Fe_{1-x}V_xOOH$/r-TiO_2 was obtained, while the lowest was obtained for r-TiO_2. The gradual decrease of degradation power of all materials could be explained by the fact that some active sites lose their ability to generate oxidative species during the next cycles. Furthermore, possible reason can be infinitesimal peeling of the photocatalysts surface layer [40]. Also, another explanation can be the irreversible adsorption of whole or some TPM degradation products on the catalyst's surface. As a result, the photocatalyst surface became partly covered with some degradation products, which reduced the ability to degrade the target compound [41].The material with the least reduced catalytic activity was $Fe_{1-x}V_xOOH$/r-TiO_2.

3. 3. Chemical oxygen demand

Measuring of COD represents one of the key factors in determining whether wastewater can be discharged into a recipient. The obtained results of COD under the optimized conditions are represented in Table 2 together with standard deviation (SD) values.

The values of COD are constantly decreasing during the degradation time which is in accordance with degradation kinetics (see 3.2.3. subchapter). Considering that the maximum permissible concentration of this pesticide in water is not regulated, monitoring of COD is of crucial importance. The initial value was lowered more than 10 times for the proposed irradiation period, and once again demonstrated the effectiveness of the fabricated composite.

Table 2. Measured COD values for TPM solution obtained in the course of the photocatalytic degradation (c_0 = 5 mg L^{-1}, 0.067 g L^{-1} of $Fe_{1-x}V_xOOH/r\text{-}TiO_2$, COD data is the triplicate measurement average)

Time, min	0	30	60	90	120	150	180
COD , mg L^{-1}	1255	1100	1000	830	480	260	100
SD (COD), mg L^{-1}	7.348	8.165	4.082	5.715	7.348	4.899	1.633

As mentioned before, the overall process has to be considered from the aspect of material costs on the global market. Sustainability and possibility for practical application highly depend on all process costs. Prices for chosen micro- and nanosized compounds for the synthesis of photocatalysts are shown in Table 3.

Table 3. Comparison of prices for commercially available compounds for synthesis of photocatalysts [42]

Compound	Price of microsize, € per 100 g	Price of nanosize, € per 100 g
r, a-TiO_2	-	316.00
r-TiO_2	145.00	261.00
a-TiO_2	32.30	476.00
ZnO	15.50	253.20
CdS	105.20	-
MoS_2	73.00	2230.00
WO_3	1180.00	2610.00

It is clear that materials in the form of nanosized particles are more expensive than the microsized ones. That is the main reason for possible use of microsize photocatalyst based on r-TiO_2. Also, high abundance and availability of this material in nature together with good performances make rutile-phased TiO_2 a simple choice. Modified TiO_2-based composites are not much more expensive. Costs of auxiliary chemicals are: $Fe(NO_3)_3{\times}9H_2O$ (49.00 € for 100 g), VCl_3 (502 € for 100 g), NH_4VO_3(48.00 € for 100 g), KOH (6.10 € for 100 g). Bearing in mind that the deposited amount of$FeVO_4$or $Fe_{1-x}V_xOOH$ is up to 10 wt.% and considering the molar ratio of mentioned reagents during the preparation of the catalyst, the justification of the synthesis of new catalysts can be confirmed.

4. CONCLUSION

Global pollution is a widespread problem with broad spectrum of negative influences on society. Wastewater treatment in conventional processes often cannot solve the issue of pollutant removal on proper and sustainable way. Therefore, oxidative processes such as photocatalysis are attracting more and more attention for applications in real systems. From results obtained by detailed investigations in this study, the following outcomes can be drawn.

1. Structural methods for materials characterization prove successful and uniform deposition of $FeVO_4$ and $Fe_{1-x}V_xOOH$ onto r-TiO_2 surface up to 5.5 wt.%.
2. Nanosized particles significantly improved the oxidative abilities of the composite by reducing band gap energies (2.68 and 2.87 eV for $Fe_{1-x}V_xOOH/r\text{-}TiO_2$ and $FeVO_4/r\text{-}TiO_2$, respectively).
3. The prepared photocatalysts have shown better photocatalytic performances toward TPM degradation subjected to artificial sunlight irradiation (reduced degradation half time) than non-modified r-TiO_2, and all processes follow the pseudo-first rate order kinetics.
4. Determined optimal conditions for degradation reaction are 0.07 g L^{-1} of catalyst and 5 mg L^{-1} of TPM water solution.
5. A slight decrease in the photocatalytic activity was observed during a 5-cycle exploitation, with the most stable being $Fe_{1-x}V_xOOH/r\text{-}TiO_2$.
6. COD values implied that the proposed treatment was effective (more than 10 times decreased value, under the legislation value).

Based on the described conclusions, it was shown that the fabricated composite photocatalysts are valuable to be applied for TPM photodegradation. Future considerations should be focused on the scale up of the laboratory process to the pilot level with feasibility studies.

Acknowledgements: This work was supported by the Ministry of Science, Technological Development and Innovation of the Republic of Serbia (Contract Nos. 451-03-47/2023-01/200023; 451-03-9/2023-14/200017; 451-03-47/2023-01/200135).

REFERENCES

[1] Schaider LA, Rodgers KM, Rudel RA. Review of Organic Wastewater Compound Concentrations and Removal in Onsite Wastewater Treatment Systems. *Environ Sci Technol.* 2017; 51(13): 7304-7317. https://doi.org/10.1021/acs.est.6b04778

[2] Syafrudin M, Kristanti RA, Yuniarto A, Hadibarata T, Rhee J, Al-Onazi WA, Algarni TS, Almarri AH, Al-Mohaimeed AM. Pesticides in drinking water-a review. *Int J Environ Res Public Health.* 2021; 18(2): 468. https://doi.org/10.3390/ijerph18020468

[3] Hassaan MA, El Nemr A. Pesticides pollution: Classifications, human health impact, extraction and treatment techniques. *Egypt J Aquat Res.* 2020; 46(3): 207-220. https://doi.org/10.1016/j.ejar.2020.08.007

[4] Jatoi AS, Hashmi Z, Adriyani R, Yuniarto A, Mazari SA, Akhter F, Mubarak NM. Recent trends and future challenges of pesticide removal techniques – A comprehensive review. *J Environ Chem Eng.* 2021; 9(4): 105571. https://doi.org/10.1016/j.jece.2021.105571

[5] Leong WH, Teh SY, Hossain MM, Nadarajaw T, Zabidi-Hussin Z, Chin SY, Lai KS, Lim SHE. Application, monitoring and adverse effects in pesticide use: The importance of reinforcement of Good Agricultural Practices (GAPs). *J Environ Manage.* 2020; 260 109987. https://doi.org/10.1016/j.jenvman.2019.109987

[6] Venugopal D, Karunamoorthy P, Beerappa R, Sharma D, Aambikapathy M, Rajasekar K, Gaikwad A, Kondhalkar S. Evaluation of work place pesticide concentration and health complaints among women workers in tea plantation, Southern India. *J Expo Sci Environ Epidemiol.* 2021; 31(3): 560-570. https://doi.org/10.1038/s41370-020-00284-3

[7] Che X, Huang Y, Zhong K, Jia K, Wei Y, Meng Y, Yuan W, Lu H. Thiophanate-methyl induces notochord toxicity by activating the PI3K-mTOR pathway in zebrafish (Danio rerio) embryos. *Environ Pollut.* 2023; 318: 120861. https://doi.org/10.1016/j.envpol.2022.120861

[8] Arena M, Auteri D, Barmaz S, Bellisai G, Brancato A, Brocca D, Bura L, Byers H, Chiusolo A, Court Marques D, Crivellente F, De Lentdecker C, Egsmose M, Erdos Z, Fait G, Ferreira L, Goumenou M, Greco L, Ippolito A, Istace F, Jarrah S, Kardassi D, Leuschner R, Lythgo C, Magrans JO, Medina P, Miron I, Molnar T, Nougadere A, Padovani L, Parra Morte JM, Pedersen R, Reich H, Sacchi A, Santos M, Serafimova R, Sharp R, Stanek A, Streissl F, Sturma J, Szentes C, Tarazona J, Terron A, Theobald A, Vagenende B, Verani A, Villamar-Bouza L. Peer review of the pesticide risk assessment of the active substance thiophanate-methyl. *EFSA J.* 2018; 16(5): e05133. https://doi.org/10.2903/j.efsa.2018.5133

[9] European Commission, Commission Implementing Regulation (EU) 2020/1498 concerning the non-renewal of approval of the active substance thiophanate-methyl, in accordance with Regulation (EC) No 1107/2009 of the European Parliament and of the Council concerning the placing of plant protection products on the market, and amending the Annex to Commission Implementing Regulation (EU) No 540/2011. *OJEU*. 2020; https://eur-lex.europa.eu/legal-content/EN/TXT/PDF/?uri=CELEX:32020R1498 (accessed December 12, 2022)

[10] Tan H, Li Q, Zhang H, Wu C, Zhao S, Deng X, Li Y. Pesticide residues in agricultural topsoil from the Hainan tropical riverside basin: Determination, distribution, and relationships with planting patterns and surface water. *Sci Tot Environ.* 2020; 722: 137856. https://doi.org/10.1016/j.scitotenv.2020.137856

[11] Saleh IA, Zouari N, Al-Ghouti MA. Removal of pesticides from water and wastewater: Chemical, physical and biological treatment approaches. *Environ Technol Innov.* 2020; 19: . https://doi.org/10.1016/j.eti.2020.101026

[12] Mukherjee A, Mehta R, Saha S, Bhattacharya A, Biswas PK, Kole RK. Removal of multiple pesticide residues from water by low-pressure thin-film composite membrane. *Appl Water Sci.* 2020; 10(12): 1-8. https://doi.org/10.1007/s13201-020-01315-y

[13] Jovanović AA, Bugarčić MD, Marinković AD, Sokić MD. Insights into the application of polyaniline-based composites in environmental engineering. *Metal Mater Data.* 2023; 1(1): 25-31. https://doi.org/10.30544/MMD1

[14] Zhang F, Wang X, Liu H, Liu C, Wan Y, Long Y, Cai Z. Recent advances and applications of semiconductor photocatalytic technology. *Appl Sci.* 2019; 9(12): 1-43. https://doi.org/10.3390/app9122489

[15] Shokri A, Sanavi Fard M. A critical review in the features and application of photocatalysts in wastewater treatment. *Chem Paper.* 2022; 76(9): 5309-5339. https://doi.org/10.1007/s11696-022-02256-3

[16] Zhang Y, Chu W. Cooperation of multi-walled carbon nanotubes and cobalt doped TiO2 to activate peroxymonosulfate for antipyrine photocatalytic degradation. *Sep Purif Technol.* 2022; 282: 119996. https://doi.org/10.1016/j.seppur.2021.119996

[17] He X, Kai T, Ding P. Heterojunction photocatalysts for degradation of the tetracycline antibiotic: a review. *Environ Chem Lett.* 2021; 19(6): 4563-4601. https://doi.org/10.1007/s10311-021-01295-8

[18] Low J, Yu J, Jaroniec M, Wageh S, Al-Ghamdi AA. Heterojunction Photocatalysts. *Adv Mat.* 2017; 29(20): 1601694. https://doi.org/10.1002/adma.201601694

[19] Xu J, Zhang T. Fabrication of spent FCC catalyst composites by loaded V2O5 and TiO2 and their comparative photocatalytic activities. *Sci Rep.* 2019; 9(1):11099. https://doi.org/10.1038/s41598-019-47155-y

[20] Kesavan G, Pichumani M, Chen SM. Influence of Crystalline, Structural, and Electrochemical Properties of Iron Vanadate Nanostructures on Flutamide Detection. *ACS Appl Nano Mater.* 2021; 4(6): 5883-5894. https://doi.org/10.1021/acsanm.1c00802
[21] Dutta DP, Ramakrishnan M, Roy M, Kumar A. Effect of transition metal doping on the photocatalytic properties of FeVO4 nanoparticles. *J Photochem Photobiol A Chem*. 2017; 335: 102-111. https://doi.org/10.1016/j.jphotochem.2016.11.022
[22] Min YL, Zhang K, Chen YC, Zhang YG. Synthesis of novel visible light responding vanadate/TiO2 heterostructure photocatalysts for application of organic pollutants. *Chem Eng J.* 2011; 175(1): 76-83. https://doi.org/10.1016/j.cej.2011.09.042
[23] Schwertman U, Cornell RM. Iron Oxides in the Laboratory. Second edition. Weinheim: Wiley VCH Verlag GmbH; 2000, 91-92.
[24] Ines M, Paolo P, Roberto F, Mohamed S. Experimental studies on the effect of using phase change material in a salinity-gradient solar pond under a solar simulator. *Sol Energy.* 2019; 186: 335-346. https://doi.org/10.1016/j.solener.2019.05.011
[25] EPA. Method 410.4, Revision 2.0: The Determination of Chemical Oxygen Demand by Semi-Automated Colorimetry. 1993
[26] Ozer D, Tunca ET, Oztas NA. Effects of fuel type on iron vanadate nanocatalyst synthesized by solution combustion method for methylene blue degradation. *J Nanopartcl Res.* 2021; 23(8): 1- 12. https://doi.org/10.1007/s11051-021-05303-4
[27] Zhao Y, Yao K, Cai Q, Shi Z, Sheng M, Lin H, Shao M. Hydrothermal route to metastable phase FeVO4 ultrathin nanosheets with exposed {010} facets: Synthesis, photocatalysis and gas-sensing. *Cryst Eng Comm*- 2014; 16(2): 270-276. https://doi.org/10.1039/c3ce41692e
[28] Cui Y, Xue Y, Zhang R, Zhang J, Li X, Zhu X. Vanadium-cobalt oxyhydroxide shows ultralow overpotential for the oxygen evolution reaction. *J Mater Chem A Mater.* 2019; 7(38):21911-21917. https://doi.org/10.1039/c9ta07918a
[29] Tamirat AG, Su WN, Dubale AA, Chen HM, Hwang BJ. Photoelectrochemical water splitting at low applied potential using a NiOOH coated codoped (Sn, Zr) α-Fe2O3 photoanode. *J Mater Chem A Mater.* 2015; 3(11): 5949-5961. https://doi.org/10.1039/c4ta06915c
[30] Frison R, Cernuto G, Cervellino A, Zaharko O, Colonna GM, Guagliardi A, Masciocchi N. Magnetite-maghemite nanoparticles in the 5-15 nm range: Correlating the core-shell composition and the surface structure to the magnetic properties. A total scattering study. *Chem Mat.* 2013; 25(23): 4820-4827. https://doi.org/10.1021/cm403360f
[31] Nithya VD, Selvan RK, Sanjeeviraja C, Radheep DM, Arumugam S. Synthesis and characterization of FeVO4 nanoparticles. *Mater Res Bull.* 2011; 46(10): 1654-1658. https://doi.org/10.1016/j.materresbull.2011.06.005
[32] Zhu X, Chen J, Yu X, Zhu X, Gao X, Cen K. Controllable synthesis of novel hierarchical V2O5/TiO2 nanofibers with improved acetone oxidation performance. *RSC Adv.* 2015; 5(39): 30416-30424. https://doi.org/10.1039/c5ra01001b
[33] Ghiyasiyan-Arani M, Salavati-Niasari M, Masjedi-Arani M, Mazloom F. An easy sonochemical route for synthesis, characterization and photocatalytic performance of nanosized FeVO4 in the presence of aminoacids as green capping agents. *J Mater Sci: Mater Electron.* 2018; 29(1): 474-485. https://doi.org/10.1007/s10854-017-7936-9
[34] George S, Pokhrel S, Ji Z, Henderson BL, Xia T, Li L, Zink JI, Nel AE, Mädler L. Role of Fe doping in tuning the band gap of TiO2 for the photo-oxidation-induced cytotoxicity paradigm. *J Am Chem Soc.* 2011; 133(29): 11270-11278. https://doi.org/10.1021/ja202836s
[35] Jovanović A, Stevanović M, Barudžija T, Cvijetić I, Lazarević S, Tomašević A, Marinković A. Advanced technology for photocatalytic degradation of thiophanate-methyl: Degradation pathways, DFT calculations and embryotoxic potential. *Process Saf Environ Prot.* 2023; 178: 423-443. https://doi.org/10.1016/j.psep.2023.08.054
[36] Lewis KA, Tzilivakis J, Warner DJ, Green A. An international database for pesticide risk assessments and management. *Hum Ecol Risk Assess.* 2016; 22(4): 1050-1064. https://doi.org/10.1080/10807039.2015.1133242
[37] Yoon H, Kim D, Park M, Kim J, Kim J, Srituravanich W, Shin B, Jung Y, Jeon S. Extraordinary Enhancement of UV Absorption in TiO2 Nanoparticles Enabled by Low-Oxidized Graphene Nanodots. *J Phys Chem C.* 2018; 122(22): 12114-12121. https://doi.org/10.1021/acs.jpcc.8b03329
[38] Alamelu K, Jaffar Ali BM. TiO2-Pt composite photocatalyst for photodegradation and chemical reduction of recalcitrant organic pollutants. *J Environ Chem Eng.* 2018; 6(5): 5720-5731. https://doi.org/10.1016/j.jece.2018.08.042
[39] Gonçalves JM, Ireno Da Silva M, Angnes L, Araki K. Vanadium-containing electro and photocatalysts for the oxygen evolution reaction: A review. *J Mater Chem A Mater.* 2020; 8(5): 2171-2206. https://doi.org/10.1039/c9ta10857b
[40] Sindhu AS, Shinde NB, Harish S, Navaneethan M, Eswaran SK. Recoverable and reusable visible-light photocatalytic performance of CVD grown atomically thin MoS2 films. *Chemosphere.* 2022; 287: 132347. https://doi.org/10.1016/j.chemosphere.2021.132347
[41] Guo T, Yang S, Chen Y, Yang L, Sun Y, Shang Q. Photocatalytic kinetics and cyclic stability of photocatalysts Fe-complex/TiO2 in the synergistic degradation of phenolic pollutants and reduction of Cr(VI). *Environ Sci Pollut Res.* 2021; 28(10): 12459-12473. https://doi.org/10.1007/s11356-020-11220-1
[42] Sigma Aldrich 2023. https://www.sigmaaldrich.com/RS/en/search (accessed May 22, 2023)

Fotodegradacija tiofanat-metila pod dejstvom svetlosti koja imitira sunčevo zračenje korišćenjem novih kompozitnih fotokatalizatora

Aleksandar A. Jovanović[1], Mladen D. Bugarčić[1], Miroslav D. Sokić[1], Tanja S. Barudžija[2], Vladimir P. Pavićević[3] i Aleksandar D. Marinković[3]

[1]*Institut za tehnologiju nuklearnih i drugih mineralnih sirovina, Beograd, Srbija*
[2]*Univerzitet u Beogradu, Institut za nuklearne nauke "Vinča" - Institut od nacionalnog značaja, Beograd, Srbija*
[3]*Univerzitet u Beogradu, Tehnološko-metalurški fakultet, Beograd, Srbija*

(Naučni rad)

Izvod

Ovaj rad ima za cilj da prikaže uticaj prisustva nanočestica na površini titanijum (IV) oksida na fotokatalitički kapacitet razlaganja prisutnog organskog polutanta pod dejstvom simulirane sunčeve svetlosti. U tu svrhu, površina rutil titanijum (IV) oksida (r-TiO_2) dekorisana je železo vanadatom ($FeVO_4$/r-TiO_2) i vanadijumom supstituisanim getitom ($Fe_{1-x}V_xOOH$/r-TiO_2). Dobijeni kompoziti su okarakterisani primenom skenirajuće elektronske mikroskopije u emisionom polju uz energetsku disperzionu spektroskopiju, difrakcije X-zraka na sprašenim uzorcima, adsorpcijom azota na tački ključanja primenom Brunauer-Emet-Teler metodologije, infracrvene spektroskopije sa Furijeovom transformacijom u modu smanjene totalne refleksije i spektroskopije difuzne refleksije ultraljubičasto-vidljivog zračenja. Oba fotokatalizatora su pokazala veću fotoaktivnost od komercijalnog r-TiO_2 za degradaciju tiofanat-metila (2,5 h umesto 5 h). Tokom ispitivanja ispitivani su faktori kao što su vreme zračenja, količina katalizatora i koncentracija pesticida. Takođe, fotokatalizatori su primenjeni u uzastopnim višecikličnim testovima degradacije da bi se ispitala njihova efikasnost tokom dužeg vremena eksploatacije. Praćenje brzine uklanjanja vršeno je pomoću spektrometrije ultraljubičastog/vidljivog zračenja i tečne hromatografije visokih performansi. Pomoćni alat za proveru potpunosti razgradnje fungicida jeste određivanje hemijske potrošnje kiseonika nakon svake faze tretmana. Koncentracija posmatrane zagađujuće materije u tretiranim uzorcima je ispod propisanog zakonskog nivoa. Pripremljeni materijali su pokazali veliku stabilnost, postojanost i fotokatalitičku aktivnost što predstavlja dobru osnovu za primenu ovog procesa u realnim postrojenjima za prečišćavanje otpadnih voda.

Ključne reči: fotokataliza; titanijum (IV) oksid; unapređeni oksidacioni procesi; zagađenje pesticidima; otpadne vode

Toxic dye removal by thermally modified lignocellulosic waste in a three-phase air-lift reactor: Kinetic insights

Anja Antanasković[1], Zorica Lopičić[1], Tatjana Šoštarić[1], Vladimir Adamović[1], Slobodan Cvetković[2], Jovana Perendija[2] and Milan Milivojević[3]

[1]*Institute for Technology of Nuclear and Other Mineral Raw Materials, Belgrade, Serbia*
[2]*University of Belgrade, Institute of Chemistry, Technology and Metallurgy, Belgrade, Serbia*
[3]*University of Belgrade, Faculty of Technology and Metallurgy, Serbia*

Abstract
This paper investigates the influence of the air flow rate in a three-phase air-lift reactor on the sorption of toxic dye, Brilliant green, onto a promising and efficient sorbent, sour cherry stone biochar. In order to gain a comprehensive insight into the sorbent/sorption behaviour, sour cherry stone biochar was characterized by Fourier transform infrared spectroscopy with attenuated total reflection, pH of the suspension, point of zero charge, scanning electron microscopy with energy-dispersive X-ray spectroscopy and X-ray diffraction. The experiments were performed in an air-lift reactor using airflows of 2.50 and 5.55 $dm^3 h^{-1}$. The experimental data of sorption kinetics experiments were fitted by non-linear form of pseudo-first and, pseudo-second models as well as the Weber-Morris model based on intraparticle diffusion. The overall sorption rate was found to be limited by the Brilliant Green mass transport rate to the sorbent at a lower airflow and thus mixing intensity, while it was kinetically controlled at a higher rate following the pseudo-second order kinetic model. Furthermore, sorption at lower air flow was delayed by mass transfer resistance through the liquid boundary layer surrounding sorbent particles. Presented results clearly indicate that airflow intensity plays a significant role in the overall sorption kinetics and support possible application of the applied biochar for efficient Brilliant Green sorption.

Keywords: Biowaste; sour cherry stone; pyrolysis, sorption; Brilliant green; kinetic study.

Available on-line at the Journal web address: http://www.ache.org.rs/HI/

ORIGINAL SCIENTIFIC PAPER

UDC: 547.458.84-027.332:667-045.38:531.3

Hem. Ind. **78(3)** 241-252 (2024)

1. INTRODUCTION

Some of the most pronounced global problems that mankind is facing today are environmental pollution and increased energy consumption. The main reasons for these problems are rapid industrial and technological developments, population growth and urbanization, as well as resource depletion. Consequently, large amounts of wastewater loaded with different organic and inorganic pollutants are generated every day, representing a huge burden on the environment. Considering that water is one of the finite natural resources, the global demand for preserving its quality is dramatically increasing [1,2]. Among various pollutants, synthetic dyes from different industries (especially from textile, leather, paper, cosmetics, tanning, printing, *etc.*) may be particularly hazardous to humans and aquatic life either because they are toxic, carcinogenic, teratogenic or mutagenic, or due to the change of water colour and prevention of sunlight permeation [1]. Having in mind the estimated future increase in the global dye market [3], an increase in the resulting water pollution is expected. The main challenges connected to the treatment of wastewater contaminated with dyes are caused by their composition and relatively high stability and resistance to degradation by oxidizing agents, aerobic digestion, heat, and light [4].

Brilliant green (BG) is a toxic, positively charged (cationic), organic dye mostly used in textile, paper, rubber, printing, and other dye-based industries [5]. It is well known that cationic dyes are more toxic than anionic ones and that they can cause serious health problems in some cases, even at extremely low concentrations (~1 mg dm^{-3}) [6]. Harmful

Corresponding authors:Anja Antanasković; Institute for Technology of Nuclear and Other Mineral Raw Materials, 86 Franchet d'Esperey St. 11000 Belgrade, Serbia
Paper received: 7 June 2023; Paper accepted: 18 August 2024; Paper published: 11 September 2024.
E-mail: a.antanaskovic@itnms.ac.rs
https://doi.org/10.2298/HEMIND230607015A

effects of BG in small doses are mainly connected to the gastrointestinal and respiratory tracts causing irritation and symptoms such as vomiting, diarrhoea, kidney irritation, nausea, coughing, and shortness of breath, while in larger doses BG may cause methemoglobinemia, cardiovascular collapse and death due to respiratory failure [5]. In addition, prolonged exposure can cause organ damage [4,7]. Therefore, it is necessary to reduce the level of the BG dye present in the wastewater before it is discharged into the environment.

Biodegradation of dyes, although very attractive, is not practical for BG removal since it may generate metabolites that are highly toxic, carcinogenic, and mutagenic [5]. Other commonly used methods for dye removal are chemical coagulation, oxidation, membrane processes, sorption, and ion exchange, but most of those processes also have some drawbacks, such as large sludge generation, high capital investments or operating costs, membrane fouling, *etc.* [8]. Although sorption has its own drawbacks, among which are sorbent regeneration problems, its advantages have made it the most promising method for continuous removal of dyes at large scale even from highly loaded wastewater [9]. By this process dyes can be removed in a simple, efficient, cost effective and environmentally friendly manner [10,11].

Many different materials have been tested and used as sorbents among which biochar has been identified as one of the potential sorbents for wastewater treatment. Biochar is produced by thermochemical decomposition of biomass in the absence of oxygen. It is a solid, carbon rich material with excellent properties (abundance of surface functional groups, chemical stability, high porosity and high surface area [12]), that make it an attractive sorbent for different applications. In addition, energy and environment inputs for biochar production are lower than those in the other frequently applied technologies for producing sorbents like activated carbon or ionic resins. For example, biochar production costs may be up to six times lower than those of the commercial activated carbon [7]. Besides its efficacious removal of many various pollutants [1,10,13], another issue that makes biochar so attractive is the wide range of waste materials that may be used for its production, which helps in avoiding landfill disposal. In Serbia, large amounts of biowaste from agriculture and food industry may be used for biochar production. Among them, fruit stones are some of the materials that represent promising candidates for further investigations. Serbia is known for its rich fruit-growing tradition and cultivation of various types of fruit, among which sour cherries are one of the most abundant in these regions. According to the data from the Statistical office of the Republic of Serbia [14], the average yearly production of sour cherries in Serbia is 164,000 t. The resulting waste may be used as raw material for biochar production, thus reducing waste disposal and obtaining promising sorbent for pollutants removal.

Kinetics of the sorption process determines the rate and efficiency of sorbate molecules binding to the surface of a sorbent material, where the overall rate of the process is determined by the slowest step. Within the sorption process, there are few steps that may determine the overall rate: film diffusion, pore diffusion and sorption on the solid surface itself. In the cases where the sorption is fast, the process rate is determined by the first two rates i.e. transport of the molecules to the solid surface. For such systems, the increase in mixing will lead to increased overall sorption rates. In addition, it is necessary to minimize the costs of the purification process using the cheapest possible methods and equipment for its accomplishment. Air-lift reactors (ALR) are almost the ideal candidates for such processes. As the first advantage, construction of these reactors is simple without any moving parts [15]. Compared to bubble columns, ALRs have better performance for treating suspensions due to lower energy inputs [16]. Compared to the reactors with mechanical mixing ALRs demand lower power inputs for the same level of mixing, which is of essential importance for low price/high volume processes which is surely the wastewater treatment [17]. Thus, energy demands of ALRs may be three times lower as compared to mechanically mixed reactors indicating the efficient use of energy [18]. In addition, performance of those reactors is almost the same for small and large scale geometries and they can easily work even with high amounts of solid phase [19]. Finally, these reactors can be easily operated in continuous mode [20,21].

The aim of this study was to examine the influence of mixing on the kinetics of dye removal in an ALR system. Sour cherry stone (SCS) was used to produce biochar (SCS-B), a novel efficient dye sorbent, which was characterised by various techniques. A crucial aspect of this study involved determining kinetics of the BG removal process under different airflow conditions. Two kinetic models (pseudo-first and pseudo-second) and one mass transport model (intraparticle diffusion) were tested to interpret the experimental data and explain the influence of mixing on the sorption mechanism of BG onto biochar.

2. EXPERIMENTAL

2. 1. Material

SCSs were collected from the local Serbian fruit processing factory. Collected stones were separated from soft fruit residues, washed in water and dried at room temperature. In order to reduce their size, a vibratory disk mill "Siebtechnik - T S250" (Siebtechnik GmbH, Germany) was used. The particles were sieved into different particle size fractions. For the purpose of this investigation, SCSs with particle size between 0.2 to 0.3 mm were used. The SCSs were pyrolysed in a Nabertherm 1300 muffle furnace (Nabertherm, Germany), at 500 °C for 1.5 h in argon atmosphere, with a heating rate of 10 °C min^{-1}. Finally, the produced SCS-B was kept in vials closed with polypropylene caps before use.

BG was purchased from Sigma-Aldrich, USA. Chemical properties of BG are listed in Table 1. The dye concentration of 1000 mg dm^{-3} was diluted to the experimental solution concentration of 50 mg dm^{-3}, with initial pH of 6.8.

Table 1. Chemical properties of Brilliant green [7]

Name	Brilliant green
Molecular formula	$C_{27}H_{34}N_2O_4S$
Molecular weight, g mol^{-1}	482.63
λ_{max} / nm	624
Solubility in water at 25 °C, g dm^{-3}	100

An internal loop air-lift reactor (with characteristics presented in Table 2) made of Pyrex glass with a concentric draft-tube (Fig. 1) was used in sorption experiments.

Table 2. Geometric characteristics of the experimental ALR

Total / Working volume, dm^3	0.3 / 0.150
Total / Liquid height, m	0.46 / 0.19
Height or the riser draft-tube, m	0.15
Reactor / riser outer diameter, m	0.035 / 0.021
Sparger type	Perforated disc with 8×1 mm orifices

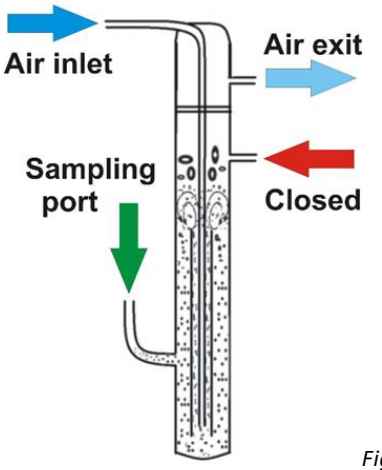

Figure 1. Air-lift design

2. 2. Sorbent characterisation

Various characterisation methods were used to study the physico-chemical properties of SCS-B.

Fourier-transform infrared spectroscopy with attenuated total reflection (FTIR-ATR) was applied to biochar before and after BG sorption in order to examine functional groups responsible for binding of the dye. FTIR analysis was performed using a Thermo Nicolet 6700 FTIR instrument (International Equipment Trading Ltd., USA) in the range of 400 to 4000 cm^{-1}. A background scan was acquired before scanning the samples.

pH values of suspensions (pH_{sus}) of the sorbent in water were determined by using the ASTM D6851-02 standard. A certain dose of sorbent (0.2 g) was added to 30 cm^3 of distilled water and kept in a closed container with mixing at room temperature for 72 h. Then, pH_{sus} was measured by a pH meter SensION3 (Hach, USA).

pH_{pzc} values of SCS and SCS-B were determined according to Milonjić *et al.*[22]. Initial pH values (pH_i) of 50 cm^3 of 0.01 mol dm^{-1} of KNO_3 solutions were adjusted in the range of 2 to 10 and were accurately noted. Then, 0.1 g of the sorbent was added to each solution and shaken for 24 h at 150 rpm. After determined period, the final pH value (pH_f) was measured and recorded.

Surface morphology of SCS and SCS-B was analysed using scanning electron microscopy (SEM), as well as Energy Dispersive X-Ray analysis (EDX) to map the presence of particular components on material surfaces. The SEM-EDX analysis was performed by a JEOL JSM-6610 LV SEM instrument (JEOL Ltd. Japan), on samples covered with a thin layer of gold.

X-ray diffraction (XRD) analysis was used to identify the crystallinity of biochar by a PW-1710 instrument (Philips, Netherlands) with Cu Kα radiation (λ = 1.54178 nm). The 2θ angle was scanned in an interval of 2θ (5 to 30°) with an angular increment of 0.02° and a time step of 1 s.

2. 3. Sorption kinetics

Sorption experiments were carried out in the internal loop ALR at two different airflows of 2.55 and 5.50 dm^3 h^{-1}, provided by using an air pump (LABOPORT N 86 KT.18, Germany). The process parameters were adopted from our previous study [7], which describes detailed investigations of BG removal by biochar of similar composition. In accordance with previous findings, 150 cm^3 of BG solution with the initial concentration of 50 mg dm^{-3} was mixed in ALR with 0.3 g of SCS-B for 120 min, at room temperature and at the selected airflow. Samples of 2 cm^3 were taken at different time intervals (0.5, 1, 2, 5, 15, 30, 45, 60, 75, 90, 105, 120 min), measured at 624 nm using a UV/VIS spectrophotometer (Spekol 1300, Analytik Jena, Germany) and then returned to the ALR. All experiments were performed in duplicate, and average values are presented.

The effectiveness (R) and the final sorption capacity at applied operational parameters (q_f) of BG sorption by SCS-B were calculated using Equations (1) and (2):

$$R = \frac{C_i - C_f}{C_i} 100 \quad (1)$$

$$q_f = \frac{(C_i - C_f)V}{m} \quad (2)$$

where C_i and C_f are initial and final concentration of BG, respectively, V is the volume of the dye solution and m is the mass of the sorbent.

In order to describe and analyse kinetics of the sorption process of BG on SCS-B, the experimental data were fitted using pseudo-first and pseudo-second models, as well as the Weber-Morris model based on intraparticle diffusion. These models are listed in Table 3.

Table 3. Models/equations used to asses Brilliant green sorption

Name of kinetic model	EEquation	Parameter	Ref.
Pseudo-first order	$q_t = q_e (1 - e^{-k_1 t})$	q_t / mg g^{-1}: mass of the sorbate per mass of the sorbent at any time t q_e / mg g^{-1}: sorption capacity at equilibrium k_1 / min^{-1}: the pseudo-first order rate constant	[23]
Pseudo-second order	$q_t = \frac{t}{\frac{1}{k_2 q_e^2} + \frac{1}{q_e}}$	k_2 / g mg^{-1} min^{-1}: the pseudo- second order rate constant	[24]
Weber-Morris model based on intraparticle diffusion	$q_t = K_d t^{0.5} + C$	K_d / mg g^{-1} $min^{1/2}$: the intra-particle diffusion parameter C / mg g^{-1}: intercept	[25]

3. RESULTS AND DISCUSSION

3. 1. Sorbent characterisation

Pyrolysis causes significant changes in physical and chemical properties of the raw material. The obtained FTIR-ATR spectra are used to identify surface functional groups of biochar before and after BG sorption. As can be seen in Figure 2, the FTIR spectra were similar, indicating that the BG sorption process had negligible effects on functional groups of biochar. The peak at 2649 cm^{-1} indicates the presence of aliphatic groups (-CH_n) in biochar [26]. The band at 1697 cm^{-1} corresponds to the stretching vibration of carbonyl (C=O) groups [27], while the peak at 1580 cm^{-1} is related to C=O stretching and aromatic C=C vibrations [26]. After the sorption of BG, new peaks appeared between 1439 and 1329 cm^{-1} which were assigned to the N-H bending vibration and the C-N stretching vibration, revealing that BG sorption involved the interaction of amino groups on the biochar surface with BG molecules [28]. The strong peak at 1173 cm^{-1} was related to the C-O stretching vibration of phenolic hydroxyl groups on the surface of biochar, which interacted with the C=O group of BG through hydrogen bonding, leading to the split of this peak into two new peaks at 1187 and 1156 cm^{-1}. The peaks observed in the range of 749 and 874 cm^{-1} in biochar were attributed to the presence of aromatic compounds, with no significant effect on dye sorption [29].

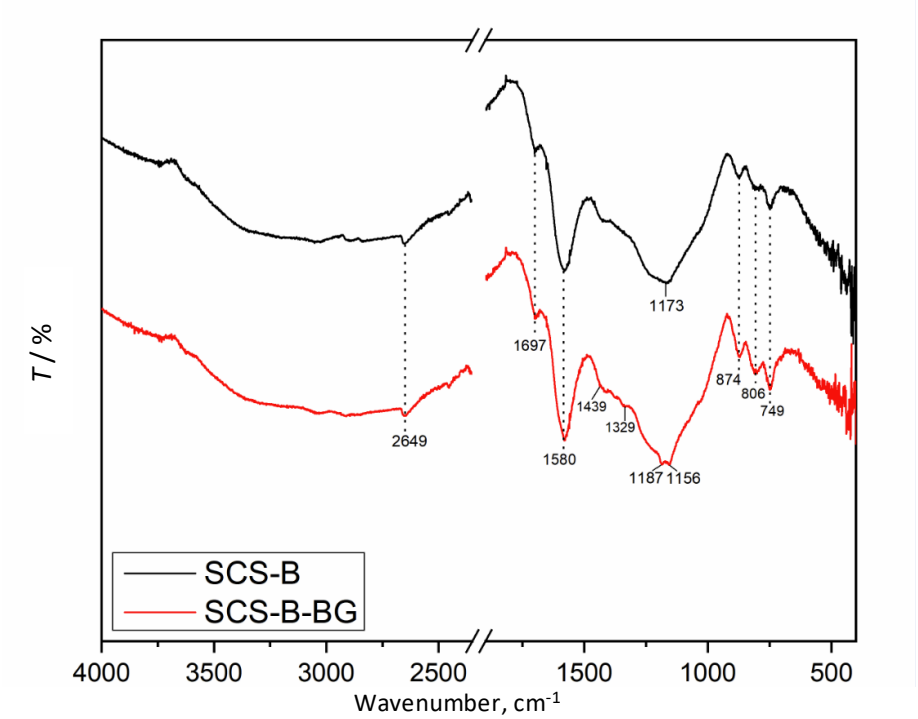

Figure 2. FTIR-ATR spectra of SCS-B before and after dye sorption

When distilled water comes in contact with a sorbent, the pH value changes due to the interaction with acidic and alkali groups on its surface. Contact pH or pH_{sus} is an indicator of the acid-alkali nature of a material surface [30]. pH_{sus} of the SCS-B was found to be 6.48, which is higher than the measured pH_{sus} value of the SCS amounting to 4.11. The low alkalinity of pH_{sus} for biochar can be attributed to the presence of acidic functional groups, such as carboxyl and phenolic groups, the presence of which was proven by FTIR. These findings are consistent with the results of Antanasković *et al.* [7], reporting that biochar originating from peach stone was more alkaline (6.91) than the native material (5.14).

The point of zero charge (pH_{pzc}) represents a pH value at which the surface of a sorbent exhibits a zero charge. The values of the pH_{pzc} may suggest possible electrostatic interactions between the sorbent and sorbate in a dye solution. At pH values below the pH_{pzc}, the material surface is positively charged, favouring the attraction of negatively charged ions, while at solution pH values above pH_{pzc}, the sorbent surface is negatively charged and can attract positively charged ions [31]. As can be seen in Figure 3, the pH_{pzc} value for SCS was 5.00, while that of SCS-B was 6.60. Thus, SCS demonstrated neutrality within a limited initial pH range (6-7), whereas the SCS-B exhibited neutrality in a wide range of initial

pH values (6-9). It was expected that the pH_{pzc} of biochar would be higher than that of raw materials due to the elimination of acidic groups and creation of basic functional groups during pyrolysis. Since the pH value of the BG solution(6.8) is higher than the pH_{pzc} value, surfaces of the biochar remain negatively charged, which favours sorption of cations, such as BG [32].

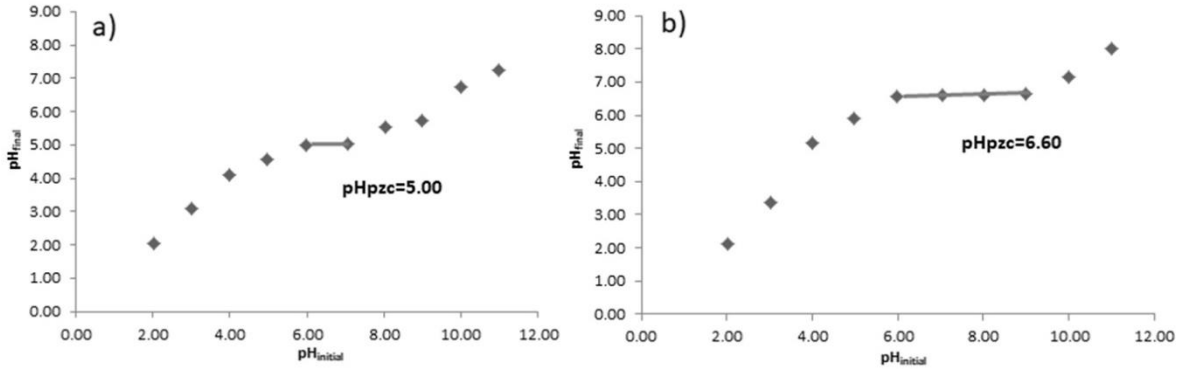

Figure 3. Determination of final pH values in the suspensions as functions of the initial values for a) SCS; b) SCS-B

SEM was used to closely examine morphology of the material surface. SCS-B has a porous structure with irregular pores of various sizes and shapes (Fig. 4a), which is a result of decomposition and volatilisation of the main components (hemicellulose, cellulose and partial lignin) during pyrolysis, which increased the surface area of the obtained biochar promoting later sorption of the dye. Using a similar material (cherry stone), Pehlivan and Kahraman [33], also confirmed that pyrolysis of lignocellulosic biomass produces a porous material with a large number of cracks and channels. The EDX analysis (Fig. 4b) revealed that the biochar was composed mainly of carbon (75.44 %), followed by oxygen (22.78 %), while the presence of magnesium, calcium and potassium was only 0.28, 1.01 and 0.49 %, respectively. These results indicated that carbon is the dominant element, as expected, while oxygen is also present, dominantly by oxygen-containing functional groups such as a carbonyl (also shown by the FTIR analysis). Similar findings were obtained by the EDX analysis previously [13], for biochar of a similar lignocellulosic structure (made from peach stone).

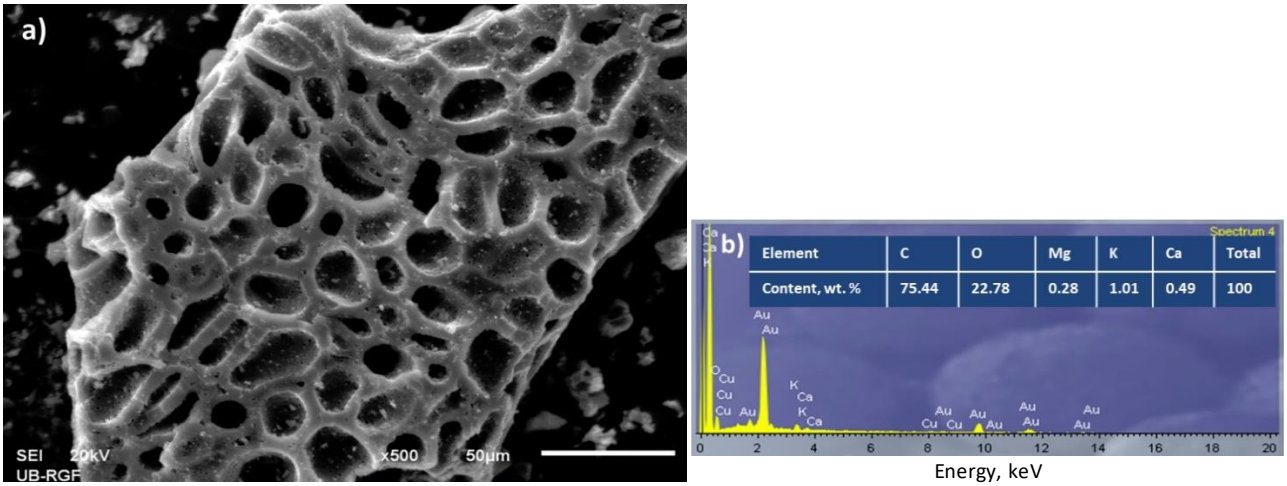

Figure 4. SEM-EDX analysis of the SCS-B: a) SEM micrograph (scale bar: 50 µm); b) EDX analysis results

The XRD pattern for SCS-B is shown in Figure 5. The appearance of two broad diffraction peaks at 2θ of 20 to 30° and 41°, corresponding to the 002 and 100 reflection planes, respectively, indicates an amorphous structure, and presence of carbon and graphite. The high peak at 24° originates from high carbon (C_{12} to C_{60}) concentration, due to high pyrolysis temperature (500 °C) [34]. The peak at 41° belongs to the C (100) plane of condensed carbonized structures [35]. These results confirmed the amorphous structure of SCS-B, which lacks a long-range order in

atomic/molecular arrangement, resulting in a porous and disordered structure [36]. Such structure contributes to the surface area increase, which improves the availability of active sites on for sorption of the large dye molecules.

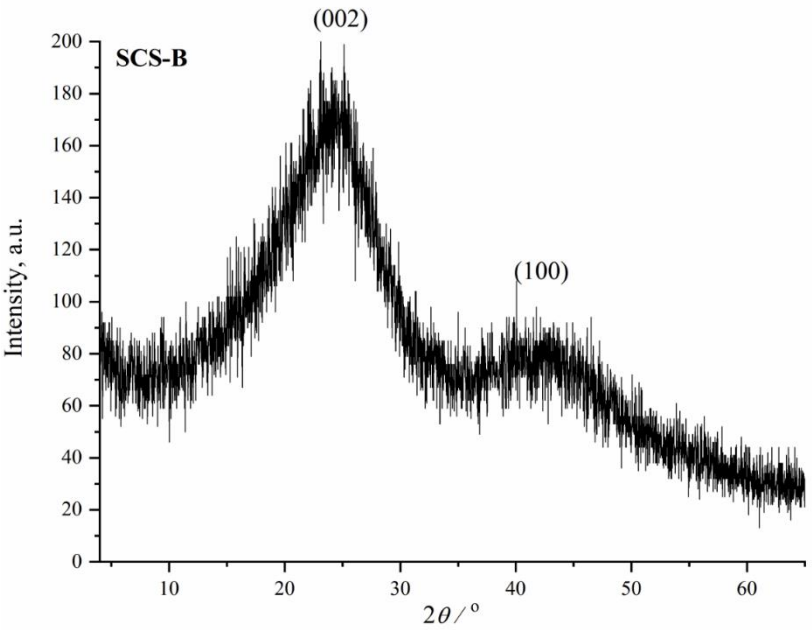

Figure 5. XRD pattern of SCS-B

3. 2. Sorption kinetics

Studies of sorption kinetics provide insights into the overall rate of the sorption process, which is a crucial factor in evaluating the efficiency of the sorbent, as well as insights into the sorption mechanism [37]. The sorption process is affected by numerous parameters and one of them is mixing, which was examined in this study. The influence of mixing at airflow rates of 2.55 and 5.50 $dm^3\ h^{-1}$ on the overall rate of dye sorption was investigated using two reaction kinetic models (pseudo-first order and pseudo-second order) and one intraparticle diffusion model. The models were applied in nonlinear forms and fitted using nonlinear regression analysis using OriginPro (2021 version) software. Figure 6 illustrates the time-dependent profiles of sorption of BG onto SCS-B, and application of the two kinetic models, while the related parameters are summarized in Table 4.

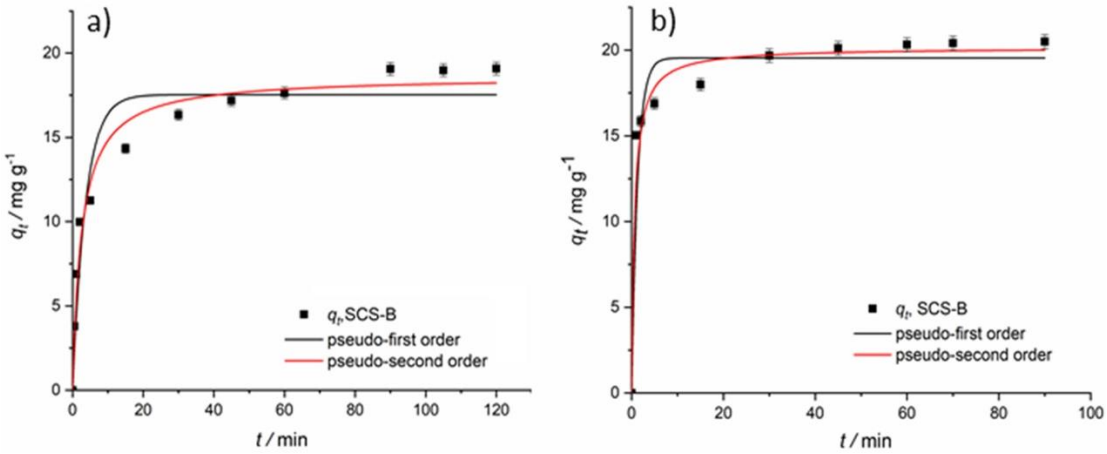

Figure 6. Sorbed BG per mass of SCS-B (q_t) as a function of time: experimental data (symbols) and the best fit predictions of the pseudo-first and pseudo second order kinetics with airflow: a) 2.55 $dm^3\ h^{-1}$; b) 5.50 $dm^3\ h^{-1}$

With the use of a higher airflow (Fig. 6b), equilibrium is reached in approximately 45 min, which is almost twice as fast as it is at the lower airflow rate (Fig. 6a), clearly indicating the effects of mass transport. The increased airflow

enhances the external mass transfer, allowing BG molecules to reach the SCS-B surface more rapidly. Thus, the application of the higher airflow of 5.50 dm³ h^{-1} has shown to be more effective in removing BG. After only 5 min, almost 70 % of dye was removed, while with the use of the airflow of 2.55 dm³ h^{-1} only 48 % was removed. Also, the statistical parameters of the models fitting (R^2 and χ^2) were lower for the lower airflow. Higher internal circulation has the potential to influence the overall rate of dye sorption by increasing the mass transport rate to the surface and possibly within the pores of the biochar [38]. Lowering of the external mass transport limitations and the diffusion distance through the film induced the higher sorption rate and the increase in the apparent overall rate constant.

Data presented in Table 4 demonstrate that reaction kinetic models have shown higher correlation with the data at the higher flowrate than at the lower where the influences of mass transport are not negligible. These data show that for the higher airflow rate, the pseudo-first order model does not fit the experimental data well, which can be also observed in Figure 6b. The correlation coefficient (R^2) for the pseudo-second order was higher (0.9892) then for the pseudo-first order (0.9700), while the chi-squared value (χ^2) was lower (0.5308) compared to the value of the pseudo-first model (1.4697). Additionally, the experimental equilibrium sorption capacity q_{exp} value (20.49 mg g^{-1}) is very close to the calculated q_{calc} values (20.15 mg g^{-1}) for the pseudo-second order kinetic model, indicating again that mass transport limitations become less prominent at the higher airflow and better mixing. Giri *et al*. [39] also reported that the pseudo second-order kinetic model could effectively explain sorption of BG using the corncob biochar, with the sorption capacity of 5.73 mg g^{-1}.

The application of the intraparticle diffusion model provides a deeper understanding of the rate limiting steps in the two experimental set-ups realized in the present study. In specific, as mentioned above, the sorption process involves several steps. Initially, the sorbate molecules migrate from the bulk solution to the liquid boundary layer, and this step depends on agitation and solution homogeneity. In the next step, these molecules diffuse through the liquid boundary layer at the sorbent surface, where they bind to the active sites, while one part of the molecules pass through the sorbent micropores and reach the interior where they bind. The overall sorption rate will be controlled by the slowest of those processes or the rate-limiting step [40].

The resistance to mass transfer within the liquid film surrounding the particle is only significant during the initial phase of diffusion [41]. Examining sorption, it is usually assumed that the sorbent particles are spherical, which leads to the expression for the initial phase $q_t/q_e < 0.4$ [42]. Accordingly, the intraparticle diffusion model was applied to the experimental data in the initial period ($q_t/q_e < 0.4$), presented in Figure 7, while the model parameters are listed in Table 4.

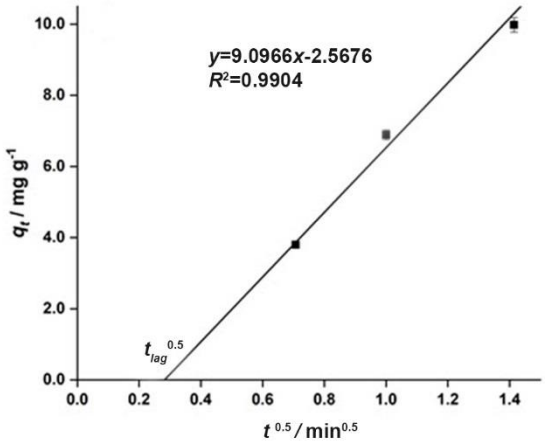

Figure 7. Application of the intraparticle diffusion model (lines) on the experimental data (symbols) of BG sorption on SCS-B in the initial period ($q_t/q_e < 0.4$) at airflow 2.55 dm³ h^{-1}

Under the airflow of 2.55 dm^3 h^{-1}, the experimental data showed a straight line with a negative y-axis intercept (C = -2.57 mg g^{-1}) and a positive x-axis intercept ($t_{lag}^{0.5}$) of 0.282 min$^{0.5}$ leading to the lag time of 0.08 min. The negative value of C indicates the effect of external film diffusion resistance, which limits the sorption rate alongside intraparticle diffusion [42,43]. Consequently, sorption is delayed for less than 5 s due to the external diffusion resistance of the film.

This short delay in sorption suggests that the resistance of the outer diffusion film was low or that other factors had a minor effect on the sorption delay. These findings are consistent with the results reported by Zhu et al. [44] who observed a negative C value and delayed sorption during the sorption of pyridine onto polymeric adsorbents.

Applying a higher airflow rate, 5.50 dm³ h^{-1}, the process was observed to be kinetically controlled, rather than controlled by intraparticle diffusion. The increased airflow rate resulted in a significant reduction of the sorbate boundary layer and the film mass transfer resistance around the sorbent particles [45]. It might be assumed that film diffusion was so rapid that it was not experimentally observed in the measurements, as the first sampling point was after 1 min, potentially after the initial phase had already been finished. The higher mixing induced by the higher airflow velocity enhances the transport rate of the dye, reducing the time dye molecules spend on the sorbent surface and consequently decreasing the diffusion time [46]. Perez Cadena *et al*. [47] investigated biological decolorization of Amaranth dye with *Trametes polyzona* in an air-lift reactor under three airflow regimes. They have concluded that the rate of decolourisation is a function of the aeration regime, where the higher aeration rate is associated with the faster decolourisation rate.

Table 4. Sorption kinetic parameters of BG removal by SCS-B with different airflows

Model	Parameter	Flow of 2.55 dm³ h^{-1}	Flow of 5.50 dm³ h^{-1}
Pseudo-first order	q_{exp} / mg g^{-1}	19.09	20.49
	q_{calc} / mg g^{-1}	17.53	19.54
	k_1 / min^{-1}	0.272	0.762
	R^2	0.9169	0.9700
	χ^2	3.360	1.4697
Pseudo-second order	$q_{e,calc}$ / mg g^{-1}	18.62	20.15
	k_2 / g mg^{-1} min^{-1}	0.021	0.075
	R^2	0.9688	0.9892
	χ^2	1.2616	0.5308
Intraparticle diffusion	K_d / mg g^{-1} $min^{1/2}$	9.10	-
	C / mg g^{-1}	-2.57	-
	R^2	0.9904	-

The sorption capacity (obtained from experimental kinetic studies under applied operational parameters) of SCS-B towards BG, has been compared with other biochars reported in the literature, which is presented in Table 5. The sorbent prepared in this study exhibited relatively high sorption capacity for BG of 20.49 mg/g, which represents the significant basis for further research.

Table 5. Comparison of calculated sorption capacities of various biochars for removal of BG dye

Biochar	Parameter				Ref.
	pH	C_i / mg L^{-1}	t / h	q_{exp} / mg g^{-1}	
Soybean straw	8.0	500	1	12.53	[5]
Peach stone	7.0	50	2	31.00	[7]
Corncob	8.1	50	3.5	5.73	[39]
Rice straw	7.0	20	3	17.61	[48]
Sour cherry stone	6.8	50	2	20.49	This study

4. CONCLUSION

In this paper, lignocellulosic waste material, originating from the food industry, was pyrolysed to produce biochar, which was then examined as a sorbent. This study demonstrates the influence of the mixing within the air-lift reactor on the overall rate of sorption of toxic dye, BG, onto the biochar. The results of the biochar characterization indicate an amorphous and porous structure, with a negatively charged surface, making it highly suitable for efficient sorption of cationic dyes, such as BG. The overall sorption rate was found to be limited by the BG mass transport rate to the sorbent at a lower airflow and thus mixing intensity, while it was kinetically controlled at a higher rate following the pseudo-second order kinetic model. The findings highlight the significant role that mixing had on the sorption process, leading

to improved removal of the toxic dye with the airflow increase. Applying higher airflow rate, the process reached equilibrium almost twice faster compared to the lower rate. The use of a higher airflow reduces the influence of the liquid boundary layer indicating again that mass transport limitations become less prominent at the higher airflow and better mixing, resulting in enhanced convective mass transfer, induced by the increase in the liquid velocity, which facilitates the dye molecules transport to the sorption sites. The obtained results indicate that three-phase air-lift reactors may be promising equipment for sorption processes allowing lower energy inputs.

Acknowledgements: This work was supported by the Ministry of Science, Technological Development and Innovation of the Republic of Serbia (grant number 451-03-66/2024-03/200023). Also, part of the research was funded by the Science Fund of the Republic of Serbia, Grant #7439, "From Waste to Food and Soil Enrichment - minimizing waste by applying circular economy in fruits/vegetables processing industry" – WasteBridge

REFERENCES

[1] Elgarahy AM, Elwakeel KZ, Mohammad SH, Elshoubaky GA. A critical review of biosorption of dyes, heavy metals and metalloids from wastewater as an efficient and green process. *Clean Eng Technol.* 2021; 4: 100209. https://doi.org/10.1016/j.clet.2021.100209

[2] Anastopoulos I, Ahmed MJ, Hummadi EH. Eucalyptus-based materials as adsorbents for heavy metals and dyes removal from (waste)waters. *J Mol Liq.* 2022; 356: 118864. https://doi.org/10.1016/j.molliq.2022.118864

[3] Siregar Global dyes & pigments market size report, 2021-2028. https://www.grandviewresearch.com/industry-analysis/dyes-and-pigments-market. Accessed January 7, 2023.

[4] Fiaz R, Hafeez M, Mahmood R. Removal of brilliant green (BG) from aqueous solution by using low cost biomass salix alba leaves (SAL): Thermodynamic and kinetic studies. *J Water Reuse Desalin.* 2020; 10(1) :70-81. https://doi.org/10.2166/wrd.2020.054

[5] Vyavahare G, Gurav R, Patil R, Sutar S, Jadhav P, Patil D, Yang YH, Tang J, Chavan C, Kale S, Jadhav J. Sorption of brilliant green dye using soybean straw-derived biochar: characterization, kinetics, thermodynamics and toxicity studies. *Environ Geochem Health.* 2021; 43(8): 2913-26. https://doi.org/10.1007/s10653-020-00804-y

[6] Bayramoglu G, Altintas B, Arica MY. Adsorption kinetics and thermodynamic parameters of cationic dyes from aqueous solutions by using a new strong cation-exchange resin. *Chem Eng J.* 2009; 152(2-3): 339-346. https://doi.org/10.1016/j.cej.2009.04.051

[7] Antanasković A, Lopičić Z, Pehlivan E, Adamović V, Šoštarić T, Milojković J, Milivojević M. Thermochemical conversion of non-edible fruit waste for dye removal from wastewater. *Biomass Convers Biorefinery.* 2023; (0123456789). https://doi.org/10.1007/s13399-023-04083-2

[8] Haskis P, Tsolis P, Tsiantouka L, Mpeza P, Barouchas P, Giannopoulos G, Pashalidis I, Anastopoulos I. Biosorption of Methylene Blue dye by Ligustrum lucidum fruits biomass: Equilibrium, isotherm, kinetic and thermodynamic studies Panagiotis. *Glob NEST J.* 2023; 25: 97-104. https://doi.org/https://doi.org/10.30955/gnj.005294

[9] Foo KY, Hameed BH. An overview of dye removal via activated carbon adsorption process. *Desalin Water Treat.* 2010; 19(1-3): 255-274. https://doi.org/10.5004/dwt.2010.1214

[10] Barquilha CER, Braga MCB. Adsorption of organic and inorganic pollutants onto biochars: Challenges, operating conditions, and mechanisms. *Bioresour Technol Reports.* 2021; 15: 100728. https://doi.org/10.1016/j.biteb.2021.100728

[11] Ahmed MJ, Danish M, Anastopoulos I, Iwuozor KO. Recent progress on corn (*Zea mays* L.)-based materials as raw, chemically modified, carbonaceous, and composite adsorbents for aquatic pollutants: A review. *J Anal Appl Pyrolysis* 2023; 172(2): 106004. https://doi.org/10.1016/j.jaap.2023.106004

[12] Srivatsav P, Bhargav BS, Shanmugasundaram V, Arun J, Gopinath KP, Bhatnagar A. Biochar as an eco-friendly and economical adsorbent for the removal of colorants (Dyes) from aqueous environment: A review. *Water.* 2020; 12(12): 3561. https://doi.org/10.3390/w12123561

[13] Lopičić Z, Avdalović J, Milojković J, Antanasković A, Ljević M, Lugonja N, Šoštarić T. Removal of diesel pollution by biochar - support in water remediation. *Hem Ind.* 2021; 75(6): 329-39. https://doi.org/10.2298/HEMIND210514029L

[14] Statistical office of the Republic of Serbia. https://www.stat.gov.rs/en-us/. Accessed May 12, 2023.

[15] Milivojević M, Andrejić D, Bugarski B. Effects of air-lift reactor dimensions on its hydrodinamic characteristics. *Hem Ind.* 2010; 64(1): 35-46. https://doi.org/10.2298/HEMIND1009035M

[16] Milivojevic M, Pavlou S, Pajic-Lijakovic I, Bugarski B. Dependence of slip velocity on operating parameters of air-lift bioreactors. *Chem Eng J.* 2007; 132(1-3): 117-23. https://doi.org/10.1016/j.cej.2007.01.026

[17] Jones SMJ, Harrison STL. Aeration energy requirements for lipid production by *Scenedesmus* sp. in airlift bioreactors. *Algal Res* 2014; 5(1): 249-57. https://doi.org/10.1016/j.algal.2014.03.003

[18] Cerri MO, Badino AC. Shear conditions in clavulanic acid production by *Streptomyces clavuligerus* in stirred tank and airlift bioreactors. *Bioprocess Biosyst Eng.* 2012; 35(6): 977-84. https://doi.org/10.1007/s00449-012-0682-8

[19] Milivojevic M, Pavlou S, Bugarski B. Liquid velocity in a high-solids-loading three-phase external-loop airlift reactor. *J Chem Technol Biotechnol.* 2012; 87(11): 1529-40. https://doi.org/10.1002/jctb.3783
[20] Veljković M, Simović M, Banjanac K, Ćorović M, Milivojević A, Milivojević M, Bezbradica D. Heterofunctional epoxy support development for immobilization of fructosyltransferase from Pectinex® Ultra SP-L: batch and continuous production of fructo-oligosaccharides. *React Chem Eng.* 2022; 7(12): 2518-26. https://doi.org/10.1039/d2re00182a
[21] Veljković M, Stepanović R, Banjanac K, Ćorović M, Milivojević A, Simović M, Milivojević M, Bezbradica D. Continuous production of fructo-oligosaccharides using selectively immobilized fructosyltransferase from *Aspergillus aculeatus* onto Purolite® A109. *J Ind Eng Chem.* 2023; 117: 149-56. https://doi.org/10.1016/j.jiec.2022.09.051
[22] Milonjić SK, Ruvarac AL, Šušić M V. The heat of immersion of natural magnetite in aqueous solutions. *Thermochim Acta.* 1975; 11(3): 261-266. https://doi.org/10.1016/0040-6031(75)85095-7
[23] Lagergren S. About the theory of so called adsorption of soluble substances. *K Sven Veternskapsakad Handl.* 1898; 24:1-39.
[24] Ho YS, McKay G. Pseudo-second order model for sorption processes. *Process Biochem.* 1999;34: 451-465.
[25] Weber, W.J. Morris JC. Kinetics of adsorption on carbon from solution. *J Sanit Eng Div.* 1963; 89: 31-60.
[26] Behazin E, Ogunsona E, Rodriguez-Uribe A, Mohanty AK, Misra M, Anyia AO. Mechanical, chemical, and physical properties of wood and perennial grass biochars for possible composite application. *BioResources.* 2016 ;11(1): 1334-1348. https://doi.org/10.15376/biores.11.1.1334-1348
[27] Sakhiya AK, Vijay VK, Kaushal P. Efficacy of rice straw derived biochar for removal of Pb+2 and Zn+2 from aqueous: Adsorption, thermodynamic and cost analysis. *Bioresour Technol Reports.* 2022; 17(6): 100920. https://doi.org/10.1016/j.biteb.2021.100920
[28] Ukkund SJ, Puthiyillam P, Alshehri HM, Goodarzi M, Taqui SN, Anqi AE, Safaei MR, Ali MA, Syed UT, Mir RA, Elfasakhany A, Eed EM, Siddiqui MIH, Mokashi I, Soudagar MEM. Adsorption method for the remediation of brilliant green dye using halloysite nanotube: Isotherm, kinetic and modeling studies. *Appl Sci.* 2021; 11(17): 8088. https://doi.org/10.3390/app11178088
[29] Keiluweit M, Nico PS, Johnson M, Kleber M. Dynamic molecular structure of plant biomass-derived black carbon (biochar). *Environ Sci Technol.* 2010; 44(4): 1247-1253. https://doi.org/10.1021/es9031419
[30] Paunovic O, Pap S, Maletic S, Taggart MA, Boskovic N, Turk Sekulic M. Ionisable emerging pharmaceutical adsorption onto microwave functionalised biochar derived from novel lignocellulosic waste biomass. *J Colloid Interface Sci.* 2019; 547: 350-360. https://doi.org/10.1016/j.jcis.2019.04.011
[31] Saghir S, Pu C, Fu E, Wang Y, Xiao Z. Synthesis of high surface area porous biochar obtained from pistachio shells for the efficient adsorption of organic dyes from polluted water. *Surfaces and Interfaces.* 2022; 34 :102357. https://doi.org/10.1016/j.surfin.2022.102357
[32] Guilhen SN, Watanabe T, Silva TT, Rovani S, Marumo JT, Tenório JAS, Mašek O, Araujo LG de. Role of Point of Zero Charge in the Adsorption of Cationic Textile Dye on Standard Biochars from Aqueous Solutions: Selection Criteria and Performance Assessment. *Recent Prog Mater.* 2022; 4(2). https://doi.org/10.21926/rpm.2202010
[33] Kahraman HT, Pehlivan E. Cr^{6+} removal using oleaster (*Elaeagnus*) seed and cherry (*Prunus avium*) stone biochar. *Powder Technol.* 2017; 306: 61-67. https://doi.org/10.1016/j.powtec.2016.10.050
[34] Chen T, Liu R, Scott NR. Characterization of energy carriers obtained from the pyrolysis of white ash, switchgrass and corn stover - Biochar, syngas and bio-oil. *Fuel Process Technol.* 2016; 142: 124-134. https://doi.org/10.1016/j.fuproc.2015.09.034
[35] Zhang S, Wang J. Removal of chlortetracycline from water by immobilized Bacillus subtilis on honeysuckle residue-derived biochar. *Water Air Soil Pollut.* 2021; 232(6): 236. https://doi.org/10.1007/s11270-021-05193-1
[36] Einfal T, Planinšek O, Hrovat K. Methods of amorphization and investigation of the amorphous state. *Acta Pharm.* 2013; 63(3): 305-334. https://doi.org/10.2478/acph-2013-0026
[37] Aljeboree AM, Alshirifi AN, Alkaim AF. Kinetics and equilibrium study for the adsorption of textile dyes on coconut shell activated carbon. *Arab J Chem.* 2017; 10: S3381-S3393. https://doi.org/10.1016/j.arabjc.2014.01.020
[38] Nassar M, Farrag T. Kinetics and Process Design for Adsorption of Maxilon Red Dye From Aqueous Solutions Using Gas Mixing. *Int Conf Chem Environ Eng.* 2012; 6(6): 1-13. https://doi.org/10.21608/iccee.2012.35794
[39] Giri BS, Gun S, Pandey S, Trivedi A, Kapoor RT, Singh RP, Abdeldayem OM, Rene ER, Yadav S, Chaturvedi P, Sharma N, Singh RS. Reusability of brilliant green dye contaminated wastewater using corncob biochar and *Brevibacillus parabrevis*: hybrid treatment and kinetic studies. *Bioengineered.* 2020; 11(1): 743-758. https://doi.org/10.1080/21655979.2020.1788353
[40] Sukla Baidya K, Kumar U. Adsorption of brilliant green dye from aqueous solution onto chemically modified areca nut husk. *South African J Chem Eng.* 2021; 35: 33-43. https://doi.org/10.1016/j.sajce.2020.11.001
[41] Fadali OA. Effect of gas strirring on external mass transfer, intraparticle diffusion and energy consumption during adsorption. *Adsorpt Sci Technol.* 2003; 21(10): 935-950. https://doi.org/10.1260/02636170360744371
[42] Obradovic B. Guidelines for general adsorption kinetics modeling. *Hem Ind.* 2020; 74(1): 65-70. https://doi.org/10.2298/HEMIND200201006O
[43] McKay G. the Adsorption of Dyestuffs From Aqueous Solutions Using Activated Carbon. Iii. Intraparticle Diffusion Processes. *J Chem Technol Biotechnol Chem Technol.* 1983; 33 A(4): 196-204. https://doi.org/10.1002/jctb.504330406

[44] Zhu Q, Moggridge GD, D'Agostino C. Adsorption of pyridine from aqueous solutions by polymeric adsorbents MN 200 and MN 500. Part 2: Kinetics and diffusion analysis. *Chemical Engineering Journal*. 2016; 306: 1223-1233. https://doi.org/10.1016/j.cej.2016.07.087

[45] McKay G, Otterburn MS, Sweeney AG. The removal of colour from effluent using various adsorbents-III. Silica: Rate processes. *Water Res.* 1980; 14(1): 15-20. https://doi.org/10.1016/0043-1354(80)90037-8

[46] Selambakkannu S, Othman NAF, Bakar KA, Karim ZA. Adsorption studies of packed bed column for the removal of dyes using amine functionalized radiation induced grafted fiber. *SN Appl Sci.* 2019; 1(2): 175. https://doi.org/10.1007/s42452-019-0184-2

[47] Pérez-Cadena R, García-Esquivel Y, Castañeda-Cisneros YE, Serna-Díaz MG, Ramírez-Vargas MR, Muro-Urista CR, Téllez-Jurado A. Biological decolorization of Amaranth dye with Trametes polyzona in an airlift reactor under three airflow regimes. *Heliyon.* 2020; 6(12). https://doi.org/10.1016/j.heliyon.2020.e05857

[48] Saif Ur Rehman M, Kim I, Rashid N, Adeel Umer M, Sajid M, Han JI. Adsorption of Brilliant Green Dye on Biochar Prepared From Lignocellulosic Bioethanol Plant Waste. *Clean - Soil, Air, Water.* 2016; 44(1): 55-62. https://doi.org/10.1002/clen.201300954

Uklanjanje toksične boje termički modifikovanim lignoceluloznim otpadom u trofaznom "air-lift" reaktoru: uvid u kinetiku procesa

Anja Antanasković[1], Zorica Lopičić[1], Tatjana Šoštarić[1], Vladimir Adamović[1], Slobodan Cvetković[2], Jovana Perendija[2] i Milan Milivojević[3]

[1]Institut za tehnologiju nuklearnih i drugih mineralnih sirovina, Beograd, Srbija
[2]Univerzitet u Beogradu, Institut za hemiju, tehnologiju i metalurgiju, Beograd, Srbija
[3]Univerzitet u Beogradu, Tehnološko-metalurški fakultet, Beograd, Srbija

(Naučni rad)

Izvod

Ovaj rad istražuje uticaj protoka vazduha u trofaznom pneumatskom reaktoru sa recirkulacijom (air-lift) pri sorpciji toksične boje Brilliant Green, pomoću sorbenta na bazi bio čađ, i dobijenog od koštica višnje. U cilju karakterizacije sorbenta korišćene su sledeće metode: infracrvena spektroskopija sa Furijeovom (Fourier) transformacijom i prigušenom totalnom refleksijom, pH vrednost suspenzije, tačka nultog naelektrisanja, skenirajuća elektronska mikroskopija sa energetski disperzivnom rendgenskom spektroskopijom i difrakcija rendgenskih zraka. Eksperimenti su izvedeni u air-lift reaktoru pri protoku vazduha od 2.50 i 5.55 $dm^3\ h^{-1}$. Eksperimentalni podaci kinetike modelovani su nelinearnim oblicima pseudo-prvog i pseudo-drugog reda, kao i Weber-Morrisovim modelom, koji se zasniva na unutar-čestičnoj difuziji. Pokazano je da je pri nižem protoku i intenzitetu mešanja, brzina sorpcije boje Brilliant Green ograničena brzinom prenosa mase ka sorbentu, dok je pri većem protoku rekacija kinetički kontrolisana u skadu sa pseudo-drugim kinetičkim modelom. Pored toga, pri nižem protoku, sorpcija je odložena usled otpora prenosa mase kroz granični sloj tečnosti oko čestica sorbenta. Prikazani rezultati jasno ukazuju da intenzitet protoka vazduha ima značajnu ulogu u ukupnoj kinetici sorpcije i podržavaju moguću primenu biočadji za efikasnu sorpciju boje Brilliant green.

Ključne reči: otpadna biomasa; koštice višnje; piroliza; sorpcija; Brilliant green; kinetika

Valorisation of energy plant *Arundo donax* cultivated in Serbia for biosorption of cobalt ions from an aqueous solution: kinetic aspect

Jovana Perendija[1], Dragana Milošević[1], Mina Popović[1], Željko Dželetović[2], Sabina Kovač[3], Jasmina Grbović Novaković[4] and Slobodan Cvetković[1]

[1]*University of Belgrade, Institute of Chemistry, Technology, and Metallurgy, National Institute of the Republic of Serbia, Belgrade, Serbia*
[2]*University of Belgrade, INEP Institute for the Application of Nuclear Energy, Zemun-Belgrade, Serbia*
[3]*University of Belgrade, Faculty of Mining and Geology, Belgrade, Serbia*
[4]*University of Belgrade, "Vinča" Institute of Nuclear Sciences, National Institute of Serbia, Centre of Excellence for Hydrogen and Renewable Energy, Belgrade, Serbia*

Abstract
Metal ions can be eliminated from aqueous solutions using biosorbent, a substance made from plant biomass. This study investigated the potential use of *Arundo donax* stems as a cheap, natural biosorbent to remove cobalt ions (Co^{2+}) from an aqueous solution. The biosorbent was characterized by the chemical composition analysis (cellulose, hemicellulose, and lignin), the point of zero charge (pH_{PZC}), by scanning electron microscopy, energy dispersive spectroscopy, X-ray diffraction analysis, and Fourier-transform infrared spectroscopy. According to the experimental data of kinetic studies, the equilibrium condition of Co^{2+} adsorption was attained 360 min after the biosorption started. The pseudo-first, pseudo-second, Elovich, and intra-particle diffusion models were used to model the kinetic experimental data. The best compliance was obtained with the pseudo-first order kinetic model, considering the highest value of the coefficient of determination R^2 (0.996) and the lowest chi-square (χ^2) value (0.757). The findings of this study can be applied to the design of batch biosorption systems for the removal of Co^{2+} ions in real industrial systems.

Keywords: Biosorbent; Co^{2+} removal; kinetic modeling.

Available on-line at the Journal web address: http://www.ache.org.rs/HI/

ORIGINAL SCIENTIFIC PAPER

UDC: 661.183.122:546.732:532.73

Hem. Ind. **78(3)** 253-264 (2024)

1. INTRODUCTION

The human population is faced with problems related to water pollution. Industrial systems generated large amounts of wastewater and after processing, the contaminated water is discharged into a recipient, posing risks to aquatic life as it contains many polluting substances. Among them, the presence of various harmful heavy metals (e.g. iron, lead, nickel, silver, lead, cadmium, copper, manganese, etc.) is one of the largest environmental issues due to moderate accumulation over time in organisms.

Cobalt can be found in the natural environment along with iron, nickel, silver, lead, copper, manganese, and other elements [1]. It is also present in igneous and sedimentary rocks. It can also be often found in nuclear power plant wastewater and wastewater from numerous other industries, including mining, metallurgical, electroplating, paints, pigments, and electronic industries. The ecosystem is negatively impacted by cobalt as a harmful element. Numerous health issues, including paralysis, diarrhea, lung irritation, and bone abnormalities, may be induced by high cobalt levels [2]. Heavy metals could be removed from wastewater by using a variety of processes, including adsorption, sedimentation and flocculation, coprecipitation, complexation, heavy metal uptake by wetlands, photo-catalysis, solvent extraction, ion exchange, chemical precipitation, membrane separation techniques, oxidation/reduction, and electro-remediation [3,4]. The use of bio-waste-derived adsorbents is recommended because of their superior efficiency, low cost, and minimal environmental problems. One such cutting-edge technique is biosorption, which is

Corresponding authors:Slobodan Cvetković, Institute of Chemistry, Technology and Metallurgy, National Institute of the Republic of Serbia, Njegoševa 12, 11000 Belgrade, Serbia
Paper received: 17 July 2023; Paper accepted: 21 August 2024; Paper published: 19 September 2024.
E-mail: slobodan.cvetkovic@ihtm.bg.ac.rs
https://doi.org/10.2298/HEMIND240713017P

based on development of biosorbents from a variety of readily available plant materials, including husks, leaves, peels, stems, branches, and pods. There are significant efforts being made in this area to prepare innovative, low-cost bio-waste-based adsorbents that are effective at removing heavy metals from wastewater [5].

Arundo donax (common name: Giant reed) is planted in many regions such as tropical Asia and the Mediterranean and cultivation of this plant has a potential considering that it is a fast-growing invasive plant [6]. In Europe, this area covers inland along the major rivers of the Iberian Peninsula and along the Mediterranean coast from Spain to Greece, including the Adriatic coast. The plant may thrive on salty and arid soils [6]. *Arundo donax* is a very suitable source of biomass because of its low cost and high production. It also contains large amounts of cellulose and lignin, which has led to its widespread use globally for a range of applications such as production of energy, paper pulp, and wooden building materials, among others. Research indicates that *A. donax* L. can withstand challenging environmental conditions, such as the presence of toxic heavy metals [7]. Its ability to accumulate heavy metals in the tissues [8] led to the use of this plant directly as a biosorbent [9,10].

This work aimed to estimate removal of Co^{2+} ions from aqueous phase by unmodified powdered stems of *A. Donax* in batch biosorption experiments. After detailed characterization of pulverized stems of *Arundo donax*, biosorption kinetics was studied. Further, the experimental results were modeled using four different kinetic models (pseudo-first, pseudo-second, Elovich, and intra-particle diffusion model). The aim also was to examine the possibility of modelling of cost-effective and environmentally friendly process for the removal of Co^{2+} from the contaminated water system.

2. MATERIAL AND METHODS

2. 1. Chemicals and materials

Sodium hydroxide, hydrochloric acid (37 %), and AAS cobalt (Co^{2+}) standard solution (1000 mg dm^{-3}) were supplied from Merck, Germany. Dilute solutions (0.1 M NaOH and 0.1 M HCl) were used for pH adjustment and synthetic Co^{2+} stock solution was prepared with ultrapure water (Milli-Q system by Merck). The waste *Arundo donax* stems used in this study were provided by the Institute for the Application of Nuclear Energy - INEP, Belgrade, Serbia. The leached chernozem as soil type was used to cultivate *Arundo donax*.

2. 2. Preparation methods

Biosorbent from waste *Arundo donax* stems was prepared as follows: the sample was washed with deionized water several times in order to remove the impurities, and then was chopped. Next, it was dried in an oven at 70 °C for 12 h, and the dried stems were chopped in a blender. The fraction with a particle size smaller than 0.5 mm was used in the experiments. The prepared biosorbent is labelled as W-ADs and was stored in plastic containers in a desiccator until use.

2. 3. Characterization of W-ADs biosorbent

1. 3. 1. Lignocellulose composition

The lignocellulose composition (cellulose, hemicellulose, and lignin) of the W-Ads biosorbent was determined in compliance with standards ISO16472:2006 and ISO13906:2008 [11,12].

2. 3. 2. Structural and morphological characterization

Fourier-transform infrared spectroscopy in attenuated total reflectance mode (ATR-FTIR) of a sample W-Ads was performed by using a Thermo Scientific Nicolet 6700 spectrometer (Thermo Fisher Scientific, USA) in the range of wavenumbers 4000 - 500 cm^{-1}. The sample morphology was analyzed by field emission scanning electron microscopy (FE-SEM), by using the instrument SEM FEI Scios2 Dual Beam System (Thermo Fisher Scientific, USA), after providing conductivity by sputtering the sample with a thin golden layer. The energy dispersive spectroscopy (EDS) analysis was performed by using an EDS detector integrated with the SEM FEI Scios2 Dual Beam System (Thermo Fisher Scientific, USA). X-ray diffraction analysis (XRD) was used to determine the phase composition of the sample using Rigaku SmartLab powder X-ray diffractometer (Rigaku, Japan) with Cu-Kα radiation, at room temperature.

2. 3. 3. Determination of the point of zero charge

For determination of the point of zero charge (pH_{PZC}), 100 mg of the biosorbent samples were shaken in 50 cm^3 of NaCl solution (0.01 M) for 24 h at 25 °C and at six different pH values (2, 4, 6, 8, 10, and 12). Afterward, the biosorbent samples were separated from the solution by decantation. The solution pH values were measured by a WTW inoLab 730 pH meter (WTW, Germany,). The pH_{PZC} value of the W-ADs biosorbent was obtained from the plot of the initial vs. final pH value (pH_{final} *vs.* $pH_{initial}$). The intersection point of the curve obtained from this plot and the diagonal gave the pH_{PZC} value [13].

2. 4. Distribution of Co^{2+} ionic species

A speciation diagram of Co^{2+} ions in an aqueous solution as a function of pH was drawn using the Visual MINTEQ software (version 3.1, Department of Land and Water Resources Engineering, Stockholm, Sweden).

2. 5. Biosorption experiments

A kinetic study in a batch system was performed with the goal to evaluate the performance of the W-ADs biosorbent. The experiment was conducted by mixing the known biosorbent dosage (2 g dm^{-3}) in 100 cm^3 Erlenmeyer flasks containing 50 cm^3 of a 100 mg $dm^{-3}$of Co^{2+} solution at 25 °C and pH 7. Samples (50 cm^3) were taken at equal time intervals. All experiments were conducted in triplicate. The Co^{2+} solutions were filtrated by a nylon syringe filter (0.22 μm). The concentration of remaining Co^{2+} ions in the solution was determined by using an AA spectrometer (PinAAcle 900T-PerkinElmer, Massachusetts, USA).

The biosorption capacity (q_e / mg g^{-1}), and removal efficiency of Co^{2+} (R_e / %), were calculated according to Equations (1) and (2):

$$q_e = (C_0 - C_e)V/m \quad (1)$$

$$R_e = 100(C_0\text{-}C_e)/C_0 \quad (2)$$

where C_0 and C_e are Co^{2+} concentrations before and after biosorption, respectively, V is the volume of solution, and m is the mass of the W-ADs biosorbent.

The kinetics of the Co^{2+} biosorption on the W-ADs was analysed, using the pseudo-first order, pseudo-second order, Elovich, and intra-particle diffusion models [14] applied to the experimental data.

2. 5. 1. Pseudo-first order model

The pseudo-first order rate can be expressed by Equation (3):

$$\ln(q_e\text{-}q_t) = \ln q_e\text{-}k_1 t \quad (3)$$

where, q_e is the equilibrium biosorption capacity (contentof Co^{2+} per mass of the biosorbent), q_t is the biosorbed content of Co^{2+} per mass of the biosorbent at the time t, and k_1 is the pseudo-first order rate constant.

2. 5. 2. Pseudo-second order model

The pseudo-second order model can be expressed by Equation (4):

$$t/q_t = \left(k_2 q_e^{\,2}\right)^{-1} + t/q_e \quad (4)$$

where k_2 is the equilibrium constant of the pseudo-second order reaction rate.

2. 5. 3. Elovich model

The simplified equation of the Elovich model is described as follows, Equation (5):

$$q_t = 1/b\,ln(ab) + 1/b\,\ln t \quad (5)$$

where a / mg g^{-1} min^{-1} is the initial biosorption rate constant, and b / g mg^{-1} is the desorption rate constant of the Elovich model.

2. 5. 4. Intra-particle diffusion model

Possibility that the biosorption rate is controlled by intra-particle diffusion was tested by using the following simplified Equation (6):

$$q_t = k_{dif} t^{1/2} \quad (6)$$

where k_{dif} is the intra-particle diffusion rate constant. For diffusion through a spherical particle, this model should be applicable if the plot passes through the origin and follows a linear trend when the following condition is met $q_t/q_e < 0.4$ (*i.e.* in the early adsorption times until 40 % of the equilibrium amount is adsorbed) [15].

3. RESULTS AND DISCUSSION

3. 1. Lignocellulose composition of W-ADs biosorbent

Contents of cellulose, hemicellulose, and lignin for the W-Ads sample are represented in Table 1.

Table 1. Lignocellulose composition analysis of the W-ADs biosorbent

Component	Content, wt.%, (dry basis)
Cellulose	36.60
Hemicellulose	25.44
Lignin	35.24

A review of the literature revealed that the contents of cellulose, hemicellulose, and lignin in *Arundo donax* vary. Close values of cellulose (35.52 and 35.6 %) and hemicellulose contents (26.81 and 24 %) as in the present study (Table 1) are found in the literature [16,17]. Lignin content for raw milled material is much higher than that for processed fibres, accounting for around 35 % [18] similarly as it was obtained in the present study (35.24 %). Some authors have reported similar values for total lignin, approximately 33.65 % [19] and 30 % [20].

Differences in the lignocellulose composition in *Arundo donax* samples are attributed to various factors such as plant maturity, region, soil physiognomies, share of stem components, sample preparation techniques, etc. The comparative analysis of stem composition showed some differences between nodes and internodes. The nodes have similar lignin contents (~21 %) but they are richer in hemicelluloses (32.0 *vs.* 28.5 %) and poorer in cellulose (29.2 *vs.* 32.9%), as compared with internodes [21].

3. 2. Structural characterization by FTIR spectroscopy

The FTIR spectrum of a W-ADs sample is presented in Figure 1. It was used for the analysis of surface functional groups, providing insights into the nature and composition of the biomass. As expected in similar plant cultures made of lignocellulose, the FTIR spectrum of a tested sample, confirmed the presence of hemicellulose, cellulose, and lignin. These three components are considered as three major components of lignocellulosic materials [22].

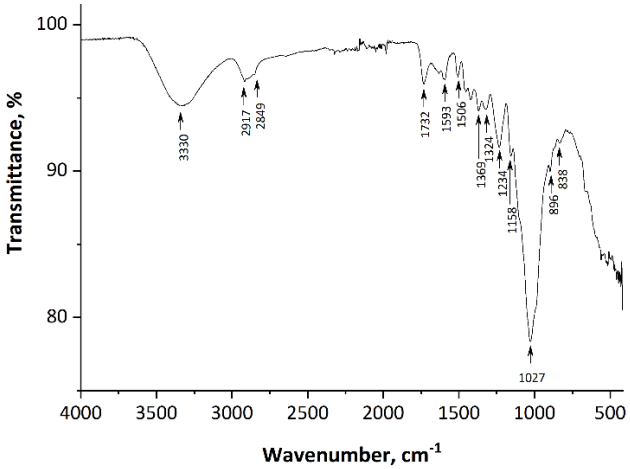

Figure 1. FTIR spectrum of a W-ADs sample

The broad band between 3400-3600 cm^{-1} was attributed to the stretching vibration of the hydrogen-bonded hydroxyl groups originating from cellulose. Bands at 2917 and 2849 cm^{-1} were assigned to C-H stretching vibrations from -CH_2 and -CH_3 components in cellulose and hemicellulose [23]. Besides the absorption band at 1732 cm^{-1} originating from a C=O stretching vibration [23] of acetyl groups in hemicellulose, the band present at 1234 cm^{-1} could also indicate a presence of hemicellulose i.e. its acetyl ester units [24]. Also, according to Galletti *et al.* [25], a small peak at 1732 cm^{-1} may indicate the presence of C=O ester bonds of ferulic and/or p-coumaric acids, which are bonded together with hemicellulose. According to Fiore *et al.* [23], the peak with a maximum cantered at 1506 cm^{-1} could be attributed to C=C stretching vibrations of the benzene ring of the lignin molecule. Bands between 1450 and 1200 cm^{-1} could be assigned to C-H vibrations of the CH_2 and CH_3 groups. In the region between 1200 and 850 cm^{-1} absorption bands typical for cellulose are noticed, as well as, in the region between 1550 and 1300 cm^{-1} corresponding to bands related to lignin [25]. It is known that materials of plant origin among other components contain polysaccharides, and bands indicating the presence of polysaccharides molecules are present in the spectral region 1000-1200 cm^{-1} corresponding to C-O-C, C-C and C-O vibrations [25]. The characteristic C-H and C-O bending vibrations of the aromatic ring in polysaccharides are observed at 1369 and 1324 cm^{-1}, respectively.

3. 3. SEM analysis of W-ADs biosorbent microstructure

The surface morphology of a W-ADs sample obtained by SEM is presented in Figure 2 showing a rough, corrugated surface layer with decreased porosity, clear gaps, and cracks. Furthermore, moderately developed surface of W-ADs can be observed with, certain impurities that are typical for raw natural materials.

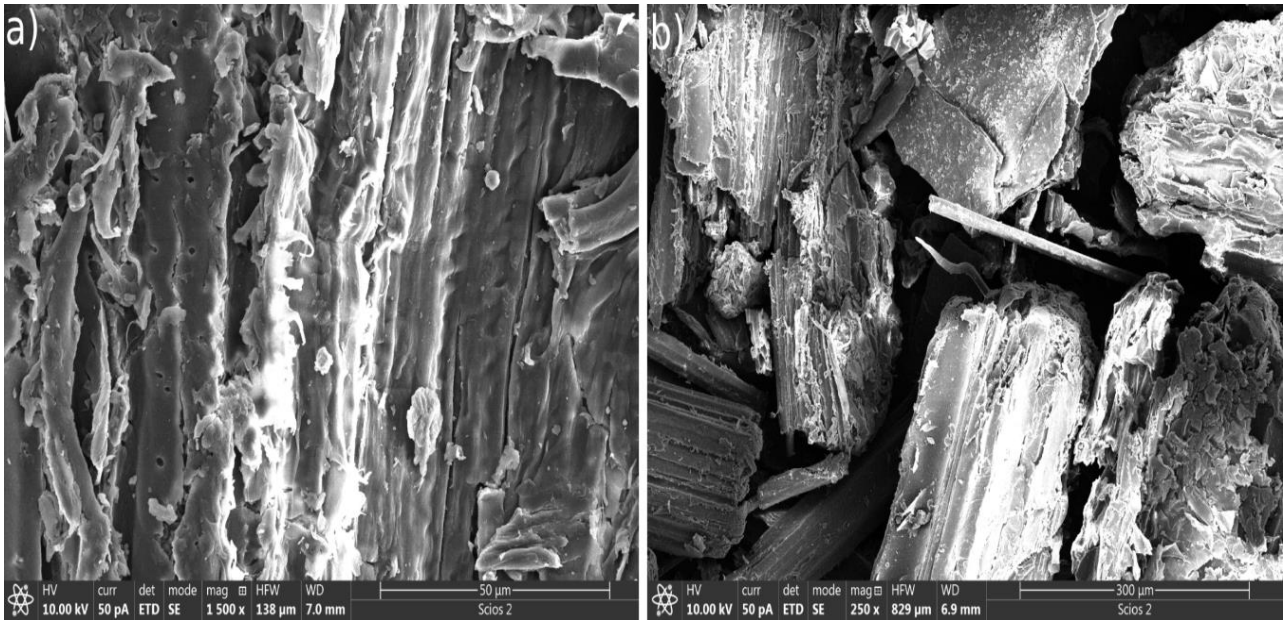

Figure 2. SEM micrographs of a W-ADs sample at different magnifications

3. 4. Energy dispersive spectroscopy analyses

EDS spectra of the biosorbent (Fig. 3) showed the presence of C and O as the major constituents, and Si to a lesser extent. The presence of Si (1.596 wt. %) indicates the existence of bilobate phytoliths in the material [26]. Besides the EDS elemental mapping for O, C and Si (Fig. 3b-d), values of the mass percentage of these elements in the tested area are shown in Figure 3e.

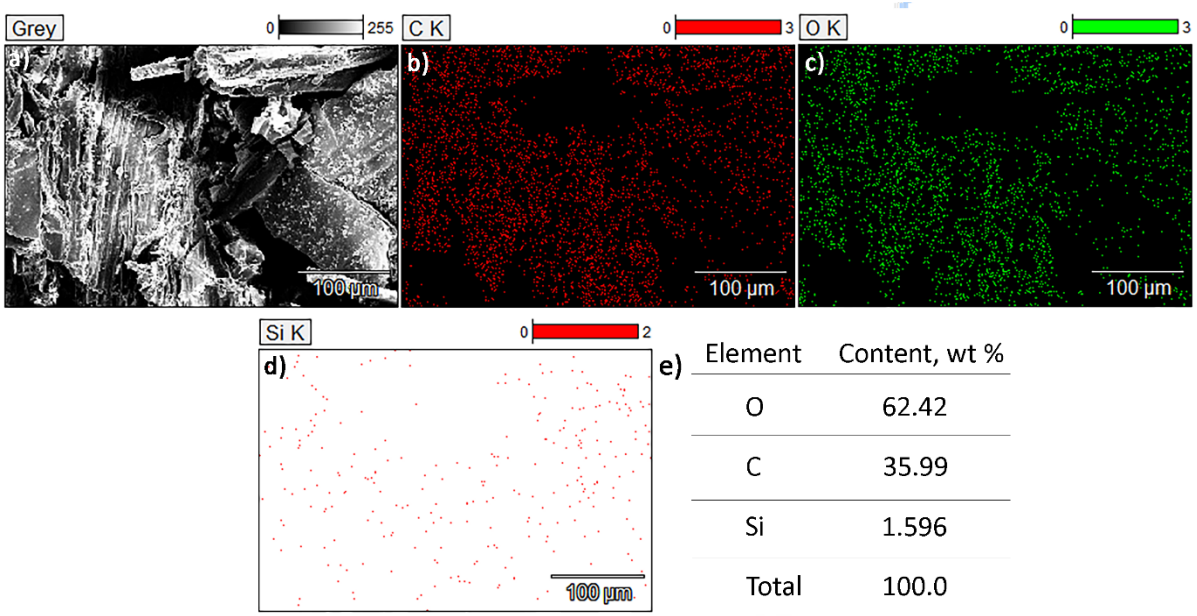

e)

Element	Content, wt %
O	62.42
C	35.99
Si	1.596
Total	100.0

Figure 3. SEM image of W-ADs a) corresponding EDS elemental mapping for O, C and Si (b-d) and element composition e)

3. 5. XRD analysis

X-ray diffraction was applied to determine the presence of amorphous and crystalline phases in the W-ADs biosorbent (Fig. 4). the obtained peak of the strongest intensity between 22 and 23° 2θ with slightly weaker reflections at 2θ ~20.5 and ~34.5°, corresponds to cellulose I. Broad peaks indicate amorphous structure *of Arundo donax*. It is a consequence of the presence of other amorphous components such as hemicellulose, lignin and disordered cellulose, which together contribute to the amorphous phase signal of the W-ADs sample.

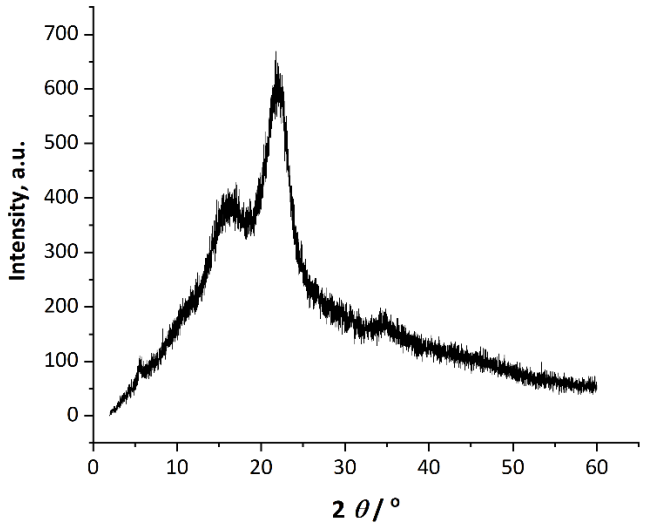

Figure 4. XRD pattern of a W-Ads sample

3. 6. Point of zero charge

Figure 5 shows determination of the point of zero charge (pH_{PZC}) value, which was estimated as 6.89. Generally, it is a well-known fact that a biosorbent surface is positively charged when the solution pH is lower than the pH_{PZC} value, and on the contrary, when pH is higher than the pH_{PZC} value, the biosorbent surface is negatively charged. Considering the determined value of 6.89, it can be concluded that higher pH values Favor biosorption of positively charged Co^{2+} ions. In addition to this value, when choosing the pH value for operating conditions, influence of Co^{2+} ion precipitation in aqueous solutions should be considered as it is pH dependent. Thus, this process was also analysed as shown in Figure 6. At a pH

value of 7.2, only very weak precipitation of $Co(OH)^+$ occurs (0.26 %) while at pH 8.2 somewhat more significant precipitation occurs yielding the distribution of biosorbed cobalt species as 97.1 % Co^{2+}, 2.6 % $Co(OH)^+$, and 0.3 % $Co(OH)_2$. With the intention to avoid the influence of precipitation on biosorption and considering the pH_{PZC} value (6.89) above which biosorption of Co^{2+} is favoured, a pH value of 7 was chosen for conduction of biosorption experiments.

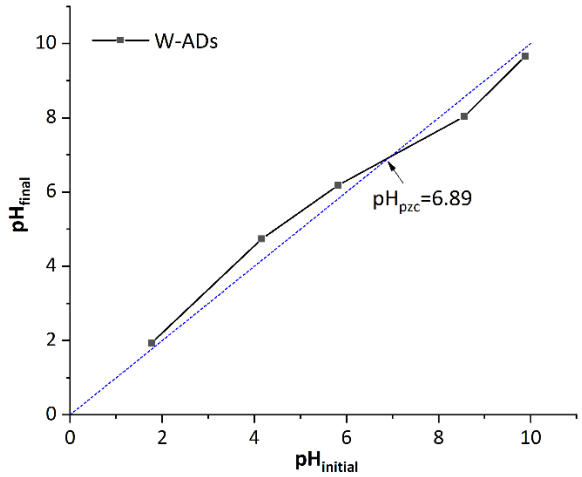

Figure 5. Determination of pH_{pzc} of the W-ADs biosorbent

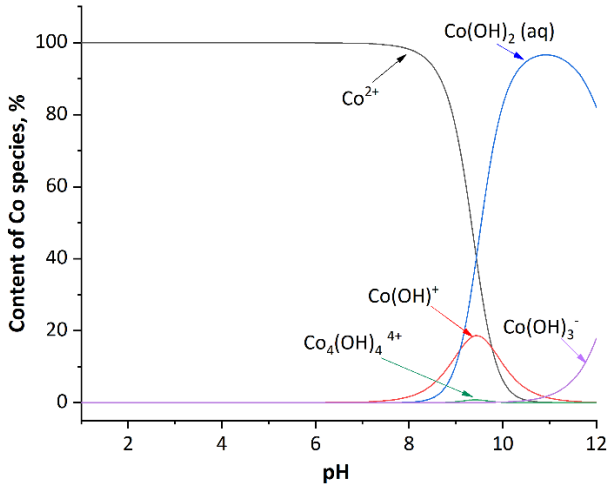

Figure 6. Speciation diagram for Co^{2+} aqueous solution as a function of pH

3. 7. Biosorption kinetics

The kinetics of Co^{2+} biosorption onto the W-ADs biosorbent over time is presented in Figure 7. The biosorbed Co^{2+} amount increased until reaching a maximum value, as expected. The obtained results indicate that the equilibrium was achieved within 360 min. This occurrence is a result of Co^{2+} ions binding to active sites on the biosorbent surfaceAfter about 360 min, saturation of W-ADs functional groups has occurred, and apparent equilibrium was reached.

The experimental results were modelled by using four different models (pseudo-first, pseudo-second, Elovich, and intra-particle diffusion model). For preliminary assessment, the experimental data were fitted by the models in linear forms (Fig. 8). The coefficients of determination *(R^2)* for the best fits of pseudo-first order model, pseudo-second order model, Elovich and intra-particle model were 0.977, 0.964, 0.901 and 0.930, respectively, showing apparently good agreements with the experimental data except for the Elovich model, which clearly deviated from the experimental data. Weaknesses of linear correlations can be observed when the experimental data were fitted with models in non-linear forms. Certain values of the coefficient of determination for a model in linear and non-linear form can quantitatively show the difference [13].

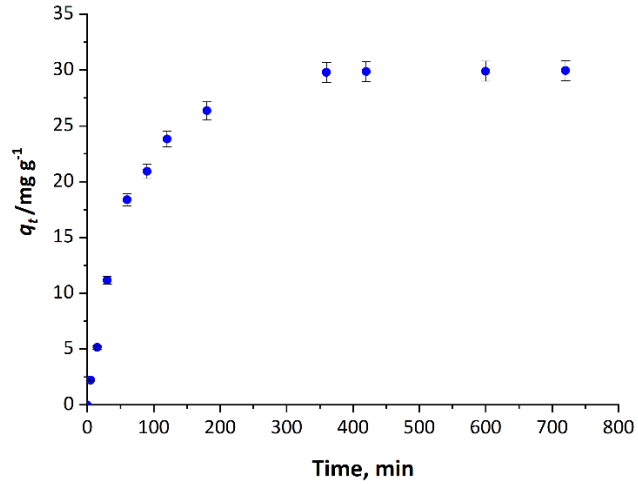

Figure 7. Biosorbed amount of Co^{2+} per the W-ADs biosorbent content over time

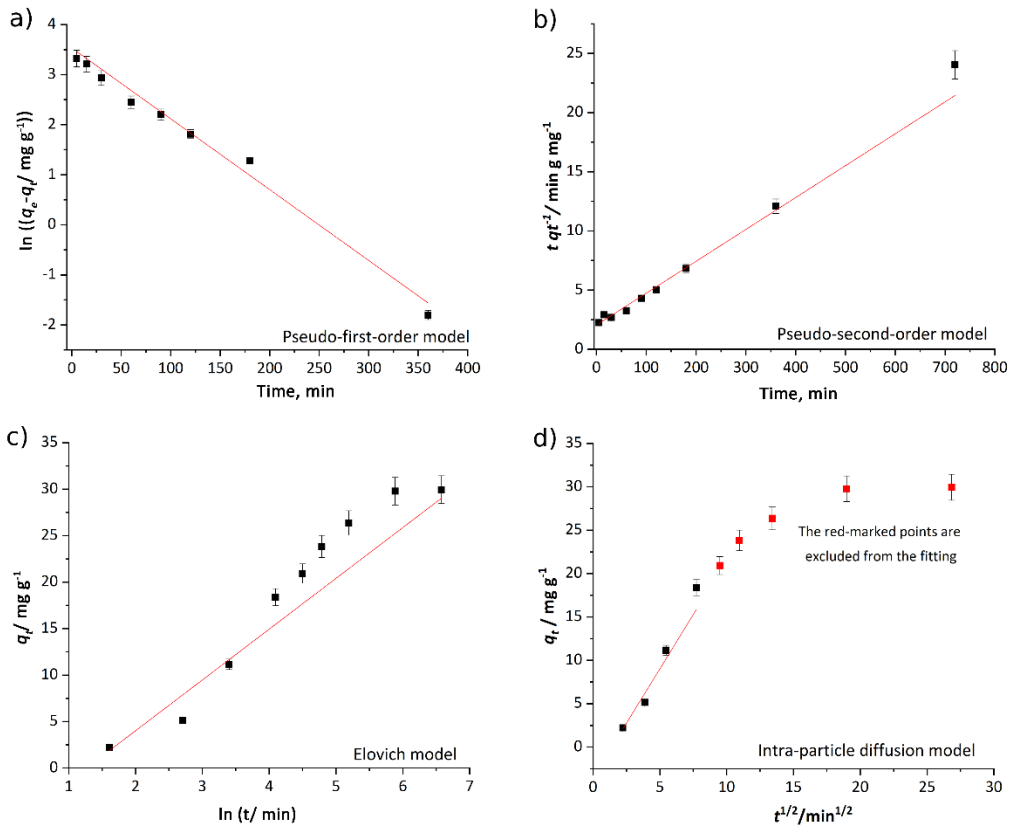

Figure 8. Kinetic plots for linear modelling of experimental biosorption data (symbols) for: a) pseudo- first order model, b) pseudo-second order model, c) Elovich model, and d) intra-particle diffusion model applied for the initial biosorption period up to $q_t/q_e < 0.4$

Considering this fact and the close values of the coefficient of determination obtained by applying the pseudo-second order, pseudo-first order, and the intra-particle diffusion model, these models were applied in non-linear forms as more precise. The results of modelling in non-linear forms are shown in Table 2. It can be seen that the linear and non-linear regression methods yielded different values of model parameters (Fig. 8 and Table 2). The coefficients of determination obtained by applying non-linear forms of the pseudo-first and pseudo-second order model were higher, while that of the intra-particle diffusion model was lower, which clearly shows how using only the linear form of a model can lead to erroneous conclusions. In order to determine the best model for biosorption kinetics it is recommended to observe the value of chi-square (χ^2) obtained by the non-linear regression method along with R^2 values [27,28] presented also in Table 2. The obtained kinetic parameters for the pseudo-first order, pseudo-second order, and the intra-particle diffusion models revealed that the pseudo-first order kinetic model provided the best agreement with experimental data, with the highest coefficient of determination and a lowest chi-square value. Additionally, this can be seen by comparison of the model predictions with the experimental data indicating the pseudo-first order model as the best (Fig. 9).

Table 2. Kinetic parameters obtained by non-linear regression analyses of different kinetic models applied to the experimental data for biosorption of Co^{2+} ions onto W-ADs biosorbent

Pseudo-first order model			
q_e / mg g^{-1}	k_1 / min^{-1}	R^2	χ^2
29.48	1.46×10^{-2}	0.996	0.757
Pseudo-second order model			
q_e / mg g^{-1}	k_2 / g mg^{-1} min^{-1}	R^2	χ^2
33.83	5.24×10^{-4}	0.991	0.851
Intra-particle diffusion model			
	K_{dif} / mg g^{-1} min$^{-0.5}$	R^2	χ^2
	1.52	0.741	15.86

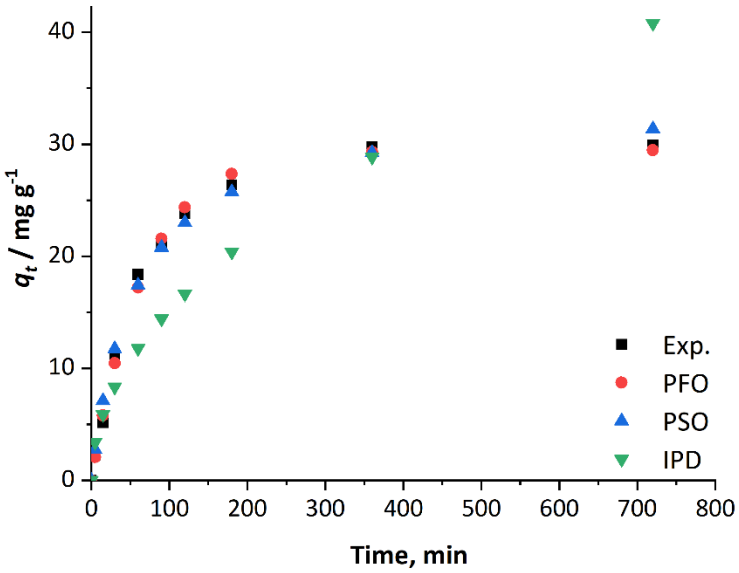

Figure 9. Biosorption experimental data and best model predictions obtained by non-linear fitting for the pseudo-first order (PFO), pseudo-second order (PSO), and intra-particle diffusion model (IPD)

Comparative kinetic data and equilibrium biosorbent capacities assessment for Co^{2+} ions removal using *Arundo donax* and various biomass biosorbents is given in Table 3.

Table 3. Comparison of kinetic modeling results (pseudo-first order (PFO) and pseudo-second order (PSO), and equilibrium biosorbent capacities of Co^{2+} ions removal using different types of biosorbents

Biosorbent	Kinetic model	R^2	Rate constant		q_e/ mg g^{-1}	Ref.
Aspergillus flavus biomass	PSO	0.999	k_2 / g mg^{-1} min^{-1}	0.0270	12.47	[29]
Pre-treated *2-Hypnea Valentiae* algae biomass	PSO	0.980	k_2 / g mg^{-1} min^{-1}	0.0072	10.98	[30]
Cocos nucifera L. leaf powder	PSO	0.997	k_2 / g mg^{-1} min^{-1}	0.1238	1.430	[31]
Modified corn silk	PSO	0.997	k_2 / g mg^{-1} min^{-1}	0.0867	9.164	[32]
Saccharum bengalense (SB)	PSO	0.903	k_2 / g mg^{-1} min^{-1}	0.0184	4.62	[33]
Alginate extracted from marine red algae biomass (*Callithamnion corymbosum* sp.)	PSO	0.999	k_2 / g mg^{-1} min^{-1}	0.0291	13.64	[34]
Lignocellulosic biosorbent-coir pith	PSO	0.990	k_2 / g mg^{-1} min^{-1}	0.0200	8.540	[35]
Spent coffee (SC)	PSO	0.999	k_2 / g mg^{-1} min^{-1}	0.1340	3.741	[36]
Arundo donax stems W-ADs biosorbent	PFO	0.977	k_1 / min^{-1}	0.0141	29.48	This study

According to the data in Table 3, the pseudo-first order and pseudo-second order kinetic models were used for describing the biosorption kinetics of Co^{2+} ions by biosorbents derived from different biomass sources, the pseudo-second order being the best in all cases, except for this study. By comparing the equilibrium capacities for Co ions for different biosorbents it was shown that biosorbent used in this study (W-Ads) is better than others.

4. CONCLUSION

Biosorbents derived from plant biomass can be promising materials for the removal of metal ions from aqueous solutions. This work investigated the possibility of using *Arundo donax* stems (W-Ads) as a natural, and inexpensive biosorbent to eliminate Co^{2+} ions from an aqueous solution. The biosorbent was characterized by using chemical composition analysis, the point of zero charge (pH_{PZC}) determination, SEM, EDS, XRD, and FTIR analyses. The conducted kinetic studies demonstrate the biosorbed amount of Co^{2+} increased with time until reaching a maximum value after approximately 360 min. In this research, the experimental kinetic data were analyzed using four different kinetic models (pseudo-first, pseudo-second, Elovich, and intra-particle diffusion model). The pseudo-first kinetic model provided the best agreement with experimental data confirmed with the highest coefficient of determination $R^2 = 0.996$, and a lowest $\chi^2 = 0.757$. The results obtained in this study can be used for scale-up in the design of batch biosorption systems for cobalt removal from aqueous solutions.

Acknowledgments: This work was financially supported by the Ministry of Science, Technological Development and Innovation of the Republic of Serbia (Grant No 451-03-47/2023-14/200026).

REFERENCES

[1] Graedel TE, Gunn G, Tercero Espinoza L. Metal resources, use and criticality. *Critical Metals Handbook.* 1st ed., Chichester, UK: John Wiley & Sons; 2014: 1-19. https://doi.org/10.1002/9781118755341.ch1.

[2] Awual MR, Hasan MM, Islam A, Asiri AM, Rahman MM. Optimization of an innovative composited material for effective monitoring and removal of cobalt(II) from wastewater. *J Mol Liq.* 2020; 298: 112035. https://doi.org/10.1016/j.molliq.2019.112035.

[3] Agarwal A, Upadhyay U, Sreedhar I, Singh SA, Patel CM. A review on valorization of biomass in heavy metal removal from wastewater. *J Water Process Eng.* 2020; 38: 101602. https://doi.org/10.1016/j.jwpe.2020.101602.

[4] Aryal M. A comprehensive study on the bacterial biosorption of heavy metals: Materials, performances, mechanisms, and mathematical modellings. *Rev Chem Eng.* 2021; 37 (6): 715-754. https://doi.org/10.1515/revce-2019-0016.

[5] Guleria A, Kumari G, Lima EC, Ashish DK, Thakur V, Singh K. Removal of inorganic toxic contaminants from wastewater using sustainable biomass: A review. *Sci Total Environ.* 2022; 823: 153689. https://doi.org/10.1016/j.scitotenv.2022.153689.

[6] Zhang D, Jiang QW, Liang DY, Huang S, Liao J. The Potential Application of Giant Reed (Arundo donax) in Ecological Remediation. *Front Environ Sci.* 2021; 9: 652367. https://doi.org/10.3389/fenvs.2021.652367.

[7] Deng H, Ye ZH, Wong MH. Accumulation of lead, zinc, copper and cadmium by 12 wetland plant species thriving in metal-contaminated sites in China. *Environ Pollut.* 2004; 132 (1): 29–40. https://doi.org/10.1016/j.envpol.2004.03.030.

[8] Nsanganwimana F, Marchand L, Douay F, Mench M. Arundo donax L., a Candidate for Phytomanaging Water and Soils Contaminated by Trace Elements and Producing Plant-Based Feedstock. A Review. *Int J Phytoremediation.* 2014; 16 (10): 982–1017. https://doi.org/10.1080/15226514.2013.810580.

[9] Mavrogianopoulos G, Vogli V, Kyritsis S. Use of wastewater as a nutrient solution in a closed gravel hydroponic culture of giant reed (Arundo donax). *Bioresour Technol.* 2002; 82 (2): 103–107. https://doi.org/10.1016/S0960-8524(01)00180-8.

[10] Song HL, Liang L, Yang KY. Removal of several metal ions from aqueous solution using powdered stem of Arundo donax L: As a new biosorbent. *Chem Eng Res Des.* 2014; 92 (10): 1915–1922. https://doi.org/10.1016/j.cherd.2014.04.027.

[11] ISO 16472:2006: Animal feeding stuffs — Determination of amylase-treated neutral detergent fibre content (aNDF), 2006.

[12] ISO 13906:2008: Animal feeding stuffs — Determination of acid detergent fibre (ADF) and acid detergent lignin (ADL) contents 2008.

[13] Abatal M, Anastopoulos I, Giannakoudakis DA, Olguin MT. Carbonaceous material obtained from bark biomass as adsorbent of phenolic compounds from aqueous solutions. *J Environ Chem Eng.* 2020; 8 (3): 103784. https://doi.org/10.1016/j.jece.2020.103784.

[14] Wang J, Guo X. Adsorption kinetic models: Physical meanings, applications, and solving methods. *J Hazard Mater.* 2020; 390: 122156. https://doi.org/10.1016/j.jhazmat.2020.122156.

[15] Obradovic B. Guidelines for general adsorption kinetics modeling. *Hem Ind.* 2020; 74 (1): 65–70. https://doi.org/10.2298/HEMIND200201006O.

[16] Bessa W, Trache D, Derradji M, *et al.* Characterization of raw and treated Arundo donax L. cellulosic fibers and their effect on the curing kinetics of bisphenol A-based benzoxazine. *Int J Biol Macromol.* 2020; 164: 2931–2943. https://doi.org/10.1016/j.ijbiomac.2020.08.179.

[17] You T, Wang R, Zhang X, Ramaswamy S, Xu F. Reconstruction of lignin and hemicelluloses by aqueous ethanol anti-solvents to improve the ionic liquid-acid pretreatment performance of Arundo donax Linn. *Biotechnol Bioeng.* 2018; 115 (1): 82–91. https://doi.org/10.1002/bit.26457.

[18] Suárez L, Barczewski M, Kosmela P, Marrero MD, Ortega Z. Giant Reed (Arundo donax L.) Fiber Extraction and Characterization for Its Use in Polymer Composites. *J Nat Fibers.* 2023; 20 (1): 1–15. https://doi.org/10.1080/15440478.2022.2131687.

[19] Krička T, Matin A, Bilandžija N, *et al.* Biomass valorisation of Arundo donax L., Miscanthus × giganteus and Sida hermaphrodita for biofuel production. *Int Agrophysics.* 2017; 31 (4): 575–581. https://doi.org/10.1515/intag-2016-0085.

[20] Barana D, Salanti A, Orlandi M, Ali DS, Zoia L. Biorefinery process for the simultaneous recovery of lignin, hemicelluloses, cellulose nanocrystals and silica from rice husk and Arundo donax. *Ind Crops Prod.* 2016; 86: 31–39. https://doi.org/10.1016/j.indcrop.2016.03.029.

[21] Shatalov AA, Pereira H. Papermaking fibers from giant reed (Arundo donax L.) by advanced ecologically friendly pulping and bleaching technologies. *BioResources.* 2006; 1 (1): 45–61. https://doi.org/10.15376/biores.1.1.45-61.

[22] Zhuang J, Li M, Pu Y, Ragauskas AJ, Yoo CG. Observation of potential contaminants in processed biomass using fourier transform infrared spectroscopy. *Appl Sci.* 2020; 10 (12): 1–13. https://doi.org/10.3390/app10124345.

[23] Fiore V, Scalici T, Valenza A. Characterization of a new natural fiber from Arundo donax L. as potential reinforcement of polymer composites. *Carbohydr Polym.* 2014; 106 (1): 77–83. https://doi.org/10.1016/j.carbpol.2014.02.016.

[24] Galia A, Schiavo B, Antonetti C, *et al.* Autohydrolysis pretreatment of Arundo donax: A comparison between microwave-assisted batch and fast heating rate flow-through reaction systems. *Biotechnol Biofuels.* 2015; 8 (1): 1–18.

https://doi.org/10.1186/s13068-015-0398-5.

[25] Raspolli Galletti AM, D'Alessio A, Licursi D, *et al.* Midinfrared FT-IR as a tool for monitoring herbaceous biomass composition and its conversion to furfural. *J Spectrosc.* 2015; 2015 (1): 1-12. https://doi.org/10.1155/2015/719042.

[26] Payá J, Roselló J, Monzó JM, *et al.* An approach to a new supplementary cementing material: Arundo donax straw ash. *Sustain.* 2018; 10 (11): 4273. https://doi.org/10.3390/su10114273.

[27] Obradovic B. Back to basics: Avoiding errors in scientific research and publications. *Hem Ind.* 2019; 73 (3):143–146. https://doi.org/10.2298/HEMIND190630018O.

[28] Ezeonuegbu BA, Machido DA, Whong CMZ, *et al.* Agricultural waste of sugarcane bagasse as efficient adsorbent for lead and nickel removal from untreated wastewater: Biosorption, equilibrium isotherms, kinetics and desorption studies. *Biotechnol Reports.* 2021; 30: e00614. https://doi.org/10.1016/j.btre.2021.e00614.

[29] Foroutan R, Esmaeili H, Rishehri SD, *et al.* Zinc, nickel, and cobalt ions removal from aqueous solution and plating plant wastewater by modified Aspergillus flavus biomass: A dataset. *Data Br.* 2017; 12: 485–492. https://doi.org/10.1016/j.dib.2017.04.031.

[30] Vafajoo L, Cheraghi R, Dabbagh R, McKay G. Removal of cobalt (II) ions from aqueous solutions utilizing the pre-treated 2-Hypnea Valentiae algae: Equilibrium, thermodynamic, and dynamic studies. *Chem Eng J.* 2018; 331 : 39–47. https://doi.org/10.1016/j.cej.2017.08.019.

[31] Hymavathi D, Prabhakar G. Optimization, equilibrium, and kinetic studies of adsorptive removal of cobalt(II) from aqueous solutions using Cocos nucifera L. *Chem Eng Commun.* 2017; 204 (9): 1094–1104. https://doi.org/10.1080/00986445.2017.1338570.

[32] Yu H, Pang J, Ai T, Liu L. Biosorption of Cu2+, Co2+ and Ni2+ from aqueous solution by modified corn silk: Equilibrium, kinetics, and thermodynamic studies. *J Taiwan Inst Chem Eng.* 2016; 62: 21–30. https://doi.org/10.1016/j.jtice.2016.01.026.

[33] Imran Din M, Mirza ML, Ata S, Athar M, Mohsin IU. Thermodynamics of biosorption for removal of Co(II) ions by an efficient and ecofriendly biosorbent (saccharum bengalense): Kinetics and isotherm modeling. *J Chem.* 2013; 2013: 1-11. https://doi.org/10.1155/2013/528542.

[34] A. R. Lucaci, D. Bulgariu, I. Ahmad. Equilibrium and Kinetics Studies of Metal Ions Biosorption on Alginate Extracted from Marine Red Algae Biomass (Callithamnion corymbosum sp.). *J Polym.* 2020; 12 (9): 1–16. https://doi.org/10.3390/polym12091888

[35] Parab H, Joshi S, Sudersanan M, Shenoy N, Lali A, Sarma U. Removal and recovery of cobalt from aqueous solutions by adsorption using low cost lignocellulosic biomass-coir pith. *J Environ Sci Heal - Part A Toxic/Hazardous Subst Environ Eng.* 2010; 45 (5): 603–611. https://doi.org/10.1080/10934521003595662.

[36] Imessaoudene D, Hanini S, Bouzidi A, Ararem A. Kinetic and thermodynamic study of cobalt adsorption by spent coffee. *Desalin Water Treat.* 2016; 57 (13): 6116–6123. https://doi.org/10.1080/19443994.2015.1041049.

Valorizacija energetske biljke *Arundo donax* uzgajane u Srbiji za biosorpciju jona kobalta iz vodenog rastvora: kinetički aspekt

Jovana Perendija[1], Dragana Milošević[1], Mina Popović[1], Željko Dželetović[2], Sabina Kovač[3], Jasmina Grbović Novaković[4] i Slobodan Cvetković[1]

[1]Univerzitet u Beogradu-Institut za hemiju, tehnologiju I metalurgiju, Institut od nacionalnog značaja za RepublikuSrbiju, Beograd, Srbija
[2]Univerzitet u Beogradu, Institut za primenu nuklearne energije- INEP, Zemun- Beograd, Srbija
[3]Univerzitet u Beogradu, Rudarsko-geološki fakultet, Beograd, Srbija
[4]Univerzitet u Beogradu, Institut za nuklearne nauke "Vinča", Institut od nacionalnog značaja za Republiku Srbiju, Centar izvrsnosti: "Centar za vodoničnu energiju i obnovljive izvore energije", Beograd, Srbija

(Naučni rad)

Izvod

Joni metala se mogu eliminisati iz vodenih rastvora korišćenjem biosorbenata, materijala dobijenih iz biljne biomase. U ovoj studiji, istraživana je potencijalna upotreba *Arundo donax* stabljike kao jeftinog, prirodnog biosorbenta za uklanjanje jona kobalta (Co^{2+}) iz vodenog rastvora. *Arundo donax* stabljika je karakterisana analizom hemijskog sastava (u pogledu sadržaja celuloze, hemiceluloze i lignina), tačke nultog naelektrisanja (pH_{PZC}), skenirajućom elektronskom mikroskopijom (*SEM*), energetskom disperzionom spektroskopijom x–zraka (*EDS*), rendgenskom difrakcionom analizom (*XRD*) i infracrvenom spektroskopijom sa Furijeovom transformacijom (*FTIR*). Istraživanja kinetike su pokazala da se vezana količina Co^{2+} jona na *Arundo donax* stabljici povećavala sa povećanjem vremena kontakta dostižući stanje ravnoteže posle 360 min. Primenjeni su kinetički modeli pseudo-prvog reda, pseudo-drugog reda, Eločičev model i model unutrašnje difuzije za opisivanje eksperimentalnih podataka. Najbolja predviđanja su dobijena primenom kinetičkog modela pseudo-prvog reda uz najveću vrednost koeficijenta determinacije R^2 = 0.996, i najmanju vrednost χ^2 = 0.757. Nalazi ove studije mogu se primeniti na projektovanje šaržnih biosorpcionih sistema za uklanjanje jona kobalta iz vodenih rastvora.

Ključne reči: biosorbent; Co^{2+} joni; karakterizacija Arundo Donax; kinetičko modelovanje

Pollution indices as useful tools for comprehensive evaluation of the soil contamination degree in the vicinity of mining and metallurgical complexes

Jelena V. Kalinović, Snežana M. Šerbula, Tanja S. Kalinović, Ana A. Radojević and Jelena S. Jordanović

University of Belgrade, Technical faculty in Bor, Bor, Serbia

Abstract

Soil pollution levels in the copper mining and metallurgical area were evaluated at 14 sampling sites in the City of Bor and its surroundings in regard to Al, As, Cu, Fe, Pb and Zn contents, as well as single and integrated pollution indices. The significance of single pollution indices provides information about pollution by a specific element, while integrated pollution indices offer an insight into cumulative pollution by the examined elements. The mean soil concentrations of As, Cu, Pb and Zn were several times higher than the world average values. The exceedances of soil remediation values were most pronounced for As (at seven sites) and Cu (at eleven sites), more than 3 and 13 times, respectively. According to the geoaccumulation index, the enrichment factor and the contamination factor, the highest soil contamination was with As and Cu, especially at the urban-industrial site. Pollution load index, Nemerow pollution index and the improved Nemerow index confirmed that the most contaminated soils were from the sites in the vicinity of the metallurgical complex and flotation tailing ponds, as well as from the sites in the prevailing wind directions compared to the less polluted soils affected by the ore mining processes. The areas affected by the serious cumulative contamination from the pyrometallurgical copper production need continuous pollution prevention, monitoring and remediation measures.

Keywords: Environmental pollution; soil quality; single and integrated soil pollution indices.

Available on-line at the Journal web address: http://www.ache.org.rs/HI/

ORIGINAL SCIENTIFIC PAPER

UDC: 628.516:[622+669]

Hem. Ind. **78(3)** 265-279 (2024)

1. INTRODUCTION

Emissions of hazardous substances into the atmosphere from the mining and smelting activities, mostly contain acid gases such as SO_2 and particulate matter (PM) with different trace elements, some of which can potentially be harmful to humans by inhalation or could be bioaccumulated through the food chain [1-3]. These pollutants cause concern for all the receiving matrices (airborne particulates, vegetation, soil, sediments, dust, waters, *etc.*) [4-6].

Essential elements (such as Cu, Ni, Zn, *etc.*) are necessary for many metabolic functions in soil and living organisms but could become toxic at concentrations above the allowed values, whereas non-essential elements (such as Pb and Cd) are potentially toxic even at very low concentrations in the soils [7]. Hazardous substances emitted into the atmosphere in the form of particulate matter and gases precipitate on the soil surfaces and vegetation in the form of dry or wet depositions [4,8].

Areas that are located in the direction of the prevailing winds are usually polluted with emissions from non-ferrous mining and smelting operations, as well as with dust and fugitive emissions rich in trace elements (*e.g.* As, Cu, Pb, *etc.*) [9,10]. Many studies aimed to assess environmental pollution at different locations, such as specific mining and smelting areas [2-4,9,11-19], urban and traffic areas [6], industrial areas [8,20-23], farmland and cultivated soils [24], national parks [5,25,26], sediments [27], *etc.*

Corresponding authors:Jelena V. Kalinović, University of Belgrade, Technical faculty in Bor
Paper received: 30 May 2023; Paper accepted: 15 May 2024; Paper published: 24 May 2024.
E-mail: jkalinovic@tfbor.bg.ac.rs
https://doi.org/10.2298/HEMIND23053007K

Data regarding the air pollution obtained from the measuring stations, usually located in the urban and residential areas, as well as the data obtained by biomonitoring using different plant species and soil, *e.g.* [11,12,28], could be used for estimation of potential influences of industrial, *e.g.* [8,21,29] and traffic, *e.g.* [6] pollution on the environment.

Soil as the most important and conditionally renewable resource in the environment, which acts as the main receiving surface area of the atmospheric deposition, represents one of the main topics in the environmental quality investigations [25,30]. Contaminated soil has a negative effect on biogeochemical cycles, the state of surface and underground waters and could result in leaching of the deposited pollutants in the substrates [4,8]. Phytoremediation represents an environmentally friendly method for recovery and the removal of trace elements from the contaminated soils [8,31,32].

Many studies conducted worldwide showed the use of different indices in the comprehensive evaluation of the soil contamination by anthropogenic activities [33-35], and for soil classification [36-38]. Some investigation benefits of using soil pollution indices are: easy and fast calculation; large international experience; national and international agencies recognising pollution assessment by indices and simple environmental risk assessment. The pollution indices could denote the presence of trace elements both from natural and anthropogenic processes [22,39]. According to literature, the occurrence of false-negative results or lack of comparability studies could be regarded as disadvantages of soil pollution indices [7].

The aim of this study was to assess the soil pollution level in the area of copper mining and smelting. In order to determine the pollution level of soil, concentrations of trace elements were compared to the corresponding limit values (*LV*) and remediation values (*RV*), proposed by the Serbian regulation, as well as by using single and integrated indices of soil pollution, such as: geoaccumulation index (I_{geo}), enrichment factor (*EF*), contamination factor (*CF*), pollution load index (*PLI*), Nemerow pollution index (*NI*), and improved (modified) Nemerow index (*INI*). In this study, the pollution indices were used for determining distribution patterns of the emitted elements and highlighting the polluted sampling sites.

2. MATERIALS AND METHODS

2. 1. Study area description

Mining activities and pyrometallurgical production of copper from sulfide ores in the City of Bor (Eastern Serbia) and its surroundings have been performed for more than 120 years. Huge quantities of acid gases such as SO_2, particulate matter (PM) and atmospheric depositions containing different elements, some of which can be highly toxic and carcinogenic, are emitted during smelting of sulfide copper concentrates, containing chalcopyrite ($CuFeS_2$), chalcosine (Cu_2S) and coveline (CuS) [28,40]. Long-term pollution of the environment resulting from the emissions of toxic elements, especially with As, characterised the Bor area as one of the most polluted in Europe, *e.g.* [13,15]. For that reason, the City of Bor and its surroundings were chosen as the study area. The climate in this area is moderately continental. The prevailing winds are in the W and WNW directions, followed by the NW, E, and ENE winds, while the least frequent winds are in the ESE, S and SSW directions [3].

The sampling sites (Fig. 1) were chosen considering the pollution sources such as: the copper smelter (denoted as the primary pollution source), and open pits, ore waste heaps, and flotation tailing ponds (secondary pollution sources). Also, the prevailing wind directions were taken into account, due to the significant influence on the dispersion and transport of the polluting substances.

Description of location of 14 sampling sites, their distance from the primary pollution source, as well as the dominant winds affecting the pollution level at the sampling sites, is presented in Table 1.

All the sampling sites were under the influence of particular pollution sources, except the sampling site B, which represented the background site. This sampling site is surrounded by mountain massifs and protected from the air pollution.

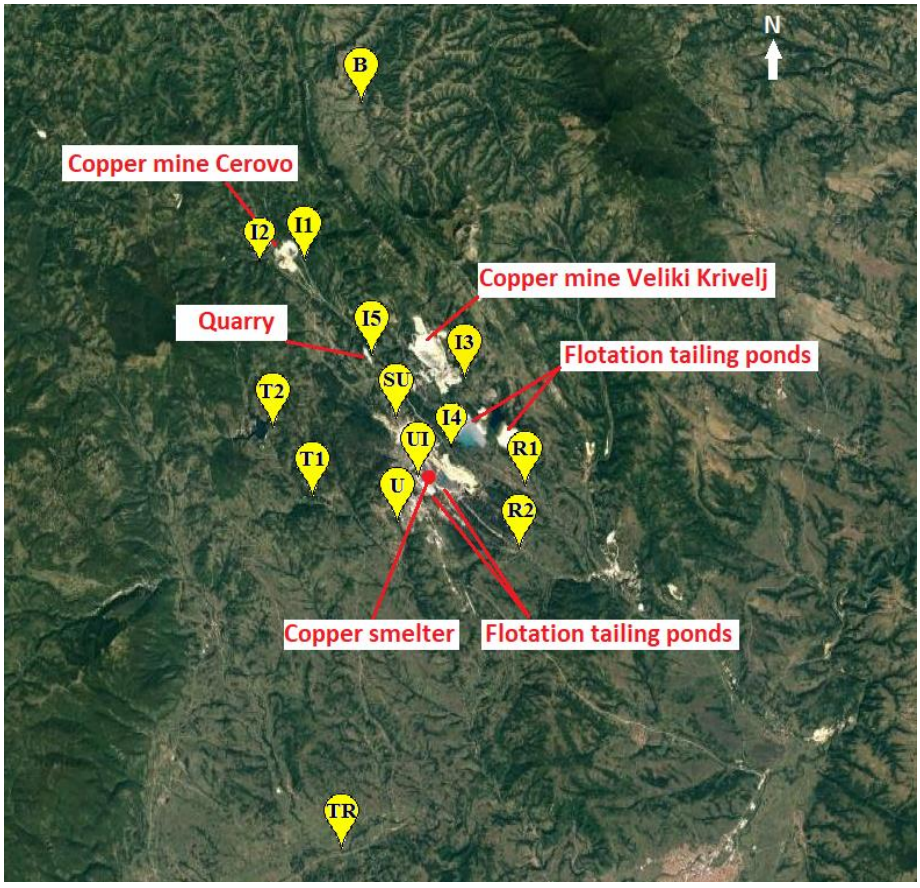

Figure 1. Map of the study area

Table 1. Description of the sampling sites

Sampling site	Location	Pollution sources	Wind direction
UI	Urban-industrial site, 0.5-2.5 km SW from the copper smelter, located in the city center	Copper smelter, flotation tailing ponds, city heating plant, traffic	ENE, NE
U	Urban site, >2.5 km SW from the copper smelter, residential area of the city	Copper smelter, traffic	ENE, NE
SU	Suburban site Brezonik, 2.5 km NW from the copper smelter	Copper smelter, flotation tailing ponds	SE, ESE
I1, I2	Industrial sites in the surroundings of the copper mine Cerovo, 11 km NW from the copper smelter	Open pit, ore waste hips	SE
I3	Industrial site in the surroundings of the copper mine Veliki Krivelj, 5.5 km N from the copper smelter	Ore waste hips, flotation tailing ponds, copper smelter	S
I4	Industrial site in the surroundings of the flotation tailing ponds of the copper mine Veliki Krivelj, 4.5 km NNE from the copper smelter	Flotation tailing ponds, ore waste hips, copper smelter	SW
I5	Industrial site in the surroundings of the quarry, 6 km NNW from the copper smelter	Dust emissions from exploiting and crushing of limestone	SSE, SE
R1	Rural settlement Oštrelj, 4.5 km ESE from the copper smelter	Flotation tailing ponds, copper smelter	WNW, WN
R2	Rural settlement Slatina, 6.5 km SE from the copper smelter	Copper smelter	WNW, WN
T1	Tourist area of the local Brestovac spa, 4.5 km WSW from the copper smelter	Periodical emissions from the copper smelter	ENE, E
T2	Tourist area of the local Bor lake, 7 km WNW from the copper smelter	Periodical emissions from the copper smelter	ESE, E
TR	The local traffic road, 20 km SSW from the copper smelter	Traffic pollution	N, NNE
B	Rural settlement Gornjane, 17 km N from the copper smelter	No air pollution from the copper smelter	S

2. 2. Sampling pattern and soil analysis

Collection of the soil samples was carried out at 14 sampling sites (Fig. 1). The soil was sampled at a depth of 10-20 cm. Soil preparation included air-drying of samples at room temperature and grinding to a fine powder [3]. Prior to chemical analyses, the soil samples were digested, following the U.S. EPA method 3050B [41], in a microwave oven (Ethos E, Milestone), with "aqua regia", *i.e.* a mixture of HNO_3 and HCl (volume ratio 1:3) (65 % HNO_3, J.T. Baker; 36.5-38 % HCl, J.T. Baker) [3]. Chemical analyses of the soil samples were performed in the accredited chemical laboratory, at the Mining and Metallurgy Institute Bor (Bor, Serbia). The concentrations of the analysed elements were determined by the simultaneous dual view inductively coupled plasma atomic emission spectrometer (ICP-AES, Spectromodel Blue). The quality of the obtained analytical data was verified by the blanks and three replicates of the same sample of soil. The concentrations of all the analysed elements are given as mg kg^{-1} dry mass.

2. 3. Data analyses

Descriptive analysis of the examined element concentrations in the soil was conducted using the SPSS version 17.0. Based on the obtained concentrations and defined limit and remediation values set by the Serbian Regulation [42], classification of the soil from each sampling site was carried out. According to this Regulation, concentration of the specific element in soil above the limit value indicates that functional properties of the soil and sustainable soil quality are endangered. The remediation value represents the concentration, which indicates that the fundamental functions of the soil are seriously disturbed, and the soil requires remediation, recovery and other measures.

Two types of the commonly used pollution indices, for assessing the environmental implications of the element contents (mg kg^{-1}) in the soil, are single (I_{geo}, *EF*, *CF*) and integrated (*PLI*, *NI*, *INI*). The single indices provide information about the pollution degree by the specific element, whereas the integrated indices provide information about pollution by more than one element, giving a comprehensive evaluation of soil contamination [26].

Geo-accumulation index (I_{geo}) is widely used for assessment of soil pollution by the specific element compared with its respective geochemical background concentration. This index was calculated by using the following equation [33,43,44]:

$$I_{geo} = \log_2 \frac{C_n}{1.5B_n} \quad (1)$$

where: C_n is the concentration of the studied element in the soil; B_n is the geochemical background concentration of the corresponding element; 1.5 is the factor used for reduction of possible variations in the background values caused by the natural pedogenic processes. In this study, the concentration of the element in soil, which is not affected by anthropogenic activities was used as the local geochemical background concentration (B_n) [33,44].

The values of I_{geo} were categorised into seven soil contamination classes [22,24,33]: $I_{geo} < 0$, unpolluted; $0 < I_{geo} \leq 1$, unpolluted to moderately polluted; $1 < I_{geo} \leq 2$, moderately polluted; $2 < I_{geo} \leq 3$, moderately to heavily polluted; $3 < I_{geo} \leq 4$, heavily polluted; $4 < I_{geo} \leq 5$, heavily to extremely polluted; $I_{geo} > 5$, extremely polluted.

Enrichment factor (*EF*) is used for assessment of the possible anthropogenic influence on the element concentration in the soil. *EF* was calculated by using the equation [10,24,36]:

$$EF = \frac{\left(\frac{C_n}{C_{ref}}\right)_{sample}}{\left(\frac{C_n}{C_{ref}}\right)_{background}} \quad (2)$$

where: C_{ref} is the concentration of the selected reference element. In this study, Al was selected as the reference element for the geochemical normalisation purposes, mostly due to its stability in soil and the lack of contamination with this element in the study area. It is considered that the enrichment of the soil originating from anthropogenic sources is present when $EF > 2$ [36]. However, soil enrichment has five categories [10,24,26,36]: $EF < 2$, deficiency to minimal enrichment; $2 \leq EF < 5$, moderate enrichment; $5 \leq EF < 20$, significant enrichment; $20 \leq EF \leq 40$, very high enrichment; $EF > 40$, extremely high enrichment.

Contamination factor (*CF*) represents the ratio between the concentration of the specific element in the soil and the corresponding background soil concentration [19,23,35]:

$$CF = \frac{C_n}{C_b} \quad (3)$$

where: C_b represents the geochemical background concentration of the corresponding element.

The *CF* value indicates the anthropogenic influence on soil contamination with the specific element [23], classified as [19,35,45,46]: $CF < 1$, low contamination; $1 \le CF < 3$, moderate contamination; $3 \le CF < 6$, considerable contamination; $CF \ge 6$, very high contamination. Higher *CF* values indicate lower retention times of the element in the soil and a higher risk to the environment [47]. The *CF* values are also used for calculation of the Nemerow pollution index (*NI*) [22]. The *CF* values usually indicate higher degrees of soil contamination with elements in comparison to the I_{geo} values [35].

Calculated values of the Pollution load index (*PLI*) represent the overall toxicity status of the soil [23]. The *PLI* value integrates all the determined elements for each sampling site, according to the equation [19,23,37]:

$$PLI = (CF_1\ CF_2\ CF_3 \ldots CF_n)^{1/n} \quad (4)$$

where: *CF* represents the value of the contamination factor for each element; n represents the number of the determined elements.

According to the values of *PLI*, the assessed pollution of soil with trace elements is classified as follows: $PLI < 0.7$, unpolluted; $0.7 \le PLI < 1$, slightly polluted; $1 \le PLI < 2$, moderately polluted; $2 \le PLI < 3$, severely polluted; $PLI \ge 3$, heavily polluted soil [19].

Nemerow pollution index (*NI*) is used for comprehensive evaluation of the soil quality, highlighting the influence of the element with the highest contamination factor (CF_{max}) [37,38] and it is calculated by the following equation [26]:

$$NI = \sqrt{\frac{CF_{mean}^2 + CF_{max}^2}{2}} \quad (5)$$

where: CF_{mean} is the mean value of contamination factors calculated for all the investigated elements; CF_{max} is the maximum value of the contamination factors calculated for all the investigated elements.

According to the values of *NI*, the quality of the soil is classified as: $NI < 0.7$, safe; $0.7 < NI \le 1.0$, precaution; $1.0 < NI \le 2.0$, slightly polluted; $2.0 < NI \le 3.0$, moderately polluted; $NI > 3.0$ seriously polluted [26,38].

Improved (modified) Nemerow index (*INI*) more accurately reflects the state of the soil by substituting other similar pollution indices, such as *CF* with the I_{geo}. The following equation was used for *INI* calculations [27,31,39]:

$$INI = \sqrt{\frac{I_{geo\text{-}max}^2 + I_{geo\text{-}ave}^2}{2}} \quad (6)$$

where: $I_{geo\text{-}max}$ is the maximum value of all the I_{geo} values and $I_{geo\text{-}ave}$ is the average value of the I_{geo} values calculated for all the investigated elements.

The values of *INI* are used for soil classification into following classes: $INI < 0.5$, uncontaminated; $0.5 \le INI < 1$, uncontaminated to moderately contaminated; $1 \le INI < 2$, moderately contaminated; $2 \le INI < 3$, moderately to heavily contaminated; $3 \le INI < 4$, heavily contaminated; $4 \le INI < 5$, heavily to extremely contaminated; $INI \ge 5$, extremely contaminated soil [31,48]. It should be noted that *INI* is considered as considerably more accurate than the *NI* value for the assessment of environmental contamination risks [31].

3. RESULTS AND DISCUSSION

3. 1. Descriptive statistics for concentrations of elements in soil

Descriptive statistics of the obtained concentrations of trace elements in the soil samples are summarised in Table 2.

The mean concentrations of As, Cu, Pb and Zn in the soil of the study area were several times higher than the world average values, while the content of Al and Fe were within these values or a little higher [49]. Classification of the soil from the study area depending on the *LV*s and *RV*s [42], is presented in Table 3 and in Supplementary material (Fig. S1).

Table 2. Results of descriptive statistical analyses of Al, As, Cu, Fe, Pb and Zn concentrations in soils sampled at the 14 sites compared to the corresponding world average values

Element	Concentration, mg kg^{-1}				Standard deviation	World average soil concentrations, mg kg^{-1} [49]
	Range	Min	Max	Mean		
Al*	2.85	3.15	5.99	4.75	0.92	1.00-5.00
As	155.30	9.67	164.98	70.29	54.56	6.83
Cu	2543.11	28.41	2571.52	708.14	651.52	38.9
Fe*	4.11	2.57	6.68	3.97	1.11	3.50
Pb	100.99	18.59	119.58	60.00	28.30	27.00
Zn	238.90	65.35	304.25	149.89	70.04	70.00

*concentration in %

The concentrations of As and Cu in soil samples exceeded the corresponding *LVs* at three and two sampling sites, respectively, while the *RVs* were exceeded at seven and eleven sampling sites, respectively. According to the exceedances of the *RVs* for As (up to 3 times) and Cu (up to 13 times), fundamental functions of the soil at most sampling sites were seriously disturbed and require remediation and other recovery measures. The exceedances of the *LVs* for Pb and Zn were recorded at three and six sampling sites, respectively, while exceedances of the *RVs* were not found for these metals. The limit and remediation values for Al and Fe were not defined by the Serbian Regulation. According to the *LVs* and *RVs*, the soil from the B site was classified as unpolluted in regard to all the studied elements. Soils from the sampling sites UI, U and SU, which were closest to the copper smelter and under the influence of dust from the flotation tailing ponds, were classified as polluted. The obtained concentration ranges of the investigated elements in the sampled soil (Table 2), as well as the exceedances of the *RV*s and *LV*s, indicated that the hazardous substances released from the copper smelter and dispersed from the flotation tailing ponds had the highest influence on the soil pollution in the study area.

Table 3. Classification of soil from the study area compared to the limit and remediation values

Element	*LV* / mg kg^{-1} [42]	*RV* / mg kg^{-1} [42]	Unpolluted soil	Polluted soil	
				C > *LV*	*C* > *RV*
As	29	55	I1, I3, TR, B	I2, I4, I5	UI, U, SU, R1, R2, T1, T2
Cu	36	190	B	I1, I2	UI, U, SU, I3, I4, I5, R1, R2, T1, T2, TR
Pb	85	530	I1, I2, I3, I4, I5, R1, R2, T1, T2, TR, B	UI, U, SU	/
Zn	140	720	I1, I2, I4, I5, R1, R2, T2, B	UI, U, SU, I3, T1, TR	/

/ - no exceedances of the *RVs*

3. 2. Assessment of the soil quality using single and integrated pollution indices

The influence of pollution from anthropogenic sources on the soil contamination around the mining and metallurgical area was evaluated by using the selected single and integrated indices of contamination, as stated in Section 2 (Materials and methods).

3. 2. 1. Geo-accumulation index (I_{geo})

The I_{geo} values for Al, As, Cu, Fe, Pb, and Zn in the soil at 13 sampling sites are shown in Figure 2. Based on the calculated I_{geo} values, soil in the study area was the most polluted with Cu, reaching the categories of heavily to extremely polluted soil at UI site, while extremely polluted soil was noted at five sites. The highest I_{geo} values for As were in the category of heavily polluted at UI, R2, T1 and T2 sites and moderately to heavily polluted soil at three sites. Moderate to heavy pollution of soil with Pb was noted at UI site. Regarding I_{geo} values, the most endangered sites with Cu, As and Pb were in immediate proximity to the copper smelter (*i.e.* UI, U, SU) and in the direction of the prevailing winds (*i.e.* R1, R2, T1, T2), indicating a strong influence of the industrial pollution. Also, it is important to emphasise that ore mining processes have less influence on the environmental pollution compared to the smelting of copper concentrates. According to I_{geo} values, soil from the study area was unpolluted to moderately polluted with Zn,

unpolluted and unpolluted to moderately polluted with Fe, while soil pollution with Al was not found. A lower category of the soil pollution with Fe and Al could indicate different origin of these elements compared to Cu, As and Pb.

In the study by Okonkwo *at al.* [19], the I_{geo} values for soils sampled around pegmatite mining sites showed that soil was unpolluted to heavily polluted by Zn, unpolluted to moderately polluted with Pb, while the I_{geo} values for Cu indicated that soils were in the category of unpolluted soil or moderately to heavily polluted soil, which was the consequence of the application of sewage sludge and copper containing fungicides. In another study [43], the I_{geo} values, calculated by using the median values of the examined elements in soils sampled in the surroundings of a tailing pond, indicated minimal soil pollution with As, Pb and Zn, whereas the sampled soil was at least moderately polluted with Cu. The highest values of I_{geo} suggested high pollution with Cu [43]. Contrary to that, based on the I_{geo} classification, the studied soils from an industrial area were not contaminated with Cu, Pb, Zn and Ni [33]. According to the I_{geo} values in an urban-rural area, low to moderate contamination with Cu, Pb and Zn was found [50]. Compared to these studies, the mean I_{geo} values for fertile agricultural soils were negative, indicating that the soils in this area were unpolluted with Al, As, Fe, Cu, Pb and Zn [24].

Based on the presented studies and results obtained here for I_{geo}, it could be observed that the soil from our study area was more polluted, especially with Cu.

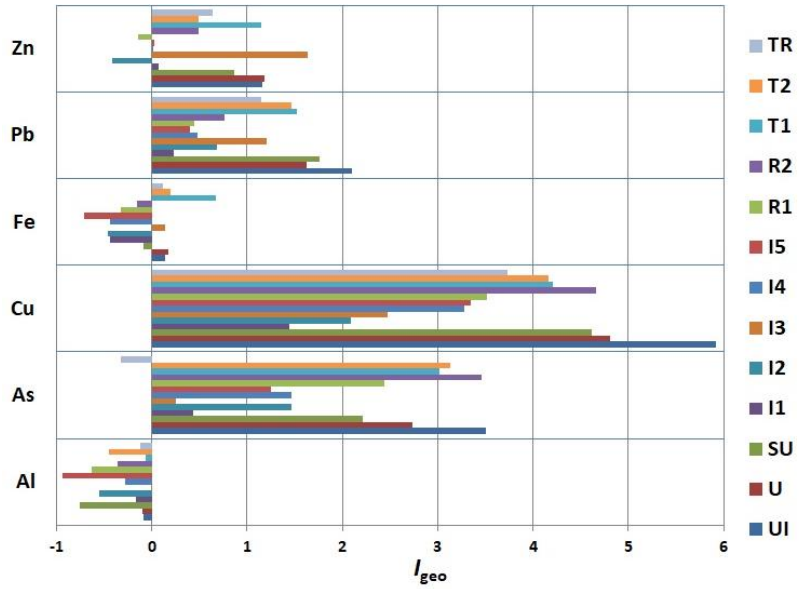

Figure 2. Geo-accumulation index (I_{geo}) values for Al, As, Cu, Fe, Pb and Zn in soils at 13 sampling sites in the study area

3. 2. 2. Enrichment factor (*EF*)

Calculated *EF* values for As, Cu, Fe, Pb, and Zn in the soil are presented in Figure 3. The most pronounced enrichment of the soil was noted for Cu. The soil at the sites UI and SU were extremely highly enriched, very highly enriched at the three sites (U, R2 and T2), while significantly enriched soil with Cu was noted at almost all the other sites. Significant enrichment was the highest category of soil enrichment with As and it was noted at the sites UI, U, SU, R1, R2, T1 and T2, as well as for Pb at the SU site. Enrichment of soil with Zn was minimal to moderate. The EF values for Fe in the soil at all the sampling sites were < 2, indicating that there was no enrichment with Fe and the origin of this element could be predominantly natural in the study area. *EF* soil index also revealed that enrichment of the examined soil was the highest with As, Cu and Pb, similar to the observations obtained with I_{geo} index.

Soil contamination in the vicinity of a former Zn-Pb ore treatment plant was estimated in literature [36]. The mean *EF* values for Cu and Fe in the topsoil were in the moderate contamination category, soil enrichment with Zn was high, while soil was in the extremely high category of contamination with Pb. In another study [43], based on the values of *EF* for Zn, As, and Pb in the soil from the surroundings of the tailing ponds, the soil was in the category of deficiency to minimally enriched, while there was moderate enrichment of soil with Cu. Very high enrichment with As (*EF* = 29.5), significant

enrichment with Cu (*EF* = 6.1), and deficiency to minimal enrichment with Zn (*EF* = 1.4) and Pb (*EF* = 1.1) were noted around Khatoon Abad Cu smelter (SE Iran) [10]. Such high values of *EF* for As and Cu confirmed the negative influence of the anthropogenic emissions of the Cu-smelter, which was in accordance with the results obtained for the soil sampled in our study. Varol [24] reported that the mean value of *EF* for As indicated moderate enrichment of the soil, while minimal soil enrichments were noted for Cu, Fe, Pb and Zn, in the Harran Plain located in Şanlıurfa province in Turkey.

Considering the data reported in the literature, it can be observed that the enrichment of soil with Cu was higher in our research, while the *EF* value for As was higher in the study of Forghani *et al.* [10]. The values of *EF* for Pb, Zn and Fe were higher in our study compared to the literature data.

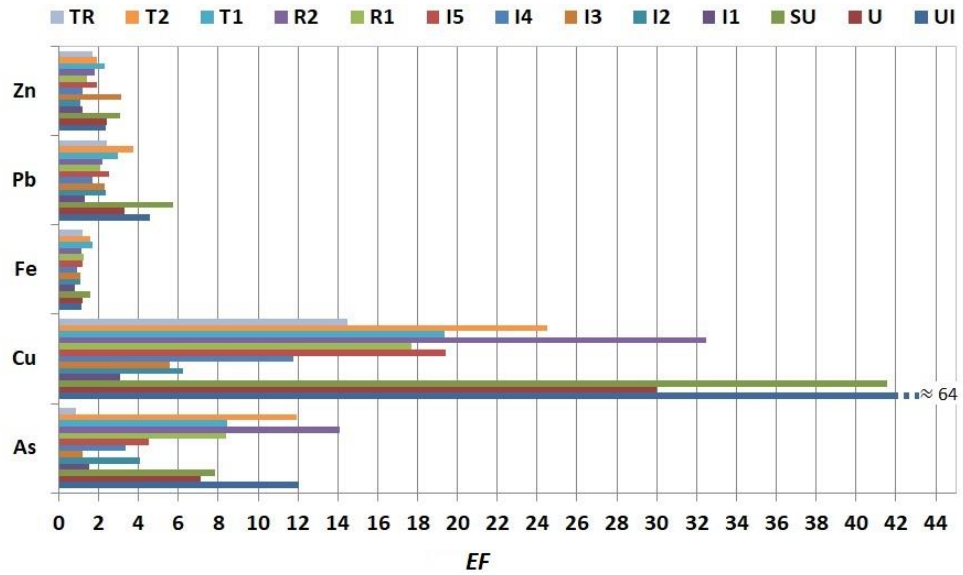

Figure 3. Enrichment factor (EF) values for As, Cu, Fe, Pb and Zn in the soils at 13 sampling sites in the study area

3. 2. 3. Contamination factor (*CF*)

A comparative presentation of *CF* values for Al, As, Cu, Fe, Pb, and Zn in the soil, depending on the sampling site is shown in Figure 4. The calculated *CFs* for Cu suggested very high contamination at almost all the sites and considerable contamination at site I1. The noted *CF* values for As, similarly as for Cu, were in the highest category of contamination, *i.e.* very high contamination at the sites UI, U, SU, R1, R2, T1 and T2, and considerable contamination at the sites I2, I4 and I5, while moderate contamination was obtained for three sites. Also, *CF* values for Pb indicated very high contamination at the site UI and considerable contamination at the sites U, SU, I3, T1, T2 and TR, and moderate contamination level at the remaining sites. Considerable soil contamination with Zn was noted at the sites UI, U, I3 and T1, while in other places soil contamination was moderate. The highest values of *CF* highlighted the strong negative influence of industrial activities, as well as the influence of prevailing wind on pollution dispersion, which was in accordance with the obtained values for I_{geo} and *EF*. The *CF* values for Al and Fe were predominantly in the category of moderate and low contamination, similarly to the data observed for I_{geo} and *EF*.

In a study on a mining area, the *CF* values indicated that soil contamination was low to considerable for Zn (0.54 to 4.00), and low to very high for Fe (1.00 to 11.34), Pb (0.70 to 10.00), and Cu (0.66 to 6.46) [19], which were similar to the results obtained in the present study. In another study [23], the *CF* values indicated that the soil contamination varied from low to considerable level, in a suburban zone around brick kilns (Jhenaidah District, south-western Bangladesh). However, the level of soil contamination with As was low, while the level of soil contamination with Al, Fe, Cu, Pb and Zn was low to moderate. In yet another research [26] the *CF* values obtained for Cu and Pb showed low to considerable contamination of soil inside the Vesuvius National Park, suggesting the influence of vehicular exhaust emissions in the tourist zone. Varol *et al.* [24] reported moderate contamination of soil with As, while they observed low contamination with Cu, Pb and Zn in agricultural area in Şanlıurfa province in Turkey. Low soil contamination with

Cu and Zn, and moderate contamination with Pb was noted at Sargodha, one of the most productive agricultural areas of Pakistan, with a fast-growing industrial setup [47].

Generally, in our study, the calculated values of *CF* for As, Cu, Pb and Zn were higher compared to the corresponding values of *CF* reported in the literature regarding different examined areas.

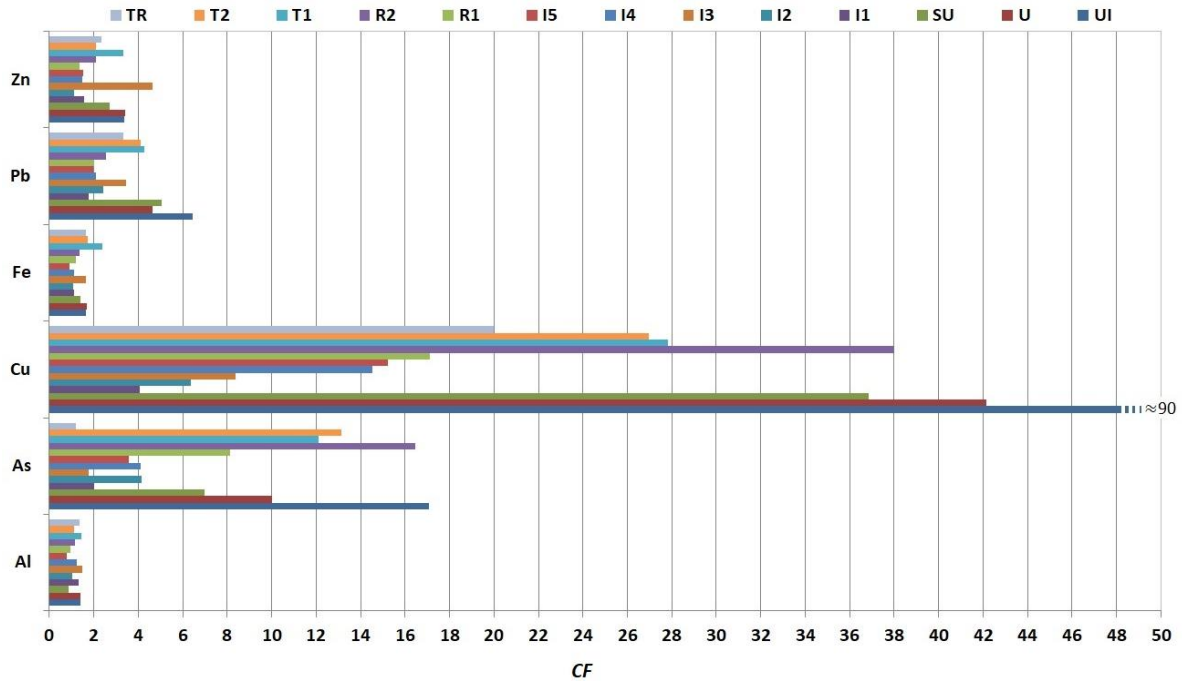

Figure 4. Contamination factor (CF) values for Al, As, Cu, Fe, Pb and Zn in the soils at 13 sampling sites in the study area

3. 2. 4. Pollution load index (PLI)

The overall soil contamination with the studied elements was estimated using *PLI* values shown in Figure 5. The obtained values of *PLI* ranged from 1.8 at the site I1 to 6.5 at the site UI. According to the *PLI* classification, the site I1 belongs to the moderately polluted, the sites I2, I3, I4 I5, R1 and TR are severely polluted, while the sites UI, U, SU, R2, T1 and T2 are in the category of heavily polluted soil. Within the elements used for the calculation of *PLI* values, As and Cu are the main pollution contributors.

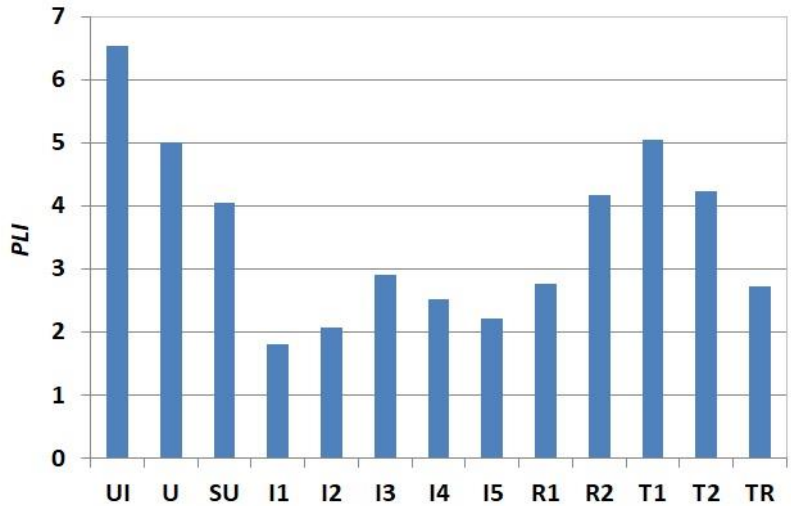

Figure 5. Pollution load index (PLI) values for the soils at 13 sampling sites in the study area

Based on the results obtained in the study by Yang *et al.* [38], the values of *PLI* for the urban soil ranged from 0.46 to 2.78, with a mean value of 0.96. The *PLI* values for soil samples from different sampling sites were reported to range from 0.8 in a nature reserve park to 2.3 in a lead/zinc mining region [37]. Low pollution levels were noted in the background area, while in the agricultural, industry, salt-lake and urban area, pollution was mainly moderate. Pollution in the mining area was the most serious [37]. The investigation of Okonkwo *et al.* [19] showed that *PLI* for soil at all the locations in the pegmatite mining area were in the range from 2 to 14, suggesting severe to heavy pollution of the soil, as in our study, but their calculated values were several times higher.

3. 2. 5. Nemerow index (NI)

The *NI* values of the examined elements in the soil samples were very high, ranging between 3.2 at the site I1 and 65.6 at the site UI (Fig. 6), indicating serious pollution at the sampling sites affected by pollution in the study area.

A study carried out in Peru investigated the area polluted by former mining activities. The *NI* values of trace elements in the soils from the leach pad area were very high, ranging between ~31 and 345, and in the soil from the mine dump area, they ranged between 28 and 211, indicating serious contamination at both sites [31], similarly as in our study, but with several times higher *NI* values. Contrary to that, in the study performed by Cui *et al.*, [20] at the old industrial area, the *NI* values ranged from 0.23 to 0.91 and from 0.17 to 0.62, indicating that soils from all the sampling sites were safe. In a study conducted in the Vesuvius National Park, the *NI* values ranged from ~1 and ~4, indicating slight to serious pollution of the soil [26]. The highest values of *NI* were noted at the end of the intense touristic activity (from April to October) that occurred in the park. In the soil from the urban Zhejiang Province located in south-eastern China, the *NI* values from all the evaluated sites were reported to range from 0.79 to 8.92, with a mean value of 1.74. Most of the values were in the category of precaution (15 %) and slightly polluted (64 %), while approximately 8 % of the sites had the *NI*>3, which indicated serious pollution of the soil [38]. *NI* values of elements in soil sampled from different zones in the northeastern Qinghai-Tibet Plateau, were unexpectedly high, ranging from 1 to 378 [37]. At 58 sampling sites, soil pollution was high, at 21 sites, the samples showed moderate *NI* values, and at 48 sites, the samples showed low pollution level, while pollution of soil from the background area was low to moderate [37].

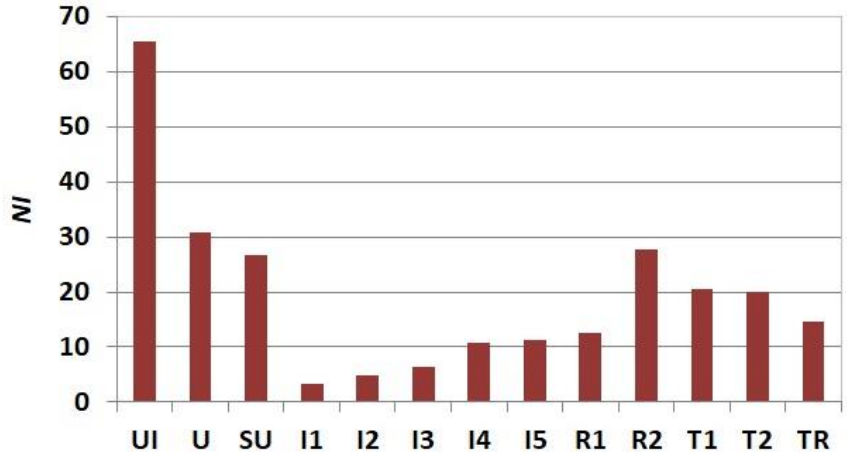

Figure 6. Nemerow index (NI) values for the soils at 13 sampling sites in the study area

PLI and *NI* showed the same trends with the highest values in the soil at the UI and the lowest at the site I1, indicating that the sites which were in the vicinity of the copper smelter and flotation tailing ponds were more polluted with the investigated elements. The sampling site I1 was located on the edge of the open pit, indicating that ore mining processes had a lower influence on the element concentration in the soil, compared to the smelting of copper concentrate and ore processing.

3. 2. 6. Improved Nemerow index (INI)

According to the calculated *INI* values (Fig. 7), the level of soil contamination was relatively high, ranging from moderately contaminated at the sites I1, I2 and I3, moderately to heavily contaminated at the sites I4, I5, R1 and TR, heavily contaminated at the sites U, SU, R2, T1 and T2, and heavily to extremely contaminated at the site UI. These data showed that soils from the most sampling sites in the study area were heavily contaminated.

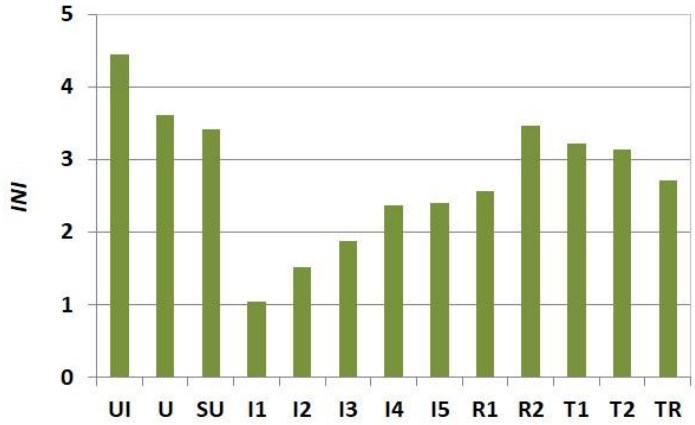

Figure 7. Improved Nemerow index (INI) values for the soils at 13 sampling sites in the study area

In a study in literature [31], the average *INI* values indicated extreme contamination (>5.0) and heavy to extreme contamination (4.67) of the soils from the mining area. Such high contamination indices highlighted the importance of effective contamination control and remediation. In the study by Santos-Francés *et al.* [48], taking the *INI* values into account, the soil was moderately to heavily contaminated, in the mining areas of La Zanja and Colquirrumi (Department of Cajamarca) and Julcani (Department of Huancavelica).

The calculated values of *INI* in the literature were similar as in our study, emphasising the effect of the industrial processes on the environmental contamination.

4. CONCLUSIONS

The purpose of this study was to provide information about the level of soil contamination with Al, As, Cu, Fe, Pb and Zn in the area endangered by pollution from the processes of copper mining and smelting. The mean concentrations of As, Cu, Pb and Zn in the soil of the study area were several times higher than the world average values. Concentrations of As and Cu in the soil exceeded the corresponding *RV*s at almost all the sampling sites, even up to 3 and 13 times, respectively. The exceedances of *LV*s for Pb and Zn were noted only at the most polluted sites. According to the single and integrated pollution indices, the quality of the soil was determined. Calculated values of single pollution indices provided insight into the degree of pollution by a specific element, while integrated pollution indices indicated cumulative pollution by the elements of interest. Based on the values of I_{geo}, *EF* and *CF* (single pollution indices) it was concluded that the highest pollution was with Cu and As, in the soils sampled in the close vicinity of the mining-metallurgical complex and flotation tailing ponds (UI, SU, U sites), as well as at the sites in the prevailing wind directions (R1, R2, T1, T2). The sampling sites significantly enriched with As actually indicated that the polluting substances containing As had the ability of dispersion over a large area due to their nature and properties, as well as that flotation tailings also were the source of particulate matters rich in As content. Mainly moderate contamination of the soil was observed in the case of Pb and Zn. The soil in the study area was not polluted with Al and Fe, suggesting their predominantly natural occurrence in the soil. The values of the *PLI*, *NI* and *INI* (integrated pollution indices) also showed serious cumulative contamination of the soil with the analysed elements from the sites closest to the copper smelter and in the prevailing wind directions, suggesting the influence of the anthropogenic activities in the study area. The main contributors of the soil pollution were Cu and As, which was expected due to the smelting of sulphide copper ore

with a high quantity of these elements. The results of this investigation indicate that the soil in the vicinity of the metallurgical complex, as well as from the sampling sites at which the prevailing winds bring the pollution from the copper smelter and flotation tailing ponds show the most serious pollution. These areas need effective environmental pollution control and prevention, as well as soil remediation particularly for highly endangered sites.

SUPPLEMENTARY MATERIAL

Additional data are available electronically at https://www.ache-pub.org.rs/index.php/HemInd/article/view/1133, or from the corresponding author on request.

Acknowledgements: *The authors are grateful to the Ministry of Science, Technological Development and Innovation of the Republic of Serbia for financial support, within the funding of the scientific research at the University of Belgrade, Technical Faculty in Bor (No. 451-03-65/2024-03/200131). Our thanks go to retired English language teacher Mara Z. Manzalovic from the University of Belgrade, Technical Faculty in Bor, for providing language assistance.*

REFERENCES

[1] Pollard AS, Williamson BJ, Taylor M, Purvis WO, Goossens M, Reis S, Aminov P, Udachin V, Osborne NJ. Integrating dispersion modelling and lichen sampling to assess harmful heavy metal pollution around the Karabash copper smelter, Russian Federation. *Atmos Pollut Res*. 2015; 6: 939-945. http://dx.doi.org/10.1016/j.apr.2015.04.003

[2] Oyebamiji A, Odebunmi A, Ruizhong H, Rasool A. Assessment of trace metals contamination in stream sediments and soils in Abuja leather mining, southwestern Nigeria. *Acta Geochim*. 2018; 37(4): 592-613. https://doi.org/10.1007/s11631-017-0256-1

[3] Kalinovic JV, Serbula SM, Radojevic AA, Milosavljevic JS, Kalinovic TS, Steharnik MM. Assessment of As, Cd, Cu, Fe, Pb, and Zn concentrations in soil and parts of *Rosa* spp. sampled in extremely polluted environment. *Environ Monit Assess*. 2019; 191: 15. https://doi.org/10.1007/s10661-018-7134-0

[4] Cowden P, Aherne J. Assessment of atmospheric metal deposition by moss biomonitoring in a region under the influence of a long standing active aluminium smelter. *Atmos Environ*. 2019; 201: 84-91. https://doi.org/10.1016/j.atmosenv.2018.12.022

[5] Mazurek R, Kowalska JB, Gąsiorek M, Zadrożny P, Wieczorek J. Pollution indices as comprehensive tools for evaluation of the accumulation and provenance of potentially toxic elements in soils in Ojców National Park. *J Geochem Explor*. 2019; 201: 13-30. https://doi.org/10.1016/j.gexplo.2019.03.001

[6] Alexandrino A, Viteri F, Rybarczyk Y, Andino JEG, Zalakeviciute R. Biomonitoring of metal levels in urban areas with different vehicular traffic intensity by using *Araucaria heterophylla* needles. *Ecol Indic*. 2020; 117: 106701. https://doi.org/10.1016/j.ecolind.2020.1067014

[7] Cai C, Xiong B, Zhang Y, Li X, Nunes LM. Critical Comparison of Soil Pollution Indices for Assessing Contamination with Toxic Metals. *Water Air Soil Pollut*. 2015; 226: 352. https://link.springer.com/article/10.1007/s11270-015-2620-2

[8] Bayouli IT, Bayouli HT, Dell'Oca A, Meers E, Sun J. Ecological indicators and bioindicator plant species for biomonitoring industrial pollution: Eco-based environmental assessment. *Ecol Indic*. 2021; 125: 107508. https://doi.org/10.1016/j.ecolind.2021.107508

[9] Fry KL, Wheeler CA, Gillings MM, Flegal AR, Taylor MP. Anthropogenic contamination of residential environments from smelter As, Cu and Pb emissions: Implications for human health. *Environ Pollut*. 2020; 262: 114235. https://doi.org/10.1016/j.envpol.2020.114235

[10] Forghani G, Kelm U, Mazinania V. Spatial distribution and chemical partitioning of potentially toxic elements in soils around Khatoon-Abad Cu Smelter, SE Iran. *J Geochem Explor*. 2019; 196: 66-80. https://doi.org/10.1016/j.gexplo.2018.09.012

[11] Kalinovic TS, Serbula SM, Radojevic AA, Kalinovic JV, Steharnik MM, Petrovic JV. Elder, linden and pine biomonitoring ability of pollution emitted from the copper smelter and the tailings ponds. *Geoderma*. 2016; 262: 266-275. https://doi.org/10.1016/j.geoderma.2015.08.027

[12] Radojevic AA, Serbula SM, Kalinovic TS, Kalinovic JV, Steharnik MM, Petrovic JV, Milosavljevic JS. Metal/metalloid content in plant parts and soils of *Corylus* spp. influenced by mining-metallurgical production of copper. *Environ Sci Pollut R*. 2017; 24 (11): 10326-10340. https://link.springer.com/article/10.1007/s11356-017-8520-9

[13] Serbula SM, Milosavljevic JS, Radojevic AA, Kalinovic JV, Kalinovic TS, Extreme air pollution with contaminants originating from the mining-metallurgical processes. *Sci Total Environ*. 2017; 586: 1066-1075. https://doi.org/10.1016/j.scitotenv.2017.02.091

[14] Milosavljevic JS, Serbula SM, Cokesa DjM, Milanovic DB, Radojevic AA, Kalinovic TS, Kalinovic JV. Soil enzyme activities under the impact of long-term pollution from mining-metallurgical copper production. *Eur J Soil Biol*. 2020; 101: 103232. https://doi.org/10.1016/j.ejsobi.2020.103232

[15] Serbula SM, Milosavljevic JS, Kalinovic JV, Kalinovic TS, Radojevic AA, Apostolovski Trujic TLj, Tasic VM. Arsenic and SO_2 hotspot in South-Eastern Europe: An overview of the air quality after the implementation of the flash smelting technology for copper production, *Sci Total Environ*. 2021; 777: 145981. https://doi.org/10.1016/j.scitotenv.2021.145981

[16] Kusin FM, Awang NHC, Hasan SNMS, Rahim HAA, Azmin N, Jusop S, Kim K-W. Geo-ecological evaluation of mineral, major and trace elemental composition in waste rocks, soils and sediments of a gold mining area and potential associated risks. *Catena*. 2019; 183: 104229. https://doi.org/10.1016/j.catena.2019.104229
[17] El Azhari A, Rhoujjati A, El Hachimib ML, Ambrosi J.Pollution and ecological risk assessment of heavy metals in the soil-plant system and the sediment-water column around a former Pb/Zn-mining area in NE Morocco. *Ecotox Environ Safe*. 2017; 144: 464-474. http://dx.doi.org/10.1016/j.ecoenv.2017.06.051
[18] Izquierdo T, Bonnail E, Abad M, Dias MI, Prudêncio MI, Marques R, Rodríguez-Vidal J, Ruiz F. Pollution and potential risk assessment of flood sediments in the urban area of the mining Copiapó basin (Atacama Desert). *J S Am Earth Sci*. 2020; 103: 102714. https://doi.org/10.1016/j.jsames.2020.102714
[19] Okonkwo SI, Idakwo SO, Ameh EG. Heavy metal contamination and ecological risk assessment of soils around the pegmatite mining sites at Olode area, Ibadan southwestern Nigeria. *Environ Nanotechnol*. 2021; 15: 100424. https://doi.org/10.1016/j.enmm.2020.100424
[20] Cui X, Geng Y, Sun R, Xie M, Feng X, Li X, Cui Z. Distribution, speciation and ecological risk assessment of heavy metals in Jinan Iron & Steel Group soils from China. *J Clean Prod*. 2021; 295: 126504. https://doi.org/10.1016/j.jclepro.2021.126504
[21] Gorena T, Fadic X, Cereceda-Balic F. *Cupressus macrocarpa* leaves for biomonitoring the environmental impact of an industrial complex: The case of Puchuncaví-Ventanas in Chile. *Chemosphere*. 2020; 260: 127521. https://doi.org/10.1016/j.chemosphere.2020.127521
[22] Kowalska JB, Mazurek R, Gąsiorek M, Zaleski T. Pollution indices as useful tools for the comprehensive evaluation of the degree of soil contamination-A review. *Environ Geochem Health*. 2018; 40: 2395-2420. https://doi.org/10.1007/s10653-018-0106-z
[23] Kumar S, Zhao M, Zhang H, Rahman MA, Luo C, Rahman MM. Distribution, contamination status and source of trace elements in the soil around brick kilns. *Chemosphere*. 2021; 263: 127882. https://doi.org/10.1016/j.chemosphere.2020.127882
[24] Varol M, Sünbül MR, Aytop H, Yılmaz CH. Environmental, ecological and health risks of trace elements, and their sources in soils of Harran Plain, Turkey. *Chemosphere*. 2020; 245: 125592. https://doi.org/10.1016/j.chemosphere.2019.125592
[25] Mazurek R, Kowalska J, Gąsiorek M, Zadrożny P, Józefowska A, Zaleski T, Kępka W, Tymczuk M, Orłowska K. Assessment of heavy metals contamination in surface layers of Roztocze National Park forest soils (SE Poland) by indices of pollution. *Chemosphere*. 2017; 168: 839-850. http://dx.doi.org/10.1016/j.chemosphere.2016.10.126
[26] Memoli V, Francesco Esposito F, Panico SC, DeMarcoa A, Barile R, Maisto G. Evaluation of tourism impact on soil metal accumulation through single and integrated indices. *Sci Total Environ*. 2019; 682: 685-691. https://doi.org/10.1016/j.scitotenv.2019.05.211
[27] El-Magd SAA, Taha TH, Pienaar HH, Breil P, Amer RA, Namour P. Assessing heavy metal pollution hazard in sediments of Lake Mariout, Egypt. *J Afr Earth Sci*. 2021; 176: 104116. https://doi.org/10.1016/j.jafrearsci.2021.104116
[28] Kalinovic TS, Serbula SM, Kalinovic JV, Radojevic AA, Petrovic JV, Steharnik MM, Milosavljevic JS, Suitability of linden and elder in the assessment of environmental pollution of Brestovac spa and Bor lake (Serbia). *Environ Earth Sci*. 2017; 76: 178. https://link.springer.com/article/10.1007/s12665-017-6485-0
[29] Wang Z, Liu X, Qin H. Bioconcentration and translocation of heavy metals in the soil-plants system in Machangqing copper mine, Yunnan Province, China. *J Geochem Explor*. 2019; 200: 159-166. https://doi.org/10.1016/j.gexplo.2019.02.005
[30] Chai L, Wang Y, Wang X, Ma L, Cheng Z, Su L. Pollution characteristics, spatial distributions, and source apportionment of heavy metals in cultivated soil in Lanzhou, China. *Ecol Indic*. 2021; 125: 107507. https://doi.org/10.1016/j.ecolind.2021.107507
[31] Cruzado-Tafur E, Torró L, Bierla K, Szpunar J, Tauler E. Heavy metal contents in soils and native flora inventory at mining environmental liabilities in the Peruvian Andes. *J S Am Earth Sci*. 2021; 106: 103107. https://doi.org/10.1016/j.jsames.2020.103107
[32] Nadgórska-Socha A, Kandziora-Ciupa M, Ciepał R. Element accumulation, distribution, and phytoremediation potential in selected metallophytes growing in a contaminated area. *Environ Monit Assess*. 2015; 187: 441. https://pubmed.ncbi.nlm.nih.gov/26088758/
[33] Taati A, Salehi MH, Mohammadi J, Mohajer R, Díez S. Pollution assessment and spatial distribution of trace elements in soils of Arak industrial area, Iran: Implications for human health. *Environ Res*. 2020; 187: 109577. https://doi.org/10.1016/j.envres.2020.109577
[34] Gujre N, Rangan L, Mitra S. Occurrence, geochemical fraction, ecological and health risk assessment of cadmium, copper and nickel in soils contaminated with municipal solid wastes. *Chemosphere*. 2021; 271: 129573. https://doi.org/10.1016/j.chemosphere.2021.129573
[35] Hołtra A, Zamorska-Wojdyła D. The pollution indices of trace elements in soils and plants close to the copper and zinc smelting works in Poland's Lower Silesia. *Environ Sci Pollut R*. 2020; 27: 16086-16099. https://doi.org/10.1007/s11356-020-08072-0
[36] Liénard A, Brostaux Y, Colinet G. Soil contamination near a former Zn-Pb ore-treatment plant: Evaluation of deterministic factors and spatial structures at the landscape scale. *J Geochem Explor*. 2014; 147: 107-116. http://dx.doi.org/10.1016/j.gexplo.2014.07.014

[37] Li L, Wu J, Lu J, Min X, Xue J, Yang L. Distribution, pollution, bioaccumulation, and ecological risks of trace elements in soils of the northeastern Qinghai-Tibet Plateau. *Ecotox Environ Safe*. (2018); 166: 345-353. https://doi.org/10.1016/j.ecoenv.2018.09.110

[38] Yang H, Wang F, Yu J, Huang K, Zhang H, Fu Z. An improved weighted index for the assessment of heavy metal pollution in soils in Zhejiang, China. *Environ Res*. 2021; 192: 110246. https://doi.org/10.1016/j.envres.2020.110246

[39] Li S, Zhao B, Jin M, Hu L, Zhong H, He Z. A comprehensive survey on the horizontal and vertical distribution of heavy metals and microorganisms in soils of a Pb/Zn smelter. *J Hazard Mater*. 2020; 400: 123255. https://doi.org/10.1016/j.jhazmat.2020.123255

[40] Serbula SM, Ilic AA, Kalinovic JV, Kalinovic TS, Petrovic NB, Assessment of air pollution originating from copper smelter in Bor (Serbia), *Environ Earth Sci*. 2014; 71 (4): 1651-1661. https://link.springer.com/article/10.1007/s12665-013-2569-7#page-1

[41] USEPA, 1996; United States Environmental Protection Agency, Acid Digestion of Sediments, Sludges, and Solids (3050B), Washington, DC, 1996.

[42] Official Gazette of Republic of Serbia, Regulation on Limit Values for Polluting, Harmful and Hazardous Substances in the Soil, No 30/2018, 2018 (in Serbian).

[43] Kabala C, Galka B, Jezierski P. Assessment and monitoring of soil and plant contamination with trace elements around Europe's largest copper ore tailings impoundment. *Sci Total Environ*. 2020; 738: 139918. https://doi.org/10.1016/j.scitotenv.2020.139918

[44] Qiao D, Wang G, Li X, Wang S, Zhao Y. Pollution, sources and environmental risk assessment of heavy metals in the surface AMD water, sediments and surface soils around unexploited Rona Cu deposit, Tibet, China. *Chemosphere*. 2020; 248: 125988. https://doi.org/10.1016/j.chemosphere.2020.125988

[45] Fiori CdS, Rodrigues APdC, Santelli RE, Cordeiro RC, Carvalheira RG, Araújo PC, Castilhos ZC, Bidone ED. Ecological risk index for aquatic pollution control: a case study of coastal water bodies from the Rio de Janeiro State, southeastern Brazil. *Geochim. Bras*. 2013; 27(1): 24-36. https://www.geobrasiliensis.org.br/geobrasiliensis/article/view/386

[46] Shaheen SM, Antoniadis V, Kwon E, Song H, Wang S-L, Hseu Z-Y, Rinklebe J. Soil contamination by potentially toxic elements and the associated human health risk in geo- and anthropogenic contaminated soils: A case study from the temperate region (Germany) and the arid region (Egypt). *Environ Pollut*. 2020; 262: 114312. https://doi.org/10.1016/j.envpol.2020.114312

[47] Hasan M, Kausar D, Akhter G, Shaha MH. Evaluation of the mobility and pollution index of selected essential/toxic metals in paddy soil by sequential extraction method. *Ecotox Environ Safe*. 2018; 147: 283-291. http://dx.doi.org/10.1016/j.ecoenv.2017.08.054

[48] Santos-Francés F, Martínez-Graña A, Rojo PA, Sánchez AG. Geochemical Background and Baseline Values Determination and Spatial Distribution of Heavy Metal Pollution in Soils of the Andes Mountain Range (Cajamarca-Huancavelica, Peru). *Int J Env Res Pub He*. 2017; 14: 859. https://www.mdpi.com/1660-4601/14/8/859

[49] Kabata-Pendias A. *Trace elements in soils and plants*. 4th ed. Boca Raton, Florida: CRC Press; 2011.

[50] Li C, Sun G, Wu Z, Zhong H, Wang R, Liu X, Guo Z, Cheng J. Soil physiochemical properties and landscape patterns control trace metal contamination at the urban-rural interface in southern China. *Environ Pollut*. 2019; 250: 537-545. https://doi.org/10.1016/j.envpol.2019.04.065

Indeksi zagađenja kao koristan alat za sveobuhvatnu procenu stepena kontaminacije zemljišta u blizini rudarskih i metalurških kompleksa

Jelena V. Kalinović, Snežana M. Šerbula, Tanja S. Kalinović, Ana A. Radojević i Jelena S. Jordanović

Univerzitet u Beogradu, Tehnički fakultet u Boru, Bor, Srbija

(Naučni rad)

Izvod

U ovom radu procenjen je nivo zagađenja zemljišta elementima Al, As, Cu, Fe, Pb i Zn na 14 mesta u gradu Boru i okolini u oblasti rudarstva i metalurgije bakra, kao i procena nivoa zagađenja pojedinačnim i integrisanim indeksima zagađenja. Značaj pojedinačnih indeksa zagađenja pruža informaciju o zagađenju određenim elementom, dok integrisani indeksi zagađenja pružaju uvid u kumulativno zagađenje ispitivanim elementima. Prosečne koncentracije As, Cu, Pb i Zn u zemljištu bile su nekoliko puta više od svetskih prosečnih vrednosti. Prekoračenja remedijacionih vrednosti bila su najizraženija za As (na sedam mesta) i Cu (na jedanaest mesta), više od 3 i 13 puta, redom. Prema geoakumulacionom indeksu, faktoru obogaćenja i faktoru kontaminacije, najveća kontaminacija zemljišta je bila sa As i Cu, naročito na urbano-industrijskom mestu. Indeksom opterećenja zagađenjem, Nemerovim indeksom zagađenja i poboljšanim (modifikovanim) Nemerovim indeksom potvrđeno je da su najviše kontaminirana zemljišta bila na mestima u blizini metalurškog kompleksa, flotacijskih jalovišta, kao i sa mesta koja se nalaze na pravcima najučestalijih vetrova u odnosu na manje zagađena zemljišta koja su bila pod uticajem procesa iskopavanja rude. Područjima pogođenim ozbiljnom kumulativnom kontaminacijom poreklom iz pirometalurške proizvodnje bakra potrebna je kontinualna prevencija zagađenja, monitoring i remedijacione mere.

Ključne reči: Zagađenje životne sredine; kvalitet zemljišta; pojedinačni i integrisani indeksi zagađenja zemljišta

Cobalt recovery from spent lithium-ion batteries by leaching in H_2SO_4-N_2 and H_2SO_4-O_2 systems followed by electrochemical deposition

Dragana V. Medić[1], Žaklina Z. Tasić[1], Maja M. Nujkić[1], Silvana B. Dimitrijević[2], Stefan S. Đorđievski[2], Slađana Č. Alagić[1] and Snežana M. Milić[1]

[1]*University of Belgrade, Technical Faculty in Bor, Bor, Serbia*
[2]*Mining and Metallurgy Institute, Bor, Serbia*

Abstract

This paper is focused on cobalt valorization from the cathode material of spent lithium-ion batteries (LIBs) by using leaching and electrochemical deposition methods. During the leaching experiments, the degrees of cathode material dissolution in H_2SO_4-N_2 and H_2SO_4-O_2 systems were compared. Maximal degrees of cobalt extraction were 40 % in the former and 47 % in the latter system under following experimental conditions: H_2SO_4 concentration of 2 mol dm^{-3}, nitrogen/oxygen volumetric flow of 2 L min^{-1}, solid phase concentration of 33 g L^{-1}, and temperature of 85 °C. The rate of cobalt extraction from the cathode material in both investigated systems was the most favorable in the first 15 min, after which there was a sudden decrease in the reaction rate. Cobalt from the leaching solution was deposited on a copper substrate by galvanostatic electrochemical deposition with a current efficiency of 84 %. The energy consumption was 5.8 kWh kg^{-1} of deposited Co. The cyclic voltammetry (CV) method was used to determine the potential of cobalt deposition, as well as side reactions taking place in the system. Scanning electron microscopy with energy dispersive spectrometry has shown that during the process of electrochemical deposition agglomeration of cobalt particles occurred (in the shape of cauliflower), while the metal was deposited in its elemental state, which was also confirmed by the results of X-ray diffraction analysis.

Keywords: Cathode material; acid leaching; lithium-cobalt oxide; recycling; metal coating.

Available on-line at the Journal web address: http://www.ache.org.rs/HI/

ORIGINAL SCIENTIFIC PAPER

UDC: (669.884+621.352):669.253

Hem. Ind. **78(3)** 281-290 (2024)

1. INTRODUCTION

Valorization of metals from spent lithium-ion batteries (LIBs) can be performed by employing the following methods: pyrometallurgical, biometallurgical and hydrometallurgical [1-3]. Among these processes, the hydrometallurgical method is most frequently used in treating spent LIBs due to low electricity consumption, low emission of pollutants, as well as high process efficiency [4]. This process of can be divided into several operations such as: discharging LIBs, their disassembling into individual components, separation of the cathode material from the current collector (aluminum), leaching of the cathode material and valorization of the metal from the leach solution. The latter process is most commonly performed by the use of one of the following methods: chemical deposition, extraction with organic solvents and electrochemical deposition [5,6]. The first method is not economically viable due to low yields of the deposited metals (< 50 %) [6]. The solvent extraction method is, on the other hand, economically viable and applicable in industrial conditions, but has a number of disadvantages such as: high solvent consumption, fire hazard caused by the solvent low flash point, environmental issues associated with the volatility of the solvents and possibility of their entering the environment. Unlike these methods, the electrochemical deposition method is acceptable from the environmental standpoint and easy to implement and control [7]. During the last three decades, 70 % of the world cobalt production has been based on the hydrometallurgical process, where the electrochemical deposition method is used as the final step in cobalt valorization [8]. This method enables production of cobalt coatings, as well as cobalt alloy coatings, with a precise control of the structure and morphology of the final product [9]. Electrochemically deposited cobalt is widely used in industry due to its favorable magnetic and electrical properties [10]. In a large number of studies *e.g.* [8,11,12],

Corresponding authors:Dragana V. Medić, University of Belgrade, Technical Faculty in Bor, Vojske Jugoslavije 12, 19210 Bor, Serbia
Paper received: 21 May 2023; Paper accepted: 23 October 2023; Paper published: 16 November 2023.
https://doi.org/10.2298/HEMIND230521027M

electrochemical deposition of cobalt is carried out from sulfate solutions to which boric acid is added, which acts as a Lewis acid (pK_a = 9.237), in order to control the micro and nanostructure of the deposited cobalt [11]. Still, the role of boric acid in the process of electrochemical reduction of cobalt ions has not been fully elucidated yet [13 -14], but many authors [15-17] consider boric acid acting as a buffer preventing formation of OH^- ions in the immediate vicinity of the electrode surface.

In the present study, hydrometallurgical treatment was applied for cobalt extraction from spent LIBs followed by electrochemical deposition to obtain cobalt coating on a copper substrate. Due to ferromagnetic properties of cobalt, it was not suitable to use a classical leaching apparatus, in which a magnet is used for the purpose of stirring the leach solution. Also, due to high cobalt concentrations in the leach solutions it is more suitable to use ultraviolet-visible spectrophotometry (UV-VIS) for monitoring the cobalt extraction degree compared to the inductively coupled plasma optical emission spectroscopy (ICP-OES), which is a predominantly used method in this type of investigation. For this reason in this leaching study, a new apparatus was designed and placed in an UV-VIS spectrophotometer to carry out the experiments. The newly created apparatus enabled continuous monitoring of the change of cobalt concentration in leach solutions, where nitrogen and oxygen were used for the purpose of stirring the solution.

Cyclic voltammetry (CV) was used for investigation of electrochemical processes taking place on the electrodes, whereas structural characterization of electrochemically deposited cobalt was performed by employing scanning electron microscopy with energy dispersive spectrometry (SEM-EDS) and X-ray diffraction analysis (XRD).

2. EXPERIMENTAL

2. 1. Materials and reagents

Spent LIBs with cathodes composed of lithium-cobalt oxide ($LiCoO_2$) were disassembled from laptops and used for the purpose of this research. Sulfuric acid (Merck, Darmstadt, Germany) was used as a leaching agent, whereas nitrogen and oxygen of purity 99.999 vol.% (Messer Tehnogas AD, Belgrade, Serbia) were used for stirring the leach solutions and providing an inert, that is, oxidizing atmosphere. In the process of electrolytic deposition of cobalt, the pH value of the leach solution was regulated with a saturated solution of sodium hydroxide (Merck, Darmstadt) and concentrated sulfuric acid (Merck, Darmstadt, Germany). The pH value of the solution was maintained by using boric acid (Zorka Pharma, Šabac) as a buffer. All chemical reagents were of *p.a.* quality.

2. 2. Experimental procedure

2. 2 .1. Preparation of the cathode material and chemical analysis

Used sets of LIBs were manually disassembled into separate cells. After discharging the LIB cells, they were disassembled into their basic components: the cathode, anode, and the separator. The cathode material was separated from the aluminum foil in a two-stage thermal treatment at 580 and 630 °C. The resulting cathode material was dried at room temperature for 24 h followed by crushing in an agate mortar with a pestle. A detailed explanation of each step in the pretreatment of LIBs was described previously [18].

To prepare a sample for chemical analysis, microwave digestion of the cathode material was performed by using a mixture of nitric and hydrochloric acid ((1:3 v/v) Merck, Darmstadt, Germany). The total metal content in the cathode material was determined by using inductively coupled plasma/optical emission spectrometer (ICP/OES Optima 8300; Perkin Elmer, USA).

2. 2. 2. Leaching tests

The leaching procedure included the following steps: 60 mL of sulfuric acid of a predefined concentration was poured into the reaction vessel and thermostated to the desired temperature (except for the experiments carried out at room temperature) with nitrogen or oxygen being blown at a constant flow of 2 L min^{-1}. Upon reaching the desired temperature, a previously measured mass of the cathode material was added. Absorption spectra were read every 3 min by using an UV-VIS spectrophotometer (UV-VIS, Beckman DU-65) with stirring being stopped 10 s prior to each

reading. The UV-VIS cuvette was directly connected to the reaction vessel, which was equipped with a thermistor, polytetrafluoroethylene (PTFE) gas introduction hose, and a heater. A detailed description and the scheme of the apparatus are reported previously [19].

2. 2. 3. Electrowinning and polarization

Electrolytic deposition of cobalt was carried out from a solution containing sulfuric acid. Due to almost identical chemical composition of the solutions obtained after cathode material dissolution in the H_2SO_4-N_2 and H_2SO_4-O_2 systems, these two solutions were mixed and thereafter considered as one system.

Due to a low initial pH value of the leach solution obtained under the optimal conditions of leaching the cathode material, the pH value of the leach solution was adjusted to 4.5 using saturated sodium hydroxide solution and concentrated sulfuric acid. To prevent the pH value in the cathode area from changing, boric acid was added to the solution, whose presence should inhibit the formation of hydroxyl-ions.

Cobalt electrochemical deposition was carried out galvanostatically at room temperature and at a current density of 200 A m^{-2} for 15 min. Copper sheet and platinum wire were used as cathode and anode, respectively. A constant current was obtained from a regulated power supply system (0 to 15 V, 10 A, DC, Veb Mlw Labortechnik Ilmenau, Germany). The difference in the cathode mass after and before the process of electrolysis was used to calculate the current efficiency.

Cyclic voltammogram was recorded on the IVIUM Xre potentiostat, IVIUM Technologies, (Netherlands), with the accompanying software. The measurements were performed in a three-electrode electrochemical system, with the copper electrode being used as a working electrode. The saturated calomel electrode (SCE) was used as a reference electrode, whereas a platinum wire was used as an auxiliary electrode. Prior to each experiment, surface of the copper electrode was polished with abrasive papers (1200, 2400 and 4000). Subsequent to polishing, the surface of the working electrode was rinsed with water and dried. Cyclic voltammogram was recorded in a potential range of -1.0 - 0.4 V and at a potential change rate of 20 mV s^{-1}.

2. 2. 4. Structural characterization

The crystal structure of the cathode deposit was investigated using an X-ray diffractometer (XRD Rigaku MiniFlex 600, Japan) equipped with a Cu X-ray source (40 kV and15 mA operation for X-ray generation). The surface morphology of the deposit was investigated using a scanning electron microscope (SEM, model: JOEL JSM-IT300LV, Japan) operated at 20 keV. Energy-dispersive X-ray spectroscopy (EDS) was utilized to determine the chemical composition of the sample. The X-ray spectrometer was connected to the scanning electron microscope, whereas the recording was performed using the Aztec software (Oxford Instruments, United Kingdom).

3. RESULTS AND DISCUSSION

3. 1. Chemical composition of the cathode material

The results of the ICP-OES analysis of the cathode material indicated the presence of cobalt (49.81 %), lithium (5.98 %), and aluminum (0.01 %). The presence and low percentage of aluminum in the cathode material might be the result of thermal separation of the cathode material from the aluminum foil [19].

3. 2. Leaching of the cathode material in H_2SO_4-N_2 and H_2SO_4-O_2 leaching systems

3. 2. 1. The effect of H_2SO_4 concentration

The effect of the initial H_2SO_4 concentration (0.5 to 3.0 mol L^{-1}) on the degree of cobalt extraction from the cathode material of spent LIBs was investigated under the following conditions: the temperature of the leach solution of 35 °C, solid phase concentration of 33 g L^{-1}, a nitrogen/oxygen volumetric flow of 2 L min^{-1}, and leaching time of 100 min. Results of the investigation with the given parameters are shown in Figure 1.

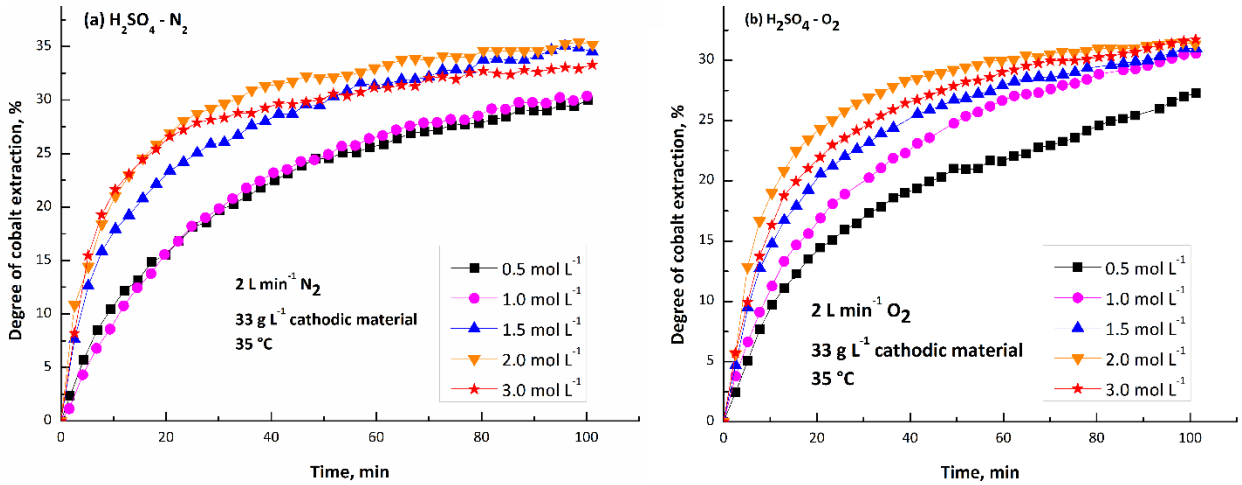

Figure 1. Effects of H_2SO_4 concentration on the degree of cobalt extraction: (a) in the system H_2SO_4-N_2, (b) in the system H_2SO_4-O_2

The obtained results (Fig. 1) show that the cobalt extraction degree increases with the increasing sulfuric acid concentration from 0.5 mol L^{-1} to 2.0 mol L^{-1}. However, a further increase in the sulfuric acid concentration to 3 mol L^{-1} leads to a decrease in the extraction degree in both investigated leaching systems. In a previous study [20], the authors stated that an increase in sulfuric acid concentration (from 2.0 mol L^{-1} to 4.0 mol L^{-1}) had a negligible effect on the cobalt extraction degree, while in another study [21] it was pointed out that a higher extraction degree is achieved when using 3 mol L^{-1} sulfuric acid compared to a lower concentration of 2 mol L^{-1}, but only in the first 20 min of the cathode material leaching. The latter result is in accordance with the results obtained in the present study for the H_2SO_4-N_2 leaching system (Fig. 1a). Considering that in the investigated sulfuric acid concentration range, the cobalt extraction degree ranged from 30-35 % for the H_2SO_4-N_2 system and 27-31 % for the H_2SO_4-O_2 system, it can be concluded that in both investigated systems the initial sulfuric acid concentration had a minor effect on the cobalt extraction degree, particularly when higher acid concentrations are used. Further analyses were performed with using 2 mol L^{-1} sulfuric acid for both investigated systems, which was considered as the optimal acid concentration during the leaching process.

3. 2. 2. The effect of solid phase concentration

To determine the effect of solid phase concentration on the cobalt extraction degree, a series of experiments was conducted at a solid phase concentration ranging from 10 to 67 g L^{-1}, sulfuric acid concentration of 2 mol L^{-1}, temperature of 35 ℃, nitrogen/oxygen volumetric flow of 2 L min^{-1}, and leaching time of 100 min and the results are presented in Figure 2.

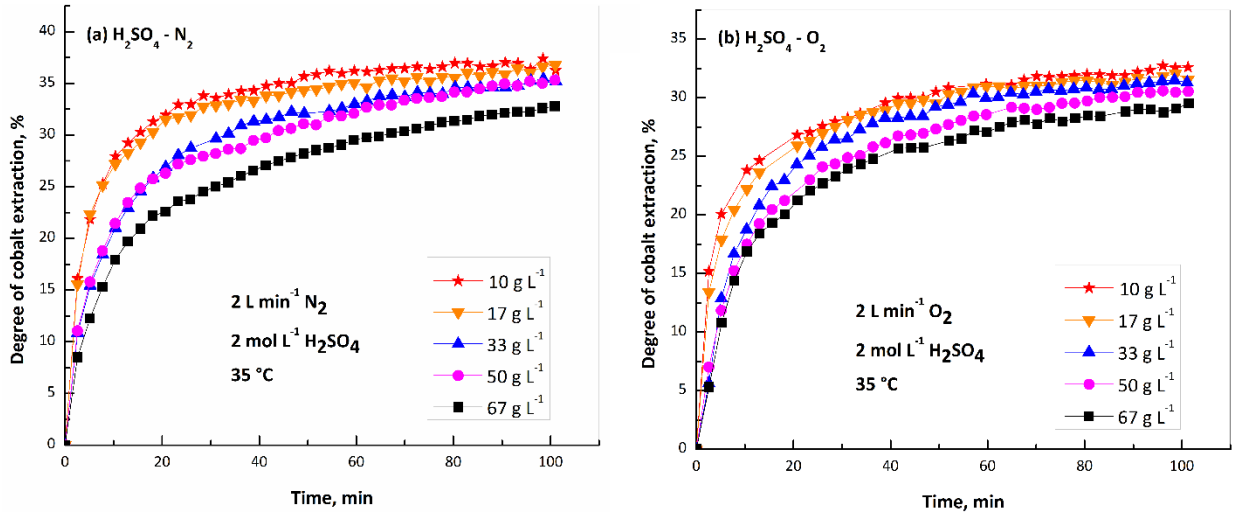

Figure 2. The effect of solid phase concentration on the degree of cobalt extraction: (a) in the system H_2SO_4-N_2, (b) in the system H_2SO_4-O_2

Based on the obtained results, it can be concluded that the cobalt extraction degree in both investigated systems decreases with increasing the solid phase concentration. The highest degrees of cobalt leaching amounting to 36 % for the H_2SO_4-N_2 system and 32 % for the H_2SO_4-O_2 system were recorded at a solid phase concentration of 10 g L^{-1}. A decrease in the cobalt leaching degree with increasing the solid phase concentration was probably caused by thickening of the suspension, which led to the increase in mass transfer resistance. Also, the increase in the solid-liquid phase ratio requires additional consumption of the leaching agent [22]. However, leaching of the cathode material in sulfuric acid at a low solid-liquid phase ratio is not economically justified [23]. Therefore, a solid phase concentration of 33 g L^{-1} in both investigated systems can be considered the optimal value and was used in further experimental research.

3. 2. 3. The effect of temperature and leaching time

The effect of temperature and leaching time on the degree of cobalt extraction in the presence of nitrogen and oxygen was investigated in the temperature range of 35-85 °C and in the time interval of 0-100 min, at a sulfuric acid concentration of 2 mol L^{-1}, solid phase concentration of 33 g L^{-1}, and nitrogen/oxygen volumetric flow of 2 L min^{-1}. The experimental results shown in Figure 3 indicate that the cobalt extraction degree increases with increasing both temperature and leaching time for both investigated leaching systems.

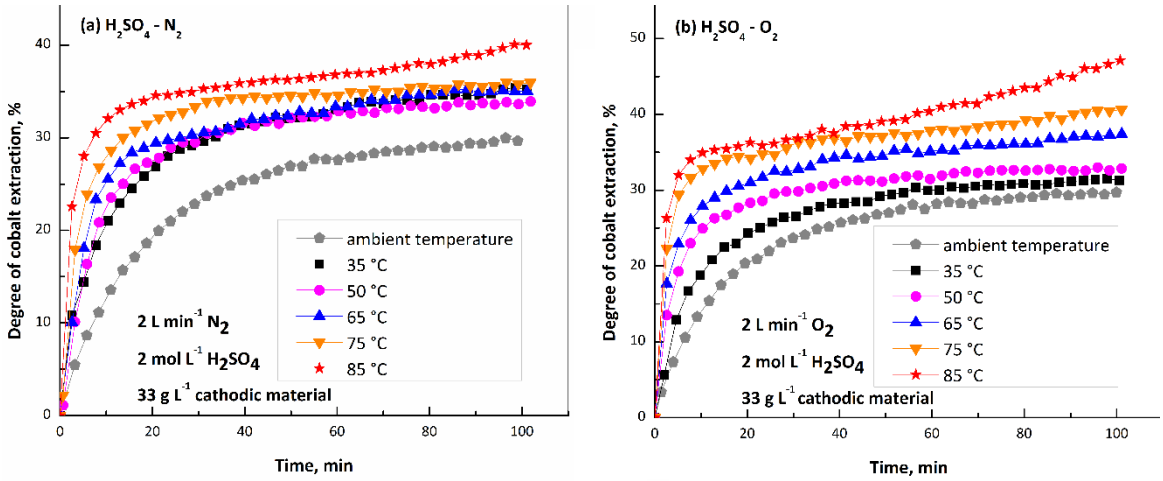

Figure 3.The effect of temperature and leaching time on the degree of cobalt extraction: (a) in the system H_2SO_4-N_2, (b) in the system H_2SO_4-O_2

The maximum cobalt extraction degrees of 40 % in the H_2SO_4-N_2 leaching system and 47 % in the H_2SO_4-O_2 system were achieved at the temperature of 85 °C and for the leaching time of 100 min. The shape of the obtained experimental curves shown in Figure 3 indicated that the rate of cobalt extraction from the cathode material in both investigated systems is most favorable in the first 15 min, after which there is a sudden decrease in the extraction rate. However, at a temperature of 85 °C, after 60 min from the start of the leaching process, an increase in the cobalt leaching degree can be observed. The cathode material leaching is an endothermic reaction that is favored at high temperatures [24]. A sudden decrease in the leaching reaction rate in the investigated systems indicates the possibility of the formation of leaching products, which slow down diffusion of the leaching agents to the cathode material surface.

Considering all obtained experimental results, it can be concluded that among the investigated parameters, temperature and leaching time have the greatest effect on the process of cathode material leaching in the presence of nitrogen and oxygen. Furthermore, the shapes of the kinetic curves of the cathode material leaching (Fig. 1 and Fig. 2) indicate that the acid concentration, as well as the solid phase concentration slightly affect cobalt extraction in both investigated leaching systems. The observed similar cobalt extraction behavior in H_2SO_4-N_2 and H_2SO_4-O_2 systems is probably the result of the poor solubility of oxygen in the leaching solution [25]. The experimental data obtained in the present leaching study indicated that neither the oxidizing oxygen atmosphere nor the inert nitrogen atmosphere provided conditions for a satisfactory cobalt extraction degree. Achieving a high degree of cobalt extraction from the cathode material requires a reducing atmosphere which may favor the reduction of Co^{3+} to Co^{2+} [26].

3. 3. Electrowinning and polarization

The electrowinning test resulted in a cobalt coating obtained with a current efficiency of 84 % and energy consumption of 5.8 kWh kg^{-1}. During the experiments, it was observed that only 5 min after the start of electrolytic cobalt deposition, cloudiness of the solution occurred throughout its entire volume as well as formation of a black coating on the platinum anode. These observations are shown in Figure 4.

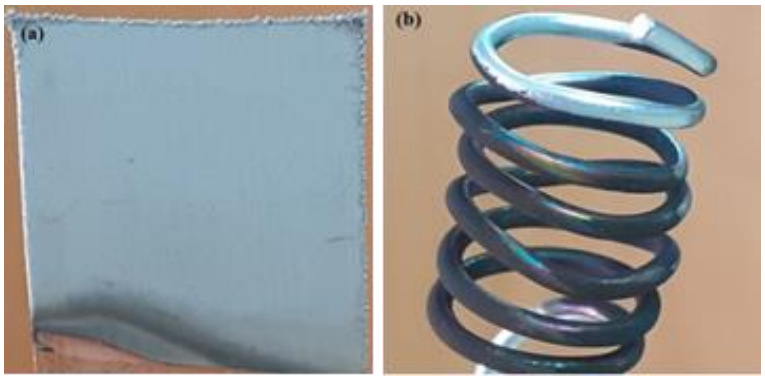

Figure 4. Appearance of the cathode (a) and the anode (b) after electrolytic deposition of cobalt from the leach solution

The layer formed on the platinum electrode probably represents cobalt oxide occurring because of Co^{2+} oxidation on the anode.

In a literature study [9] it was assumed that at pH values of the solution below 4, cobalt reduction is accompanied with simultaneous hydrogen evolution. During the process of electrolytic deposition of cobalt, H^+ ions are adsorbed on the surface of the deposited cobalt according to the following reactions:

$$Co^{2+}_{(aq)} + 2e^- \rightarrow Co_{(s)} \quad (1)$$

$$H^+_{(aq)} + Co_{(s)} + e^- \rightarrow CoH_{(ads)} \quad (2)$$

$$H^+_{(aq)} + CoH_{(ads)} + e^- \rightarrow Co_{(s)} + H_{2(ads)} \quad (3)$$

At a solution pH above 4, it was assumed that cobalt electrolysis proceeds with the formation of $Co(OH)_2$ according to the following reactions [9]:

$$2H_2O + 2e^- \rightarrow 2OH^-_{(aq)} + H_{2(g)} \quad (4)$$

$$Co^{2+}_{(aq)} + 2OH^-_{(aq)} \rightarrow Co(OH)_{2(s)} \quad (5)$$

$$Co(OH)_{2(s)} + 2e^- \rightarrow Co_{(s)} + 2OH^-_{(aq)} \quad (6)$$

The polarization behavior of the cathode during cobalt electrochemical deposition from a solution obtained by mixing two leaching solutions H_2SO_4-N_2 and H_2SO_4-O_2 at pH 4.5 is shown in Figure 5.

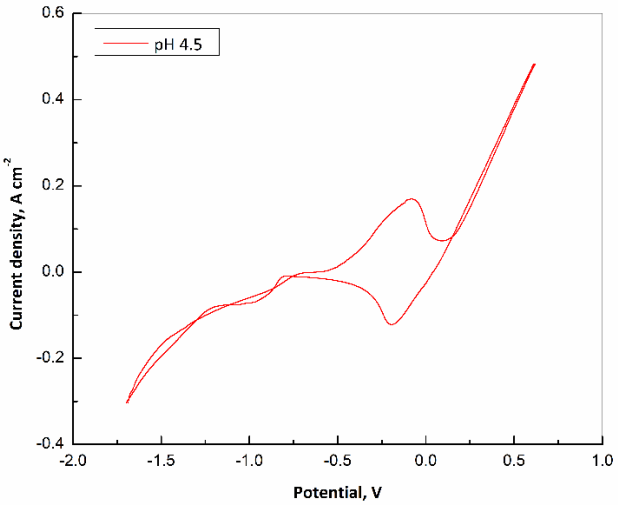

Figure 5. Polarization behavior of the cathode during cobalt electrochemical deposition from the leaching solution obtained in H_2SO_4-N_2 and H_2SO_4-O_2 systems

According to the Nernst equation, the deposition potential for cobalt is -0.51 V. Cyclic voltammogram shown in Figure 5 indicates a shift of the cobalt extraction potential to a more negative region. More specifically, in the presence of boric acid, the process of Co^{2+} reduction starts at a potential of -0.81 V, which could be the result of boric acid adsorption on the electrode surface. Boric acid probably acts as a surfactant, inhibiting direct cobalt ion reduction and resulting in an increase in the cathode potential of cobalt deposition [11]. Similar observations were reported in literature [27] during an investigation of the effect of boric acid in the process of electrolytic deposition of nickel. In the anodic part of the voltammogram at -0.07 V a peak can be observed, which may be a consequence of cobalt oxidation [28], while in the cathodic part of the voltammogram at -0.19 V there is a peak that can be attributed to the reduction of the passive film. Within the given potential range, lithium ions do not affect the process of electrochemical deposition of cobalt since the cathode potential for lithium deposition is -3.02 V. Similar observations were reported in literature [9].

3. 4. Structural characterization

Morphology of electrochemically deposited cobalt from the leach solution at an initial pH value of 4.5 is shown in Figure 6. The SEM microphotographs indicate that agglomeration of cobalt particles occurred in the form of cauliflower (Fig. 6a), which can be seen more clearly at a higher magnification (Fig. 6b).

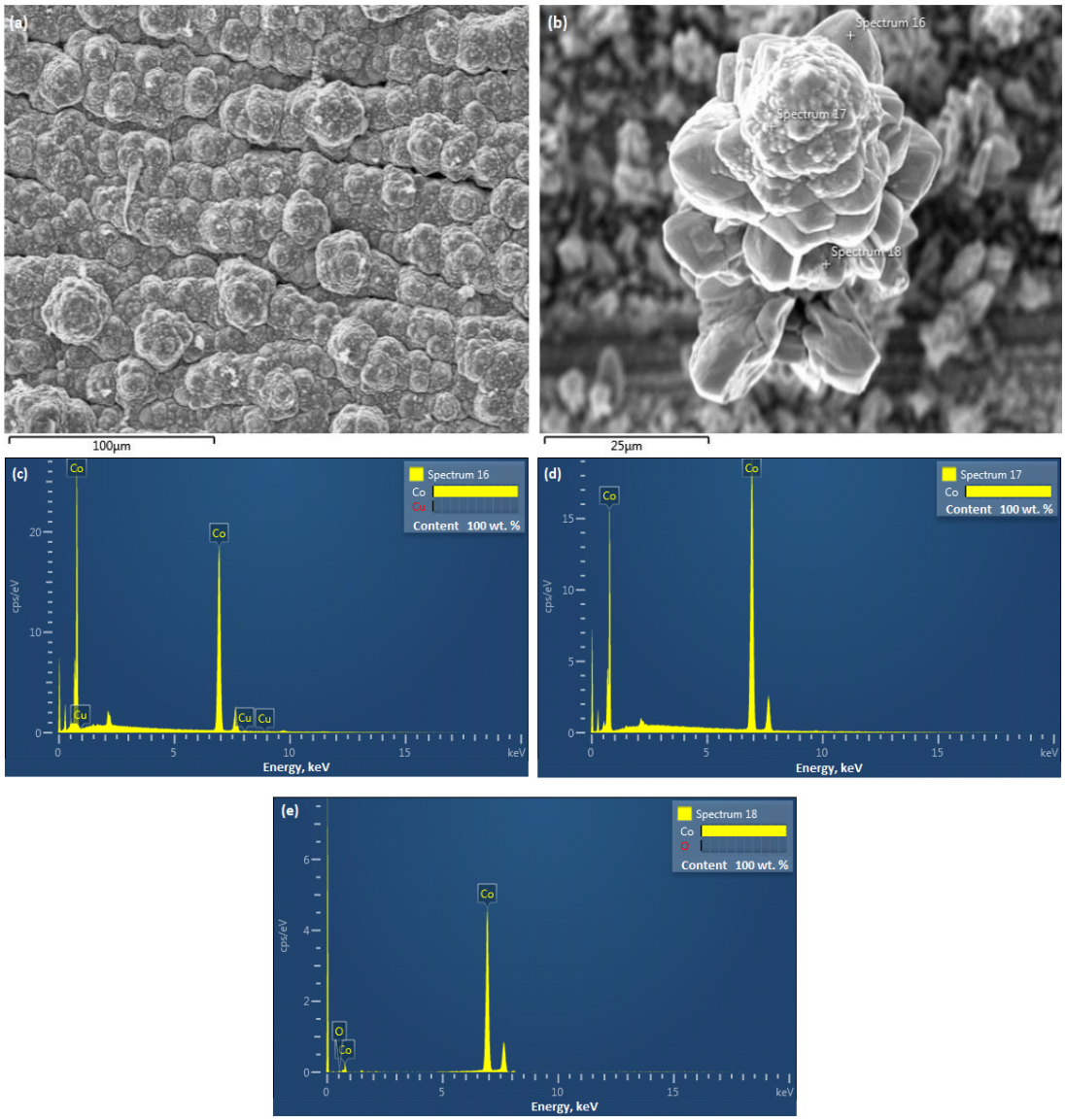

Figure 6. SEM micrographs (a: scale bar = 100 µm; b: scale bar = 25 µm) and EDS analyses results (c,d,e) of cobalt deposits obtained by electrochemical deposition from the leaching solution obtained in H_2SO_4-N_2 and H_2SO_4-O_2 systems

The presented agglomerates of a cauliflower shape, were formed under conditions of a side reaction of hydrogen ion reduction [29], which is characteristic of electrolytic deposition of cobalt. The energy spectra recorded at three different positions of the formed aggregates indicate a dominant presence of cobalt, whereas oxygen recorded in spectrum 18 is present in a small amount. A low copper content is observed in spectrum 16, which can be interpreted as the result of using a copper electrode as the cathode in the course of electrolytic deposition of cobalt from the leach solution.

Cobalt is deposited in its elemental state, which is confirmed by the XRD analysis (Fig. 7).

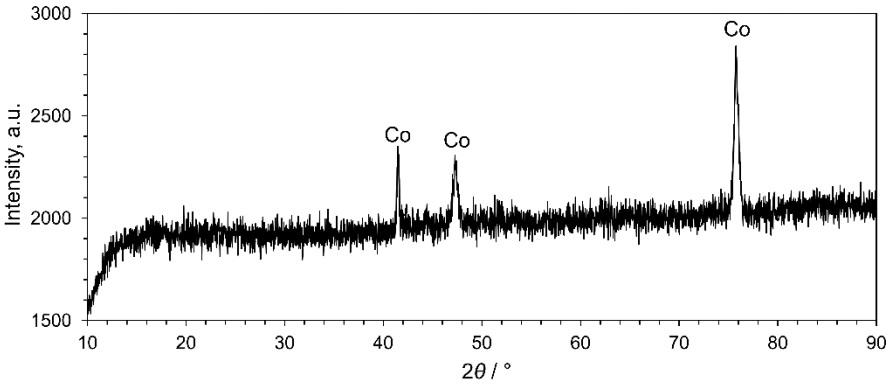

Figure 7. Diffractogram of cobalt particles obtained in the process of electrochemical deposition of cobalt from the leaching solution obtained in H_2SO_4-N_2 and H_2SO_4-O_2 systems

The recorded diffractogram of cobalt particles obtained in the process of electrochemical deposition confirms the assumption reported in literature [15-17] that boric acid acts as a buffer in the investigated system, preventing formation of OH^- ions, which enables deposition of elemental cobalt on a copper cathode.

4. CONCLUSION

The treatment of spent LIBs presented in this study enabled valorization of cobalt in the form of a metal coating on a copper substrate. The apparatus constructed for leaching the cathode material proved to be an effective solution for continuous monitoring of the changes in cobalt concentration in the leach solutions. The similar appearance of the leaching curves in the H_2SO_4-N_2 and H_2SO_4-O_2 systems is probably the result of poor solubility of oxygen in the leach solution. The presented results of electrochemical deposition indicate that boric acid has a dual role in the process of cobalt electrochemical deposition. In specific, boric acid in the leach solution acts as a buffer, preventing formation of OH^- ions and simultaneously affecting the morphology of deposited cobalt. Future research should be focused on increasing the efficiency of the process by introducing a reducing agent (*e.g.* copper powder, hydrogen peroxide, sulfur dioxide) into the leaching system. Also, processes for obtaining metallic cobalt coatings on different metal substrates should be developed and optimized.

Acknowledgements: *The research presented in this paper was performed with the financial support of the Ministry of Science, Technological Development, and Innovation of the Republic of Serbia, within the funding of the scientific research work at the University of Belgrade, Technical Faculty in Bor, according to the contract number 451-03-47/2023-01/200131, and within the funding of the scientific research work at the Mining and Metallurgy Institute Bor, according to the contract number 451-03-47/2023-01/200052.*

REFERENCES

[1] Guo Y, Zhao YL, Lou X, Zhou T, Wang Z, Fang C, Guan J, Chen S, Xu X, Zhang RQ. Efficient degradation of industrial pollutants with sulfur (IV) mediated by $LiCoO_2$ cathode powders of spent lithium ion batteries: A "treating waste with waste" strategy. *J Hazard Mater*. 2020; 399: 123090. https://doi.org/10.1016/j.jhazmat.2020.123090

[2] Chen X, Ma H, Luo C, Zhou T. Recovery of valuable metals from waste cathode materials of spent lithium-ion batteries using mild phosphoric acid. *J Hazard Mater*. 2017; 326: 77–86. https://doi.org/10.1016/j.jhazmat.2016.12.021

[3] Wang MM, Zhang CC, Zhang FS. Recycling of spent lithium-ion battery with polyvinyl chloride by mechano chemical process. *Waste Manage*. 2017; 67: 232–239. https://doi.org/10.1016/j.wasman.2017.05.013

[4] Meng Q, Zhang Y, Dong P, Liang F. A novel process for leaching of metals from $LiNi_{1/3}Co_{1/3}Mn_{1/3}O_2$ material of spent lithium ion batteries: Process optimization and kinetics aspects. *J Ind Eng Chem*. 2018; 61: 133–141. https://doi.org/10.1016/j.jiec.2017.12.010

[5] Yang Y, Sun W, Bu Y, Zhang C, Song S, Hu Y. Recovering metal values from spent lithium ion battery via a combination of reduction thermal treatment and facile acid leaching. *ACS Sustain Chem Eng*. 2018; 6: 10445−10453. https://doi.org/10.1021/acssuschemeng.8b01805

[6] Othman EA, Van der Ham AGJ, Miedema H, Kersten SRA. Recovery of metals from spent lithium-ion batteries using ionic liquid $[P_{8888}]$[Oleate]. *Sep Purif Technol*. 2020; 252: 117435. https://doi.org/10.1016/j.seppur.2020.117435

[7] Prabaharan G, Barik SP, Kumar N, Kumar L. Electrochemical process for electrode material of spent lithium ion batteries. *Waste Manage*. 2017; 68: 527−533. https://doi.org/10.1016/j.wasman.2017.07.007

[8] Patnaik P, Padhy SK, Tripathy BC, Bhattacharya IN, Paramguru RK. Electrodeposition of cobalt from aqueous sulfate solutions in the presence of tetra ethyl ammonium bromide. *Trans Nonferrous Met Soc of China* 2015; 25: 2047−2053. https://doi.org/10.1016/S1003-6326(15)63814-6

[9] Garcia EM, Santos JS, Pereira EC, Freitas MBJG. Electrodeposition of cobalt from spent Li-ion battery cathodes by the electrochemistry quartz crystal microbalance technique. *J Power Sources* 2008; 185: 549−553. https://doi.org/10.1016/j.jpowsour.2008.07.011

[10] Bhuiyan MS, Taylor BJ, Paranthaman M, Thompson JR, Sinclair JW. Microstructure and magnetic properties of electrodeposited cobalt films. *J Mater Sci.* 2008; 43: 1644−1649. https://doi.org/10.1007/s10853-007-2383-2

[11] Rafsanjani-Abbasi A, Rahimi E, Shalchian H, Vahdati-Khaki J, Babakhani A, Hosseinpour S, Davoodi A. Recycled Cobalt from Spent Li-ion Batteries as a Superhydrophobic Coating for Corrosion Protection of Plain Carbon Steel. *Materials* 2018; 12: 90. https://doi.org/10.3390/ma12010090

[12] Rigsby MA, Spurlin TA, Reid JD. The Multi-Functional Role of Boric Acid in Cobalt Electrodeposition and Superfill. *J Electrochem Soc*. 2020; 167: 112507. https://doi.org/10.1149/1945-7111/aba640

[13] Santos JS, Trivinho-Strixino F, Pereira EC. Investigation of $Co(OH)_2$ formation during cobalt electrodeposition using a chemometric procedure. *Surf Coat Technol.* 2010; 205: 2585−2589. https://doi.org/10.1016/j.surfcoat.2010.10.005

[14] Zhou J, Wang SF, Song XS. Electrodeposition of cobalt in double-membrane three-compartment electrolytic reactor. *Trans Nonferrous Met Soc of China* 2016; 26: 1706−1713. https://doi.org/10.1016/S1003-6326(16)64279-6

[15] Zech N, Landolt D. The influence of boric acid and sulfate ions on the hydrogen formation in Ni-Fe plating electrolytes. *Electrochim Acta* 2000; 45: 3461−3471. https://doi.org/10.1016/S0013-4686(00)00415-1

[16] Ho HY, Chen WB, Fu TY, Chen SJ. On the Electrodepositing of Cobalt Nanoparticles on ITO in the Presence of Boric Acid. *IEEE Trans Magn.* 2014; 50: 2100304. https://doi.org/10.1109/TMAG.2013.2277758

[17] Altimari P, Schiavi PG, Rubino A, Pagnanelli F. Electrodeposition of cobalt nanoparticles: An analysis of the mechanisms behind the deviation from three-dimensional diffusion-control. *J Electroanal Chem*. 2019; 851: 113413. https://doi.org/10.1016/j.jelechem.2019.113413

[18] Medić D, Milić S, Alagić S, Đorđević I, Dimitrijević S. Classification of spent Li-ion batteries based on ICP-OES/X-ray characterization of the cathode materials. *Hem Ind.* 2020; 74: 221−230. https://doi.org/10.2298/HEMIND200114012M

[19] Medić VD, Sokić MD, Nujkić MM, Đorđievski SS, Milić SM, Alagić ČS, Antonijević MA. Cobalt extraction from spent lithium-ion battery cathode material using a sulfuric acid solution containing SO_2. J Mater Cycles Waste Manage. 2023; 25: 1008–1018. https://doi.org/10.1007/s10163-022-01580-w

[20] Nayl AA, Elkhashab RA, Badawy SM, El-Khateeb MA. Acid leaching of mixed spent Li-ion batteries. *Arab J Chem*. 2017; 10: S3632−S3639. https://doi.org/10.1016/j.arabjc.2014.04.001

[21] Jha MK, Kumari A, Jha AK, Kumar V, Hait J, Pandey BD. Recovery of lithium and cobalt from waste lithium ion batteries of mobile phone. *Waste Manage*. 2013; 33: 1890−1897. https://doi.org/10.1016/j.wasman.2013.05.008

[22] Jiang F, Chen Y, Ju S, Zhu Q, Zhang L, Peng J, Wang X, Miller JD. Ultrasound-assisted Leaching of Cobalt and Lithium from Spent Lithium-ion Batteries. *Ultrason Sonochem*. 2018; 48: 88–95. https://doi.org/10.1016/j.ultsonch.2018.05.019

[23] Gao W, Zhang X, Zheng X, Lin X, Cao H, Zhang Y, Sun ZHI. Lithium Carbonate, Recovery from Cathode Scrap of Spent Lithium-ion Battery - a Closed-loop Process. *Environ Sci Technol*. 2017; 51: 1662−1669. https://doi.org/10.1021/acs.est.6b03320

[24] Zhu SG, He WZ, Li GM, Zhou X, Zhang XJ, Huang JW. Recovery of Co and Li from spent lithium-ion batteries by combination method of acid leaching and chemical precipitation. *Trans Nonferrous Met Soc of China* 2012; 22: 2274−2281. https://doi.org/10.1016/S1003-6326(11)61460-X

[25] Kaskiala T. Determination of oxygen solubility in aqueous sulfuric acid media. *Miner Eng*. 2002; 15: 853−857. https://doi.org/10.1016/S0892-6875(02)00089-4

[26] Ndalamo J, Mulaba-Bafubiandi AF, Mamba BB. UV/visible spectroscopic analysis of Co^{3+} and Co^{2+} during the dissolution of cobalt from mixed Co-Cu oxidized ores. *Int J Min Met and Mater*. 2011; 18: 260−269. https://doi.org/10.1007/s12613-011-0432-y

[27] Šupicová M, Rozik R, Trnková L, Oriňáková, Gálová M. Influence of boric acid on the electrochemical deposition of Ni. *J Solid State Electrochem*. 2006; 10: 61−68. https://doi.org/10.1007/s10008-005-0656-8
[28] Metikoš-Huković M, Babić R. Passivation and corrosion behaviours of cobalt and cobalt–chromium–molybdenum alloy. Corros Sci. 2007; 49: 3570–3579. https://doi.org/10.1016/j.corsci.2007.03.023
[29] Avramović Lj, Maksimović VM, Baščarević Z, Ignjatović N, Bugarin M, Marković R, Nikolić ND. Influence of the Shape of Copper Powder Particles on the Crystal Structure and Some Decisive Characteristics of the Metal Powders. *Metals* 2019; 9: 56. https://doi.org/10.3390/met9010056

Valorizacija kobalta iz istrošenih litijum-jonskih baterija luženjem u sistemima H_2SO_4-N_2 i H_2SO_4-O_2 i metodom elektrohemijskog taloženja

Dragana V. Medić[1], Žaklina Z. Tasić[1], Maja M. Nujkić[1], Silvana B. Dimitrijević[2], Stefan S. Đorđievski[2], Slađana Č. Alagić[1] i Snežana M. Milić[1]

[1]Univerzitet u Belgradu, Tehnički Facutet u Boru, Bor, Srbija
[2]Institut za ruderstvo i metalurgiju, Bor, Srbija

(Naučni rad)

Izvod

Tema rada je valorizacija kobalta iz katodnog materijala istrošenih litijum-jonskih baterija (LIBs) primenom metoda luženja i elektrohemijskog taloženja. Tokom eksperimenata luženja upoređivani su stepeni rastvaranja katodnog materijala u sistemima H_2SO_4-N_2 i H_2SO_4-O_2. Maksimalni stepeni ekstrakcije kobalta od 40 % u sistemu luženja H_2SO_4-N_2 i 47 % u sistemu H_2SO_4-O_2 postignuti su pod sledećim eksperimentalnim uslovima: koncentracija H_2SO_4 2 mol L^{-1}, zapreminski protok azota/kiseonika 2 L min^{-1}, koncentracija čvrste faze od 33 g L^{-1}, i temperatura od 85 °C. Kinetika ekstrakcije kobalta iz katodnog materijala, u oba ispitivana sistema, bila je najpovoljnija u prvih 15 min, nakon čega je došlo do naglog smanjenja brzine reakcije. Kobalt je deponovan iz rastvora za luženje na bakarnu podlogu metodom galvanostatskog taloženja sa iskorišćenjem struje od 84 %. Potrošnja energije je bila 5.8 kWh kg^{-1} deponovanog kobalta. Metoda ciklične voltametrije (CV) korišćena je za određivanje potencijala taloženja kobalta, kao i sporednih reakcija koje se odvijaju u sistemu. Metodom skenirajuće elektronske mikroskopije sa energetsko disperzivnom spektrometrijom utvrđeno je da je tokom procesa elektrohemijskog taloženja kobalta došlo do aglomeracije čestica kobalta (u obliku karfiola) i da je kobalt deponovan u njegovom elementarnom stanju, što je potvrđeno rezultatima rendgenske difrakcione analize.

Ključne reči: katodni materijal; kiselinsko luženje; litijum kobalt oksid; reciklaža; metalna prevlaka

Development of an eco- friendly mobile plant for car wash wastewater recovery

Dunja S. Sokolović[1] and Radmila M. Šećerov Sokolović[2]

[1]*University of Novi Sad, Faculty of Technical Sciences, Novi Sad, Serbia*
[2]*University of Novi Sad, Faculty of Technology, Novi Sad, Serbia*

Abstract

The global increase in the number of vehicles has a negative impact on the sustainable development due to the increased energy consumption, noise, and air pollution, as well as the increased water consumption used for car wash. The car wash is one of the main after-sale services in the automobile sector. If car wash wastewater (CWW) could be reused, fresh water customarily used in car washing could be preserved. To achieve this goal, it is necessary to implement "on-site" wastewater treatment systems (*i.e.* at car wash stations). In this research, a novel pilot plant is developed for „on site" treatment of CWW. This pilot plant presents combined methods. It consists of three innovative modules: a multipurpose reactor (for coagulation/flotation, aeration/oxidation), deep bed filter (for filtration), and a two-stage bed coalescer (for coalescence filtration). In all these units packing materials are very light (expanded polystyrene (EPS) and polyurethane (PU)) and therefore energy consumption is significantly low. The pilot plant has a simple and light construction, so that it can be easily moved. It has shown very high COD reduction efficiency as well as removal efficiencies of suspended solids, and oil/grease, thus exhibiting high potentials for water recovery at car wash stations.

Keywords: Car wash station, on-site wastewater treatment, new modular technology, reclaimed water, environmental protection.

Available on-line at the Journal web address: http://www.ache.org.rs/HI/

ORIGINAL SCIENTIFIC PAPER

UDC: 628.19:622.675.6: 681.7.052

Hem. Ind. **78(3)** 291-302 (2024)

1. INTRODUCTION

In the year 2020, around 1.5 billion cars were estimated in the world [1]. The permanent increase in the number of vehicles globally threatens sustainable development because of the increase in energy consumption, increased noise, increased air pollution, as well as the increase of water consumption used for car wash.

The crucial after-sales service in the automobile sector is the car wash [2]. Many different technologies are applied for vehicle washing in the car wash industry. The water consumption per vehicle depends on the type and size of the vehicle (*i.e.* bike, car, bus, or truck), on the applied washing technology as well as on the type of chemicals used [3-7] and it can vary from 60 up to 1300 l per car [3-9].

Car wash technologies could be divided into two main groups: non-automatic car wash like hand wash and self-service wash, and automatic car wash like tunnel wash (conveyor wash), roll-over wash and touch-free wash [3,7]. In tunnel wash, the car is pulled through the washing installation (consisting of brushes, nozzles, *etc.*) while in the roll-over wash the washing installations move over the car. In touch-free technology, the car is parked in a bay and washed by special nozzles delivering high-quality soft water at an optimal temperature and at high water pressures of 480 to 690 kPa [3,7].

Car wash industry consumes huge amounts of water, consequently leading to generation of huge amounts of waste-water. As water consumption depends on the type of car wash installation and the car size, consequently it was reported that from a car wash an average of 150 to 600 l wastewater is produced [10]. Composition of car wash wastewater (CWW) varies dramatically depending on the vehicle soiling level, size and type, as well as on the washing technology that is applied. Impurities in the car wash wastewater (CWW) mainly originate from traffic, car operation and service, as well as from washing chemicals [7]. Generally, it is thought that car washing wastewater is not highly contaminated compared

Corresponding authors: Dunja Sokolović, University of Novi Sad, Faculty of Technical Sciences, Trg Dositeja Obradovića 6, 21000 Novi Sad, Serbia
Paper received: 9 July 2023; Paper accepted: 21 September 2024; Paper published: 4 October 2024.
E-mail: dunjaso@uns.ac.rs
https://doi.org/10.2298/HEMIND230709020S

with other industrial wastewater [10]. Yet, this is a large misconception because CWW contains high concentrations of surfactants (different detergents), oils, waxes, greases, suspended solids (like sand and dust), *etc.* [7,8,11].

If CWW is discharged into a recipient without any treatment, it could cause eutrophication in water ecosystems and toxicity to aquatic environment [11,12]. CWW is often discharged into sewage systems without any treatment [13]. Yet, emulsified oil and suspended solids could be dangerous for sewer systems due to possible clogging [7,13]. Therefore, it is very important to treat CWW at the place where it is generated *i.e.* at the car wash station. However, only a small number of these stations have a wastewater treatment system on-site [10,11,14].

From an environmental protection viewpoint and effective utilization of water resources, it is very beneficial to implement more on-site wastewater treatment systems providing possibilities for water recovery (reuse). If CWW after treatment could be reused, utilization of fresh water could be drastically decreased [8,11,14-17]. CWW reclamation requires the separation of suspended solids and oils/greases before it can be reused [5,15]. The required quality of reclaimed water depends on the wash stage at which it will be used (i.e. pre-soak, wash, rocker panel/undercarriage, first rinse and final rinse) [8,11,14]. So, lower water quality is needed for pre-soak, wash, rocker, panel/undercarriage steps, while for the first and final rinses water quality should be very high. At most car wash stations that have systems for CWW recovery, reclaimed water is not used for the final rinse, as it would require very expensive CWW treatment technology that is usually not cost-effective [8,11,14].

There are many methods used for CWW treatment, but not all of them are suitable for “on-site” installation at car wash stations, because of different cost-effectiveness.

The methods used for CWW treatment are coagulation, adsorption, membrane filtration electro-chemical processes, biological treatment, combined methods or hybrid methods [7,18,19]. Coagulation is the most utilized method for treatment of CWW, as it is applied in more than 70 % of water treatment plants. Coagulation is highly effective in removing total suspended solids (TSS) and turbidity from CWW, but it is not so effective in the reduction of chemical oxygen demand (COD), *i.e.* organic compounds [7,18-20]. Adsorption is also a very often applied method in wastewater treatment but not for CWW treatment, because of the complex CWW composition [7,19- 21]. Membrane filtrations that could be applied for CWW such as microfiltration (MF), ultrafiltration (UF), nanofiltration (NF) and reverse osmosis (RS) are highly effective methods for removing solids and organic matter [7,10,12,22-24]. However, a huge disadvantage in the application of these methods for CWW treatment is frequent membrane fouling, high price, and very high-energy consumption [7,8,11,14,19,21-24].

Still, use of only one individual method may not effectively remove all pollutants from CWW. This approach is especially not feasible in full-scale systems and combined/hybrid methods are more effective and even more economically viable [7,21,25].

As previously said, the number of cars is drastically increasing every year, leading to an increase in number of car wash stations located in high population of the residential and urban areas [10]. Only in the EU, around 250 million cars are registered in the year 2020 [1,26]. The car wash stations consume a high amount of fresh water, generating at the same time huge quantities of wastewater. Therefore, it is important to reduce the amount of fresh water used for car washing. The need for implementation of wastewater systems at car wash station (“on site”) is rising every day. In several European countries, like Scandinavian countries, Germany, Austria, Netherlands and Belgium water recycling in car wash stations is already legislated [22,24,26,27]. For example, in Belgium minimum of 70 % of CWW has to be recycled, while in Germany and Austria, this percent is even higher, and it is 80 %. On the other hand, in Scandinavian countries and the Netherlands, the maximal allowed consumption of fresh water per car is 60 to 70 litter [22,26,27].

The aim of this research was to develop a low-cost, compact, highly efficient, eco-friendly, and mobile plant for CWW treatment that could be installed “on site” for water recovery. This pilot plant for CWW treatment was developed and investigated “on site” at a car wash station of one car workshop in Serbia.

2. MATERIALS AND METHODS

2. 1. Raw wastewater

Raw car wash wastewater was obtained from a car wash station of a car workshop in Serbia. Each vehicle that has to be serviced at the car workshop is washed before it enters the car workshop. This car wash station includes the following activities that affect wastewater quality: anticorrosion protection, engine wash, and complete car wash. These activities produce highly polluted wastewater that contains high organic loads, oils and suspended solids. Characteristics of the raw car wash wastewater monitored during an 8-month period are presented in Table1.

Table 1. *Characteristics of raw car wash wastewater (CWW) used, 60 samples*

	COD, mg dm^{-3}	Content of total solids, mg dm^{-3}	Loss of ignition, mg dm^{-3}	Content of suspended solids, mg dm^{-3}	Content of oil, mg dm^{-3}	pH
Mean	703	1321	786	384	54	7.78
Minimum	222	900	296	104	10	7.60
Maximum	3333	2671	1800	1520	518	7.90

The car wash technology applied in this car wash station was tunnel wash, where the car is pulled through the washing installation containing brushes, nozzles, *etc.*

2. 2. Pilot plant

This pilot plant consists of three innovative modules in which combined methods for CWW treatment are applied. In the first module coagulation/flotation, aeration and mixing are simultaneously performed, followed by the second module applying deep bed filtration and third module performing coalescence. The pilot plant was working discontinuously, and the separation efficiency was evaluated by 8 tests carried out for 8 months. In this way all seasons were covered, which certainly had a significant impact on wastewater quality. Each test lasted until the pressure drop reached a determined value, afterwards the deep bed filter needed to be washed. Thus, the test duration was from 17 to 60 h depending on the influent CWW quality. The novel modular pilot plant has a capacity of 1.0 m^3 h^{-1}.

The pilot plant treated 331 m^3 of car wash wastewater during 331 h, in total.

There were four sampling points at the pilot plant: at the plant inlet and outlet, as well as in-between all three units. In this way, it was possible to monitor not just separation efficiency of the pilot plant, but also the separation efficiency of all three modules. The samples of 1 dm^3 were taken, every working hour of the Pilot plant and from these current samples, a daily composite sample was formed, which was further analyzed.

Efficiency of wastewater purification (E) was calculated based on pollutant concentration in the influent, C_i, and the effluent water C_e, using equation:

$$E = \frac{C_i - C_e}{C_i} \quad (1)$$

2. 3. Selection of coagulants and flocculants

Coagulants and flocculants and their optimum dosages were determined by jar tests. These tests were performed for all wastewater samples that were treated by the pilot plant to determine the optimal clarification conditions. Aluminum sulphate and ferric chloride were tested as coagulants, in the concentration range of 60.0 to 400.0 mg dm^{-3}, while polyacrylamide and sodium aluminate were tested as flocculants, in the concentration range of 0.5 to 2.5 mg dm^{-3}.

2. 4. Analytical methods

2. 4. 1. Determination of oil concentration

The oil concentration in influent and effluent was determent by Fourier transform spectrometry, FTIR (spectrophotometer Thermo Nicolet 5700, Netherlands). Wastewater samples were stabilized and adjusted to pH 2 by adding HCl. The oil was extracted from the water samples by CCl_4.

2. 4. 2. Determination of chemical oxygen demand and other characteristics of wastewater

Chemical oxygen demand (COD) was determined by the colorimetric method using the Hach DR/3000 spectrophotometer (Hach Company, USA). $K_2Cr_2O_7$ was used as an oxidizing agent. H_2SO_4, Ag_2SO_4 and $K_2Cr_2O_7$ were added to the water sample. The sample is then heated for 2 h at a temperature of 148 °C. After cooling the sample, the COD value is determined. Total solids, loss of ignition, and suspended matter were determined gravimetrically.

2. 5. Properties of packing materials

The packing materials used in this Pilot plant were three different types of expanded polystyrene (EPS) particles as well as PU fibers. The EPS particles were kindly supplied by INA-OKI Zagreb (Croatia), while PU fibers were obtained as a waste material from the furniture, generated as the excess parts from tailoring chairs and beds from a local store. The EPS particle size and density depend on the initial particle size as well as on the duration of the thermal expanding process [28]. Density of the materials was measured by the weighing method. The bed porosity was calculated based on the material density and bed bulk density. The bed permeability was calculated by performing the Darcy's experiment as explained in detail in our previous research [29].

Properties of the bed materials and the resulting packed beds in different pilot plant modules are summarized in Table 2.

Table 2. The properties of bed materials and unit packed beds

Property	Unit / Module			
	Multireactor	Deep bed filter		Bed coalescer
	Bed materials			
		EPS		PU
Mean diameter, mm	6.5	1.8	2.2	-
Effective diameter, mm	6.5	1.6	2.0	-
Uniformity	1.0	1.6	1.4	-
Bulk density, kg m^{-3}	30	94	16	50
Density, kg m^{-3}	52.8	173	25	1200
Bed porosity, %	43.0	50.0	36.0	95.8
Permeability, 10^{-9} m^2	-	5.86	6.79	5.40

3. RESULTS AND DISCUSSION

The novel pilot plant, shown in Figure 1., presents combined methods for „on-site" treatment of car wash wastewater (CWW). This pilot plant consists of three innovative modules:

1. the multipurpose reactor (MR),
2. deep bed filter (DBF), and
3. two-stage bed coalescer (TBC),

and one tank (TA).

The multipurpose reactor and deep bed filter are open vessel, but the coalescer is under pressure. Therefore, it was necessary to place a tank between the deep bed filter and the coalescer. The capacity of this novel modular pilot plant is 1.0 m^3 h^{-1}.

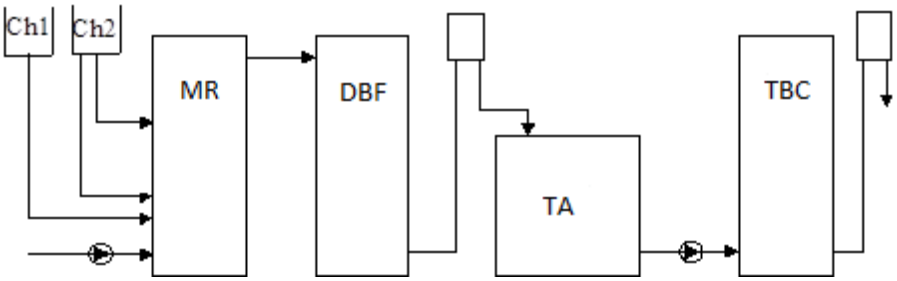

Figure 1. Pilot plant: multireactor (MR), two dosage vessels (Ch1 and Ch2), deep bed filter (DBF), tank (TA), and a two-stage bed coalescer (TBC)

The multipurpose reactor is first unit in the pilot plant. This reactor is a bubble column, 3 m in height, consisting of three pipes 1 m in length, each. Two beds (0.30 m in length, each) formed of expanded polystyrene (EPS) granules, are placed at the connecting spots of the pipes (Fig. 2). Diameter of EPS granules is 6.5 mm in this module and the bulk density of the beds is 30 kg m^{-3} with porosity of 43 % (Table 2). The interspace between the beds is 0.7 m. The application of large EPS granules in these beds is minimizing the possibility of clogging/blocking the EPS bed with suspended solids and newly formed flocs.

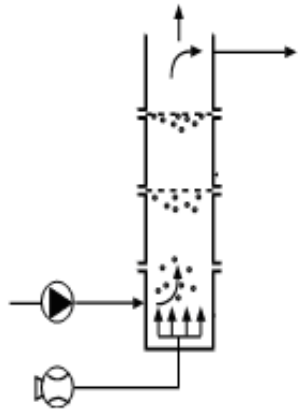

Figure 2. Multipurpose reactor with two EPS beds

Since EPS is lighter than water, the beds are fixed from the top with the aid of two perforated plates acting also as water distributors. The co-current gas-liquid flow is applied. Air diffusers at the bottom, distribute the compressed air in small bubbles thus providing very good mixing. Addition of coagulants and flocculants is possible simultaneously at the same spot of the column, or with a small time difference at different spots of the column.

This special construction of the bubble column allows the simultaneous occurrence of several processes, like aeration/oxidation, mixing, coagulation and flotation. Therefore, this unit is named multireactor.

Obtained results for chemical oxygen demand (COD) measurements for CWW before and after the multireactor (MR) for tests 1 lasting 54.5 h and test 3 lasting 29.5 h are presented in Figure 3. The maximal COD values at the MR inlet and outlet in test 1 were 2763 and 322 mg dm^{-3}, respectively, while the average COD reduction efficiency achieved was 68.4 %. Similarly, in test 3., the maximal COD values at the MR inlet and outlet were 2189 and 138 mg dm^{-3}, respectively, while the average COD reduction efficiency was 65.3 %.

The MR was working at the car wash station for 331 h in total without any operative problems. Due to the very light bed material in this MR formed of EPS granules, this device is very light and therefore mobile. The MR construction is simple providing very intensive mixing and effective aeration/oxidation. For that reason, it is a very good choice for treatment of water with high concentrations of organic compounds, such as CWW.

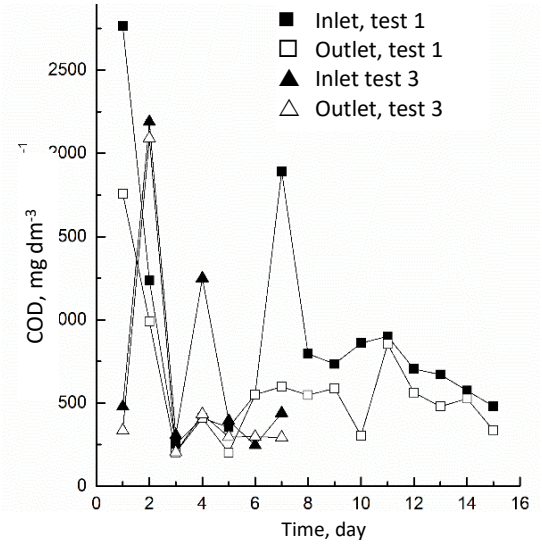

Figure 3. COD at the inlet and outlet of the multireactor in tests 1 and 3

The second unit in the pilot plant is a deep bed filter. In this deep bed filter the filter bed is formed from EPS granules, not from sand which is traditionally used bed material in deep bed filters. Although mostly used, sand as filter media in deep bed filtration has some significant disadvantages. First of all, sand is a high-density material, requiring heavy equipment with a concrete foundation [28]. It is very important to point out that EPS is ten-fold lighter than sand. Therefore, the EPS deep bed filter is very light and consequently it could be mobile. Secondly, the filter cycle for a sand filter bed, especially when wastewater is highly polluted, is very short because of stratification phenomena [28]. The relative density of the bed material (heavier or lighter than water) influences the direction of bed washing (upstream or downstream). For heavy filter media, such as sand, the filter bed has to be washed upstream (backwashed), causing the stratification phenomena. On the other hand, as EPS granules are lighter than water, they float in water, so that the bed formed from EPS granules is washed downstream without the possibility of stratification to occur. In specific, each particle fraction remains at its own position in the bed, irrespective of the washing cycle [28]. Sand filter bed washing requires also high pressures and large quantities of water. As an example, the compressor must be applied for fluidization of sand bed. For fluidization of sand grain of 2 mm, minimum velocity is about 112 m h^{-1} [28]. The total time for washing of sand filter beds is approximately 40 min [28]. On the other hand, for fluidization and washing of an EPS bed, 110 cm in length, only a water head of 1 m and water velocity of 80 m h^{-1} during 5 min is needed [28]. It is clearly seen that the energy demand is much higher for sand filter beds as compared to those of EPS granules. Finally, for the same wastewater quality, the filtration cycle for the EPS filter bed is much longer (between 30 and 50 h), compared to the sand filter bed (between 9 and 30 h). Based on all these facts, it could be concluded that the use of EPS granules as a filter medium drastically decreases both capital and operating costs [28].

When the pressure drop in the EPS filter bed increases dramatically, the filtration cycle is over, and the bed has to be washed. Bed washing is possible in the column by downstream fluidization of the bed. This is performed by opening a valve and applying the adequate water flow. Besides the occasional filter bed washing, there is no need for filter bed recovery, because of the unlimited lifetime of the EPS material.

The deep-bed filter, used in these experiments, is 2.5 m heigh, with the bed length of 110 cm (Fig. 4). EPS granules in the filter bed, had a diameter of approximately 1.8 mm and bulk density of 94 kg m^{-3}. The formed filter bed had the porosity of 50 % and 5.86 10^{-9} m^2 permeability (Table 2). Design of this deep-bed filter is described in detail in our previous research where it was tested and optimized for filtration of a model suspension of iron hydroxide [28].

The deep bed filter, described previously [28], was for the first time tested in the present study with real wastewater samples, and in combined methods in the „on site“ pilot plant at a car wash station.

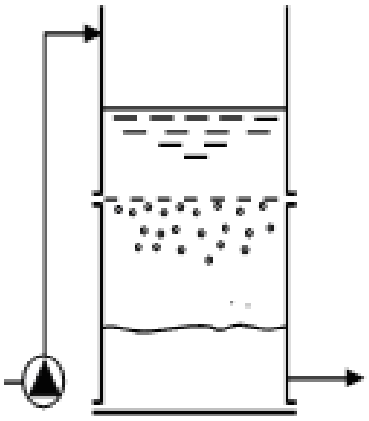

Figure 4. Deep bed EPS filter

Duration of the filter cycle depended on the concentration of suspended solids (SS) in the wastewater. When the SS concentration is high, the tests were shorter, than those for water with lower SS concentrations. As an example, test 8 lasted 40 h, while test 4 lasted 29.5 h. The obtained results of CWW filtration by this deep bed filter are shown in Fig. 5. The maximal SS concentrations at the filter inlet and outlet in test 8 were 544 and 10 mg dm^{-3}, respectively, while the average removal efficiency was 95.4 %. The respective values for test 4 were 766 and 25 mg dm^{-3}, with the SS removal efficiency of 91.7 %.

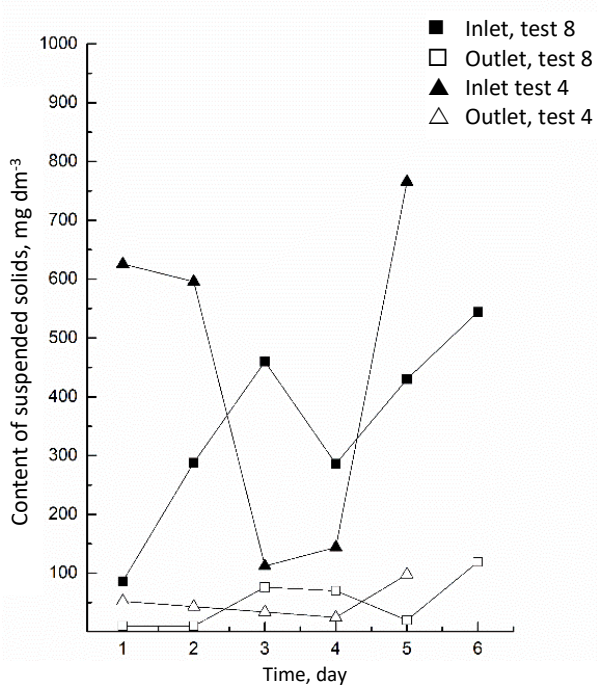

Figure 5. Suspended solids at the inlet and outlet of the deep bed filter in tests 4 and 8

The experimental two-stage bed coalescer consisted of a vertical pipe-in-pipe system presented in Figure 6 [30]. The inner pipe is filled with polyurethane PU fibers, while the outer pipe is filled with granular EPS. Wastewater first goes vertically up from the bottom of the coalescer through the outer pipe *i.e.* the EPS bed. When it reaches the top of the unit it changes direction and it starts to flow vertical down through the inner pipe filled with the PU material, and then it exits the unit.

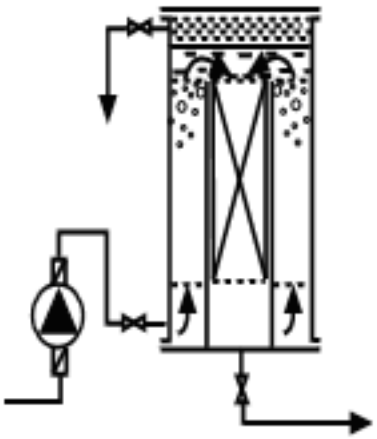

Figure 6. Two-stage bed coalescer [30]

The two-stage bed coalescer used in the present study represents an example of two-stage filtration where both filter beds are in the same coalescer body. The role of each filter bed is specific. The applied fluid velocity allows formation of an oily film at the entrance of both filter beds. In this way, coalescence is drastically increased, because the droplets are easily attached in oily films. Coalescence of large and medium droplets occurs in the EPS filter bed, while coalescence of very small droplets occurs in the PU filter bed. Coalesced droplets detach from oily films of the beds and settle at the top of the unit, from where they are discontinuously discharged by a valve. Therefore, the filter bed cannot be exhausted. The PU filter bed has also an unlimited lifetime as the EPS filter bed.

This two-stage bed coalescer is tested on real and model formation water as well as on hardening wastewater in our previous research where it has shown high separation efficiency of heavily polluted oily water [30]. However, this unit has never been tested „on-site“ for car wash wastewater treatment, and it was never applied in combined methods in the Pilot plant.

Oil concentrations at the filter inlet and outlet in tests 5 and 8. are presented in Figure 7.

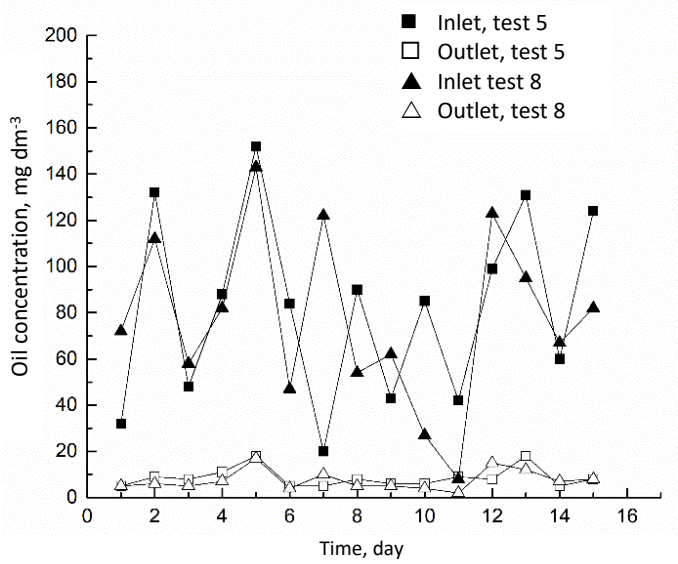

Figure 7. Oil concentrations before and after the two-stage bed coalescer in tests 5 and 8

Test 5 lasted 47.8 h, while test 8 lasted 40.0 h. The maximal inlet and outlet oil concentrations of TBC in test 5 were 152 and 18 mg dm^{-3}, while the oil separation efficiency achieved was 93 %. The respective values in test 8 were 143 and 17 mg dm^{-3} with the oil separation efficiency of 95 %.

The presented results show that all the modules exhibited high separation efficiencies and when combined in the pilot plant the treated water quality could reach very high levels. Mean, maximal and minimal values of COD at the pilot plant inlet and outlet, test duration and month in which the test was realized are shown for all 8 tests in Table 3.

Table 3. Experimental results of COD reduction in treated CWW in the pilot plant in 8 tests

Test number	COD at inlet, mg dm^{-3}			COD at outlet, mg dm^{-3}			Duration, h	Month
	Mean	Maximum	Minimum	Mean	Maximum	Minimum		
1	836	2763	192	117	322	51	54.5	Jun./Aug.
2	894	1952	299	122	150	48	17.0	Dec./Jan.
3	757	2189	247	90	138	39	30.3	Jan.
4	580	1600	187	136	463	19	29.5	Feb.
5	386	594	194	64	140	39	47.8	Feb/Mar.
6	190	255	75	41	165	10	61.5	Mar./Apr.
7	134	337	38	29	48	14	50.5	May
8	137	222	73	36	67	5	40.0	May

Maximal COD value at inlet of the Pilot plant is in the range from 2763 to 222 mg dm^{-3} while the maximal COD value range at outlet of the Pilot plant is from 463 to 48 mg dm^{-3}. The respective ranges of minimal COD values at the inlet of the Pilot plant are from 299 to 38 mg dm^{-3}, while at the outlet it is from 51 to 5 mg dm^{-3}.

The mean COD reduction efficiency for the whole pilot plant, for all tests, was in the range of 74 % up to 88 % (Fig. 8). It could be concluded that this pilot plant has shown very high efficiency for COD removal from the car wash wastewater.

The oil separation achieved in the whole pilot plant for tests 1, 3, and 6. is shown in Figure 9. The duration of the tests was 54.5 h, 30.3 h, and 61.5 h, respectively. The maximal oil concentrations at the plant inlet and outlet for test 1. was 481 and 21 mg dm^{-3}, for test 3. it was 231 and 17 mg dm^{-3}, while for test 6. it was 428 and 18 mg dm^{-3}. The separation efficiency of the oil removal by this pilot plant for these three tests was 96%, 95%, 95%, respectively.

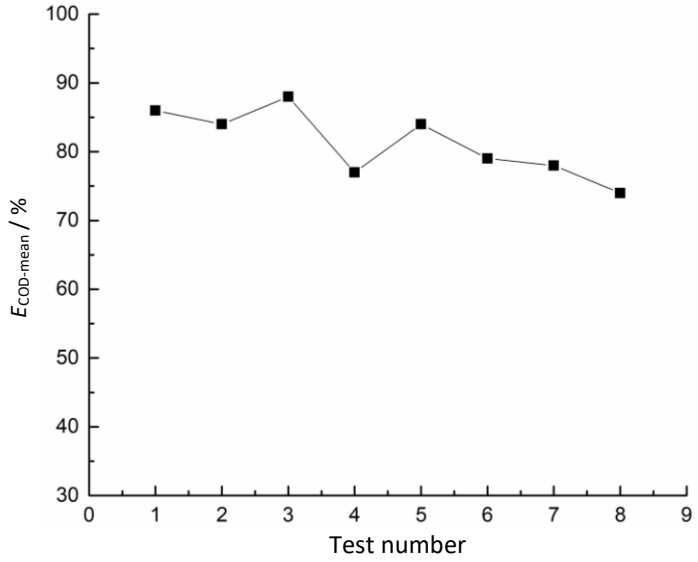

Figure 8. The mean COD reduction efficiency ($E_{COD\text{-}mean}$) for the whole pilot plant in 8 experimental tests

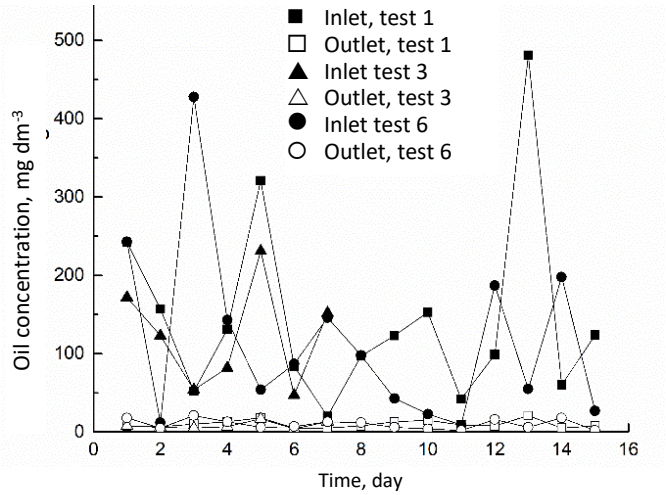

Figure. 9. Oil concentrations at the pilot plant inlet and outlet in tests 1, 3 and 6

The total amount of car wash wastewater was treated without losses by the pilot plant so that the ratio of raw wastewater and treated wastewater was 1:1. However, the amount of treated water that could be reused for car washing is 90 %, because 10 % of the treated water is used for the washing cycle of the filter bed in the second module.

The developed pilot plant is a low-cost plant, due to very low capital and operational costs. The capital costs are much lower compared to those of conventional devices. The novel modules are much lighter because the beds are made of very light materials i.e. of EPS and PU. For this reason, these devices do not need a heavy concrete foundation, and their walls are not as thick as the walls of conventional devices. Also, the bed materials are very cheap (EPS) or free-of-charge (PU), especially when the material is waste material, as PU is in the present case. The operating costs of this pilot plant consist only of the price of electricity needed for one pump and an air compressor and the prices of chemicals applied in the first device (MPR). The bed materials used in this pilot plant have unlimited lifetime, therefore there are not any operational costs for regeneration.

4. CONCLUSION

The novel pilot plant for „on site“ treatment of car wash wastewater at car wash stations presents combined methods in which three innovative modules are combined. In the first module, named multipurpose reactor, coagulation, flotation, aeration and oxidation are performed followed by the second module performing filtration through a deep bed filter of

expanded polystyrene. Finally, in the third, last module, coalescence of dispersed oil is performed in a specially constructed coalescer. The modules have shown very high separation efficiencies, and when they are connected in combined methods like this novel pilot plant, they produce high quality of reclaimed car wash wastewater.

In all these three modules, packaging materials are very light*, i.e.* the expanded polystyrene is lighter than water, while the density of polyurethane, used only in the coalescer, is close to that of water. For this reason, the pilot plant has simple and light construction, and therefore it could be easily moved, *i.e.* it represents a mobile plant. Also, due to the use of light packing materials, especially EPS, energy consumption is significantly lower as compared to that in conventional units. Therefore, both capital and operating costs are much lower, compared to conventional devices for the treatment of car wash wastewater.

The presented pilot plant is an eco-friendly device because it could be easily installed „on site“ at car wash stations, it is low-cost, compact, highly efficient, and mobile, with low energy consumption with the potential to be fully automated if needed.

Acknowledgements*: This research has been supported by the Ministry of Science, Technological Development and Innovation (Contract No. 451-03-65/2024-03/200156) and the Faculty of Technical Sciences, University of Novi Sad through project "Scientific and Artistic Research Work of Researchers in Teaching and Associate Positions at the Faculty of Technical Sciences, University of Novi Sad" (No. 01-3394/1)*

This work is dedicated to Professor Dr Željko Grbavčić. The authors are very grateful for his unlimited support, unselfish sharing of knowledge and fruitful collaboration.

REFERENCES

[1] Kuan WH, Hu CY, Ke LW, Wu JM. A Review of On-Site Carwash Wastewater Treatment. *Sustainability* 2022; 14(10): 5764. https://doi.org/10.3390/su14105764

[2] Monney I, Buamah R, Donkor EA, Etuaful R, Nota HK, Ijzer H. Treating waste with waste: The potential of synthesized alum from bauxite waste for treating car wash wastewater for reuse. *Environ Sci Pollut Res.* 2019; 26(13): 12755-1264. https://doi.org/10.1007/s11356-019-04730-0

[3] Ghaly AE, Samir Mahmoud N, Ibrahim MM, Mostafa EA, Abdelrahman et al. Water Use, Wastewater Characteristics, Best Management Practices and Reclaimed Water Criteria in the Carwash Industry. *Int J Biopro Biotechnol Adv.* 2021; 7(1): 240-261. https://www.researchgate.net/publication/351269422_Water_Use_Wastewater_Characteristics_Best_Management_Practices_and_Reclaimed_Water_Criteria_in_the_Carwash_Industry_A_Review

[4] Shifflett A. Five factors of carwash cleaning. Operation and Management, *Carwash News*, https://www.carwash.com/5-factors-carwash-cleaning/ Accessed on Decembar 5, 2023

[5] Monney I, Donkor EA, Buamah A Clean vehicle, polluted waters: Empirical estimates of water consumption and pollution loads of the carwash industry. *Heliyon.* 2020; 6(5): e03952. https://doi.org/10.1016/j.heliyon.2020.e03952

[6] Torkashvand, J.; Farzadkia, M.; Younesi, S.; Gholami, M. A systematic review on membrane technology for carwash wastewater treatment: Efficiency and limitations. *Desalin Water Treat.* 2021; 217: 31-41. https://doi.org/10.5004/dwt.2021.26534

[7] Sarmadi M, Foroughi M, Saleh HN, Sanaei D, Amin, Zarei A, Ghahrchi M, Bazrafshan E. Efficient technologies for carwash wastewater treatment: a systematic review, *Environ Sci Poll Res.* 2020; 27: 34823-34839. https://doi.org/10.1007/s11356-020-09741-w

[8] Zaneti R, Etchepare R, Rubio J. Car wash wastewater reclamation. Full-scale application and upcoming features. *Resour Conserv Recycl.* 2011; 55(11): 953-939. https://doi.org/10.1016/j.resconrec.2011.05.002

[9] Al-Odwani A, Ahmed M, Bou-Hamad S. Carwash water reclamation in Kuwait. *Desalination.* 2007; 206(1-3): 17-28. https://doi.org/10.1016/j.desal.2006.03.560

[10] Lau WJ, Ismail AF, Firdaus S. Car wash industry in Malaysia: Treatment of car wash effluent using ultrafiltration and nanofiltration membranes. *Sep Purif Technol.* 2013; 104:26-31. https://doi.org/10.1016/j.seppur.2012.11.012

[11] Zaneti R, Etchepare R, Rubio J. More environmentally friendly vehicle washes: Water reclamation. *J Clean Prod.* 2012; 37: 115-124. https://doi.org/10.1016/j.jclepro.2012.06.017

[12] Espinoza-Montero PJ, Martínez-Huitle CA, Loor-Urgilés LD. Technologies employed for carwash wastewater recovery. *J Clean Prod.* 2023; 401 :136722. https://doi.org/10.1016/j.jclepro.2023.136722

[13] Bhatti ZA, Mahmood Q, Raja IA, Malik AH, Khan MS, Wu D. Chemical oxidation of carwash industry wastewater as an effort to decrease water pollution. *Phys Chem Earth.* 2011; 36(9-11):465-469. https://doi.org/10.1016/j.pce.2010.03.022

[14] Zaneti RN, Etchepare R, Rubio J. Car wash wastewater treatment and water reuse - A case study. *Water Sci Technol.* 2013; 67(1): 82-88. https://doi.org/10.2166/wst.2012.492

[15] Pintilie L, Torres CM, Teodosiu C, Castells F. Urban wastewater reclamation for industrial reuse: An LCA case study. *J Clean Prod.* 2016; 139: 1-14. https://doi.org/10.1016/j.jclepro.2016.07.209

[16] Torkashvand J, Pasalari H, Gholami M, Younesi S, Oskoei V, Farzadkia M. On-site carwash wastewater treatment and reuse: a systematic review. *Int J Environ Anal Chem.* 2022; 102(15): 3613-3627. https://doi.org/10.1080/03067319.2020.1772773

[17] Rodriguez Boluarte IA, Andersen M, Pramanik BK, Chang CY, Bagshaw S, Farago L, Jegatheesan V, Shu L. Reuse of car wash wastewater by chemical coagulation and membrane bioreactor treatment processes. *Int Biodeterior Biodegrad.* 2016; 113: 44-48. https://doi.org/10.1016/j.ibiod.2016.01.017

[18] Brown, C. Water Conservation in the Professional Car Wash Industry. *Report for International Car Wash Association*, Washington DC, USA, .2000. https://www.carwash.org/%20operatorinformation/research/Pages/EnvironmentalReports.aspx Accessed on July 2023

[19] Sarmadi M, Zarei AA, Ghahrchi M, Sepehrnia B, Meshkinian A, Moein H, Nakhaei S, Bazrafshan E. Carwash wastewater characteristics-a systematic review study. *Desalination Water Treat.* 2021; 225: 112-148. https://doi.org/10.5004/dwt.2021.26972

[20] Hu, C.-Y.; Kuan, W.-H.; Ke, L.-W.; Wu, J.-M. A Study of Car Wash Wastewater Treatment by Cyclo-Flow Filtration. *Water.* 2022; 14, 1476. https://doi.org/10.3390/w14091476

[21] Bazrafshan E, Kord Mostafapoor F, Soori MM, Hossein Mahvi A. Application of Combined Chemical Coagulation and Electro-Coagulation Process for Carwash Wastewater Treatment, *Fresenius Environ Bull.* 2012; 21(9a) 2694-2701 https://www.researchgate.net/publication/234719709_Application_of_combined_chemical_coagulation_and_electrocoagulation_process_to_carwash_wastewater_treatment

[22] Boussu K., Kindts C., Vandecasteele C., Van der Bruggen B., Applicability of nanofiltration in the carwash industry, *Sep Purif Technol.* 2007; 54(2): 139-146 https://doi.org/10.1016/j.seppur.2006.08.024

[23] N. Abdullah, N. Yusof, W.J. Lau, J. Jaafar, A.F. Ismail, Recent trends of heavy metal removal from water/wastewater by membrane technologies, *J Ind Eng Chem.* 2019; 76: 17-38 https://doi.org/10.1016/j.seppur.2023.125707

[24] Gryta M, Wozniak P, Application of polypropylene microfiltration membranes for separation of wastewater from car wash *Sep Purif Technolo.* 2024; 331: 125707. https://doi.org/10.1016/j.seppur.2023.125707

[25] Veit, MT, Novais ÍGV, Juchen PT, Trevisani Juchen P, Moreno Palácio S, da Cunha Gonçalves G, Zanette JC. Automotive Wash Effluent Treatment Using Combined Process of Coagulation/Flocculation/Sedimentation–Adsorption. *Water Air Soil Pollut.* 2020; 231: 494. https://doi.org/10.1007/s11270-020-04862-x

[26] Europe: Increase of water regulations car wash industry, https://www.waternewseurope.com/europe-increase-of-water-regulations-car-wash-industry/ Accessed on June 7, 2023

[27] 2017 European car wash consumer study, International Carwash Association. https://www.prowash.fi/wp-content/uploads/2017/11/ICA-European-Consumer-Study-2017.pdf Accessed on June 7, 2023

[28] [Šećerov Sokolović R, Sokolović S, Govedarica D. Performance of expanded polystyrene particles in deep bed filtration. *Sep Purif Technol.* 2009; 68(2): 267-272. https://doi.org/10.1016/j.seppur.2009.05.019

[29] Kostić MH, Sokolović D, Sokolović S, Laminger T, Kiralj A. The effect of fibre morphology on packing phenomena and bed properties in coalescers. *Hem Ind.* 2022; 76(4): 197-208. https://doi.org/10.2298/HEMIND211224016K

[30] Šećerov Sokolović R, Sokolović S, Šević S. Oily water treatment using a new steady-state fiber-bed coalescer. *J Hazard Mater.* 2009; 162(1): 410-415. https://doi.org/10.1016/j.jhazmat.2008.05.054

Razvoj ekološki prihvatljivog mobilnog postrojenja za regeneraciju otpadnih voda iz autoperionica

Dunja S. Sokolović[1] i Radmila M. Šećerov Sokolović[2]

[1]*Univerzitet u Novom Sadu, Fakultet tehničkih nauka, Novi Sad, Srbija*
[2]*Univerzitet u Novom Sadu, Tehnološki fakultet, Novi Sad, Srbija*

(Naučni rad)

Izvod

Stalni porast broja vozila na globalnom nivou negativno utiče na održivi razvoj zbog povećane potrošnje energije, buke i zagađenja vazduha, kao i povećane potrošnje vode koja se koristi za pranje vozila. Dominantni postprodajni servis u automobilskom sektoru je pranje automobila. Ako bi se otpadna voda iz autoperionica mogla ponovo koristiti u procesu pranja vozila, umesto sveže vode, mogla bi se značajno smanjiti potrošnja sveže vode. Kako bi se postigao ovaj cilj, neophodno je implementirati sisteme za prečišćavanje otpadnih voda „na mestu nastanka" tj. u autoperionicama. U ovom istraživanju razvijeno je novo Pilot postrojenje za tretman, „na mestu nastanka", otpadnih voda generisanih pranjem vozila u autoperionicama. Ovo pilot postrojenje predstavlja kombinaciju više metoda. Sastoji se od tri inovativna modula: višenamenskog reaktora (za koagulaciju/flotaciju, aeraciju/oksidaciju), filtera sa nasutim slojem (za filtraciju) i koalescera (za koalescentnu filtraciju). U svim ovim modulima materijali od kojih su formirani nasuti slojevi su izrazito laki (ekspandirani polistiren (EPS) i poliuretan (PU)), stoga je za njihovo pranje potrebna energija značajno niža nego kada je upitanju pesak koji se najčešće koristi kao filterski sloj. Pilot postrojenje ima jednostavnu konstrukciju i malu težinu, tako da se lako može premeštati po potrebi. Ovo novo razvijeno postrojenje pokazalo je veoma visoku efikasnost smanjenja HPK-a, kao i efikasnost uklanjanja suspendovanih materija i ulja, što ukazuje na njegov visok potencijal za rekuperaciji vode u autoperionicama.

Ključne reči: autoperionica, otpadna voda od pranja automobila, nova modularna tehnologija, ponovna upotreba vode, zaštita životne sredine

Proračun i optimizacija skrubera za prečišćavanja otpadnih gasova koji sadrže amonijak

Zorana Lj. Arsenijević[1], Ivona R. Radović[2], Mirjana Lj. Kijevčanin[2] i Tatjana S. Kaluđerović Radoičić[2]

[1]Univerzitet u Beogradu, Institut za hemiju tehnologiju i metalurgiju – institut od nacionalnog značaja, Beograd, Srbija
[2]Univerzitet u Beogradu, Tehnološko-metalurški fakultet, Beograd, Srbija

Izvod

U ovom radu izvršen je proračun i dimenzionisanje dvostepenog skrubera sa pakovanim slojem za prečišćavanje otpadnog gasa iz hemijske industrije koji sadrži amonijak u koncentraciji od 1400 mg m^{-3}. Za proračun su korišćene osnovne jednačine materijalnog bilansa, ravnotežni podaci, kao i generalizovana korelacija za pad pritiska. Prilikom proračuna i analize različitih konfiguracija korišćen je Katmar softver koji koristi generalizovanu korelaciju za pad pritiska za određivanje prečnika skrubera na osnovu dozvoljenog pada pritiska i udaljenosti od uslova plavljenja. Utvrđeno je da se optimalni rezultati postižu u dvostepenom uređaju, korišćenjem sumporne kiseline (70 %) za hemisorpciju amonijaka. Kao punjenje u koloni odabrani su Palovi prstenovi dimenzije 50 mm izrađeni od polipropilena. U radu su analizirane kolone prečnika D_c = 2; 2,1 i 2,2 m. Sa aspekta protoka tečne faze prečnik kolone D_c = 2 m zadovoljava, a prema specifikaciji punjenja pad pritiska kroz ukupnu visinu sloja punjenja je oko 900 Pa. Utvrđeno je da se gradijent pritiska, a samim tim i ukupni pad pritiska u koloni smanjuje povećanjem prečnika kolone. Međutim, sa povećanjem prečnika kolone raste minimalni protok tečne faze potreban za kvašenje punjenja, te se potreban protok tečne faze povećava. Uzimajući u obzir sve procesne parametre, kao i zahtevanu efikasnost prečišćavanja otpadnog gasa, predložena je optimalna konfiguracija uređaja.

Ključne reči: Apsorpcija; dvostepeni skruber; pakovani sloj; uklanjanje amonijaka.

Available on-line at the Journal web address: http://www.ache.org.rs/HI/

STRUČNI RAD

UDC: 66.074.48:7.023.43:005.591.1

Hem. Ind. **78(2)** 303-314 (2024)

1. INTRODUCTION

Apsorpcija u tečnosti je jedna od široko korišćenih metoda za tretman otpadnih gasova u cilju smanjenja emisije zagađujućih materija. Apsorpcija može biti čisto fizički fenomen, pri kome se komponenta gasne smeše koja se uklanja samo rastvara u tečnosti. Sa druge strane, hemisorpcija je proces u kome je apsorpcija praćena hemijskom reakcijom u tečnoj fazi između rastvorenog gasa i reaktanta iz tečnosti. Apsorpcija u tečnosti se može izvršiti u različitim kontaktnim uređajima u kojima je najznačajnije ostvariti što bolji prenos mase, odnosno veliku kontaktnu površinu između gasovite i tečne faze [1-3].

Jedan od najčešće korišćenih uređaja za prečišćavanje gasova apsorpcijom je skruber [4-7]. Skruberi se ubrajaju u grupu mokrih separatora. U odnosu na suve separatore, skruberi imaju brojne prednosti – manjih su dimenzija, omogućavaju istovremeno prečišćavanje i hlađenje gasova, kao i vraćanje rastvorljivih supstanci u proces nakon izdvajanja. Rad mokrih skrubera je bezbedniji za ljude i okolinu jer ne postoji mogućnost eksplozije ukoliko je izabrana odgovarajuća tečnost, a korozivne i otrovne materije se lako izdvajaju i neutrališu iz gasnog toka. Mokri skruberi nemaju pokretnih delova, relativno su jednostavne konstrukcije i jeftiniji su za održavanje u odnosu na separatore koji koriste suve postupke separacije. Problemi koji se mogu javiti kod skrubera sa mokrim postupkom separacije su pojava korozije i zamrzavanje tečnosti tokom zime. Ukoliko se koristi voda za prečišćavanje, izlazni gas može biti zasićen parom, a voda sa dna skrubera se u nekim slučajevima mora dodatno prečistiti.

Postoji veliki broj različitih konstrukcija skrubera poput kolona sa raspršivanjem, Venturi skrubera, centrifugalnih skrubera, skubera sa punjenjem (pakovani i fluidizovani sloj) ili sa podovima [6,8]. Princip rada je indentičan za sve tipove skrubera. U skruberu dolazi do kontakta tečne i gasovite faze i do prelaska komponenata iz gasovite u tečnu fazu nekim

Corresponding authors:Tatjana S. Kaluđerović Radoičić, Univerzitet u Beogradu, Tehnološko-metalurški fakultet, Karnegijeva 4, Beograd, Srbija
Paper received: 11 September 2023; Paper accepted: 16 September 2024; Paper published: 24 September 2024.
E-mail: tanjak@tmf.bg.ac.rs
https://doi.org/10.2298/HEMIND230911019A

od mehanizama izdvajanja. Efikasnost skrubera zavisi od tipa uređaja, veličine kapi tečne faze i osobina odnosno rastvorljivosti komponenata koje se uklanjaju. Centrifugalni skruberi imaju najmanju efikasnost uklanjanja dok Venturi skruberi i skruberi sa pakovanim slojem mogu dostići efikasnost i od 99 % [5,9].

1. 1. Princip rada skrubera

Princip rada skrubera sa pakovanim slojem (punjenjem) prikazan je na Slici 1.

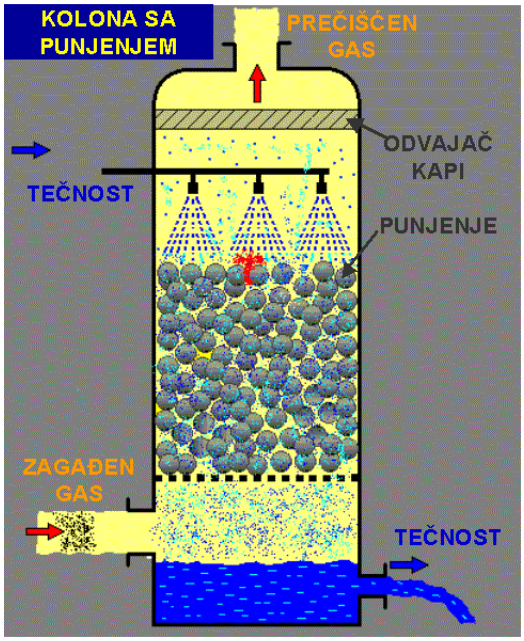

Slika 1. Šematski prikaz skrubera sa pakovanim slojem

Skruberi sa pakovanim slojem imaju sledeće karakteristike: (i) omogućavaju primenu velikih protoka tečnosti, (ii) vreme kontakta između gasa i tečnosti je dugo, (iii) maksimalni protoci gasa i tečnosti ograničeni su, za definisani presek kolone, plavljenjem i odnošenjem kapi, (iv) plavljenje nastaje kada brzina gasa, pri konstantnom protoku tečnosti, postane toliko visoka da sprečava protok tečnosti naniže kroz kolonu; u tački plavljenja postaje nemoguć suprotnostrujni tok gasa i tečnosti. Najčešći tipovi punjenja koja se koriste su lomljeni materijali, Rašigovi, Palovi, Lesingovi i spiralni prstenovi, Berlova i Intaloks (*Intalox*) sedla, metalne i plastične ljuske i strukture, gredice, lopte, mrežasto punjenje i drugi. Važne karakteristike punjenja koje se razmatraju prilikom projektovanja skrubera su cena, specifična površina po jedinici zapremine punjenja, otpor strujanju fluida, mehanička i hemijska otpornost i vek trajanja. Pad pritiska većine komercijalnih punjenja je od 200-800 Pa/$m_{visine\ sloja}$ i opada sa porastom poroznosti punjenja.

1. 2.Proračun skrubera sa pakovanim slojem

Prilikom proračuna skrubera, poznate veličine su protok i karakteristike ulaznog gasa koji se prečišćava, njegova temperatura, pritisak i pH vrednost. Sastav, odnosno koncentracija komponenata u izlaznom gasu, je definisan važećom zakonskom regulativom, a poznate veličine su još i sastav i temperatura tečnosti koja se koristi za apsorpciju. Prilikom proračuna skrubera određuje se potreban protok tečnosti, prečnik kolone koji je neophodan da se izvrši proces apsorpcije, kao i visina pakovanog sloja. Takođe, potrebno je uspostaviti odgovarajući odnos protoka tečnosti i gasa za stabilan rad uređaja.

Određivanje potrebnog protoka tečnosti. Protoci i sastavi ulaznih i izlaznih struja su određeni materijalnim bilansom, odnosno operativnom linijom, jednačina (1):

$$Y_1 - Y_2 = \frac{L_m}{G_m}\left(X_2 - X_1\right) \tag{1}$$

gde su:

G_m / mol h^{-1} - molski protok inertne gasne faze,
L_m / mol h^{-1} - molski protok inertne tečne faze,
X - molski odnos rastvorene supstance u čistoj tečnosti
Y - molski odnos rastvorene supstance u čistom gasu
1, 2 - ulazna i izlazna struja, redom.

Za zadate procesne parametre na osnovu ravnotežne i operativne može se odrediti minimalni odnos protoka tečne i gasne faze $(L_m/G_m)_{min}$ odakle i minimalni protok tečne faze. Realna vrednost protoka tečne faze je 25-100 % veća od minimalnog protoka. Najčešće se prilikom projektovanja skrubera koristi vrednost protoka 50 % veća od minimalnog [9].

Određivanje prečnika kolone. Glavni parametar koji utiče na veličinu kolone sa pakovanim slojem je brzina gasa pri kojoj gas počinje da odnosi kapljice tečnosti ka vrhu kolone. Ako bi se protoci faza održavali konstantnim, a prečnik kolone smanjivao, u jednom trenutku tečnost bi počela da se zadržava u šupljinama pakovanja, mešanje između faza bi se smanjivalo, a pad pritiska rastao – odnos protoka u tom trenutku se naziva tačka opterećenja. Daljim smanjivanjem prečnika kolone, tečnost ispunjava sve šupljine i formira sloj iznad pakovanja. U tom trenutku pad pritiska značajno poraste, a kontakt faza je minimalan: ovo stanje se naziva plavljenje [9]. Utrđeno je da su optimalno projektovane kolone kada je brzina gasa 50-75 % od brzine plavljenja.

Procedura za određivanje optimalnog prečnika kolone bazira na generalizovanoj korelaciji za pad pritiska (*engl.* Generalized Pressude Drop Correlation, GPDC) prikazanoj na Slici 2 [4].

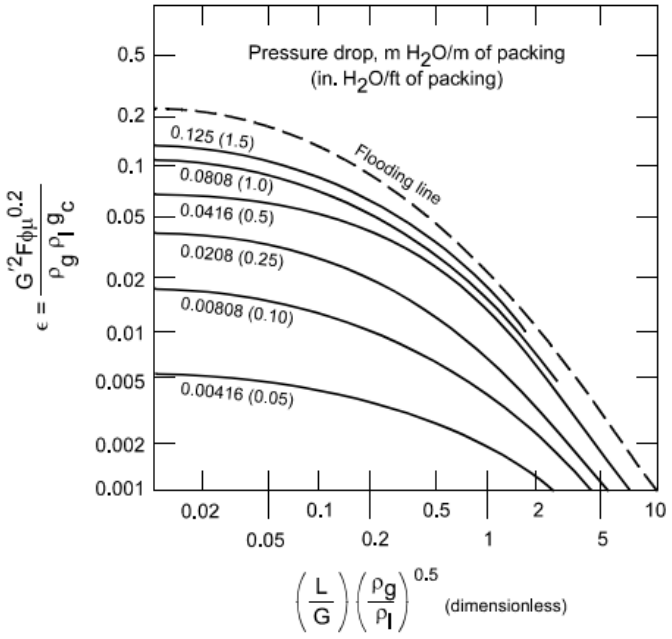

Slika 2. Generalizovana korelacija za pad pritiska i plavljenje [4]

Sa Slike 2 se vidi da je *x*-osa funkcija svojstva gasa i tečnosti dok *y*-osa pored gasa i tečnosti u razmatranje uzima i karakteristike pakovanja poput sferičnosti i poroznosti. Isprekidana linija predstavlja liniju plavljenja i daje minimalni prečnik kolone pri kome neće doći do plavljenja.

Procedura proračuna je da se za izračunatu vrednost apscise očitava koeficijent ε, za liniju plavljenja. Preuređivanjem jednačine na ordinati, izračunava se G' - maseni protok gasa po jedinici površine poprečnog preseka pri plavljenju, odnosno maseni fluks gasa pri plavljenju, jednačina (2):

$$G' = \left[\frac{\varepsilon \rho_g \rho_l g}{a \phi \mu_l^{0,2}}\right]^{0,5} \tag{2}$$

gde su:

ρ_g i ρ_l / kg m^{-3} - gustina gasne i tečne faze, redom,
a / m^2 m^{-3} -specifična površina pakovanja,
ϕ - odnos specifične težine tečnosti i specifične težine vode

μ_l / Pa s - viskoznost tečne faze
g / m s^{-2} - gravitaciona konstanta,

Realna vredost fluksa gasne faze se usvaja kao 50-75 % ove vrednosti. Iz poznate vrednost operativnog protoka gasne faze i vrednosti fluksa, izračunava se površina poprečnog preseka cilindrične kolone A, jednačina (3):

$$A=\frac{G'}{G_{\text{radni}}} \tag{3}$$

Određivanje visine pakovanog sloja. Visina pakovanog sloja utiče na brzinu i efikasnost apsorpcije i izračunava se prema jednačini (4):

$$Z=\frac{G'}{K_{OG}aP}\int_{Y_2}^{Y_1}\frac{\mathrm{d}Y}{\left(Y-Y^*\right)} \tag{4}$$

gde su:

Z / m - visina pakovanog sloja
K_{OG} / mol m^{-2} s^{-1} Pa^{-1} - koeficijent prolaza mase izražen u jedinicama gasne faze
a / m^2 m^{-3} - specifična površina punjenja
P / Pa - ukupan pritisak u sistemu
Y_1 - ulazni molski odnos zagađujućeg gasa
Y_2 - izlazni molski odnos zagađujućeg gasa
Y^* - molski odnos zagađujućeg gasa u stanju ravnoteže

U Jednačini (4) množilac integrala ima dimenzije dužine (m) i definisan je kao visina prenosne jedinice, dok je izraz pod integralom bezdimenzionalan i predstavlja broj prenosnih jedinica potrebnih za formiranje ukupne visine, tako da je visina pakovanja, jednačina (5):

$$Z = \text{HTU}\times\text{NTU} \tag{5}$$

gde su:

HTU, m - visina prenosne jedinice, m
NTU, m - broj prenosnih jedinica.

Ukoliko dolazi do odigravanja hemijske reakcije ili je zagađujuća materija izuzetno rastvorljiva, kao što je slučaj u ovom radu, broj prenosnih jedninica zavisi samo od molskog udela gasa na ulazu i izlazu iz kolone, jednačina (6) [9]:

$$\text{NTU}=\ln\frac{Y_1}{Y_2} \tag{6}$$

Za određivanje visine prenosne jedinice mogu se koristiti brojne korelacije koje se mogu naći u literaturi [4-6,8], a zasnivaju se na poznavanju vrste pakovanja, protocima i karakteristikama tečne i gasne faze i koncentraciji zagađujućeg gasa.

U ovom radu predstavljen je proračun skrubera sa pakovanim slojem za uklanjanje amonijaka iz otpadnih gasova hemijske industrije [10-14]. Amonijak se iz vazduha može ukloniti apsorpcijom zahvaljujući njegovoj dobroj rastvorljivosti u vodi. Sama apsorpcija se najčešće pospešuje hemijskom reakcijom sa sumpornom kiselinom kako bi se povećala efikasnost procesa. Punjenje koje se nalazi u skruberu povećava dodirnu površinu između gasa i tečnosti koja se raspršuje na vrhu skrubera i teče naniže prekrivajući pakovani sloj i zidove kolone. U procesu apsorpcije dolazi do prenosa zagađujuće materije iz gasa u tečnost i na vrhu kolone se dobija prečišćen gas.

2. METODA PRORAČUNA SKRUBERA – KATMAR SOFTVER

Program "Packed Column Calculator" – Katmar softver (Katmar Software Inc, Kanada) omogućava proračun potrebnog prečnika skrubera sa pakovanim slojem, na osnovu dozvoljenog pada pritiska, udaljenosti od uslova plavljenja ili udaljenosti od maksimalnog radnog kapaciteta (*engl.* Maximum Operating Capacity, MOC). Za kolone poznatog prečnika se može proceniti uticaj promene radnih uslova ili uticaj korišćenja različitih pakovanja [15].

Program uključuje dve metode projektovanja koje se najčešće koriste. Prva od njih je generalizovana korelacija pada pritiska (*engl.* Generalized Pressure-Drop Correlation, GPDC), koju je prvobitno razvio Leva [16] i ovde se koristi u obliku koji je dao Ekert (Eckert) [17]. Drugi metod je onaj koji je razvio Robins (Robbins) [18]. Obe korišćene korelacije su empirijske.

Ove dve metode se međusobno dopunjuju u tome što je GPDC zasnovan na originalnom radu koji koreliše podatke o plavljenju koji su zatim prošireni na režim manjih protoka tečnosti, dok se Robinsova metoda zasniva na protoku gasa kroz suve slojeve pakovanja.

Drugi razlog za korišćenje dve metode je da se ukaže da metode projektovanja pakovanih kolona nisu apsolutne i da različite korelacije daju različite odgovore. Ovo ima veze sa prirodom procesa koliko i sa razlikama između korelacija.

Kada se metode primene za kolone projektovane za tipične režime rada, različite korelacije će težiti da daju slične rezultate i dodatno će potvrditi pouzdanost proračuna. Međutim, kada se koriste na granicama mogućih operativnih režima, rezultati će se najčešće razlikovati, što ukazuje da se radi u rizičnijoj oblasti i da je naknadna provera potrebna i opravdana [14].

3. REZULTATI I DISKUSIJA

U skruber, sa donje strane, ulazi vazduh temperature 65 °C, na pritisku 101 kPa, zapreminskog protoka 20.000 $m^3\ h^{-1}$, koji sadrži 1400 mg m^{-3} (2000 ppm) amonijaka, NH_3. Kao tečna faza se u skruberu koristi sumporna kiselina koncentracije 70 %, masenog protoka 27.964 kg h^{-1} (zapreminski protok 17,6 $m^3\ h^{-1}$). Prilikom kontakta gasne i tečne faze dolazi do hemisorpcije amonijaka sumpornom kiselinom i do stvaranja amonijum sulfata, $(NH_4)_2SO_4$, Jednačina (7):

$$2NH_3+H_2SO_4 \rightarrow (NH_4)_2SO_4 \quad (7)$$

Skruber je projektovan tako da se proces uklanjanja amonijaka odvija u dva stepena, kao što je prikazano na Slici 3.

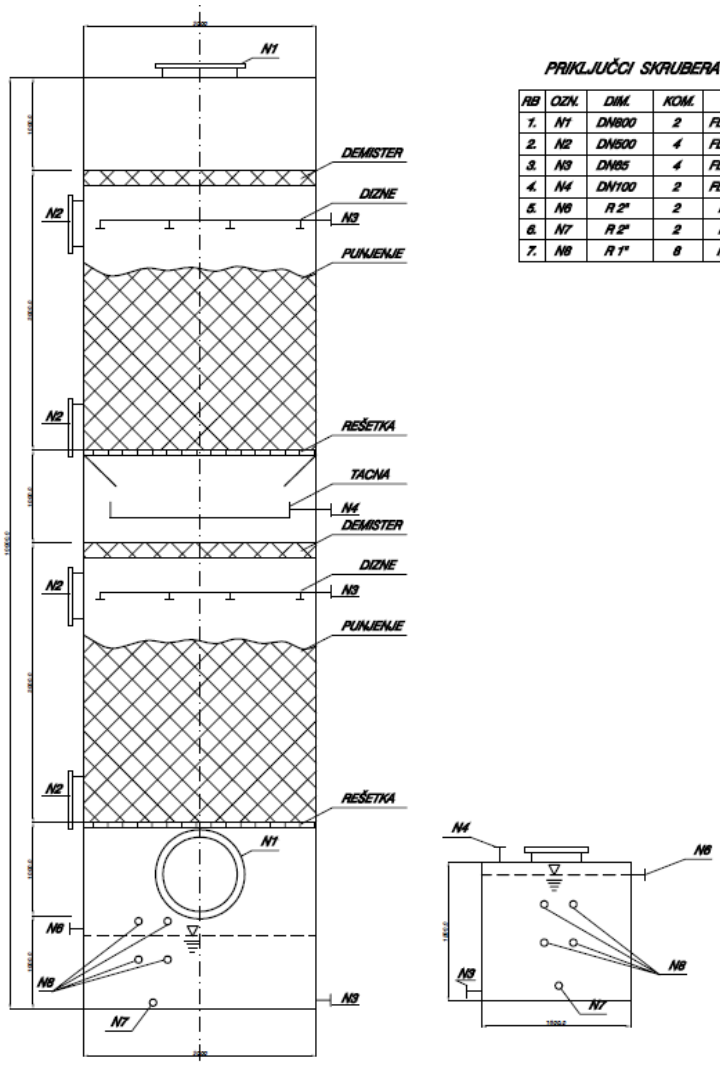

PRIKLJUČCI SKRUBERA

RB	OZN.	DIM.	KOM.	TIP
1.	N1	DN800	2	FLANŠNA
2.	N2	DN500	4	FLANŠNA
3.	N3	DN65	4	FLANŠNA
4.	N4	DN100	2	FLANŠNA
5.	N5	R 2"	2	MUF
6.	N7	R 2"	2	MUF
7.	N8	R 1"	8	MUF

Slika 3. Prikaz predloženog skrubera sa potrebnim dimenzijama (D_{skrub} = 2,0 m; H_{ukupno} = 10,0 m)

U prvom stepenu vrši se izdvajanje najveće količine prisutnog amonijaka, dok se u drugom stepenu vrši poliranje dobijenog gasa, kako bi se garantovalo postizanje maksimalno dozvoljenih koncentracija amonijaka u gasu koji se ispušta u okolinu. Projektovana izlazna koncentracija NH_3 u izlaznom gasu iz skrubera iznosi 3,5 mg m^{-3}, pri ulaznoj koncentraciji od 1400 mg m^{-3}. Efikasnost svakog od stepena skrubera iznosi 95 %, tako da je ukupna efikasnost oba stepena 99,8 %.

Kao punjenje u prikazanoj koloni, odabrani su Palovi prstenovi dimenzije 50 mm izrađeni od polipropilena (Slika 4).

PLASTIC PALL RINGS P-Series	The PALL RING COMPANY
Veličina	50 mm (2“)
Specifična površina	100 m^2 m^{-3}
Slobodna površina	95 %
Nasipna gustina	45 kg m^{-3}
Br. komada po jedinici zapremine	5960 m^{-3}
Faktor pakovanja	80 m^{-1}

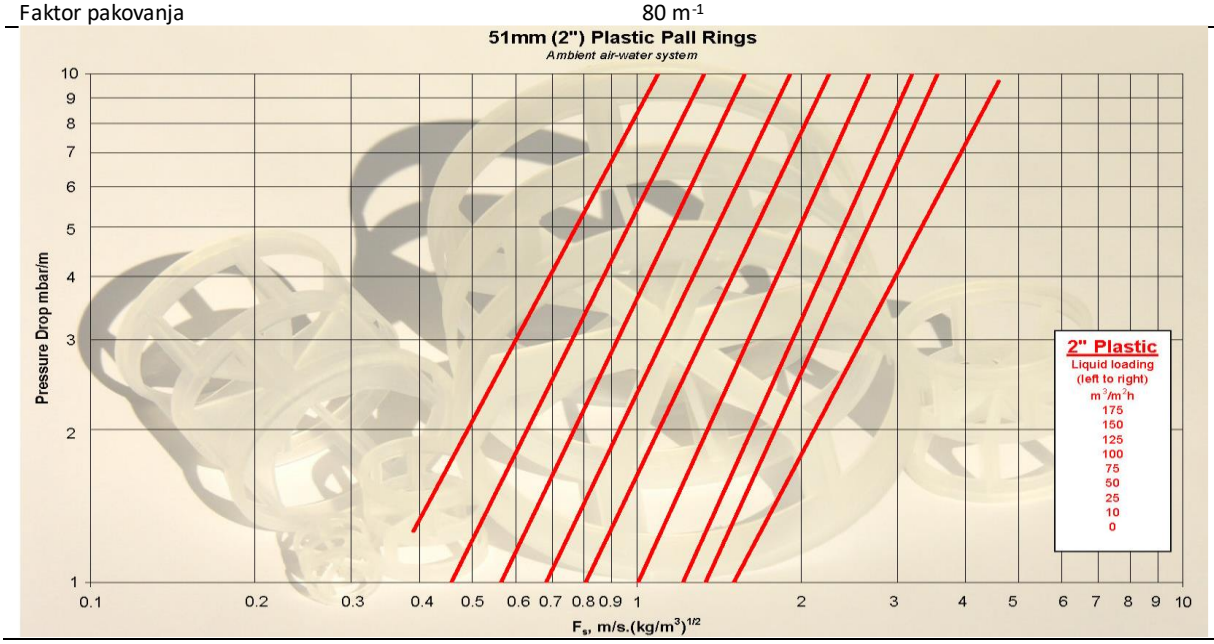

Slika 4. Odabrano punjenje – Palovi prstenovi od polipropilena dimenzije 50 mm, proizvođač: The Pall Ring Company Ltd., UK (https://www.pallrings.co.uk/products/pall-rings-plastic/) [19] *($Fs=U_{gas}\,\rho_{gas}^{0,5}$, (m s^{-1})(kg m^{-3})^{0,5}, F-faktor za gas)*

U cilju postizanja visoke efikasnosti procesa uklanjanja NH_3 iz gasne faze (veće od 90 % u svakom od stepena) potrebno je održavati pH vrednost rastvora koji recirkuliše na vrednosti manjoj od 2. Iz tog razloga potrebno je dodavati 110 kg h^{-1} (68 dm^3 h^{-1}) 70 % sumporne kiseline na dno stepena 1, kao i 5,5 kgh^{-1} (3,5 dm^3 h^{-1}) 70 % sumporne kiseline na dno stepena 2, kao što je prikazano u Tabeli 1.

Kao što se iz Tabele 1 može videti, postizanje pH vrednosti rastvora < 2 moguće je ostvariti i korišćenjem sumporne kiseline nižih koncentracija.

Tabela 1. Potrebno dovođenje rastvora H_2SO_4 i odvođenje otpadnog rastvora iz skrubera za različite koncentracije kiseline

		Koncentracija H_2SO_4, %					
		30		40		70	
		dovođenje kiseline	odvođenje otpadnog rastvora	dovođenje kiseline	odvođenje otpadnog rastvora	dovođenje kiseline	odvođenje otpadnog rastvora
stepen 1	Maseni protok, kg h^{-1}	256	282	192	218	110	136
	Zapreminski protok, dm^3 h^{-1}	210	221	150	171	68	107
stepen 2	Maseni protok, kg h^{-1}	13	14	10	11	5,5	7
	Zapreminski protok, dm^3 h^{-1}	10	11	7,5	8,5	3,5	5

U Tabeli 1 su prikazane vrednosti potrebnih protoka dodavanja kiseline na dno skrubera za koncentracije 30, 40 i 70%, kao i vrednosti protoka otpadnog rastvora za iste koncentracije korišćene kiseline. Treba naglasiti da svako snižavanje koncentracije sumporne kiseline koja se koristi u recirkulaciji dovodi do potrebe za odvođenjem veće količine otpadnog rastvora iz skrubera, koji je u tom slučaju nižeg nivoa zasićenja. Tako, na primer, ukoliko se koristi sumporna kiselina koncentracije 70 %, iz prvog stepena skrubera je potrebno odvoditi 107 dm^3 h^{-1} rastvora amonijum sulfata (koji predstavlja otpadnu vodu), dok ukoliko se koristi sumporna kiselina koncentracije 30 %, ta vrednost iznosi 221 dm^3 h^{-1}.

Imajući u vidu količinu otpadnog rastvora koji nastaje u skruberu i koji je potrebno odvoditi na dalji tretman, usvojeno je korišćenje sumporne kiseline koncentracije 70 %. Protok kiseline koja se dodaje se automatski reguliše podešavanjem pH vrednosti rastvora na vrednost < 2, te zavisi od koncentracije NH_3 u ulaznom gasu, kao i od koncentracije kiseline koja se koristi.

Ukoliko se koristi 70% H_2SO_4, iz skrubera se odvodi otpadni rastvor nastalog amonijum sulfata, i to iz prve faze 136 kg h^{-1} (oko 107 dm^3 h^{-1}, u zavisnosti od koncentracije nastalog amonijum sulfata) i iz druge faze 7 kg h^{-1} (oko 5,5 dm^3 h^{-1}). Izlazni protoci otpadnog rastvora amonijum sulfata regulišu se kontrolisanjem nivoa tečnosti u rezervoarima na dnu obe faze u skruberu.

Treba imati u vidu da je sumporna kiselina veoma slabo isparljivo jedinjenje. Zbog izuzetno niskih vrednosti napona pare H_2SO_4, a naročito SO_3 [18] smatra se da su gubici kiseline usled isparavanja praktično jednaki nuli na atmosferskom pritisku i na temperaturama na kojima će se odvijati proces apsorpcije amonijaka u skruberu. Takođe, prisustvo amonijaka u rastvoru dodatno stabilizuje molekule sumporne kiseline, reagujući sa njima uz nastajanje amonijum-sulfata, što dodatno smanjuje isparljivost.

Termička razgradnja sumporne kiseline, prema hemijskoj Jednačini (8):

$$H_2SO_4 \rightarrow SO_{3(g)}+H_2O_{(g)} \quad (8)$$

započinje na temperaturi između 300 i 330 °C, i završava se na oko 700°C. S obzirom da se proces hemisorpcije amonijaka u skruberu odvija na temperaturama od 62 do 70°C, nije moguća termička razgradnja sumporne kiseline, te tako ni pojava sumpornih oksida na izlazu iz skrubera.

Procesni parametri i proračunate dimenzije skrubera, za tri varijante prečnika prikazani su u Tabeli 2.

Tabela 2. Procesni parametri i dimenzije tri varijante prečnika skrubera

Procesni parametri			
Prečnik skrubera, m	2,0	2,1	2,2
Pritisak. kPa		101	
Temperatura gasa (Tg_{ul}), °C		62 do maksimalno 70	
Protok vazduha na Tg_{ul}, m^3 h^{-1}		20000	
Protok rastvora kiseline (20 % iznad minimalnog), m^3 h^{-1}	17,64	19,45	21,35
Zapreminski fluks gasa, m^3 m^{-2} h^{-1}	6366,20	5774,33	5261,32
Zapreminski fluks rastvora kiseline (20 % iznad minimalnog), m^3 m^{-2} h^{-1}		5,62	
Minimalni zapreminski fluks rastvora kiseline za adekvatno kvašenje punjenja, m^3 m^{-2} h^{-1}		4,68	
Odnos zapreminskih protoka tečnost/gas, dm^3 m^{-3}	0,88	0,97	1,07
*Gradijent pritiska u sloju punjenja skrubera (dijagram pritiska za odabrano punjenje), Pa m^{-1}	180	140	120
*Pad pritiska u sloju punjenja skrubera u jednom stepenu (dijagram pritiska za odabrano punjenje), Pa	450	350	300
Gradijent pritiska u skruberu pri plavljenju, Pa m^{-1}		2019,3	
Koncentracija rastvora kiseline, zap.%		70	
Koncentracija NH_3 ulaz, mg m^{-3}		1400	

Procesni parametri			
Prečnik skrubera, m	2,0	2,1	2,2
Koncentracija NH_3 izlaz, mg m^{-3}		14	
Efikasnost skrubera, &		99	
Dimenzije skrubera			
Prečnik, m	2,0	2,1	2,2
Visina punjenja stepen 1, m		2,5	
Visina punjenja stepen 2, m		2,5	
Ukupna visina skrubera, m	10	10,5	11
Punjenje: Palovi prstenovi – podaci dati na Slici 4			

*Korišćen je dijagram za pad pritiska dat u specifikacijama odabranog punjenja (Slika 4)

Proračun procesnih parametara skrubera je rađen primenom Katmar softvera. Na Slici 5 prikazan je primer proračuna za prečnik skrubera od 2 m za ulazne podatke navedene u Tabeli 2.

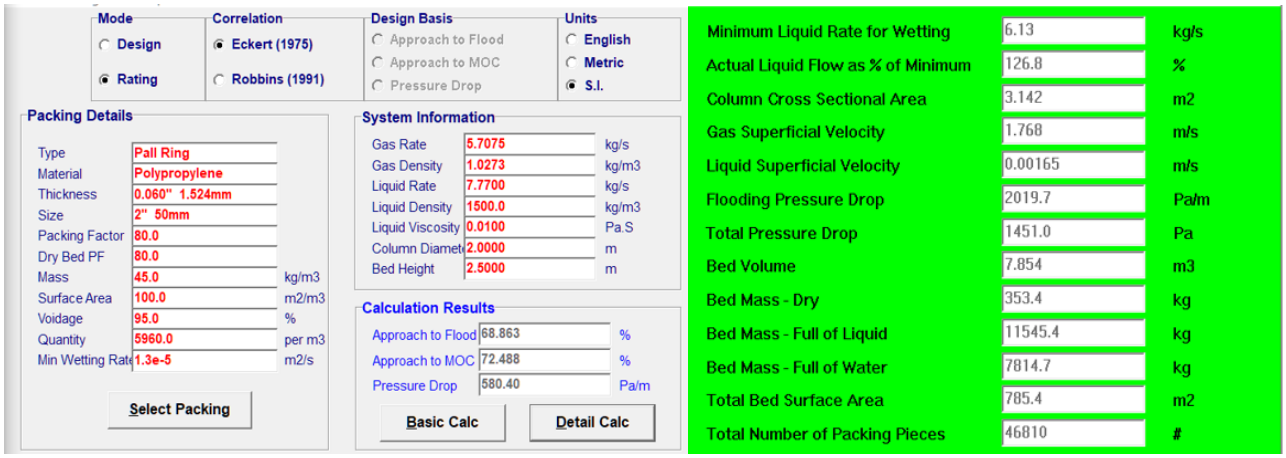

Slika 5. Rezultati proračuna primenom Katmar softvera za skruber sa rastvorom sumporne kiseline (crveno-ulazni podaci, sivo-rezultat proračuna)

Program omogućava izračunavanje potrebnog prečnika za nove kolone (opcija Design u programu), koriste ći dozvoljeni pad pritiska, ili približavanje plavljenju ili približavanje maksimalnom radnom kapacitetu kao ulazni (zadati) parametar. Postojeće kolone poznatog prečnika se takođe mogu analizirati za predložene promene u radnim uslovima (opcija *Rating* u programu, videti Sliku 5).

U softveru je omogućena i vizualizacija dobijenih rezultata na dijagramima. Program uključuje mogu ćnost prikazivanja krivih i radne tačke u Generalizovanoj korelaciji za pad pritiska u formatu koji je predložio Ekert [16], (Slika 6). Na ovom dijagramu je data kriva plavljenja i standardne linije za pad pritiska. Na operativnom dijagramu se odmah može videti osetljivost na promene brzina protoka gasa i tečnosti (Slika 7).

Kao što se može videti iz Tabele 2, gradijent pritiska (Pa m^{-1}), a samim tim i ukupni pad pritiska (Pa) u koloni se smanjuje povećanjem prečnika kolone. Smanjenje ukupne visine sloja punjenja ne utiče značajno na smanjenje ukupnog pada pritiska (gradijent pritiska ostaje nepromenjen za isti prečnik kolone). Prema dijagramu iz specifikacije odabranog punjenja - Palovi prstenovi 50 mm, gradijent pritiska je oko 180 Pa m^{-1} za D_c = 2 m, a ukupni pad pritiska je oko 900 Pa u sloju punjenja u oba stepena (2×2,5 m). Prema istom dijagramu, za D_c = 2,2 m gradijent pritiska je oko 120 Pa m^{-1}, a ukupni pad pritiska kroz sloj punjenja u oba stepena je oko 600 Pa.

Treba imati u vidu da što je veći prečnik kolone potreban je i veći minimalni protok tečnosti za adekvatno kvašenje punjenja, za kolonu D_c = 2 m treba 7,77 kg s^{-1} tečnosti, a za D_c =2,2 m treba 9,40 kg s^{-1}, što je za 20 % veći protok u odnosu na D_c =2 m (Tabela 2). Da bi se u kolonu unelo dovoljno tečnosti za efikasno formiranje vlažnog filma tečnosti preko cele površine pakovanja, kao smernica za rad i dizajn kolone koristi se minimalna brzina vlaženja (*engl.* minimum wetting rate, MWR). Minimalna brzina vlaženja je funkcija površine materijala za pakovanje i fizičkih svojstava tečnosti, posebno viskoznosti i površinskog napona. Pakovanje treba testirati na kvašenje u radu pre nego što se završi projektovanje kolone i izbor pakovanja. Pojedini proizvođači pakovanja daju u specifikacijama i vrednost MWR.

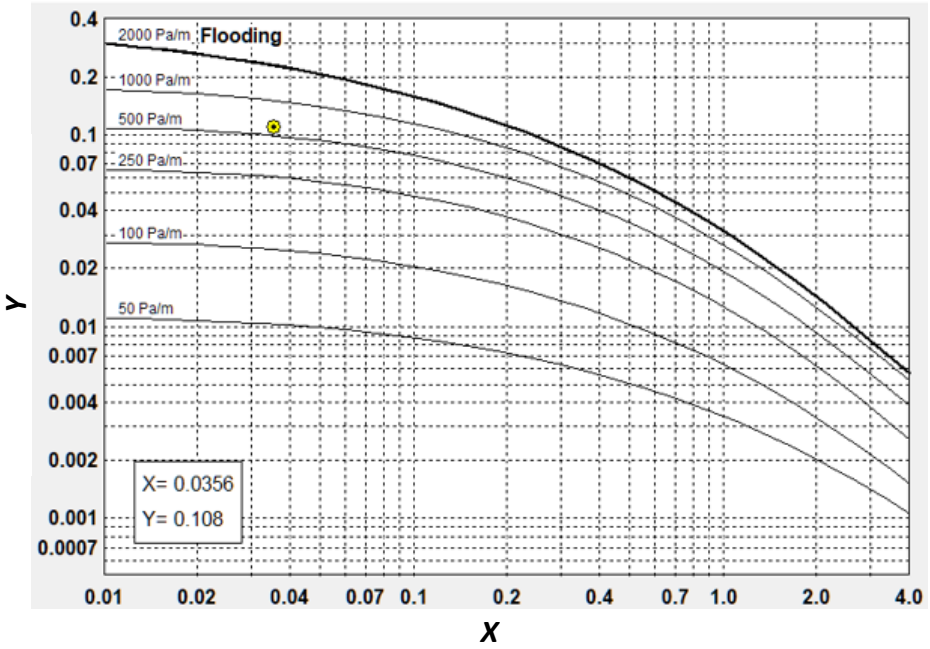

$$X=\left(\frac{L}{G}\right)\left(\frac{\rho_g}{\rho_l}\right)^{0,5},\quad Y=\left(\frac{G^2}{g}\right)a\mu_l^{0,2}\left(\frac{\left(\rho_w/\rho_l\right)^2}{\rho_g\rho_l}\right)$$

Slika 6. Maseni protok gasne faze u funkciji masenog protoka tečne faze dobijene primenom Katmar softvera (Generalizovana korelacija za pad pritiska [16])

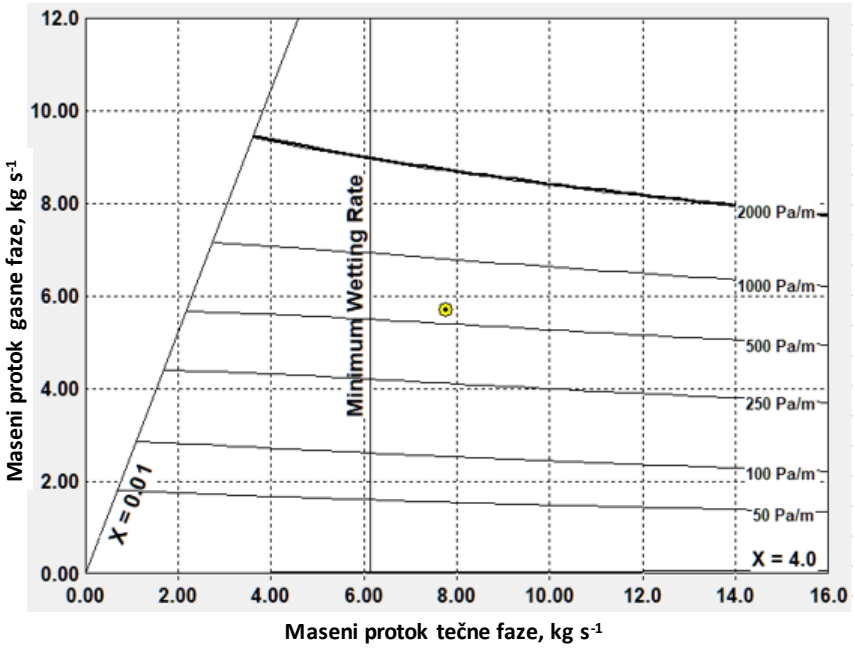

Slika 7. Operativni dijagram: maseni protok gasne faze u funkciji masenog protoka tečne faze dobijen primenom Katmar softvera

Sa aspekta protoka tečne faze prečnik kolone D_c = 2 m zadovoljava, a prema specifikaciji punjenja datoj na Slici 4 pad pritiska kroz ukupnu visinu sloja punjenja bi bio oko 900 Pa. S obzirom da na ukupni pad pritiska utiču, pored punjenja (koje predstavlja najznačajniji otpor) i interni delovi kolone, kolena, odvajači kapi i sl, potrebno je u saradnji sa proizvođačem opreme odabrati optimalan prečnik kolone, koji će zadovoljiti eventualno ograničenje po pitanju maksimalno dozvoljenog pada pritiska, a sa druge strane omogućiti optimalan rad skrubera sa stanovišta neophodnog protoka tečne faze.

4. ZAKLJUČAK

Optimalni procesni parametri i dimenzije uređaja za proces uklanjanja amonijaka korišćenjem skrubera sa pakovanim slojem određeni su razmatranjem materijalnog i energetskog bilansa procesa, na osnovu izračunavanja koeficijenata prenosa mase između gasne i tečne faze, kao i na osnovu proračuna potrebnog protoka tečne faze u skruberu koja obezbeđuje adekvatno kvašenje punjenja i pad pritiska u koloni. Zaključeno je da se gradijent pritiska u koloni, a samim tim i ukupni pad pritiska smanjuje povećanjem prečnika kolone. Smanjenje ukupne visine sloja punjenja ne utiče značajno na smanjenje ukupnog pada pritiska (gradijent pritiska ostaje nepromenjen za isti prečnik kolone). Treba imati u vidu da što je veći prečnik kolone potreban je i veći minimalni protok tečnosti za adekvatno kvašenje punjenja. U radu su analizirane kolone prečnika D_c = 2 m; 2,1 i 2,2 m. Na osnovu analize potrebnog protoka tečne faze odabran je prečnik kolone D_c = 2 m. U ovom slučaju pad pritiska u sloju iznosi oko 900 Pa. Međutim, na ukupni pad pritiska utiču, pored punjenja (koje predstavlja najznačajniji otpor) i interni delovi kolone, kolena, odvajači kapi i sl, te se optimalan prečnik kolone koji će zadovoljiti i eventualno ograničenje po pitanju maksimalno dozvoljenog pada pritiska, mora odabrati u saradnji sa proizvođačem opreme.

Prikazana metoda ima veliki značaj u projektovanju opreme za uklanjanje zagađujućih gasova, a dobijeni rezultati pokazuju da se ona uspešno može koristiti u projektovanju skrubera za prečišćavanje gasova sa visokim sadržajem amonijaka.

5. NOMENKLATURA

Latinična slova

a / m^2 m^{-3} - specifična površina punjenja
A / m^2 - površina poprečnog preseka kolone
D / m - prečnik kolone
g / m s^{-2} - gravitaciona konstanta
G / kg h^{-1} - maseni protok gasne faze
G_m / mol h^{-1} - molski protok inertne gasne faze
G' / kg m^{-2} h^{-1} - maseni fluks gasne faze pri plavljenju
HTU, m - visina prenosne jedinice
K_{OG} / mol m^{-2} h^{-1} Pa^{-1} - koeficijent prolaza mase izražen u jedinicama gasne faze
L_m / mol h^{-1} - molski protok inertne tečne faze
L / kg h^{-1} - maseni protok tečne faze
NTU, m - broj prenosnih jedinica
P / Pa - pritisak
F_s / (m s^{-1})(kg m^{-3})^{0,5} - faktor za gas
X - molski odnos rastvorene supstance u čistoj tečnosti
Y - molski odnos rastvorene supstance u čistom gasu
Z / m - visina sloja

Grčki simboli

μ_l / Pa s - viskoznost tečne faze
ϕ / - odnos specifične težine tečnosti i specifične težine vode
ρ_g / kg m^{-3} - gustina gasne faze
ρ_l / kg m^{-3} - gustina tečne faze

Indeksi

1 - ulaz
2- - izlaz
* - stanje ravnoteže
G - gas
L - tečnost

REFERENCES

[1] Bhatia MV. *Packed Tower and Absorption Design*. In Cheremisinoff PN, Young RA, eds. *Air Pollution Control and Design Handbook.* New York, NY: Marcel Dekker; 1977. https://doi.org/10.1007/978-981-13-7488-3

[2] Richards JR. *Control of Gaseous Emissions*. *APTI Course 415*. U.S. Environmental Protection Agency; 1995. https://www.4cleanair.org/wp-content/uploads/APTI/415combined.pdf

[3] Srivastava RK, Jozewicz W, Singer C. SO_2 scrubbing technologies. *Environ Prog.* 2001; 20(4): 219-28. https://doi.org/10.1002/ep.670200410

[4] *Wet Scrubber System Study*. NTIS Report PB-213016; U.S. EPA, Research Triangle Park, NC, 1972. https://nepis.epa.gov/Exe/ZyNET.exe/9101LF9J.txt?ZyActionD=ZyDocument&Client=EPA&Index=Prior%20to%201976&Docs=&Query=&Time=&EndTime=&SearchMethod=1&TocRestrict=n&Toc=&TocEntry=&QField=&QFieldYear=&QFieldMonth=&QFieldDay=&UseQField=&IntQFieldOp=0&ExtQFieldOp=0&XmlQuery=&File=D%3A%5CZYFILES%5CINDEX%20DATA%5C70THRU75%5CTXT%5C00000023%5C9101LF9J.txt&User=ANONYMOUS&Password=anonymous&SortMethod=h%7C-&MaximumDocuments=1&FuzzyDegree=0&ImageQuality=r75g8/r75g8/x150y150g16/i425&Display=hpfr&DefSeekPage=x&SearchBack=ZyActionL&Back=ZyActionS&BackDesc=Results%20page&MaximumPages=1&ZyEntry=1&slide#

[5] Joseph GTPE, Beachler DS. *Scrubber System Operation Review*., 2nd ed., North Carolina State University; 1998. https://www.studocu.com/es-mx/document/universidad-veracruzana/operaciones-fisicas-unitarias/design-review-of-absorbers-used-for-gaseous-pollutants-removal/10718576

[6] Hesketh HD. Wet scrubbers. 2nd ed., New York, NY: Routledge; 2017. https://doi.org/10.1201/9780203733899

[7] U.S. Environmental Protection Agency, 1998. Wet-Film (Packed Tower) Scrubbers. 2012; 1-15. www.yosemite.epa.gov/oaqps/eogtrain.nsf.gov

[8] Schifftner KC, Hesketh HE. *Wet scrubbers*. United States: 1983. https://www.osti.gov/biblio/6626241

[9] McCabe WI, Smith JC, Harriot P *Unit Operations of Chemical Engineering*, McGraw-Hill International Editions, New York, 1993. ISBN 0-07-044844-2. https://evsujpiche.files.wordpress.com/2014/06/unit-operations-of-chemical-engineering-5th-ed-mccabe-and-smith.pdf

[10] Strigle RE Jr. *Packed Tower Design and Applications - Random and Structured Packings*. 2nd ed., Houston, London, Paris, Zurich, Tokyo: Gulf Publishing Company; 1994. ISBN 0-88415-179-4. https://www.scribd.com/doc/81675448/Packed-Tower-Design-and-Applications-R-F-Strigle-1994

[11] Phillips J. Control and pollution prevention options for ammonia emissions: VIGYAN Inc. (Technical Report), United States; 1995. https://www.osti.gov/biblio/104094

[12] Hadlocon LJ, Manuzon RB, Zhao L. Optimization of ammonia absorption using acid spray wet scrubbers. *Transactions of the ASABE*. 2014; 57(2): 647-659. https://doi.org/10.13031/trans.57.10481

[13] Ashtari AK, Majd AM, Riskowski GL, Mukhtar S, Zhao L. Removing ammonia from air with a constant pH, slightly acidic water spray wet scrubber using recycled scrubbing solution. *Front Environ Sci Eng*. 2016; 10; 3. https://doi.org/10.1007/s11783-016-0869-3

[14] Piche S, Larachi F, Grandjean BPA. Flooding Capacity in Packed Towers: Database, Correlations, and Analysis. *Ind. Eng Chem Res*. 2001; 40: 476-487. https://doi.org/10.1021/ie000486s

[15] Packed Column Calculator, Version 2.1, March 2010, Katmar Software, http://www.KatmarSoftware.com

[16] Leva M. Tower Packings and Packed Tower Design. United States Stoneware Company: Akron, OH, 1953. https://babel.hathitrust.org/cgi/pt?id=mdp.39015000476294&seq=11

[17] Eckert JS. How tower packings behave. *Chem Eng*. 1975; 2(8): 70-76. https://www.coursehero.com/file/p5fbd1p/Eckert-J-S-1975-How-tower-packings-behave-Chemical-Engineering-v-82-pp-70-Ellis/

[18] Robbins L. Improve pressure drop prediction with a new correlation. *Chem Eng Prog*. 1991; 87(5): 87-90. ISSN 0360-7275. https://api.semanticscholar.org/CorpusID:113682503

[19] The Pall Ring Company Ltd., UK. https://www.pallrings.co.uk/products/pall-rings-plastic/

Design and optimization of a packed bed scrubber for purification of waste gas containing ammonium

Zorana Lj. Arsenijević[1], Ivona R. Radović[2], Mirjana Lj. Kijevčanin[2] i Tatjana S. Kaluđerović Radoičić[2]

[1]University of Belgrade, Institute of Chemistry, Technology and Metallurgy, National Institute of the Republic of Serbia, Belgrade, Serbia
[2]University of Belgrade, Faculty of Technology and Metallurgy, Belgrade, Serbia

(Technical paper)

Abstract

In this work, a two-stage packed bed scrubber was designed and optimized for purification of industrial waste gas containing ammonia at a concentration of 1400 mg m-3. Basic material balance equations, equilibrium data, and the generalized pressure drop correlation were used for the calculation. For the analysis of different configurations, Katmar software was utilized, which uses the generalized pressure drop correlation in order to calculate the scrubber diameter based on the allowable pressure drop and proximity to flooding conditions. It was found that optimal results are achieved in a two-stage device, using 70 vol.% sulfuric acid for chemisorption of ammonia. Pall rings, 50 mm in size and made of polypropylene, were selected as a column packing. Performances of scrubbers of three column diameters (i.e., Dc=2; 2.1 and 2.2 m) were analyzed. From the aspect of the liquid phase flow, the column diameter of 2 m provides satisfactory results. According to the packing specifications, the pressure drop through the packing layer would be about 900 Pa. It was found that the pressure gradient, and therefore the total pressure drop in the column decreases with increasing the column diameter. However, as the diameter of the column increases, the minimum flow rate of the liquid phase required to wet the packed bed increases, so the required liquid flow rate increases. Taking into account all of the analyzed process parameters, as well as the required purification degree of the waste gas, the optimal configuration of the device was proposed.

Keywords: absorption; two-stage scrubber; packed bed; ammonia removal